CYLINDRICAL MICROWAVE RESONATOR SENSORS FOR MEASURING MATERIALS UNDER FLOW

Ebbe Gustaf Nyfors

Report S243
May 2000

Dissertation for the degree of Doctor of Science in Technology to be presented with due permission for public examination and debate in Auditorium S4 at the Helsinki University of Technology (Espoo, Finland) on the 26th of May, 2000, at 12 o'clock noon.

Helsinki University of Technology
Department of Electrical and Communications Engineering
Radio Laboratory
P.O. Box 3000
FIN-02015 HUT, Finland
Telefax +358 9 4512152

ISBN 951-22-4983-9
ISSN 1456-3835
Libella Painopalvelu Oy

PREFACE

This thesis is based mainly on work carried out at Multi-Fluid (that in 1999 merged with Smedvig Technologies and became Roxar) in Stavanger, Norway, during the years 1995-1999, and in part on work carried out at the Radio Laboratory of the Helsinki University of Technology in the mid 1980's.

I wish to express my gratitude to Professor Martti Tiuri, who initially introduced me to the world of microwave sensors, to Professor Antti Räisänen, who was my supervisor, and to Professor Pertti Vainikainen, Dr.Tech. Matti Fisher, and Dr.Tech. Anssi Toropainen for many years of collaboration in the same research group, and for valuable comments and suggestions regarding the manuscript. I am also grateful to Dr.Tech. Taavi Hirvonen and Dr.Tech. Pekka Jakkula for interesting discussions regarding the HFSS simulations and applications of microwave sensors.

I wish to express my gratitude to Hans-Olav Hide, Arnstein Wee, and my other colleagues at Multi-Fluid/Roxar, who gave me the opportunity to work with the development of microwave sensors for the oil industry and fuelled my interest by providing research and development challenges, and for many interesting discussions regarding the applications. Especially I am grateful to Årstein Bringsvor, Jörn Bolstad, Jone Mellemstrand, and Stein Rörtveit, who have participated in the projects in various ways, and to Frode Knudsen, who initially asked the question that ignited the research on sectorial and semisectorial waveguides and their applications.

Finally, I wish to express my deep gratitude to my parents Marita and Börje, and my wife Brit and our children Malin and Emil for their support and patience.

Sandnes, January 3, 2000

Ebbe Nyfors

ABSTRACT

In this thesis the various possibilities of implementing microwave sensors for measureing materials flowing in pipes are studied, with special emphasis on full-bore resonator sensors. With such resonator sensors a method to confine the electromagnetic energy in the sensor must be used. Two main principles are studied in detail, the principle of resonance below cut-off, and the design using end grids. The first principle is shown to allow sensors with fairly open, or even completely nonintrusive structures to be designed. The second often involves sectorial or semisectorial structures. The waveguide modes in sectorial and semisectorial waveguides are therefore analyzed.

From the analysis of the sectorial waveguides came the idea for a new type of resonator sensor based on the principle of resonance below cut-off, the cylindrical fin resonator sensor (CFR). Various design aspects of this sensor are studied based on calculations, measurements, and simulations using the Hewlett-Packard HFSS software. A sensor suitable for measuring the composition of mixtures of hydrocarbons and water is developed based on the discussion. The sensor has a simple mechanical structure and is less expensive to manufacture than the end grid sensors.

Various designs of end grids are compared based on theoretical considerations, simulations, and measurements, and recommendations for optimized designs are given. The ring grid with eight sectors and a ratio of radii of roughly 40% is shown to provide the best isolation for a given thickness of the grid.

A new type of resonator sensor based on semisectorial resonance modes, is developed for measuring the mixture ratio of oil and water in an oil well deep in the ground, where the temperature and pressure are high. The sensor is designed for installation in the annulus (i.e. the annular space between the casing or liner and the production tubing in a well), where it can be used for measuring the inflow from a specific zone in a smart well. The emphasis is on matching the spatial constraints and achieving the desired frequency response, which is analyzed theoretically, simulated with the HFSS, and finally measured.

A humidity sensor for harsh environments is developed. The emphasis is on the choice of resonance mode to achieve the best immunity to contamination, and on the design of the end grids. Both calculations and field tests are presented.

Predicting the height of the resonance peak under changing measurement conditions is treated also on a general level in the thesis. This issue is important, when the coupling probes are designed based on results from simulations with HFSS.

The accuracy of the results obtained with HFSS is studied based on observations of scatter in the results, the dependence of the results on the convergence parameter ΔS, and by comparing the calculated and measured results. It is shown that the cut-off frequency and the resonant frequency are predicted with a higher accuracy than the quality factor.

CONTENTS

LIST OF SYMBOLS

A	attenuation, power transmission coefficient [dB], width of rectangular waveguide [m], arbitrary constant
a	power transmission coefficient, inner radius of pipe [m], larger radius of semisectorial waveguide [m], constant in polynomial
a_r	power transmission coefficient at resonant frequency
B	height of rectangular waveguide [m], arbitrary constant
B_{hp}	half-power width of resonance peak [Hz]
b	radius of center conductor in coaxial structure [m], radius of ring in ring grid [m], smaller radius of semisectorial waveguide [m], constant in polynomial
b_i	inner radius of ring (or finite thickness) in ring grid [m]
b_o	outer radius of ring (of finite thickness) in ring grid [m]
C	arbitrary constant
c	speed of light in vacuum [m/s], constant in polynomial
D	arbitrary constant
D_p	inner diameter of pipe [m]
DE	maximum deviation between polynomial model and solved data points
d	length of isolating pipe below cut-off [m], length of slanting part of fin [m], constant in polynomial
d_{cc}	distance between sensors used for cross-correlation [m]
dev	mean deviation between polynomial model and solved data points
d_g	length of end grid [m]
d_i	diameter of dielectric material in probe [m]
d_p	diameter of center pin in probe [m]
$\mathbf{E}$	electric field strength vector [V/m]
$\mathbf{E}_a$	electric field strength vector of aperture [V/m]
$\mathbf{E}_p$	electric field strength vector of probe [V/m]
$\mathbf{E}_r$	electric field strength vector of resonator [V/m]
E_0	arbitrary constant in equations for electric field strength
E_z	axial component of electric field strength [V/m]
E_φ	tangential component of electric field strength in cylindrical co-ordinates [V/m]
E_ρ	radial component of electric field strength in cylindrical co-ordinates [V/m]
e	constant in polynomial
f	frequency [Hz], constant in polynomial
f_c	cut-off frequency [Hz]
f_{cs}	cut-off frequency of resonance mode in sensor [Hz]

f_{c0}	cut-off frequency in empty pipe [Hz]
f_r	resonant frequency [Hz]
f_{r0}	resonant frequency of empty resonator [Hz]
$f_{r,nml}$	resonant frequency of TE_{nml} or TM_{nml}
f_{rt}	theoretical (calculated) resonant frequency [Hz]
$\mathbf{H}$	magnetic field strength vector [A/m]
$\mathbf{H}_a$	magnetic field strength vector of aperture [A/m]
$\mathbf{H}_l$	magnetic field strength vector of loop [A/m]
$\mathbf{H}_r$	magnetic field strength vector of resonator [A/m]
$\mathbf{H}_t$	tangential magnetic field strength vector [A/m]
H_0	arbitrary constant in equations for magnetic field strength
H_z	axial component of magnetic field strength [A/m]
H_φ	tangential component of magnetic field strength in cylindrical co-ordinates [A/m]
H_ρ	radial component of magnetic field strength in cylindrical co-ordinates [A/m]
h	height of fin [m]
$\mathbf{J}$	current dencity vector [A/m^2]
$\mathbf{J}_s$	surface current dencity vector [A/m]
K_e	relative error of peak height, when using Q_e instead of Q_{e1} and Q_{e2}
K_{ext}	relative error of peak height, when using Q_{ext} instead of Q_{e1} and Q_{e2}
k	wavenumber [1/m]
k_c	cut-off wavenumber [1/m]
k_{cr}	cut-off wavenumber of rectangular waveguide [1/m]
k_1	constant for sensor filled with MUT, defined by Eq. (4.6)
L	length of cavity sensor, fin, or transmission line [m]
l	total length of cables in FSA measurement circuit [m], 3rd index of a resonance mode
l_p	length of protruding part of center pin of probe (=intrusion) [m]
m	2nd index of a waveguide or resonance mode
n	integer, 1st index of a waveguide or resonance mode
$\hat{\mathbf{n}}$	normal unit vector
P	power [W]
$P(\rho)$	function describing radial dependence of fields in cylindrical waveguide
P_l	loss power [W]
P_{ld}	dielectric loss power [W]
P_{rad0}	Radiated power, when $d = 0$
p	polynomial
p_{nm}	cut-off wavenumber of TM_{nm} wave mode in cylindrical waveguide
p'_{nm}	cut-off wavenumber of TE_{nm} wave mode in cylindrical waveguide
p_{tot}	total absolute pressure [Pa]
Q	quality factor
Q_d	dielectric quality factor
Q_e	external quality factor defined by Eq. (6.13)
Q_{e1}, Q_{e2}	external quality factor of one coupling probe
Q_{ext}	external quality factor

Q_l	loaded quality factor
Q_m	metal quality factor
Q_{m0}	metal quality factor of empty resonator
Q_{rad}	radiation quality factor
Q_{rad0}	radiation quality factor, when $d = 0$
$Q_{\text{rad,0}}$	radiation quality factor of empty resonator
Q_u	unloaded quality factor
Q_{u0}	unloaded quality factor of empty resonator
R_e	ratio of external quality factors of two probes with uneven coupling
R_L	gas constant of dry air [J/(mole·K)]
R_W	gas constant of water vapour [J/(mole·K)]
R^2	correlation coefficient
r	ratio of radii, $r = b/a$
r_d	ratio of diameter of center pin to diameter of dielectric in probe
r_ε	ratio of permittivity of dielectric in probes to permittivity of MUT
S	surface area [m^2],
	salinity [% by weight]
S_{nm}	parameters of scattering matrix
s	constant in field strength equations
T	time it takes for a wave to travel back and forth a distance L [s],
	absolute temperature [^oK],
	period of modulation [s]
t	thickness of fin [m]
$\hat{\mathbf{u}}_z$	unit vector of z co-ordinate
$\hat{\mathbf{u}}_\varphi$	unit vector of φ co-ordinate
$\hat{\mathbf{u}}_\rho$	unit vector of ρ co-ordinate
V	volume [m^3]
v	velocity of a plane wave [m/s]
v_f	velocity of flow [m/s]
v_g	group velocity [m/s]
v_p	phase velocity [m/s]
W	total stored energy [J]
W_e	energy of electric field [J]
W_0	total stored energy in sensor, when $d = 0$ [J]
WC	watercut [% by volume]
X	humidity ratio, i.e. ratio of mass of water vapour to mass of dry air
x	rectangular co-ordinate [m]
y	rectangular co-ordinate [m]
$Z_{e,vm}$	impedance of TM_{vm}
$Z_{h,vm}$	impedance of TE_{vm}
Z_w	impedance of plane wave [Ω]
z	rectangular co-ordinate [m], axial cylindrical co-ordinate [m]
α	real part of γ[1/m],
	wedge angle of fin [deg.]
β	imaginary part of γ[1/m]
β_s	propagation factor of resonance mode in sensor at f_r [1/m]
Γ	voltage reflection coefficient
Γ_r	voltage reflection coefficient at resonant frequency

γ	propagation constant in transmission line [1/m]
ΔA_r	correction factor for peak height [dB]
Δf	frequency resolution of the FSA method [Hz]
Δf_r	change of resonant frequency [Hz]
ΔP_{rad}	change of radiated power [W]
ΔS	parameter calculated by HFSS, indication of the degree of conversion
Δt	time interval [s]
Δt_{cc}	time delay corresponding to cross-correlation maximum [s]
ΔW_c	energy dissipated during one cycle [J]
$\Delta\phi_c$	phase shift in the cables of an FSA circuit [rad]
$\Delta\phi_s$	phase shift at transmission through a sensor [rad]
$\Delta\phi_t$	total phase shift during one revolution in an FSA circuit [rad]
ε	permittivity [F/m]
ε_0	permittivity in vacuum, $8.854 \cdot 10^{-12}$ [F/m]
ε_{MUT}	relative permittivity of MUT
ε_r	relative permittivity
ε_r'	real part of relative permittivity
ε_{rc}'	real part of relative permittivity of insulation in cable
ε_{ri}	relative permittivity of dielectric material in probes
ε_r''	imaginary part of relative permittivity
λ	wavelength [m]
λ_0	wavelength in vacuum [m]
λ_{pw}	wavelength of plane wave [m]
λ_{pw0}	wavelength of plane wave in vacuum [m]
λ_{wg}	wavelength in waveguide [m]
μ	permeability [H/m]
μ_0	permeability in vacuum, $4\pi \cdot 10^{-7}$ [H/m]
μ_r	relative permeability
μ_r'	real part of relative permeability
μ_r''	imaginary part of relative permeability
ν	index giving number of “half-wave” field patterns in sector φ_0
ρ	radial cylindrical co-ordinate [m]
σ	conductivity [S/m]
σ_{eff}	effective conductivity [S/m]
σ_w	conductivity of water [S/m]
$\Phi(\varphi)$	function describing angular dependence of fields in cylindrical waveguide
ϕ	phase angle [rad]
ϕ_0	phase constant in reflection frequency response of resonator [rad]
φ	tangential cylindrical co-ordinate [rad]
φ_0	angle of sector [rad]
ω	angular frequency [rad/s]

LIST OF ABBREVIATIONS

CFR	cylindrical fin resonator sensor
EC	end cross sensor
FMCW	frequency modulated continuous wave
FSA	feedback self-oscillating amplifier
HFSS	High Frequency Structure Simulator (product name)
MCA	Microwave Consistency Analyzer (product name)
MFI	name of Multi-Fluid/Roxar products
MUT	material under test
NA	network analyzer
PEEK	Polyetheretherketone (plastic material used as dielectric in probes)
RR	rectangular resonator
VCO	voltage controlled oscillator

1 INTRODUCTION

1.1 Scope and Background

The measurement of material composition is a widely encountered problem in the industry. Often the material to be measured is flowing in a pipe, either as a liquid or as solid particles in pneumatic or liquid assisted transportation. In such cases microwave sensors provide an attractive solution, because microwaves penetrate most materials allowing the measurement to be representative for the cross section of the pipe. For example, in the petroleum industry the problem is often to measure the mixing ratio of oil, water, gas, and sometimes also the speed of flow. Two particular problems, representing the extremes in complexity, are the measurement of the watercut, i.e. the water content of an oil/water mixture (or the liquid part if gas is present) expressed in % by volume, and the so-called multi-phase measurement of the production rates of oil, water, and gas expressed in m^3/h. The present commercial sensors for measuring fluids in the petroleum industry are based on various techniques (either single or a combination of several): Capacitive sensors, dual-energy gamma sensors, separation with measurement of the flow of the phases, venturi meters, and microwave sensors.

The scope of this thesis is microwave sensors for measuring materials flowing in metal pipes, in particular microwave resonator sensors. The emphasis is on the principles how to design the sensors to achieve desired characteristics. Some realized sensors, mainly from the petroleum industry, will be described. Of central importance are sensor applications based on sectorial and semisectorial waveguides, and these will be analyzed in detail by the author.

The author has been involved in developing microwave sensors, both during the years 1980-1995 with the Radio Laboratory at Helsinki University of Technology, and since 1995 with Multi-Fluid and Roxar in Stavanger, Norway. Multi-Fluid is the company that made sensors for measuring fluids in the petroleum industry, and that in 1999 merged with Smedvig Technologies and became Roxar. The work described in the thesis has mainly been conducted at Multi-Fluid/Roxar, while some of the underlying principles have been developed at the Radio Laboratory.

1.2 Objectives

The desired characteristics of a microwave sensor for measuring materials flowing in a pipe vary, dependent of the application. They are related to flow characteristics, measurement characteristics, and frequency response characteristics affecting the measurement electronics, mechanical characteristics, and manufacturing cost. A desired feature is to have as few intrusive parts hindering the flow as possible, and the sensor spool piece should be as short as possible. A simple mechanical structure with low manufacturing cost, is an advantage. The space constraints can be extraordinary, as in the downhole sensor described in Ch. 7. A clean frequency response with no confusing peaks is necessary, when measuring resonator sensors, with for example simple feedback self-oscillating amplifier (FSA) electronics.

The objective of the work has been to develop general principles for implementing microwave resonator sensors in pipes, analyze the waveguide modes in

sectorial and semisectorial waveguides as building blocks in such sensors, and to develop sensors with optimal characteristics for a few particular applications, with different demands on the characteristics.

In the cylindrical fin resonator sensor for water content of oil, the objective has been to develop a simple mechanical structure, with low intrusiveness, and a clean frequency response for low-cost applications.

In the development of the end grid sensor for water content of oil, the objective has been to optimize the end grids with respect to high isolation, cleanliness of the frequency response (a high cut-off frequency results in a cleaner frequency response), ease of manufacturing, and short length resulting in low manufacturing costs for the spool piece.

In the downhole sensor the objective has been to develop a design that matches the physical constraints of measuring in the annulus between two pipes, has a clean frequency response that can be measured with the FSA method, minimizes the pressure drop, and matches the design criteria of the downhole environment related to temperature, pressure, and corrosion.

The most important objectives in developing the sensor for measuring humidity in air, has been to achieve a high quality factor, high stability, and low sensitivity to contamination.

1.3 Contents of the Thesis

The structure of the thesis is the following: Chapter 2 gives an overview of the various groups of microwave sensors, particularly for measurement in pipes. Chapter 3 describes the general characteristics of microwave resonator sensors. Chapter 4 discusses the various principles of implementing microwave resonator sensors in pipes. Chapter 5 describes the waveguide modes of sectorial and semisectorial waveguides. Chapter 6 describes the cylindrical fin resonator sensor as an application of sectorial waveguides. The application as a low-cost watercut sensor is also described. Chapter 7 describes resonator sensors implemented using end grids. First the full-bore high-accuracy watercut sensors, then the downhole watercut sensor, also as an application of semisectorial waveguide, and last the humidity sensor. Chapter 8 gives an account of the accuracy of the simulations performed with HFSS. Chapter 9 summarizes the needs for further studies.

2 MICROWAVE SENSORS

2.1 Basics of Microwave Sensors

The general demand for sensors has grown with the automatization of industrial processes. Many of the new measurement problems have been solved by various kinds of microwave sensors [Nyfors and Vainikainen, 1989a]. Microwave sensors have therefore become more and more common in different areas of the industry.

For the sake of clarity, the word "microwave" must be defined here. It has not been defined exactly in the literature like for example the acronym VHF, which denotes frequencies in the range 30 - 300 MHz. It is generally agreed that the wavelength is more significant than the frequency in relation to the word. The American Heritage Dictionary [The American Heritage Dictionary, 1985] says "**microwave** *n*. An electromagnetic wave having a wavelength in the approximate range from one millimetre to one metre, the region between infrared and short-wave radio wavelengths". In the sensors described in this thesis the wavelength is always of the same order of magnitude as the sensor. When for example in certain types of sensors a high content of water results in a low measurement frequency, the wavelength stays constant. Because there is also a need for a collective name for the sensors, they will all be called microwave sensors

Microwave sensors are based on the interaction of microwaves with matter. This interaction may be in the form of reflection, refraction, scattering, emission, absorption, or change of speed and phase. Depending on how the measurement is arranged and which phenomenon the sensor is based on, microwave sensors are divided into groups [Nyfors and Vainikainen, 1989a]. The most important groups are resonators, transmission sensors, reflection and radar sensors, radiometers, holographic and tomographic sensors, and special sensors. Microwave sensors are used to measure a wide range of quantities like distance, movement, shape, and particle size, but the largest group of applications are related to measurement of material properties.

Material measurements with microwaves are based on the fact that the interaction between microwaves and the medium of propagation is completely determined by the relative permittivity and permeability

$$\begin{aligned} \varepsilon_r &= \varepsilon_r' - j\varepsilon_r'' \\ \mu_r &= \mu_r' - j\mu_r'' \end{aligned} \tag{2.1}$$

of the medium. For most practical materials that are the subject of measurement with microwave sensors μ_r = 1. In this thesis only the permittivity will therefore be considered to affect the interaction, unless otherwise stated. Different materials have different permittivity, and the permittivity of a mixture depends on the permittivity of the components, the composition (the relative abundance of the components), and the structure [von Hippel, 1954], [Becher, 1965], [Hasted, 1973]. By measuring the permittivity of the mixture, one therefore gets information about the composition. In a simple case of two components, the sum of which is 100%, there is only one unknown if the structure, and the permittivity of the components are assumed to be known (e.g. oil drops in water or water drops in oil), making it possible to deduce the composition

from one measurement of e.g. resonant frequency. Generally the permittivity is, however, also influenced by factors like temperature and density (actually density is a special case of composition mainly involving the relative amount of air), and structure (e.g. the shape of the inclusions in a host material). There may also be more than two components in the mixture (e.g. oil, water, and gas) adding to the total amount of unknowns. In such cases multiparameter microwave measurements (e.g. resonant frequency and quality factor or, insertion loss and phase) or several types of sensors are often used. For a discussion on microwave multiparameter measurements see [Nyfors and Vainikainen, 1989a]. The most common additional sensors measure density and temperature.

2.2 Advantages and Disadvantages of Microwave Sensors

The possibilities and challenges, when designing sensors based on depend to a large degree on the specific application, but some general remarks can be given. Below is a list that summerizes the most important features of microwave sensors for material measurements. It should be noted that all statements do not apply to all existing sensors (it is for example in many cases possible to design microwave sensors for non-contact measurements, if desired, but most sensors are in practice designed for being in contact with the object).

- Microwave sensors do not need mechanical contact with the object. Therefore, performing on-line measurements from a distance is usually possible, without interference to the process.
- Microwaves penetrate all materials except for metals. The measured result therefore represents a volume of the material, not only the surface.
- Microwave sensors see a very good contrast between water and most other materials, making them well suited for water content measurements.
- Microwave resonator sensors are inherently stable because the resonant frequency is related to the physical dimensions.
- Microwave sensors are insensitive to environmental conditions, such as water vapour and dust (contrary to infrared sensors), and high temperatures (contrary to semiconductor sensors).
- Microwave sensors are generally less sensitive to material build-up than capacitive sensors.
- At low frequencies (capacitive and resistive sensors), the dc conductivity often dominates the electrical properties of a material. The dc conductivity depends strongly on temperature and ion content. At microwave frequencies, the influence of the dc conductivity often disappears.
- At the power levels used for measurements with microwave sensors, microwaves (nonionizing radiation) are safe (contrary to radioactive [ionizing] radiation).
- Microwave sensors are fast (contrary to radioactive sensors, where because of the statistical nature of the signal the accuracy depends on the measurement time, the absorption, and the activity of the source).
- The microwaves do not affect the material under test in any way.

However, there may be some disadvantages:

- The higher is the frequency, the more expensive are the electronic components.
- Microwave sensors must be calibrated separately for different materials.
- The sensors are often adapted to a specific application, resulting in low universal applicability.
- The sensors are sensitive to more than one variable. Additional sensors are therefore in some cases necessary for compensation.
- Because of the relatively long wavelengths, the achievable spatial resolution is limited.

2.3 On-Line Microwave Sensors for Pipes

There are several possible ways to arrange a microwave sensor measurement in a pipe. They all have different characteristics, which make them suitable for different applications. Because the new sensors described in this thesis are all for measuring in pipes, a brief overview of the main groups with a few examples will be given here.

2.3.1 Free-Space Transmission Sensors

The basic geometrical configuration is to have two dielectric windows on opposite sides of the pipe with a transmitting antenna on one side and a receiving antenna on the other side (Fig. 2.1). On the way between the antennas the microwave signal penetrates the material flowing in the pipe, also called MUT (material under test). The permittivity of the MUT affects both the phase and the amplitude of the signal. The advantage with this configuration is the simplicity, and the main problem is the sensitivity to reflections in various parts of the system, like the dielectric windows and interfaces inside the material dependent on the flow regime. The reflections in the system cause ripples on the frequency response, and the amplitude is much more

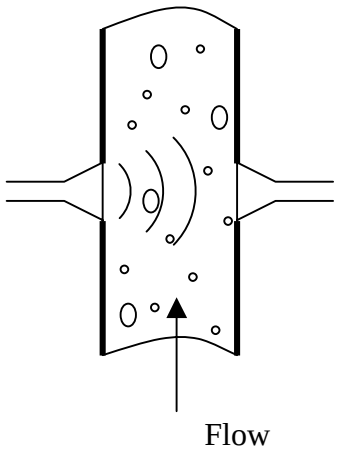

Figure 2.1 The basic geometrical configuration of a free-space transmission sensor in a pipe.

affected than the phase. If the sensor is based on measuring only one microwave parameter, a higher accuracy is therefore achieved by measuring the phase than by measuring the attenuation [Klein, 1981]. For an analysis on the effect of internal reflections in transmission sensors, see [Nyfors and Vainikainen, 1989a].

If the MUT flowing in the pipe has small losses, the waveguide modes that will be excited in the pipe, or the reflections from the pipe walls, will also strongly affect the transmission properties [Brodwin and Benway, 1980]. Especially if the measurement is done on a fixed frequency, the errors will be large, when the changing permittivity of the flow moves the cut-off frequencies relative to the measurement frequency. By performing a frequency sweep and averaging, the error can be decreased. When using a frequency that is much higher than the lowest cut-off frequency, the conditions resemble more closely free-space conditions, but there is still the problem with reflections from the walls. For a lossy MUT the influence of the pipe is smaller. In many cases the best solution is to use the FMCW (Frequency-Modulated Continuous Wave) technique, which is often used in radars. The FMCW technique discriminates signals in time, thus being able to exclude the reflections that arrive slightly later than the main signal. The FMCW technique measures the signal delay, which is closely related to phase measurement in sensors, but lacking the 2π ambiguity in phase. Both the phase and the signal delay depend on the speed of propagation, which depends on the permittivity.

A good example of a successful application is the microwave consistency analyzer (MCA) produced by Valmet Automation [Jakkula, 1998], for measuring the consistency of pulp in the paper industry. It is based on the FMCW technique to measure the signal delay. The frequency sweep is from 2 - 3 GHz. The MCA comes in two versions, one measuring across the pipe like in Fig. 2.1, and an insert version shown in Fig. 2.2. The insert version is used for big pipes, where the attenuation would be too high across the pipe, whereas the other version is used for smaller pipe diameters. The insert version is only used for consistency up to 15 %, because of the

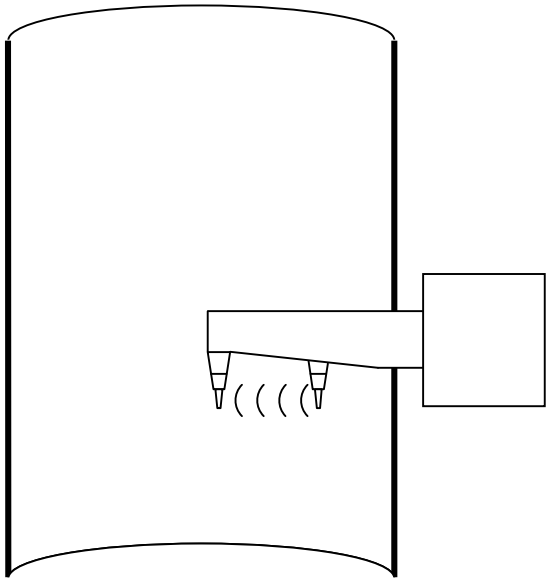

Figure 2.2 The principal design of the insert version of the Valmet Automation MCA for measuring consistency in pulp.

risk of clogging. The version measuring across the pipe utilizes patch antennas instead of horns, probably for better impedance matching.

2.3.2 Special Transmission Sensors

A transmission sensor needs a reference channel for making phase measurements. Normally the reference channel is external to the sensor. If it is also directed through the sample, but in a different way than the main channel, special features can be achieved. An example is the MFI MultiPhase Meter made by Roxar (www.roxar.com), which is used for measuring flow rates of oil, water, and gas. It has one transmitting antenna and two receiving antennas at different distances on the circumference. With this configuration the channels are more alike, which cancels some error sources like the frequency response of the antennas. The MultiPhase Meter also measures on varying frequency to avoid errors caused by the waveguide modes in the pipe. In addition the meter has another set of three antennas separated a certain distance in the direction of the flow. By performing the same measurements on both sets and cross-correlating the results, the speed is derived.

2.3.3 Guided Wave Transmission Sensors

Instead of letting the microwaves propagate freely from the transmitter to the receiver through the MUT, they can be guided in, for example, a stripline, coaxial cable, or dielectric waveguide. The MUT is brought in contact with the electric field on a section of the line, thus affecting the propagation factor (phase and attenuation). The advantages with guided wave sensors are better control of impedance matching and less influence from the pipe. A disadvantage is that the electric field that senses the permittivity of the MUT, is only the fringing field. The sensitivity is therefore smaller and the sensor measures only a small fraction of the total amount flowing in the pipe. The sensor is also sensitive to contamination on the surface from which the fringing field protrudes, much like capacitive sensors. For homogeneous mixtures without risk of contamination, a guided wave transmission sensor may be a good alternative.

One design, which is mainly intended for liquids, is shown in Figure 2.3 [Jakkula, 1988]. It consists of a dielectric ring immersed in a groove that has been cut in the wall on the inside of the pipe. The microwaves propagate in the ring as in a dielectric waveguide. For low permittivity in the liquid the microwaves propagate through total reflection with little loss. The evanescent field on the outside of the waveguide is in contact with the liquid and affects the propagation constant. When the permittivity rises above a limit, the waveguide becomes leaky and the attenuation increases even without an increase of the dielectric loss. The sensor thus behaves differently for different mixing ratios. By the right choice of design parameters, high sensitivity can be achieved in a specific range of mixing ratio. This sensor only measures the liquid flowing along the wall. It has found successful applications in the chemical industry but it was found to give wrong results for pulp, where the fibres and the water separate close to the wall because of the speed gradient [Jakkula, 1998]. Of the same reason, the guided wave transmission sensors are generally not suited for applications in the petroleum industry, except for emulsions of oil and water with very small drop size.

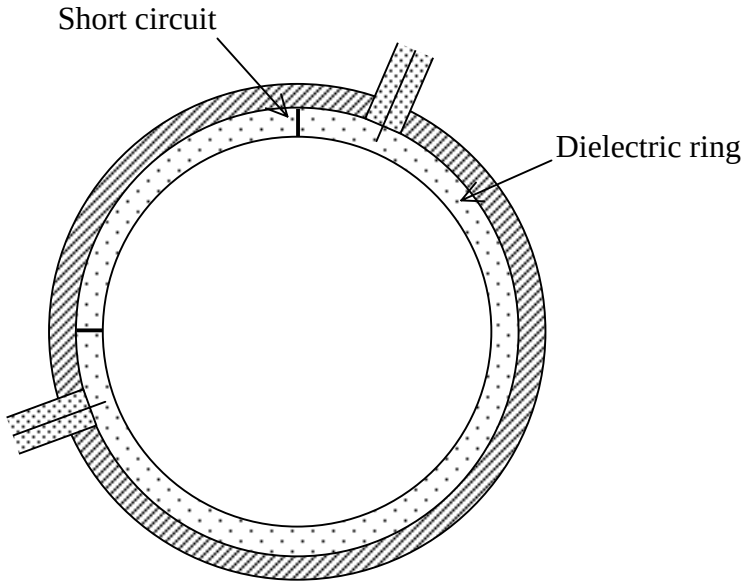

Figure 2.3 Dielectric waveguide transmission sensor for measureming the water content in a liquid in a process pipe [Jakkula, 1988].

2.3.4 Reflection Sensors

A reflection sensor is based on measuring the reflection coefficient for a wave reflected from the end of a transmission line. The design is made such that the fringing field at the end is in contact with the MUT, which thus affects the phase and magnitude of the reflection coefficient. A typical example is the open-ended coaxial sensor, which is a convenient device for measuring permittivity over a broad frequency range [Stuchly and Stuchly, 1980], [Nyfors and Vainikainen, 1989a], [Hewlett-Packard Application Note 1217-1], [Colpitts, Pelletier, and Cogswell, 1992], [Bramanti and Bramanti, 1995]. This sensor is widely used in permittivity measurements in the laboratory and is available as optional equipment for network analyzers. The advantages are the broad frequency range, typically two decades, and the minimal need for sample preparation – the sample must have a minimum size not to perturb the fringing field, and a plane surface of the size of the sensor. A disadvantage is the sensitivity to an air gap, e.g. as a result of surface roughness, between the sensor and the sample. For soft samples or liquids the problem does not exist. Because of the small volume of sample affecting one measurement, inhomogeneous mixtures cause a lot of scatter between individual measurements. Proper averaging may remove the problem.

The open-ended coaxial sensor can be used for on-line measurements in a pipe, as schematically shown in Figure 2.4. Because it measures with the fringing field at the front surface of the sensor, it only measures a small fraction of the mass flowing in the pipe and it is sensitive to contamination. It is suitable for measuring homogeneous mixtures without risk of contamination. For these it provides a simple sensor solution that can be used for performing broadband measurements. If different phenomena affect the permittivity in different parts of the microwave spectrum, like ion conductivity and Debye relaxation losses, independent information is retrieved

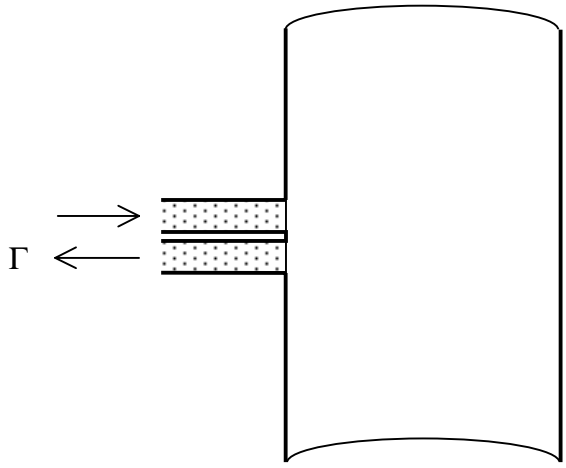

Figure 2.4 The principle of an open-ended coaxial cable as a reflection sensor mounted for measuring on-line in a pipe. The material flowing in the pipe affects the fringing field at the front surface of the sensor thus affecting the measured reflection coefficient.

from different parts of the spectrum. Such broadband measurement is a special case of multiparameter measurement. Because of the small volume affecting the measurement, the open-ended coaxial sensor is generally not suited for applications in the petroleum industry, except for emulsions of oil and water with very small drop size.

2.3.5 Tomographic Sensors

Tomographic sensors produce an image of the interior of an object, typically from a cross section. The term is best known from medicine, where various magnetic resonance and x-ray methods are used for studying the interior of patients. In microwave tomography a transmitter is transmitting a wave that penetrates the MUT. On the other side of the sample of the MUT is an array of receivers measuring the phase and amplitude of the wave front at different locations. Various geometrical configurations have been used for the location of the receivers. In a pipe they would typically be distributed along the circumference. From the measured wave front the distribution of the permittivity in the intervening space can be calculated. The achievable resolution is about half a wavelength in the sample. The method is limited to cases without multiple internal reflections, i.e. cases with low or moderate contrast in permittivity between components. For a general description of the basic principles of imaging microwave sensors, se for example Ch. 8 in [Nyfors and Vainikainen, 1989a]. A more detailed description of microwave tomography has been given in [Bramanti and Salerno, 1992].

Microwave tomography is an advanced technique for studying the structure of the flow in a pipe. Especially in cases with mixtures of liquid and gas the phases separate producing various flow regimes, like annular flow, bubble flow, mist flow, churn flow, and slug flow. The occurrence of the various flow regimes depends on several parameters, of which the most important are mixing ratio, viscosity of components, speed of flow, orientation of pipe, and pressure. Several flow regimes may appear in the same application at different times. Because all microwave sensors

are to some degree affected by the flow regime, the tomographic technique may be a good supplement, giving additional information about the flow regime. Another sensor may then have different calibrations for different flow regimes or the tomographic sensor may be used directly to deduce the mixing ratio of gas and liquid from the microwave image of the cross section of the flow. For each image of the cross section of the flow regime a large number of measurements is needed, and the calculations needed to produce the image are complicated. The speed of measurement and calculation will therefore limit the time resolution of the changes in the flow regime. Typically it will be possible to distinguish large slugs but not individual bubbles or drops. Microwave tomography requires complicated electronics and the array of sensors with cables may be difficult to implement in applications, where the pressure is high.

2.3.6 Resonator Sensors

Microwave resonators can be implemented in many different ways for measuring in pipes. These resonator sensors can be divided in two different classes: Those, which are filled with the MUT, and those with a considerable part of the field outside the MUT. The former group is limited to measuring materials with low losses. If the losses become too high, the resonance disappears. In the petroleum industry this typically means oil-continuous fluids (water drops in oil). An example is the MFI WaterCut Meter made by Roxar, where a cavity resonator has been implemented by isolating a section of the pipe with end grids. The latter group can be made to tolerate very lossy materials, but their characteristics are more difficult to handle theoretically leading to more cumbersome calibration processes. An example is the MFI FullCut Meter made by Roxar, which is a coaxial resonator with a part of the field inside the dielectric material that covers the centre conductor. The FullCut sensor is able also to measure water-continuous mixtures (oil drops in water).

The new sensors described later in this thesis are all microwave resonators. Separate chapters will therefore be devoted to the theory of the microwave resonator as a sensor (Ch. 3) and a review of the principles of implementing resonators in pipes, with some examples (Ch. 4).

2.4 Summary

It has been shown that microwave sensors have several potential advantages as on-line sensors for material measurements in pipes. There are also many ways of implementing the sensors with different measurement properties as a result. Various kinds of fringing-field sensors (guided wave transmission sensors, reflection sensors) can be used with homogeneous mixtures. Resonator sensors or free-space transmission sensors can be used, when a measurement over the whole cross section of the pipe is desired. Tomographic sensors can be used for collecting more information giving a picture of the flow regime. All the kinds of sensors mentioned can be implemented with completely nonintrusive structures, if desired.

3 MICROWAVE RESONATORS

3.1 Introduction

This chapter describes the general characteristics of microwave resonators from the sensor point of view. It is intended to give the reader some of the background information necessary to understand the following chapters. The approach is slightly different from most textbooks that treat resonators generally or as a filter application. The text is partly based on the presentation given by the author in Chapter 3 of [Nyfors and Vainikainen, 1989a].

3.2 The Resonance Phenomenon

A resonator is a structure that has at least one natural frequency of oscillation, a resonant frequency. When the resonator oscillates, energy is converted from one kind to another and back. If more energy is fed to the resonator at the same frequency and in phase with the on-going oscillations, energy will be absorbed and stored in the oscillator. A resonator is therefore a structure that can store energy such that it is continuously converted with a specific speed between two kinds of energy.

Different types of resonators are for example acoustic, mechanical, and electromagnetic resonators. In an acoustic resonator the air molecules move in waves such that kinetic energy alternates with pressure. In a mechanical resonator deformation of a body causes a stress force that causes movement that causes stress and so forth. The size, shape, density, and the modulus of elasticity determine the speed of the process, i.e. the resonant frequency. In electromagnetic resonators electric and magnetic energy alternate. In a simple *LC* circuit (a loop with an inductor *L* and a capacitor *C*) charge in the capacitor (electric energy) causes a current, which causes a magnetic field (magnetic energy) in the inductor, which keeps the current going until the capacitor is reversely charged, and so forth. The speed of the process, i.e. the resonant frequency, is determined by the values of capacitance and inductance. In a microwave resonator electromagnetic waves travel back and forth between reflecting points resulting in a standing wave pattern, where the energy pulsates between electric and magnetic energy. The size and shape of the structure and the dielectric and magnetic properties of the medium, where the microwaves propagate, determine the resonant frequency.

Microwave resonators generally have many resonant frequencies. The frequency of the excitation (source of energy to be stored) determines the frequency of oscillation, but considerable build up of energy in the resonator takes place only, when the frequency of excitation is close to a resonant frequency.

The conversion of energy from one kind to another normally involves losses. In a microwave resonator the losses may be caused by radiation, finite conductivity in the metal parts, or dielectric or magnetic loss. Energy also escapes to the measurement circuit. If energy is continuously fed into a resonator, the amount of energy stored will grow until energy is dissipated with the same speed as new energy is stored. If the excitation of a resonator stops, the amplitude of oscillation will decrease exponentially with a speed determined by the quality factor. If a resonator is excited by an impulse

(a tap on a tuning fork or an electromagnetic impulse in a microwave resonator) it will ”ring” for some time on the resonant frequency till the energy has been dissipated.

3.3 The Resonance Condition

All microwave resonators that are normally used as sensors, can be thought of as formed by a section of transmission line bounded by impedance discontinuities in both ends. The transmission line can be made of any kind of structure supporting electromagnetic waves, such as hollow waveguide, coaxial line, slotline, stripline, dielectric waveguide, or two-conductor line. The role of the impedance discontinuities is to cause the propagating wave to be reflected. Where the transmission line is open-circuited, the reflection coefficient is $\Gamma = +1$ (i.e. the phase angle $\phi = 0$), and where the line is short-circuited, $\Gamma = -1$ ($\phi = \pi$). If the impedance discontinuity differs from those mentioned, or purely reactive terminations ($|\Gamma| = 1$, $\phi \neq 0$ & π), the reflection will be partial ($0 \leq |\Gamma| \leq 1$) and the resonator leaky.

The field in the resonator is excited by the external circuit through some kind of coupling, which may be for example an aperture (small hole), coupling loop, coupling probe, or coupling through the leaky ends. The coupling device radiates a wave into the resonator. The wave propagates along the transmission line and is reflected in alternating directions at the discontinuities.

Resonance occurs, i.e. the resonance condition is fulfilled, if the exciting field is in phase with the reflected components. Hence, they will interfere constructively and destructively to give a standing wave pattern. This will happen only at certain frequencies (resonant frequencies). A standing wave with a strong field will build up, thus storing a great amount of energy. Equilibrium is reached at the level where the loss power in the resonator (in the metal or dielectric, by radiation, or by escaping through the couplings) equals the excitation power. At resonance, the energy alternates between the electric field and the magnetic field, which contain the same amount of energy.

The resonance condition is fulfilled, when the mode wavelength compared to the dimensions of the resonator take on specific values. These values depend on the kind of termination, which bounds the resonator. The reflected wave components are in phase with the exciting field if the total phase change experienced by the wave on its way back and forth along the transmission line, is a multiple of 2π:

$$\frac{2\pi}{\lambda} \cdot 2L + \phi_1 + \phi_2 = n \cdot 2\pi \tag{3.1}$$

where L is the length of the transmission line, ϕ_1 and ϕ_2 are the phase angles of the reflection coefficients, and n is an integer. The first term on the left in (3.1) is the phase change of the wave on its way back and forth. Equation (3.1) can be written in the form

$$L = \left(\frac{n}{2} - \frac{\phi_1 + \phi_2}{4\pi} \right) \lambda \tag{3.2}$$

If the resonator is open-circuited at both ends, $\phi_1 = \phi_2 = 0$, and (3.2) gives for the length:

$$L = \frac{n\lambda}{2} = \frac{\lambda}{2}, \lambda, \frac{3\lambda}{2}, ... \tag{3.3}$$

If the resonator is short-circuited at both ends, $\phi_1 = \phi_2 = \pi$, and the same result as above is obtained:

$$L = \left(\frac{n}{2} - \frac{1}{2}\right)\lambda = \frac{\lambda}{2}, \lambda, \frac{3\lambda}{2}, ... \tag{3.4}$$

If the resonator is short-circuited at one end and open-circuited at the other, $\phi_1 = \pi$ and $\phi_2 = 0$, and (3.2) gives

$$L = \left(\frac{n}{2} - \frac{1}{4}\right)\lambda = \frac{\lambda}{4}, \frac{3\lambda}{4}, \frac{5\lambda}{4}, ... \tag{3.5}$$

For each situation, there is an infinite number of solutions satisfying the resonance condition. Therefore, each resonator has an infinite number of resonant frequencies for each wave mode. The lowest resonance is at the frequency for which the wavelength is two or four times the length of the resonator, depending on the terminations.

For the exact calculation of the resonant frequency, the relation between wavelength and frequency must be known. For TEM waves (in coaxial or other line with minimum two conductors) the relation is very simple. Because they have no cut-off frequency, the wavelength in the transmission line is the same as that of a plane wave in the same dielectric medium. In hollow waveguides the relation is slightly more complicated, because the wavelength of the waveguide mode is always longer than that of the corresponding plane wave:

$$\lambda_{wg} = \frac{\lambda_{pw}}{\sqrt{1 - \left(\frac{f_c}{f}\right)^2}} \tag{3.6}$$

where λ_{wg} is the wavelength in the waveguide, λ_{pw} is the wavelength of the corresponding plane wave, and f_c is the cut-off frequency of the wave mode in the waveguide. In the case of waveguides with a cut-off frequency, the wavelength λ_{wg} should be used in (3.1) – (3.5).

Equation (3.6) shows that λ_{wg} becomes infinite at the cut-off frequency. In this situation also $n = 0$ is a possible solution of (3.1), if the structure can support the wave mode in question. If a section of hollow waveguide is short-circuited in both ends, it can support TM modes. The resonant frequency is $f_r = f_c$ in such cases, independent of the length of the resonator. The field pattern then lacks structure in the axial direction of the resonator. TE waves can not exist with $n = 0$, when the ends are short-circuited, because the transverse electric field must be zero at the ends. If the ends are open-

circuited, the structure can support TE modes with $n = 0$, but not TM modes, because they have an axial electric field, which must terminate at a metal surface. Because an open circuit in a hollow waveguide is not as exact in location as a metal wall, there will be ”end-effects” with fringing fields, but in practice the resonant frequency of such TE modes is close to the cut-off frequency. The principle behind the use of such resonators as sensors will be treated in Ch. 4, and the fin resonator as a practical application in Ch. 6.

3.4 Resonant Frequency and Quality Factor as a Function of Permittivity, Resonator Filled with a Dielectric Material

3.4.1 Resonant Frequency

In the previous section it was shown that the resonance condition (3.1) requires that the size of the resonator measured in wavelengths be constant, for example $\lambda/4$ or $\lambda/2$ for the first resonance. Because an electromagnetic wave travels slower through a dielectric medium (dielectric for short) than in vacuum, the wavelength at a specific frequency will be shorter in the dielectric. Therefore, if a resonator (the space where the electromagnetic field is located) is filled with a dielectric, the resonance condition will be met at a lower frequency than for the empty resonator. The wavelength as a function of the material constants is can be derived from the basic representation of the electric field of a plane wave travelling in the x direction:

$$\begin{aligned} &E = E_0 e^{-jkx}, \quad k = k' - jk'' = \omega\sqrt{\mu\varepsilon} = \mathrm{Re}\left\{\omega\sqrt{\mu\varepsilon}\right\} - j\,\mathrm{Im}\left\{\omega\sqrt{\mu\varepsilon}\right\} \\ &\Rightarrow \lambda = \frac{2\pi}{k'} = \frac{1}{\mathrm{Re}\left\{f\sqrt{\mu\varepsilon}\right\}} \end{aligned} \tag{3.7}$$

where μ is the magnetic permeability and ε is the permittivity of the medium. From here on values relative to the values in vacuum (ε_0, μ_0) will be used and denoted with the subscript r, and the relative permeability will be assumed to be $\mu_r = 1$. Because the speed of light in vacuum is given by

$$c = \lambda_0 f = \frac{1}{\sqrt{\mu_0\varepsilon_0}} \tag{3.8}$$

Equation (3.7) can be rewritten

$$\lambda = \frac{\lambda_0}{\mathrm{Re}\left\{\sqrt{\varepsilon_r}\right\}} = \frac{c}{f\,\mathrm{Re}\left\{\sqrt{\varepsilon_r}\right\}} \tag{3.9}$$

Combining (3.9) with the requirement that the wavelength be constant gives the change in resonant frequency caused by the dielectric ε_r compared to vacuum:

$$\frac{1}{f_{r0}} = \frac{1}{f_r \,\mathrm{Re}\left\{\sqrt{\varepsilon_r}\right\}}$$
$$\mathrm{Re}\left\{\sqrt{\varepsilon_r}\right\} = \frac{f_{r0}}{f_r} \tag{3.10}$$

where f_{r0} is the resonant frequency of the empty resonator and f_r that of the filled resonator. For the case of $\varepsilon_r' >> \varepsilon_r''$ (3.10) becomes

$$\varepsilon_r' \approx \left(\frac{f_{r0}}{f_r} \right)^2 \tag{3.11}$$

Equation (3.11) is valid in most cases of dry or moderately moist dielectrics and for example an oil-continuous mixture of oil and water. It is not valid, especially at low frequencies, when the bulk ion conductivity is considerable, as for example in a water-continuous mixture of oil and water, when the water contains salts. Because the resonance phenomenon disappears when the dielectric is very lossy, cases when (3.11) is not valid are of little interest in this study. However, it must be remembered that (3.11) is not exact in cases of lossy dielectrics, i.e. when the resonance peak is broad.

Because ε_r' is always larger than 1 (except for plasma), the resonant frequency can only become lower, when the resonator is filled with a dielectric. As was shown, obtaining the real part of the permittivity with a resonator is very simple: First the resonant frequency is measured with the empty resonator, and then with the resonator filled with the dielectric material to be measured. Equation (3.11) then gives the permittivity. If the permittivity varies with the frequency, it must be remembered that the obtained value is valid only at the frequency f_r.

3.4.2 Quality Factor

A resonance has two main characteristics, the resonant frequency and the quality factor *Q*. The latter tells how lossy the resonator is, i.e. the speed with which the stored energy is dissipated. The quality factor is defined as

$$Q = \frac{2\pi \times \text{energy stored in the resonator}}{\text{energy dissipated during one cycle}} = \frac{\omega \times \text{stored energy}}{\text{loss power}} \tag{3.12}$$

The loss power can be separated into different parts, depending on the source of the loss. Taking the reciprocal of (3.12), the *Q*-factor can be written as a sum:

$$\frac{1}{Q_u} = \frac{1}{Q_d} + \frac{1}{Q_m} + \frac{1}{Q_{\mathrm{rad}}} \tag{3.13}$$

where Q_u is the unloaded Q-factor, Q_d takes into account only the loss in the dielectric, Q_m accounts for the loss in the metal parts, and Q_{rad} accounts for the loss through radiation. Q_u is the ”real” Q-factor of the resonator, but it is impossible to measure directly. To make it possible to measure the resonant frequency and quality factor, the resonator must be coupled to the measurement circuit through some coupling devices, e.g. loops, probes, or holes. This will ”load” the resonator, which means that part of the stored energy escapes through the coupling devices. Consequently the measured Q-factor will be the loaded Q-factor, Q_l. Therefore the reciprocal of the external Q-factor, $1/Q_{\text{ext}}$, must be added to (3.13) to obtain Q_l:

$$\frac{1}{Q_l} = \frac{1}{Q_u} + \frac{1}{Q_{\text{ext}}} = \frac{1}{Q_d} + \frac{1}{Q_m} + \frac{1}{Q_{\text{rad}}} + \frac{1}{Q_{\text{ext}}} \tag{3.14}$$

If there are two coupling devices of different size, or if they are located in places with different field strength, one will have a stronger coupling to the resonant mode than the other. In that case two separate external quality factors (Q_{e1} and Q_{e2}) can be used. As mentioned above, the resonator can be regarded as part of a transmission line bounded by two discontinuities. An equation was given in [Nyfors and Vainikainen, 1989a, Eq. (3.19)] expressing Q_u in terms of the transmission line parameters: The propagation factor $\gamma = \alpha + j\beta$, and the reflection coefficients Γ_1 and Γ_2. However, the given equation appears to be in error for waveguides with a cut-off frequency. The correct equation will therefore be derived here.

If first only the loss factor α is taken into account (assuming complete reflections) and assuming that the excitation power equals the loss power (steady state oscillations), the power of the waves being reflected back and forth is constant P_0. If the distance between the reflecting points (i.e. the length of the resonator) is L, the group velocity is v_g, and the time it takes for the waves to return to a starting point after being reflected from both ends is T, the total stored energy is

$$W = P_0 T = \frac{P_0 2L}{v_g} \tag{3.15}$$

The power of a wave propagating along a transmission line with the loss factor α is

$$P = P_0 e^{-2\alpha z} \tag{3.16}$$

where z is the co-ordinate in the direction of propagation. The excitation power needed to keep the power constant, and therefore also the loss power in the resonator, is then

$$P_l = -\frac{\mathrm{d}P}{\mathrm{d}z}(z=0) \cdot 2L = 2\alpha P_0 2L \tag{3.17}$$

The energy dissipated during one cycle is then

$$\Delta W_c = P_l \cdot \frac{1}{f} = \frac{2\alpha P_0 2L}{f} \tag{3.18}$$

The definition of the quality factor in (3.12) now gives

$$\frac{1}{Q_u} = \frac{\Delta W_c}{2\pi W} = \frac{2\alpha P_0 2L v_g}{2\pi f P_0 2L} = \frac{2\alpha v_g}{\omega} \tag{3.19}$$

In a hollow waveguide the phase velocity v_p is larger than v, the velocity of a plane wave in the same dielectric medium as the waveguide is filled with. The group velocity v_g, with which the power travels, is lower than v. They are known to be

$$\begin{aligned} v_g &= v\sqrt{1-\left(\frac{f_c}{f}\right)^2} \\ v_p &= \frac{v}{\sqrt{1-\left(\frac{f_c}{f}\right)^2}} = \frac{\omega}{\beta} \end{aligned} \tag{3.20}$$

From (3.19) and (3.20):

$$\frac{1}{Q_u} = \frac{2\alpha}{\beta}\left[1-\left(\frac{f_c}{f}\right)^2\right] \tag{3.21}$$

The effect of the reflection coefficients can now be easily added by comparing the effect of the loss factor and the reflections, on the total loss. The power of a wave after one journey back and forth with complete reflections, and with incomplete reflections are:

$$\begin{aligned} &\text{Complete reflections}: \; P = P_0 e^{-4\alpha L} \\ &\text{Incomplete reflections}: P = P_0 \left|\Gamma_1\right|^2 \cdot \left|\Gamma_2\right|^2 e^{-4\alpha L} = P_0 e^{-4\alpha L + 2\log_e\left|\Gamma_1\right| + 2\log_e\left|\Gamma_2\right|} \end{aligned} \tag{3.22}$$

Equations (3.21) and (3.22) now give

$$\frac{1}{Q_u} = \frac{2\alpha L - \log_e\left|\Gamma_1\right| - \log_e\left|\Gamma_2\right|}{\beta L} \cdot \left[1-\left(\frac{f_c}{f}\right)^2\right] \tag{3.23}$$

which is the correct equation for the unloaded quality factor (or the loaded quality factor if the leaky ends are used for coupling) of a resonator expressed in terms of the transmission line parameters. Equations for calculating α are given in many books on microwave engineering. In [Nyfors and Vainikainen, 1989a] equations for coaxial cable, two-conductor line, rectangular, and circular waveguides are given. The reflection coefficients can be obtained by using known models for the discontinuities (e.g. [Saad, 1971]), simulating with software based on the finite element method, or measuring.

Equation (3.23) can not be used in the case of cavities based on waveguide resonance modes with $f_r = f_c$, mentioned in Sec. 3.3. The leakage through the ends in these resonators must be treated as loss by radiation. The metal quality factor Q_m, can be calculated using methods described e.g. in [Collin, 1966] or [Ramo et al., 1984].

3.5 Frequency Response of a Single Resonance – Measuring f_r and Q

The resonant frequency and the quality factor can be measured in two different ways, by the method of reflection coefficient or transmission coefficient. The former method requires only one coupling and the latter two. They have different advantages [Nyfors and Vainikainen, 1989a], [Vainikainen, 1991] depending on the application.

3.5.1 Method of Reflection Coefficient

The method of reflection coefficient means that a wave is transmitted along the cable toward the resonator and the reflected power is measured. The ratio between the reflected and incident power is the reflection coefficient $|\Gamma|^2$. Based on an equivalent circuit, see e.g. [Sucher and Fox, 1963], the magnitude and phase of the reflection coefficient can be approximated in the vicinity of the resonant frequency by the following equations:

$$
\begin{aligned}
|\Gamma|^2 &= 1 - \frac{4\dfrac{Q_l}{Q_u}\left(1-\dfrac{Q_l}{Q_u}\right)}{1+Q_l^2\left(\dfrac{f}{f_r}-\dfrac{f_r}{f}\right)^2} \\
\phi &= \phi_0 - \arctan\left[\frac{2Q_l\left(\dfrac{f}{f_r}-\dfrac{f_r}{f}\right)\cdot\left(1-\dfrac{Q_l}{Q_u}\right)}{2\dfrac{Q_l}{Q_u}-1+Q_l^2\left(\dfrac{f}{f_r}-\dfrac{f_r}{f}\right)^2}\right]
\end{aligned}
\qquad (3.24)
$$

where ϕ is the phase of the power reflection coefficient and ϕ_0 is a constant that depends on the way of coupling. For coupling loops, apertures and other short-circuit-like devices (inductive coupling) $\phi_0 \cong \pi$, and for coupling probes (capacitive coupling) $\phi_0 \cong 0$, in the undercoupled case ($Q_{ext} > Q_u$), which is usual for measurement resonators. For overcoupled resonators ($Q_{ext} < Q_u$), π should be added to the values given above. At the resonant frequency, the reflection coefficient has a minimum value because of the loss in the resonator. At other frequencies, the field, and therefore the loss power, in the resonator will be small. The loaded Q-factor determines the sharpness of the resonance. The higher is the loss, the broader is the resonance peak. Very high loss smears it out completely. Figure 3.1 shows an example of the reflection coefficient as a function of frequency. The minimum gives f_r, and together with the half-power width B_{hp} they give Q_l:

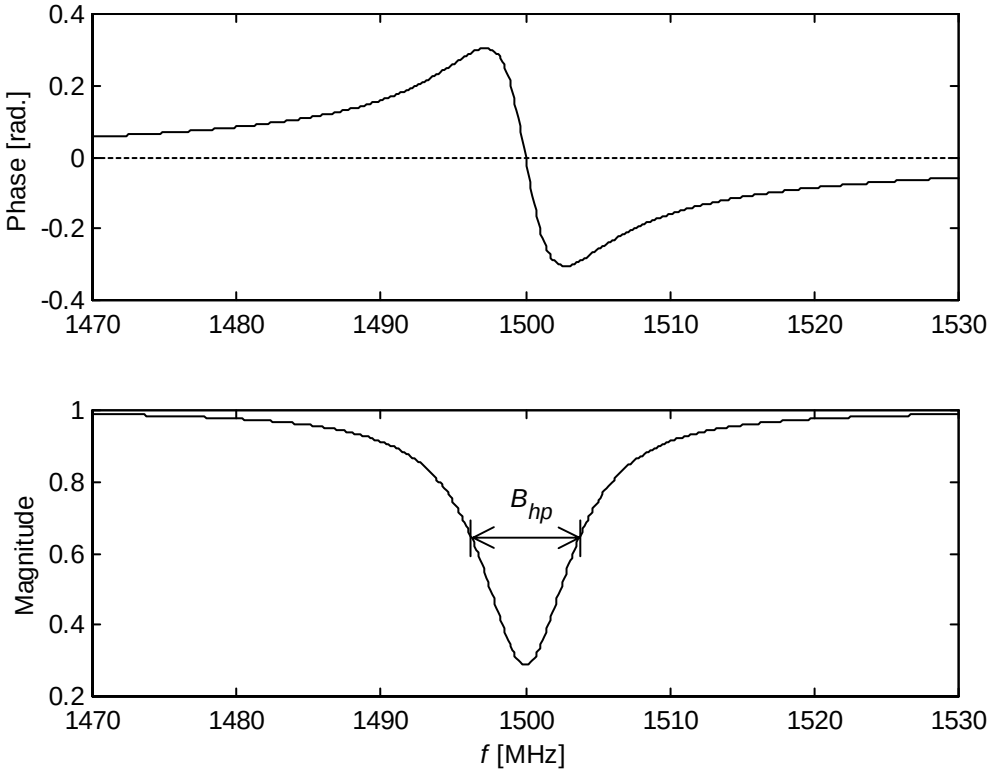

Figure 3.1 The magnitude and phase of the power reflection coefficient for a resonator with f_r = 1500 MHz, Q_l = 200, and Q_u = 260. The width of the peak (B_{hp}) is measured half way down the dip.

$$Q_l = \frac{f_r}{B_{hp}} \tag{3.25}$$

where B_{hp} is measured halfway down the dip of the reflection response in (3.24). The unloaded quality factor can be calculated from the loaded quality factor and the power reflection coefficient at the resonant frequency $|\Gamma_r|^2$. From (3.24):

$$Q_u = \frac{2Q_l}{1 \pm |\Gamma_r|} \quad \begin{cases} + = \text{undercoupled} \\ - = \text{overcoupled} \end{cases} \tag{3.26}$$

3.5.2 Method of Transmission Coefficient

The method of transmission coefficient means that the field in the resonator is excited through one coupling, and measured through another coupling. The ratio between the received power and the incident power is the power transmission coefficient *a*. It depends on Q_l and the strength of the coupling, i.e. the size of the loops or probes and their location relative to the field pattern. Based on an equivalent circuit, see e.g. [Sucher and Fox, 1963], approximate equations can be derived for the magnitude and phase of the power transmission coefficient in the vicinity of the resonant frequency. If both probes couple with equal strength, the equations are:

$$a = \frac{\left(1 - \frac{Q_l}{Q_u}\right)^2}{1 + Q_l^2\left(\frac{f}{f_r} - \frac{f_r}{f}\right)^2} = \frac{\left(\frac{Q_l}{Q_{\text{ext}}}\right)^2}{1 + Q_l^2\left(\frac{f}{f_r} - \frac{f_r}{f}\right)^2} \qquad (3.27a)$$

$$\phi = \phi_0 - \arctan\left[Q_l\left(\frac{f}{f_r} - \frac{f_r}{f}\right)\right]$$

If the couplings are different, the equation for a must be rewritten in a form containing the two separate external quality factors, Q_{e1} and Q_{e2}:

$$a = \frac{\frac{4Q_l^2}{Q_{e1}Q_{e2}}}{1 + Q_l^2\left(\frac{f}{f_r} - \frac{f_r}{f}\right)^2} \qquad (3.27b)$$

The constant ϕ_0 is either 0, $\pm\pi/2$, or π, depending on the locations and types of coupling. There is a phase difference of π between adjacent lobes in a standing wave pattern, so if only one type of coupling is used, only 0 and π are possible. If the types are mixed, probes couple to the electric field, but loops couple to the magnetic field, which is $\pm\pi/2$ out of phase compared to the local electric field. This results in $\phi_0 = \pm\pi/2$. Furthermore, turning the loop by π causes a phase shift of π. The graphs of (3.27) are shown in Figure 3.2. Only at frequencies close to the resonant frequency will any significant field build up in the resonator. Therefore, no signal is transmitted ($a \approx 0$) far from the resonant frequency. It should, however, be reminded that Equations (3.24) and (3.27) only describe the shape of a resonance peak close to the resonant frequency. A microwave resonator has an infinite number of resonances, and far from any resonance the capacitive or inductive direct coupling between the coupling probes or loops dominates. The frequency response of a resonator measured over a broad frequency band will therefore be more complex than described by these simple models.

The loaded quality factor can again be calculated from the measurements of resonant frequency and peak width:

$$Q_l = \frac{f_r}{B_{hp}} \qquad (3.28)$$

where B_{hp} is the width of the resonance curve (3.27) at the level where the power transmission is half of the maximum value.

If the probes have equally strong coupling, the unloaded quality factor can be directly calculated from Q_l and the transmission coefficient at the resonant frequency, a_r. From (3.27a):

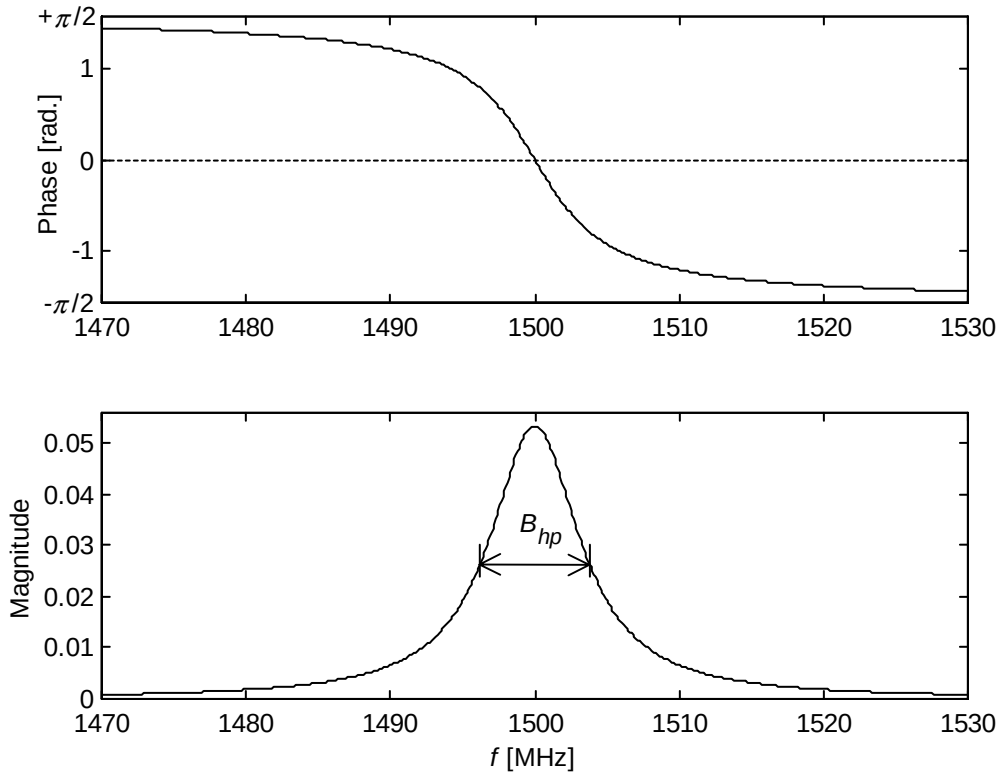

Figure 3.2 The magnitude and phase of the power transmission coefficient for a resonator with f_r = 1500 MHz, Q_l = 200, and Q_u = 260. The width of the peak (B_{hp}) is measured at half power (-3 dB) compared to maximum power transmission.

$$Q_u = \frac{Q_l}{1-\sqrt{a_r}} \tag{3.29}$$

If the probes have unequally strong coupling, the ratio of the separate external quality factors must be known, before the unloaded quality factor can be calculated from a power transmission measurement. Because the relative strengths of coupling are determined by the relative field strengths of the resonance mode at the locations of the probes, the ratio of the external quality factors will be approximately constant for a sensor. It is therefore enough to measure the ratio once. To obtain the ratio, the reflection coefficient must be measured from both sides. If the other port is short-circuited while the reflection coefficient is measured from the other port, (3.25) gives Q_{ln} and (3.26) gives Q_u, and Q_{en} is then given by

$$\frac{1}{Q_{en}} = \frac{1}{Q_{ln}} - \frac{1}{Q_u} \tag{3.30}$$

Now the ratio is

$$R_e = \frac{Q_{e1}}{Q_{e2}} \tag{3.31}$$

When R_e is known, the unloaded quality factor can be calculated from the loaded quality factor and the transmission coefficient at the resonant frequency:

$$Q_{e1} = \sqrt{\frac{4Q_l^2 R_e}{a_r}}$$
$$Q_{e2} = \frac{Q_{e1}}{R_e} \qquad (3.32)$$
$$\frac{1}{Q_u} = \frac{1}{Q_l} - \frac{1}{Q_{e1}} - \frac{1}{Q_{e2}}$$

Depending on which method is used, the resonant frequency, the width of the peak, and the minimum reflection coefficient or the maximum transmission coefficient are needed for calculating Q_l using (3.25) and (3.26), or (3.28) and (3.29) or (3.32).

3.6 Calculation of the Complex Permittivity of a Dielectric Material Measured with a Resonator

When a resonator is used as a sensor for measuring the complex permittivity of a material on-line in the industry or of samples in the laboratory, the quantities to be measured are the resonant frequency, the loaded quality factor, and the reflection coefficient or the transmission coefficient at the resonant frequency. In addition the same quantities are supposed to have been measured for the empty resonator as a basic calibration.

The real part of the permittivity (ε_r') can be directly calculated from the measured resonant frequency of the empty and the filled resonator, by using Eq. (3.11), as shown above. In the case of very lossy samples, it should be remembered that (3.11) is an approximation of (3.10) and the accuracy should therefore be checked, when the imaginary part (ε_r'') has been calculated.

The imaginary part of the permittivity of the sample causes losses in the resonator. The losses of the sample are accounted for by the dielectric quality factor Q_d. To obtain ε_r'' from the measurements, Q_d must first be deduced. Eq. (3.14) shows that the measured Q_l in addition to the dielectric losses also depends on losses in the metal parts (Q_m), losses by radiation (Q_{rad}), and coupling losses caused by the measurement circuit (Q_{ext}). These other losses must first be evaluated and eliminated before Q_d can be obtained.

The coupling losses can be eliminated by calculating the unloaded quality factor Q_u using Eq. (3.26) in the case of reflection measurements or, Eq. (3.29) in the case of transmission coefficient measurements, if the coupling coefficients are equal. If the couplings are unequal, Eq. (3.32) should be used.

Still Q_m and Q_{rad} need to be evaluated. The loss by radiation is highly dependent on the resonator. ”Closed” resonators, like cavity resonators with solid walls, do not radiate at all, and many ”open” ones, like some stripline resonators [Fischer, 1995], [Fischer et al., 1988, 1989, 1990a, 1990b, 1991, 1995], [Nyfors et al., 1984, 1988a, 1988b, 1989a, 1989b, 1989c, 1993], [Vainikainen et al., 1985, 1986, 1987a, 1987b], [Tiuri et al., 1987], radiate very little. In these cases the approximation

$Q_{\text{rad}} \approx \infty$ can be used. Otherwise, Q_{rad} must usually be calibrated as a function of frequency and loaded quality factor, e.g. by measuring a series of samples with known ε_r, because calculation is difficult and the accuracy would be poor in most cases. For the accurate measurement of ε_r'' of low loss samples, only nonradiating resonators should be used.

The metal quality factor can be calculated at the frequency of the empty resonator, f_{r0}, from the measurements of the empty resonator. From (3.14):

$$\frac{1}{Q_{m0}} = \frac{1}{Q_{u0}} - \frac{1}{Q_{\text{rad},0}} \tag{3.33}$$

where the subscript 0 refers to the empty resonator. If $Q_{\text{rad}} \approx \infty$, the calculated unloaded quality factor is directly the metal quality factor. In other cases, $Q_{\text{rad},0}$ can be measured by building an identical resonator using another metal with different conductivity. $1/Q_{\text{rad}}$ is then

$$\frac{1}{Q_{\text{rad},0}} = \frac{\dfrac{1}{Q_{u01}} - \dfrac{1}{Q_{u02}}\left(\dfrac{\sigma_2}{\sigma_1}\right)^{1/2}}{1 - \left(\dfrac{\sigma_2}{\sigma_1}\right)^{1/2}} \tag{3.34}$$

where σ_1 and σ_2 are the conductivities of the two metals [Nyfors and Vainikainen, 1989a]. To achieve a good accuracy with this method the difference between the two conductivities should be considerable. The loss in the metal parts, however, is frequency dependent. Therefore Q_{m0} must be reduced from the resonant frequency of the empty resonator, f_{r0}, to the resonant frequency of the filled resonator, f_r. The equation for doing the reduction can be derived from the definition of the quality factor (3.12), by studying the dependence of the loss power and the stored energy on the magnetic field. As a result of the resonance condition the field pattern of a certain resonance mode in the resonator is constant, independent of the resonant frequency. Because the electric field energy equals the magnetic field energy, and the local magnetic field energy content is proportional to the square of the field strength, the total stored energy is proportional to the volume integral of the square of the magnetic field:

$$\text{stored energy} \propto \int_V |\mathbf{H}|^2 \, \mathrm{d}V \tag{3.35}$$

The loss in the metal parts is proportional to the surface integral of the surface resistance times the square of the surface current density. It has been shown [Collin, 1966, pp. 324-325] that

$$\text{loss power} \propto \sqrt{\omega} \int_S |\mathbf{H}|^2 \, \mathrm{d}S \tag{3.36}$$

From (3.12), (3.35), and (3.36):

$$Q_m \propto \frac{\omega \times \int_V |\mathbf{H}|^2 \mathrm{d}V}{\sqrt{\omega} \int_S |\mathbf{H}|^2 \mathrm{d}S} \tag{3.37}$$

Because the field pattern is constant, also the ratio of the integrals in (3.37) is constant leading to

$$Q_m \propto \sqrt{\omega} \tag{3.38}$$

which means that the metal loss will increase, when the resonant frequency is lowered by filling the resonator with a dielectric. This is important to note because erroneous expressions are found in some textbooks, e.g. [Gardiol, 1984], as also pointed out by [Sihvola, 1985]. The equation for reducing the metal quality factor, which was measured with the empty resonator, to the resonant frequency of the resonator filled with the sample is now:

$$Q_m = \sqrt{\frac{f_r}{f_{r0}}}\, Q_{m0} \tag{3.39}$$

The dielectric quality factor Q_d can now be calculated.

To get the relation between Q_d and ε_r'', consider a resonator with perfectly conducting walls and no other loss than the dielectric loss [Collin, 1966, p. 325]. The quality factor given by (3.12) is then the dielectric quality factor. If the sample in the resonator is homogeneous, the total stored energy is

$$W_E = \frac{\varepsilon_r' \cdot \varepsilon_0}{2} \int_V |\mathbf{E}|^2 \mathrm{d}V \tag{3.40}$$

The imaginary part of the permittivity can be written as an effective conductivity:

$$\begin{aligned} &\varepsilon_r = \varepsilon_r' - j\varepsilon_r'' = \varepsilon_r' - j\frac{\sigma_{\text{eff}}}{\omega\varepsilon_0} \\ &\Rightarrow \sigma_{\text{eff}} = \omega\varepsilon_r''\varepsilon_0 \end{aligned} \tag{3.41}$$

Because a volume current is proportional to the conductivity and the electric field

$$\mathbf{J} = \sigma\mathbf{E} \tag{3.42}$$

the loss power in the dielectric is

$$P_{ld} = \frac{1}{2}\int_V \mathbf{J} \cdot \mathbf{E}^* \mathrm{d}V = \frac{\omega\varepsilon_r''\varepsilon_0}{2} \int_V |\mathbf{E}|^2 \mathrm{d}V \tag{3.43}$$

Hence the dielectric quality factor is

$$Q_d = \frac{\omega W_E}{P_{ld}} = \frac{\varepsilon_r'}{\varepsilon_r''} \tag{3.44}$$

Collecting the results into one equation:

$$\varepsilon_r'' = \varepsilon_r' \left(\frac{1}{Q_u} - \frac{1}{Q_{\text{rad}}} - \frac{1}{Q_{m0}} \cdot \sqrt{\frac{f_{r0}}{f_r}} \right) \tag{3.45}$$

If the resonator does not radiate, or if Q_{rad} is very high (3.45) reduces to

$$\varepsilon_r'' = \varepsilon_r' \left(\frac{1}{Q_u} - \frac{1}{Q_{u0}} \cdot \sqrt{\frac{f_{r0}}{f_r}} \right) \tag{3.46}$$

where Q_u and Q_{u0} are calculated from (3.26), (3.29) or (3.32), depending on the measurement method. If the dielectric loss is high, the metal loss (and often also the radiation loss) can be neglected, leading to the approximate equation:

$$\varepsilon_r'' \approx \varepsilon_r' \cdot \frac{1}{Q_u} \tag{3.47}$$

It was here assumed that the resonator is filled with the material to be measured, called the sample, or that the field does not extend beyond the sample. For these cases, the equations give accurate results for the complex permittivity. If the assumption is not fulfilled, the equations can still be used in many cases. The values given for ε_r by the equations will be smaller than the real values. They are often called *effective values*. The relation between the effective and the real values of the sample depend on the type of resonator, resonant wave mode, and location, size, and shape of the sample. This relation can be calculated exactly in some special cases, or if the sample causes only a very small change in resonant frequency, approximately using the perturbation method, see e.g. [Nyfors and Vainikainen, 1989a], [Harrington, 1961], or [Waldron, 1960]. Otherwise the resonator sensor must be empirically calibrated using samples of known ε_r. In the new sensors and applications described later in this thesis, the sensors are completely filled with the sample. The case of a partially filled resonator will therefore not be dealt with here any further.

3.7 Cavity Resonator

The new resonator sensors, which are described later in this thesis, are cavity resonators. Cavities will therefore be briefly treated here on a general basis.

A resonator made of a piece of hollow waveguide is a cavity resonator. It is usually short-circuited in both ends either with solid metal walls, as in a laboratory sensor for measuring isolated samples, or with some kind of end grids to allow the material to flow through in on-line industrial sensors. In some cases the ends may be open, as briefly mentioned in Sec. 3.3. The various end structures will be treated in detail in Chs. 4, 6, and 7.

Any wave mode that can propagate in a waveguide and be reflected at the impedance discontinuities (i.e. the end structures), has resonances in the cavity. In hollow waveguides the wave modes are called TE_{nm} and TM_{nm} modes. The resonances for a mode occur at the frequencies, where the length of the cavity is a multiple of the half-wavelength of that mode. The resonant modes are called TE_{nml} or TM_{nml}, where the integers n, m, and l refer to the number of electric field maxima in the standing wave pattern along the x, y, and z directions for rectangular waveguides, or φ, ρ, and z directions for circular waveguides. In the non-standard case of a cavity with one open-ended and one short-circuited end, the index l would, however, not be an integer but an integer + ½. As mentioned in Sec. 3.3, some modes can also be supported with l = 0. This happens for TM modes, when the ends are short-circuited, and for TE modes, when the ends are open-circuited. These modes have no field maximum but a constant field in the z direction. In the case of cavities based on sectorial or semisectorial waveguides, which are described in Ch. 5, the index n may obtain non-integer real values. Every cavity has an infinite number of resonances.

The resonant frequency for a mode in a waveguide is

$$f_{r,nml} = \frac{c}{2}\left[\left(\frac{k_c}{\pi}\right)^2 + \left(\frac{l}{L}\right)^2\right]^{1/2} \tag{3.48}$$

where k_c is the cut-off wavenumber of the waveguide mode and L is the length of the resonator. For a rectangular cavity resonator this gives

$$f_{r,nml} = \frac{c}{2}\left[\left(\frac{n}{A}\right)^2 + \left(\frac{m}{B}\right)^2 + \left(\frac{l}{L}\right)^2\right]^{1/2} \tag{3.49}$$

where A and B are the width and height of the waveguide. For a circularly cylindrical resonator the resonant frequency of a TE_{nml} mode is

$$f_{r,nml} = \frac{c}{2}\left[\left(\frac{p'_{nm}}{\pi a}\right)^2 + \left(\frac{l}{L}\right)^2\right]^{1/2} \tag{3.50}$$

For TM_{nml} modes p'_{nm} should be replaced by p_{nm}. For a definition of the p values, see Ch. 5. In some cases more than one mode will have the same resonant frequency. They are called *degenerate modes*.

Because of the large number of resonances the cavity resonator sensor, including the type and location of the coupling devices, must be designed in such a way as to avoid the interference from other modes. This is not a big problem for cavities completely filled with an isotropic and homogeneous dielectric, because all resonant frequencies are shifted in the same way as a function of the permittivity. In partly filled resonators the frequency shift of each mode depends on the location of the sample with respect to the electric field of that mode. The order of the resonance modes in the frequency response may therefore change, when the sample is inserted or, when the permittivity of the sample changes. The potentially interfering modes can be easily identified by studying the electric field patterns (see e.g. Fig. 3.12 in [Nyfors

and Vainikainen, 1989a]) with respect to the location of the sample. The dimensions of the cavity should be chosen so that the distance in frequency is as large as possible between the mode, which is used for measurement purposes, and the other modes, especially those identified as potentially interfering modes. A chart showing the order of the resonances in a circularly cylindrical cavity resonator is shown in Fig. 3.3. It has been calculated using (3.50) and the *p* values given in Table 5.2.

The fields of the resonance modes can be calculated from the fields of two wave components travelling in opposite directions in a waveguide. When the boundary conditions at the ends are known, the fields can be solved. The fields of the modes in standard rectangular and circularly cylindrical cavities are given in e.g. [Nyfors and Vainikainen, 1989a].

3.7.1 Using TE_{011} in Laboratory Measurements

The mode TE_{011} is a particularly interesting mode for laboratory measurements of the permittivity of individual samples. The metal loss is low giving a high quality factor for the empty resonator, which makes possible the measurement of low-loss samples, like dry snow [Nyfors, 1982], [Sihvola et al., 1985], [Tiuri et al., 1984].

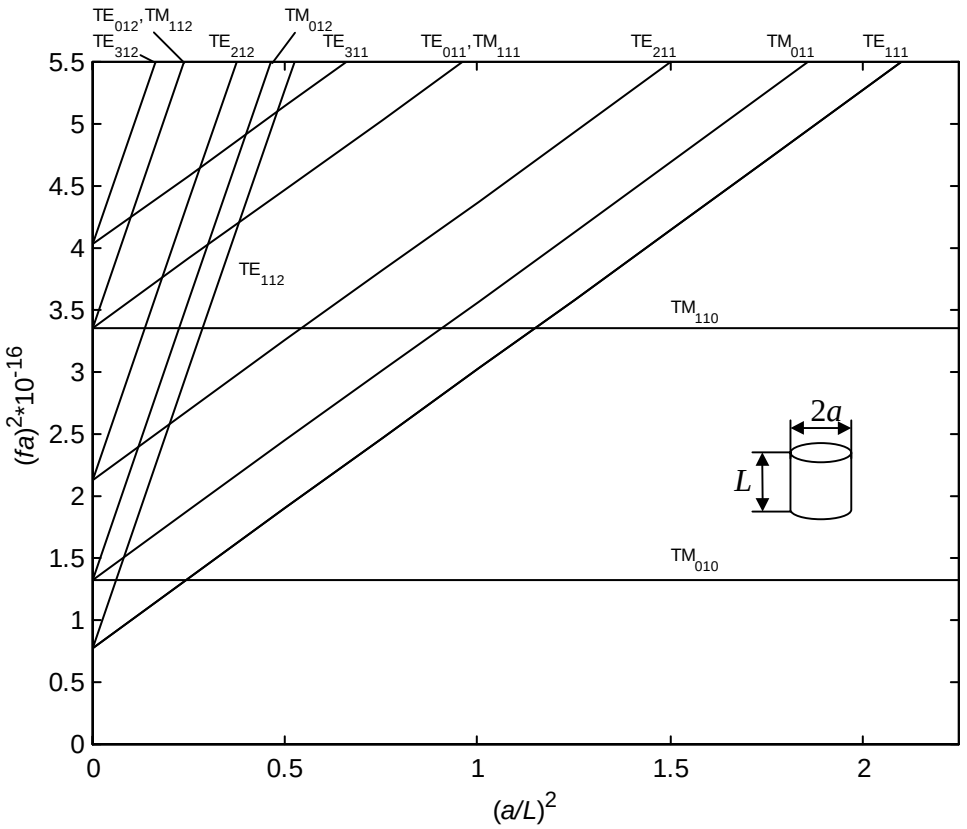

Figure 3.3 The chart shows the order of the resonances as a function of the radius (a) to length (L) ratio of a circularly cylindrical cavity resonator, with short-circuited ends. The chart has been calculated using Eq. (3.50) and the p values given in Table 5.2. An individual resonator would be represented by a vertical line at the location of the squared ratio $(a/L)^2$ of that resonator. In a short cavity the mode with the lowest resonant frequency is TM_{010}. Note that the frequency scale is quadratic.

The surface current on the walls on the inside of a cavity resonator is related to the magnetic field at the wall. The direction of the current is always perpendicular to the magnetic field. For a perfectly conductive wall, and in practice for normal metal walls, the surface current [A/m] is

$$\mathbf{J}_s = \hat{\mathbf{n}} \times \mathbf{H}_t \tag{3.51}$$

where $\mathbf{H}_t$ is the tangential magnetic field and $\hat{\mathbf{n}}$ is the normal vector at the wall. Because the magnetic field of the TE_{011} mode is axial at the cylindrical walls, and radial at the ends, the currents run along the circumference on the cylindrical walls and in concentric circles at the ends. No currents run across the joints between the cylindrical part and the end plates. As a consequence, the resonance mode is not sensitive to the quality of the contact between these parts. A practical resonator therefore uses one end plate as a lid allowing the insertion of the sample. The lid does not have to be fastened with a large number of screws for each measurement to get a good contact allowing the currents to pass undisturbed, as is the case with other modes. Holding the lid in place, such that there will be no radiating gap, is enough.

The modes TE_{011} and TM_{111} are degenerate modes, as is evident from Fig. 3.3. When using TE_{011} for measurements, the coupling loops must be located such that the coupling to TM_{111} is minimized. The loops can for example be located midway between the ends, where the magnetic field of TM_{111} is zero.

3.7.2 Using TM_{010} in Cavity Resonator Sensors

If the sensor is short, the lowest mode is TM_{010}, with a relatively long distance to the next mode. This is practical in industrial sensors, when the peak is low and broad (lossy sample) and in the presence of ripple, which is never completely avoided in a practical system. A long distance to the next peak then minimizes the risk of confusion of peaks. Sensors based on the TM_{010} mode will be treated in greater detail in Ch. 7.

3.7.3 Coupling Devices

To be able to perform measurements with a resonator, it must be coupled to some external electronics through coupling devices. If the method of reflection coefficient is used, only one coupling device is needed, and two in the case of the method of transmission coefficient. The possible choices for coupling devices are, however, the same for both measurement methods. In this section the most often used devices are described. The discussion is more or less restricted to qualitative matters, because the exact calculation of the coupling properties and the resulting external quality factor is generally not possible in practice. These matters are studied in more detail in Ch. 6 based on simulations.

A coupling device generates an electromagnetic field that in many cases can be approximately modelled by an electric or magnetic dipole moment, which couples to the corresponding field of the resonance mode. The excited field is directly

proportional to the dipole moment, which means that, for example, the power transmission coefficient depends on the fourth power of the dipole moment, if the probes are identical. For a theoretical discussion on excitation of cavities, see Sec. 7.8 in [Collin, 1966], or Ch. 7 in [Collin, 1991].

Coupling Probe

If the centre conductor of the feeding coaxial cable is extended a small distance into the resonator, it forms a coupling probe (Fig. 3.4a). The length of the probe is small compared to the wavelength, and the input impedance is therefore nearly equivalent to that of an open circuit. The current in the probe is small, but the voltage creates an electric field between the probe and the adjacent wall of the resonator. The field radiates energy into the resonator like a small monopole antenna. The dipole moment is approximately proportional to the square of the length of the probe, but depends also on the thickness of the probe, the diameter of the outer conductor, and the permittivity of the insulator.

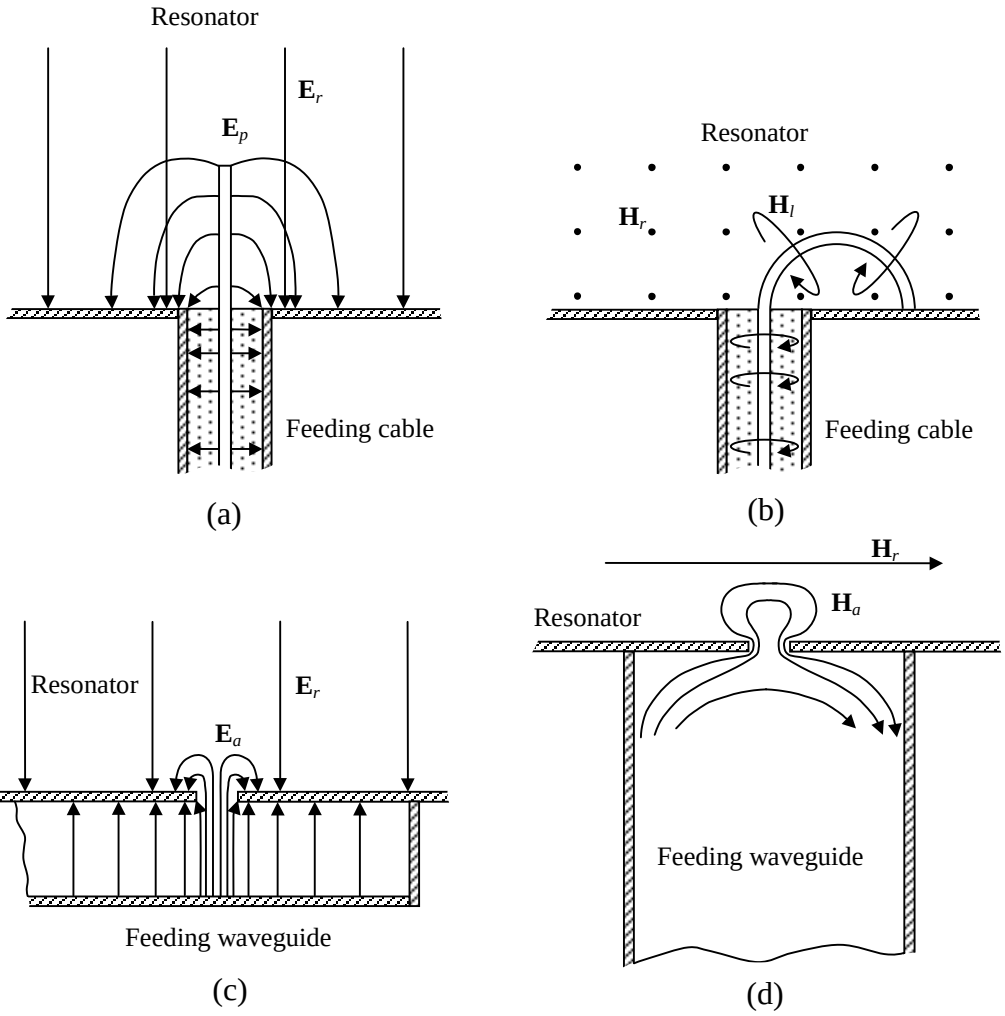

Figure 3.4 The most frequently used devices for coupling the measurement signal to a cavity resonator sensor: (a) Probe, (b) Loop, (c) Electric aperture, (d) Magnetic aperture.

The probe couples to the electric field that is perpendicular to the wall at the location of the probe. The coupling is stronger the closer to a field maximum the probe is located. Coupling to unwanted modes can be avoided by locating at least one of the probes in a place, where the electric field of such a mode is zero.

An advantage of the coupling probe is that of easy tuning. The probe can initially be made longer than necessary, and then trimmed until the desired coupling is obtained.

Coupling Loop

If the centre conductor of the feeding coaxial cable is extended a small distance into the resonator and then bent and grounded to the wall, it forms a coupling loop (Fig. 3.4b). The size of the loop is usually much smaller than the wavelength. Therefore the voltage is nearly zero but the current is large, and the input impedance is nearly equivalent to that of a short circuit. The current generates a magnetic field that radiates like a magnetic dipole tangential to the wall. The dipole moment is proportional to the loop area. The radiation couples to the magnetic field of a resonance mode that is tangential to the wall and perpendicular to the plane of the loop. Therefore the orientation of the loop is also important. The closer to a magnetic field maximum of a mode the probe is located and the larger is the loop area, the stronger is the coupling to the mode. Coupling to unwanted modes can be avoided by locating at least one of the probes in a place, where the magnetic field of such a mode is zero, or by orienting the loop such that the magnetic field of the unwanted mode is parallel to the plane of the loop.

A small advantage with a coupling loop is that it is more rugged than a thin or long coupling probe. A disadvantage is the more difficult tuning. In practice it is also more difficult to design a simple loop structure that is tight (for the measurement of liquids under high pressure) and is easy to assemble.

Coupling Aperture

If a waveguide is used as the feeding transmission line, the aperture (Fig. 3.4.c&d) is the natural coupling device. It is usually a small circular hole in the waveguide wall or the shorted end. Depending on the location of the aperture in the waveguide, the tangential magnetic field or normal electric field will penetrate the aperture and couple to the resonance mode. The strength of the coupling (the electric or magnetic dipole moment) is proportional to the third power of the radius of the aperture. The coupling depends, of course, on the location of the aperture with respect to the field of the resonance mode and the direction of the field lines in the case of magnetic coupling.

Other Methods of Coupling, and Practical Considerations

Resonators can also be excited through capacitive coupling or free-space coupling. The most frequently used type of capacitive coupling is an air gap, e.g. in the case of

microstrip resonators. Free-space coupling can be used in the case of open resonators, but for cavity resonators the probe, the loop, or the aperture usually provides the best solution.

In addition to the strength of the coupling to the desired mode, the frequency response around the resonance peak may also be important. The proximity to other modes compared to the range of variation of the resonant frequency determines the risk of confusion of modes. The direct coupling (capacitive between probes or inductive between loops) determines the height of a ”continuum” level around the peak, and may make the identification of a low peak difficult. To minimize the direct coupling the probes should be located as far apart and have as small intrusive structures as possible. To minimize the risk of confusion of modes the probes should be located (and oriented in the case of loops or apertures) such that coupling to the adjacent modes is avoided.

3.8 Some General Aspects of Using Microwave Resonators as Sensors

3.8.1 Two-Parameter Measurements with Resonator Sensors

A wide area of applications of microwave resonator sensors involves measuring the composition of a material stream or of isolated samples. Using microwave resonators for performing material measurements is based on measuring the permittivity, which depends on the composition, via the interaction of microwaves with the material, as described above. Because the permittivity is complex and both the real and the imaginary part can be deduced from measurements of the resonant frequency and the quality factor, microwave resonators can be used for performing two-parameter measurements on a single frequency. In terms of the interaction between the microwaves and the material, both the speed of propagation and the rate of attenuation (absorption of power) are then measured. Based on these measurements, e.g. the moisture and the density of the material can be deduced (e.g. [Kent and Kress-Rogers, 1986], [Nakayama, 1987]).

Generally, to be able to solve the unknowns of a system of n unknowns, n equations are needed. Each measurement gives one equation. A microwave resonator sensor can provide two equations. In systems with more than two unknowns, additional measurements are needed. Frequently encountered supplementary measurements include temperature, pressure, and radioactive density sensors.

In many cases only one parameter, usually the resonant frequency, is measured with the resonator sensor. A reason may be that there is only one unknown, but more often the reason is that the quality factor depends on several parameters like ion conductivity and relaxation loss, which are associated with dissolved substances (e.g. salts) and polar molecules respectively. Measuring the quality factor therefore also introduces new unknowns, which may be of little interest. A more detailed account of microwave multiparameter measurements has been given by the author in Ch. 2 of [Nyfors and Vainikainen, 1989a].

3.8.2 Measuring Speed of Flow

Resonators with a sufficiently open structure can be used for measuring on a continuous flow of material. In addition to the composition measurement, the speed of flow is often also of interest in such cases, thus making possible the calculation of the flow rates of the individual components. The speed of flow can be measured with microwave resonators using various correlation techniques based on one sensor with multiple field maxima (e.g. [Kobayashi and Miyahara, 1985] or [Montreuil and Nachman, 1992]) or two separate consecutive sensors. Regardless of the technique, a condition for good speed measurements is that the variations in the stream are large enough to be detected with high speed.

When two consecutive sensors are used, the same variations are seen by both sensors but with a delay in the sensor located downstream. When coincident time serieses of measurements from the two sensors are cross correlated, the delay Δt_{cc} is given by the relative shift of the serieses that gives the highest correlation. From the time delay and the known distance d_{cc} between the sensors, the speed of flow v_f is easily calculated:

$$v_f = \frac{d_{cc}}{\Delta t_{cc}} \tag{3.52}$$

When only one sensor is used, it must have an electric field pattern with at least two field maxima in the direction of the flow. If the flow is in the direction of the length axis of the transmission line, which forms the resonator, possible resonance modes are those with index $l \geq 2$. When the inhomogeneities of the flow (e.g. larger drops of water) flow through the sensor, they cause a change in the resonant frequency and quality factor twice, each time they pass a field maximum. By calculating the autocorrelation of the measurement signal, the time delay is found, and the speed can be calculated from (3.52) in the same way as with two sensors, but now d_{cc} is replaced by d_{ac}, which is the distance between the consecutive field maxima.

3.8.3 Loss Limitations

The basic condition for performing measurements with a resonator sensor is that the resonance peak can be found and measured with enough accuracy. If the used peak is close to other resonances or the frequency response of the measurement system contains ripple, the detection and correct identification of the peak requires a higher quality factor, than if the peak is isolated and clean. From the characteristics of the measurement system, and the accuracy requirements of the application, a lower limit may be defined for Q_l. When measuring lossy samples, the other sources of loss in (3.14) are small compared to the dielectric loss in the sample. A limit for the conductivity and other losses in the measured material can therefore be found from (3.44) and (3.41).

The limitation discussed above concerns the permittivity of the measured sample, i.e. the mixture. It must be pointed out that depending on the structure of the mixture, the conductivity of one of the components in the mixture may me much higher than the limit found for the mixture. For example, in an oil-continuous mixture

of oil and water (the oil is the continuous phase and the water exists as isolated drops) the dielectric quality factor Q_d reaches a minimum for a water conductivity of roughly $\sigma_w \approx 5$ S/m. For higher or lower conductivity the mixture is less lossy. In practice an oil-continuous mixture of oil and water is always measurable (i.e. the quality of the peak is high enough that the peak can be identified) with a resonator, while water-continuous mixtures are measurable only in the case of nearly fresh water. This situation is correctly predicted with most models that describe the permittivity of a mixture as a function of the permittivity of the components, i.e. so-called mixing formulas (see Ch. 2 in [Nyfors and Vainikainen, 1989a]), when the host component (continuous phase) is considered nonconductive and the inclusions conductive, and vice versa.

4 PRINCIPLES FOR IMPLEMENTING RESONATOR SENSORS IN PIPES

4.1 Introduction

In the industry there is often a need to measure various parameters of materials flowing in pipes. The material may be a mixture of liquids, liquids and gases, or solid particles in pneumatic or liquid assisted transportation. Often the flow speed is one of the unknowns wanted to be measured, in addition to some material parameters. When the material properties, which are subject to measurement, affect the complex permittivity of the material or mixture, microwave sensors can often be used. Typical applications are the measurement of the water content of oil, consistency in pulp, and the moisture and instantaneous density of a flow of wooden chips, grain, coal, or limestone, to name a few. The permittivity of water is high compared to most other materials, which makes the microwave sensors particularly well suited for various applications involving the measurement of water content. Because of the complex nature of the permittivity, the sensors may be used for performing two-parameter measurements, thus providing a means for example to compensate for density variations while performing moisture measurements. For a good collection of examples of microwave sensors for performing material measurements involving water, see [Kraszewski, A., Ed., 1996].

The above-described measurements may be conveniently performed on-line, while the material is being transported in a pipe. Microwave techniques provide a variety of possibilities for implementing sensors for such applications. Some of the solutions were presented in Chapter 2. The general principles, how to implement microwave resonator sensors in pipes, will be described in this chapter.

4.2 Resonator Sensors Operating below the Cut-Off Frequency of the Pipe

A sensor that is designed for measuring material in movement must have a relatively open structure to allow the material flow to pass unhindered. Especially if the material stream consists of solid particles, the sensor should have as little intrusive parts as possible not to cause congestion. At the same time it is desirable that the sensor measures the whole flow. On the other hand, the more open the sensor structure is, the more prone it is to radiate.

One way to achieve open resonator structures that do not radiate, is to use frequencies that are low enough. If the sensor is designed so as to have a resonant frequency, which is below the lowest cut-off frequency in the pipe, the energy can not radiate out into the pipe even from an open sensor structure, because it cannot propagate in the pipe. Therefore the sensor will not radiate and a quality factor is achieved, which is as high as for a completely closed structure. This basic principle was developed by the author and his colleagues at the Radio Laboratory of Helsinki University of Technology and patented in Finland [Tiuri et al., 1986]. Structures based on this principle may be very open in the pipe, allowing the flow to pass more or less without any mechanical interference from the sensor.

4.2.1 Isolation Provided by a Pipe below Cut-Off

Electromagnetic energy on a frequency below the cut-off frequency does not propagate in the pipe. It does, however, penetrate into the pipe from the location of excitation as an exponentially decaying evanescent or fringing mode. The fields pulsate in every location with the same phase. The fact that the fields penetrate into the pipe means that a certain length of pipe is needed on each side of the resonator to provide enough isolation. This length depends on the relative distance in frequency between f_r and f_c, and on the required limit for the radiation losses represented by Q_{rad}. Normally this is no problem, because the pipe continues for a long distance both upstream and downstream. However, any changes of diameter, intrusive thermowells, bends, or valves within the length of pipe that is required for sufficient isolation, disturb the resonator. The value of Q_{rad} is also of importance when testing and calibrating the sensor before installation.

The isolation provided by a section of waveguide below cut-off can be calculated from the propagation factor in a hollow waveguide

$$\beta = \sqrt{k^2 - k_c^2} = \frac{2\pi}{\lambda_{pw}}\sqrt{1-\left(\frac{f_c}{f}\right)^2} \tag{4.1}$$

where k_c is the cut-off wave number of the lowest mode in the pipe, and λ_{pw} is the wavelength given by (3.9) of a plane wave at frequency f in the medium, with which the pipe is filled, i.e. the MUT. When $f < f_c$, β becomes imaginary:

$$\beta = j\frac{2\pi}{\lambda_{pw}}\sqrt{\left(\frac{f_c}{f}\right)^2 - 1} \tag{4.2}$$

describing an exponentially decaying field. This decay is not caused by absorption but by reflection, much in the same way as outside the passband of a lossless filter. Taking the negative solution of the square root, as being the physical one, the decay of the power as a function of the distance z is given by

$$P(z) = P_0 e^{-j2\beta z} = P_0 e^{-2\left(\frac{2\pi}{\lambda_{pw}}\sqrt{\left(\frac{f_c}{f}\right)^2 - 1}\right)z} \tag{4.3}$$

Here the loss in the imperfectly conducting metal walls has been omitted, because it is insignificant compared to the exponential decay below cut-off. At the frequency f the power reflection coefficient from a pipe of length d is then

$$|\Gamma|^2 = 1 - \frac{P(d)}{P_0} = 1 - e^{-2\left(\frac{2\pi}{\lambda_{pw}}\sqrt{\left(\frac{f_c}{f}\right)^2 - 1}\right)d} \tag{4.4}$$

Equation (3.23) can now be used for calculating the radiation quality factor Q_{rad}, assuming that the pipe can radiate freely from the ends at the distance d from the sensor. Even if the pipe continues such that it can not radiate, the calculation is useful

for choosing the minimum distance to any potentially disturbing object or discontinuity in the pipe. If the Q_{rad}, which is calculated for a pipe length equal to the distance to a discontinuity, is above the limit specified for the design, the discontinuity can be assumed not to disturb the sensor. The loss factor α in (3.23) contains the losses from the metal walls and the MUT inside the sensor and can be taken into account separately in Q_m and Q_d. If α is therefore omitted here, (3.23) gives the radiation quality factor:

$$\frac{1}{Q_{\mathrm{rad}}} = \frac{-\log_e\left(1 - e^{-\frac{4\pi d}{\lambda_{pw}}\sqrt{\left(\frac{f_c}{f_r}\right)^2 - 1}}\right)}{\beta_s L}\left[1 - \left(\frac{f_{cs}}{f_r}\right)^2\right] \tag{4.5}$$

where f_r is the resonant frequency, β_s is the propagation factor in the sensor at f_r, and f_{cs} is the cut-off frequency in the sensor.

Resonator and Pipe Completely Filled by the MUT

If the resonator and the pipe are completely filled with the MUT, the ratios f_c/f_r and f_{cs}/f_r will stay constant although f_r, f_{cs}, and f_c will change, when the permittivity of the MUT changes. The wavelength λ_{pw} and the factor β_s will also stay constant because of the resonance condition that requires that the length of the resonator expressed in wavelengths is constant. Thus the length d that is needed to achieve a certain Q_{rad} is independent of the permittivity of the MUT. Because the ratio f_{cs}/f_r and the factor β_s are always constant in cases, when the resonator sensor is filled by the MUT, a constant k_1 may be defined, which is constant for the sensor:

$$k_1 = \frac{1 - \left(\frac{f_{cs}}{f_r}\right)^2}{\beta_s L} \tag{4.6}$$

Now (4.5) can be written as

$$\frac{1}{Q_{\mathrm{rad}} \cdot k_1} = -\log_e\left(1 - e^{-\frac{4\pi d}{\lambda_{pw}}\sqrt{\left(\frac{f_c}{f_r}\right)^2 - 1}}\right) \tag{4.7}$$

Figure 4.1 shows graphs of $Q_{\mathrm{rad}} \cdot k_1$ as a function of d/λ_{pw} for various values of f_c/f_r. If the resonant frequency is close to the cut-off frequency, a large value of d is needed.

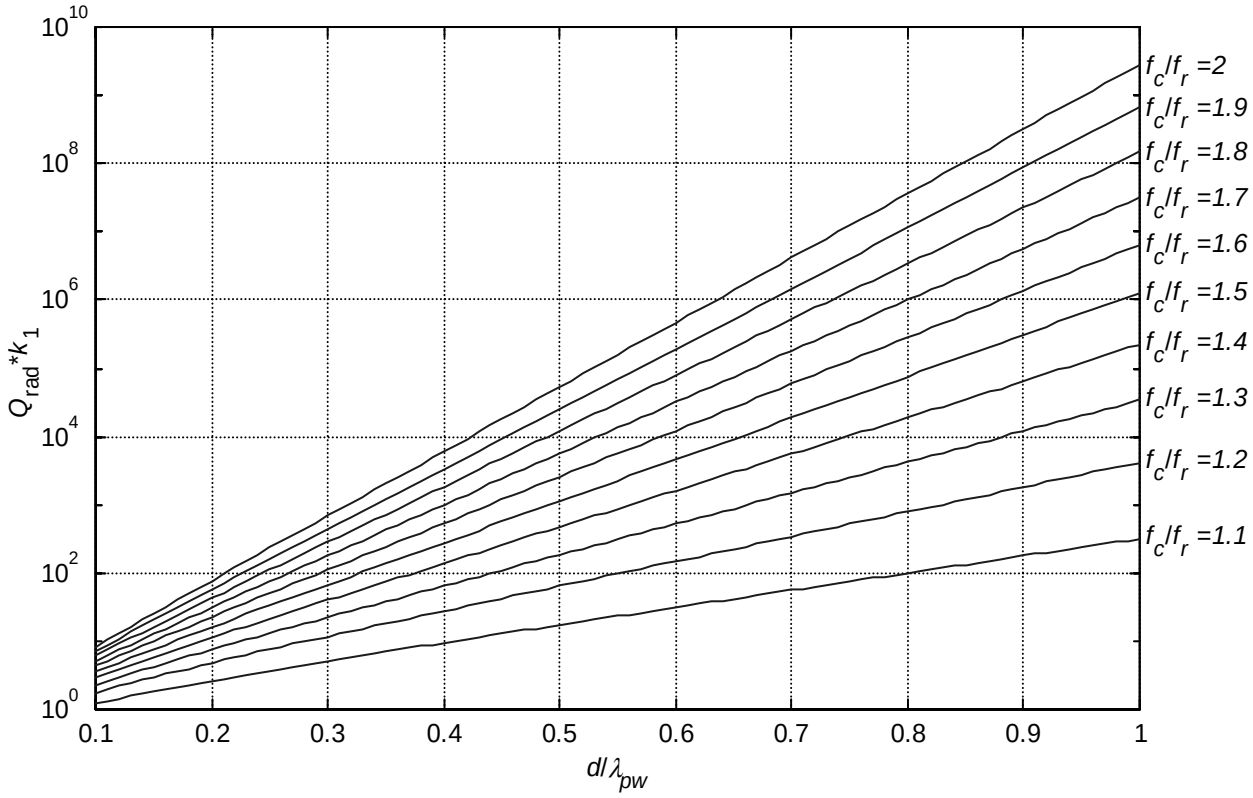

Figure 4.1 The diagram shows graphs calculated with Eq. (4.7), illustrating the minimum length of pipe needed on both sides of a below-cut-off resonator sensor to achieve a desired isolation. (See text for explanation of the symbols.)

Resonator Partly Filled and Pipe Completely Filled by the MUT

If the pipe is completely filled but the sensor is not, the ratio f_{cs}/f_r will change with the permittivity, but more significant changes will happen in f_c/f_r and λ_{pw}. The relative decrease in f_c for an increase in permittivity will be larger than in f_r, resulting in a larger value of d corresponding to a given value of Q_{rad}. For example, if only a small fraction of the sensor is filled by the MUT, the relative changes in the resonant frequency will be small and the ratio f_{cs}/f_r will be almost unchanged, but λ_{pw} and f_c in the pipe will change according to

$$\lambda_{pw} = \frac{\lambda_{pw0}}{\sqrt{\varepsilon_r'}}$$
$$f_c = \frac{f_{c0}}{\sqrt{\varepsilon_r'}} \qquad (4.8)$$

Here it was assumed that $\varepsilon_r'' << \varepsilon_r'$, because the below-cut-off decay has a meaning only as long as the dielectric loss in the pipe is small. At the limit, when the sensor contains only a very small amount of the MUT and the change in f_r caused by a large change in the permittivity is negligible, (4.5) changes to

$$\frac{1}{Q_{\text{rad}}} = \frac{-\log_e\left(1 - e^{-\frac{4\pi d}{\lambda_{pw0}}\sqrt{\left(\frac{f_{c0}}{f_r}\right)^2 - \varepsilon_r'}}\right)}{\beta_s L}\left[1 - \left(\frac{f_{cs}}{f_r}\right)^2\right] \qquad (4.9)$$

All factors in (4.9) are nearly constant, except for the permittivity under the square root. Eq. (4.9) gives the worst case for the increase in the length of pipe d needed to achieve a given Q_{rad}, when the permittivity increases.

Practical Considerations

The loss in the MUT usually increases with increasing permittivity, which causes the decrease in resonant frequency. From (3.13) it is seen that the unloaded quality factor will then be dominated by the dielectric loss and not the radiation loss, when the permittivity of the MUT is high. If the MUT may have low losses also for a high permittivity, this must be taken into account in choosing the value of d for a sensor. Before choosing the value of d for a sensor, the worst case must be identified and used as a basis for the calculations.

The radiation quality factor calculated with (4.7) or (4.9) must be considered as a minimum value, because the derivation of the equations was based on the assumption that the concept of reflection coefficient is relevant, i.e. that the resonant mode is the same as the lowest mode in the pipe. In practice the efficiency, with which the resonant mode launches the lowest mode into the pipe, depends on the structure of the resonator and the electromagnetic field configuration at the ends of the resonator. Especially sensors, where the MUT fills only a small fraction of the resonator, tend to have structures that do not couple efficiently to the modes in the pipe. However, the relative dependence of Q_{rad} on d/λ_{pw} is expected to be accurately given by (4.7) and (4.9).

In the case of sensors, where the length-related third index of the used resonance mode is $l = 0$ ($f_r = f_{cs}$), Eq. (3.23) can not be used directly, as mentioned before. Hence also (4.7) applies only to modes with $l \neq 0$. However, the calculation of the isolation provided by a section of pipe below cut-off is clearly significant also for resonators with $l = 0$.

In the case of sensors for which the above used concept of reflection coefficient is not relevant, the attenuation in the pipe below cut-off may be considered as a reduction of radiation. For example sensors that are large compared to the diameter of the pipe, or sensors with $l = 0$, may have a considerable radiation quality factor already for zero length of the pipe ($d = 0$). In many cases the radiation from such a resonator without the pipe can be approximately calculated using methods from the field of antenna engineering, considering the holes as aperture antennas. When the radiated power relative to the stored energy has been calculated for $d = 0$, the effect of the pipe can be taken into account using (4.3) and the definition of the quality factor in (3.12):

$$\frac{1}{Q_{\text{rad}}} = \frac{P_{\text{rad0}} e^{-2\left(\frac{2\pi}{\lambda_{pw}}\sqrt{\left(\frac{f_c}{f_r}\right)^2 - 1}\right)d}}{\omega W_0} = \frac{e^{-2\left(\frac{2\pi}{\lambda_{pw}}\sqrt{\left(\frac{f_c}{f_r}\right)^2 - 1}\right)d}}{Q_{\text{rad0}}} \tag{4.10}$$

where P_{rad0} is the radiated power and W_0 is the stored energy, when $d = 0$. The exponent of the exponential function will be small for any practical length of the pipe. Considering that

$$-\log_e(1-x) \approx x, \quad \text{when} \quad x << 1 \tag{4.11}$$

it can be seen from (4.7) that

$$k_1 \approx \frac{1}{Q_{\text{rad0}}} \tag{4.12}$$

However, in the case of sensors that are not completely filled with the MUT, k_1 and Q_{rad0} will change with the permittivity, but again the largest change will be in the exponent.

4.2.2 Examples of Sensors with a Resonant Frequency below the Cut-Off of the Pipe

Nonintrusive Cavity Sensor

In cavity resonators with the same relative dimensions, the resonant frequency is inversely proportional to the size. Because larger cavities have lower resonant frequencies, the resonant frequency of the used mode can be made lower than the cut-off frequency of the pipe by making the cavity sensor large compared to the pipe. Figure 4.2 shows one example of how this idea can be realized as it was suggested by the author and his colleagues in the Finnish patent [Tiuri et al., 1986]. The cavity is formed by a section of pipe with larger diameter than the rest of the pipe. The cylindrical cavity has holes in the end plates, where the pipe is connected. The size of the holes is the same as the inner diameter of the pipe, and inside the cavity is a dielectric sleeve, such that the MUT can flow in a pipe of unchanged diameter. The advantage with this type of sensor is that it is completely nonintrusive, whereas the large size of the sensor may be a disadvantage.

The resonator is only partly filled with the MUT, which means that the shift in the resonant frequency as a function of the permittivity is smaller than for a completely filled resonator, and is therefore not given by the simple formula derived in Ch. 3, Eq. (3.11). The holes in the end plates will also affect the fields of the resonant mode in the cavity, such that the field distribution is only approximately given by the field equations of the mode in an ideal cylindrical cavity. The permittivity of the MUT will also affect the field distribution. If the pipe is very small compared to the size of the sensor, the field distribution will be close to that of the undisturbed mode, and the frequency shift can be approximately calculated using the perturbation method (see e.g. [Nyfors and Vainikainen, 1989a], [Harrington, 1961], or [Waldron, 1960]). However, in most practical cases the size of the pipe is so large that

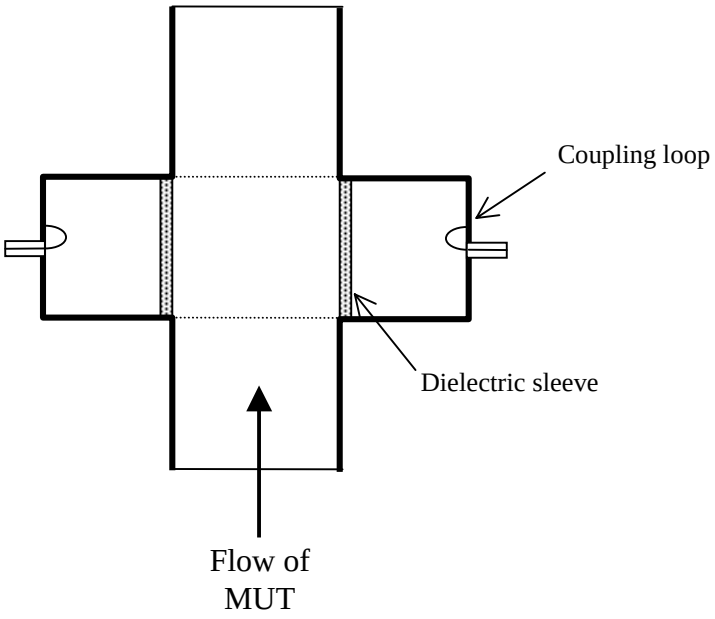

Figure 4.2 Nonintrusive cylindrical cavity resonator sensor for measuring materials flowing in a pipe. The resonant frequency is below the cut-off frequency of the pipe, which therefore prevents escape of energy by radiation into the pipe [Tiuri et al., 1986].

the accuracy of the perturbation method is poor. The best solution is then to simulate the frequency shift and the change in the quality factor with dedicated software, and to build a mathematical model based on the simulations. The model can then be checked and refined by comparison to measurements of materials of known permittivity. Alternatively the model can be based entirely on measurements, but then a larger number of measurements is needed.

Because this nonintrusive sensor is only partly filled with the MUT, it is less sensitive and the dielectric loss in the MUT effects Q_d less than in completely filled sensors. It can therefore be used for measuring materials with higher losses than if it was completely filled. The sensitivity can be further reduced by a proper choice of the resonant mode.

The choice of resonant mode is important for achieving the desired characteristics of the sensor. If it is desirable to have as much sensitivity as possible, a mode with the electric field maximum in the centre should be chosen, like e.g. TE_{111}, or TM_{010}. If low sensitivity is desirable, a mode like TE_{011}, with an electric field minimum at the centre axis, may be a good choice. It should be remembered though that the holes in the sensor may affect various modes differently, especially if the diameter of the holes is large compared to the length or the diameter of the sensor. It should also be remembered that because the various modes have different sensitivity, adjacent modes may come close to the used mode and cause interference, or the order of the modes may even change, as the permittivity of the MUT changes. To avoid the risk of confusion of modes, the resonant mode and the dimensions of the resonator should be chosen with care. A first design may be based on qualitative sensitivity estimates made from pictures of the modes (see e.g. [Nyfors and Vainikainen, 1989a],

[Ramo et al., 1984], or [Saad, 1971]) and identification of potentially interfering modes from the diagram in Fig. 3.3.

An example of a commercial sensor based on this principle is the nonintrusive version of the MFI WaterCut Meter made by Roxar, which is used in applications where the flow contains solid particles that may cause a risk for clogging in a normal WaterCut sensor with end grids (see Ch. 7). One such application is the measurement of rubber slurry in the rubber industry.

Coaxial Resonator Sensor

By mounting a metal rod with dielectric supports axially at the centre of a pipe, the section with the rod turns into a coaxial transmission line (Fig. 4.3). This can be used as a sensor for materials under flow, as suggested by the author and his colleagues in [Tiuri et al., 1986]. Because the rod is held in place by dielectric supports such that the ends are electrically open, the resonance condition in (3.3) gives that the first resonance occurs, when the rod is half a wavelength long. By making the rod long enough, the resonant frequency will be lower than the cut-off frequency of the pipe. In a cylindrical pipe the mode with the lowest cut-off frequency is TE_{11} (see Ch. 5). The corresponding free-space cut-off wavelength is

$$\lambda_{c,\text{pipe}} = \frac{2\pi a}{p'_{11}} = 1.71 \cdot D_p \tag{4.13}$$

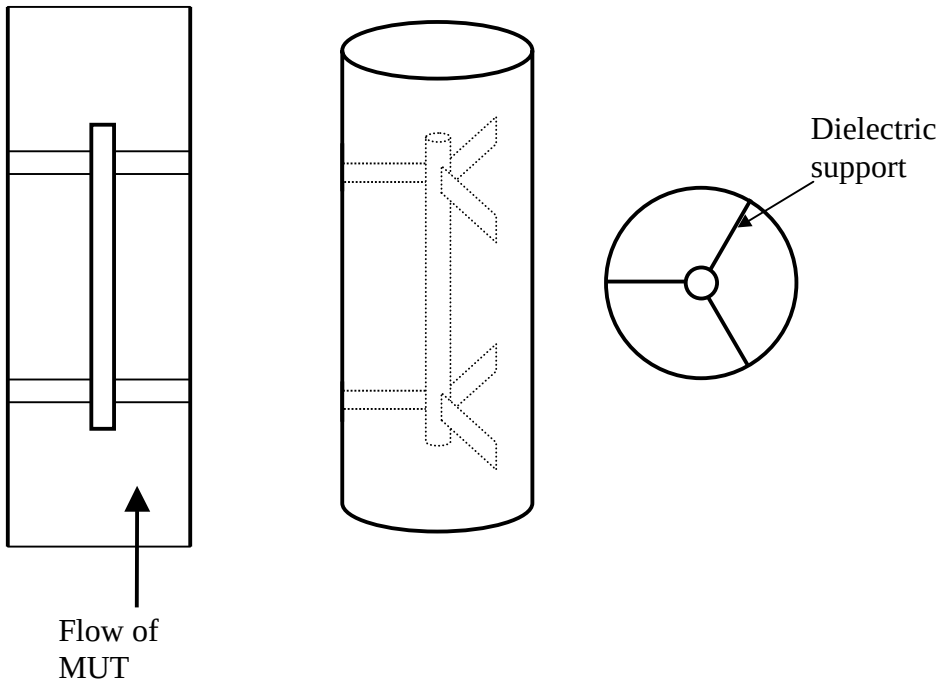

Figure 4.3 A coaxial sensor for measuring materials flowing in a pipe [Tiuri et al., 1986]. A rod acting as the centre conductor is mounted in the centre with dielectric supports. The resonant frequency is below the cut-off frequency of the pipe, which therefore prevents the escape of energy by radiation into the pipe.

where D_p is the inner diameter of the pipe. Making the rod longer than $0.85 \cdot D_p$ therefore assures that the resonant frequency is below the cut-off of the pipe. The circularly symmetrical TEM field in the coaxial sensor will not couple efficiently to the TE_{11} mode, which does not have circular symmetry. Achieving good isolation is therefore possible with relatively short sections of pipe outside the ends of the rod.

For the frequency response to be clean in the neighbourhood of the resonance peak, the resonant frequency should also be well below the cut-off frequency of the lowest waveguide mode of the coaxial section. This mode is also called TE_{11}, but should not be confused with the modes with the same name in hollow waveguides. The free-space cut-off wavelength of the coaxial TE_{11} mode is

$$\lambda_{c,\mathrm{coax}} = 1.873 \frac{\pi}{2}(a+b) \tag{4.14}$$

where a and b are the outer and inner radii of the coaxial structure (see e.g. [Saad, 1971], or [Marcuvitz, 1951]). If for example $a = 3b$:

$$\lambda_{c,\mathrm{coax}} = 1.96 D_p \tag{4.15}$$

which is a lower frequency than the cut-off frequency of the pipe, given by (4.13). The TE_{11} mode will not be in resonance at the same frequency as the normal TEM mode even above the cut-off frequency, because the wavelength of the waveguide mode is longer, as given by (3.6). To avoid confusion of modes, it is usually desirable to have an as long distance in frequency from the used mode to the other modes as possible. Given by (3.3) the next resonance of the TEM mode is, when the rod is one wavelength long, i.e. the second resonance is one octave higher than the first one. The largest distance is therefore achieved, when the first resonance of the TE_{11} mode is also at least twice the first resonant frequency of the TEM mode. With the example above ($a = 3b$) this is achieved, when the length of the rod is $L > 2.61 D_i$.

In practice the effective length of the rod will be slightly longer than the physical length, because of the fringing fields at the ends. Because the electric field maxima are located at the open ends of the rod, while the magnetic field maximum is located midway between the ends, only the electric field fringes at the ends. The fringing field therefore acts like load capacitors, which shift the relative phase between the electric field and the magnetic field at the ends, making the transmission line look slightly longer.

An advantage with this type of sensor is that the outer diameter is small. A disadvantage is that the rod and the dielectric supports block a part of the cross section of the pipe. It is therefore best suited for liquids, or a flow containing also solid particles if the diameter of the pipe is large, such that the relative blockage can be made small.

An example of a commercial sensor based on this principle is the FullCut version of the MFI WaterCut Meter made by Roxar, which is used for measuring mixtures of oil and water.

Transversal Stripline Resonators in Rectangular Pipes

If a metal strip is mounted transversally in a rectangular pipe with one end shorted to the wall of the pipe and the other end open, or if it is shorted in both ends, it will form some kind of a quasi-TEM line structure with the pipe. In the patent [Tiuri et al., 1986] the author and his colleagues have suggested two such sensor structures, which are based on the principle of resonance below the cut-off frequency of the pipe.

Figure 4.4 shows a rectangular pipe with a metal strip attached perpendicularly to the wall such that the attached end is shorted and the other end is open. The strip reaches across the pipe to a point past the centreline. The strip and the pipe together form a parallel-plate TEM line structure, i.e. a stripline across the pipe. According to the resonance condition in Eq. (3.5) the stripline is in resonance, when it is a quarter of a wavelength long. Because the cut-off wavelength of the TE_{10} mode (which is the lowest mode in a rectangular waveguide) in the rectangular pipe is twice as long as the width of the broader wall, the resonance will be below cut-off, when the strip reaches past the centreline. However, because of the fringing field in the open end of the strip, and the relatively large distance between the walls compared to the length of the strip, the resonant frequency is only approximately given by the length of the strip. It should also be noted that this structure bears a resemblance to the sectorial waveguide (Ch. 5) with a sector angle of 2π, and the cylindrical fin resonator sensor based on this waveguide. The cylindrical fin resonator sensor will be described later in Ch. 6. Based on this resemblance it can be expected that waveguide modes, which are related to the sectorial waveguide modes in cylindrical pipes (Ch.5), can exist in the rectangular pipe with a fin. That means that if one starts with a cylindrical fin resonator and changes the shape of the outer conductor from cylindrical to rectangular in a

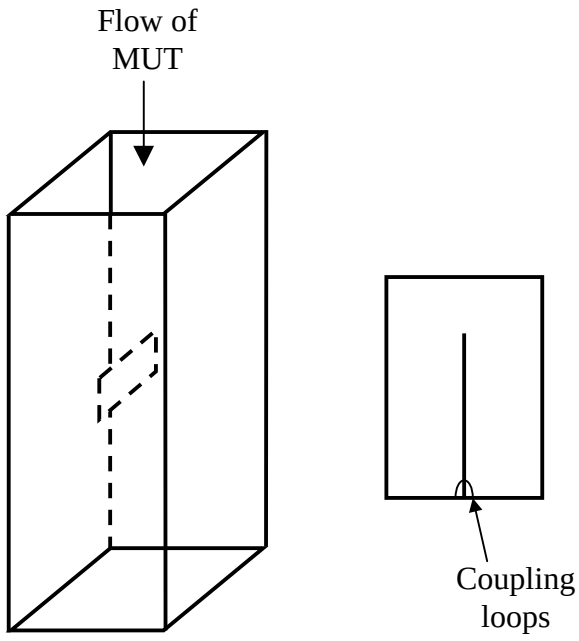

Figure 4.4 A stripline resonator sensor in a rectangular pipe, formed by a strip attached perpendicularly to the wall of the pipe [Tiuri et al., 1986]. The resonant frequency will be below the cut-off frequency of the pipe, when the strip is longer than approximately half of the width of the broad wall.

continuous process, there should be a continuous transition from e.g. the $TE_{½10}$ mode to a related mode in the stripline resonator in Fig. 4.4. To study the existence of such modes, and to get the cut-off frequency and the corresponding resonant frequency more accurately, simulations were performed with the Hewlett-Packard HFSS (High Frequency Structure Simulator) software version 5.1 for PC, which uses the finite element method.

A waveguide with a rectangular cross section of 37.5 mm x 75 mm is known to have a cut-off frequency of 2 GHz (TE_{10}). Such a waveguide with a fin attached to the narrow wall, also called a ridged waveguide, was simulated with HFSS. Figure 4.5 shows the waveguide and the electric field pattern resulting from the simulations. Comparing this field pattern to that of the $TE_{½1}$ mode in Fig. 5.3 shows that they are clearly related. The results for the cut-off frequency as a function of the height of the fin are shown in Fig. 4.6.

Next a resonator was simulated. The height of the fin was 45 mm and the length (in the axial direction of the waveguide) was 10 mm. Assuming that the first resonance should be a mode with the third index $l = 0$ (see Sec. 3.3), as in the cylindrical fin resonator, the resonant frequency should be approximately equal to the cut-off frequency. The simulation gave a resonant frequency of $f_r = 1.367$ GHz, whereas the cut-off frequency for the waveguide with the same height of the fin was 1.392 GHz. The difference is only 1.8%, which confirms the assumption of the resonant mode. Figure 4.6 also shows the resonant frequency calculated assuming that the structure is a $\lambda/4$ long stripline resonator, without any correction for the fringing field at the end of the fin. I.e. the length of the resonator was taken equal to the length of the strip. The stripline model gives a resonant frequency that is between 17% and 34% higher than the simulated resonant frequency, which is probably close to the real resonant frequency.

The advantage with the sensor in Figure 4.4 is the simple structure. The sensor can be made as an insert sensor, with the strip and the coupling loops attached to a flange. The disadvantage is the uneven distribution of the sensitivity over the cross section of the pipe. The electric field strength is highest on the surface of the strip in the region of the open end.

Only solid particles, like for example wooden chips, are likely to be transported in rectangular pipes. If the particles are sticky, they may to some degree accumulate on the strip (and the walls), which would cause a shift of the zero point calibration. Accumulation of material can in many cases be avoided, e.g. by coating the strip with a material preventing accumulation.

If the pipe is mounted vertically and the flow of particles is evenly distributed over the cross section of the pipe, the sensor can be used for measuring the instantaneous mean density of particles in the MUT in the pipe. If the mean size of the particles is constant, and if they are dropped through the pipe from a fixed height, the speed of the flow is likely to be relatively constant. In that case, the mean density and the speed of the flow give the mass flow of the particles. If both the resonant frequency and the quality factor are measured, e.g. both the mass flow and the moisture of the particles can be measured.

The speed of the flow can also be measured with the cross correlation method, which was briefly described in Ch. 3. Two strips are then mounted in the pipe with a certain distance between them in the direction of the flow. For example, if the MUT is fed by a screw conveyor to the top of the pipe, from where it is dropped past the

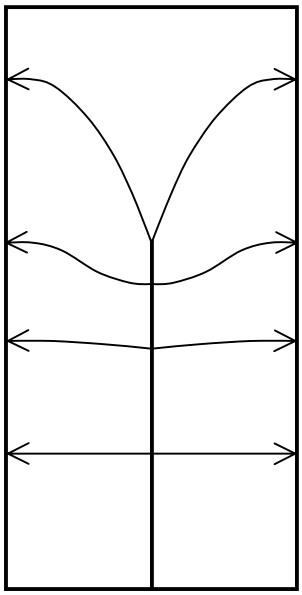

Figure 4.5 A cross section of the waveguide that was simulated with HFSS. The size of the waveguide is 37.5 mm x 75 mm, and the height of the fin as shown is 45 mm. The electrical field pattern is also indicated as resulting from the simulator. The mode is clearly related to the $TE_{½1}$ mode in a sectorial waveguide, shown in Fig. 5.3.

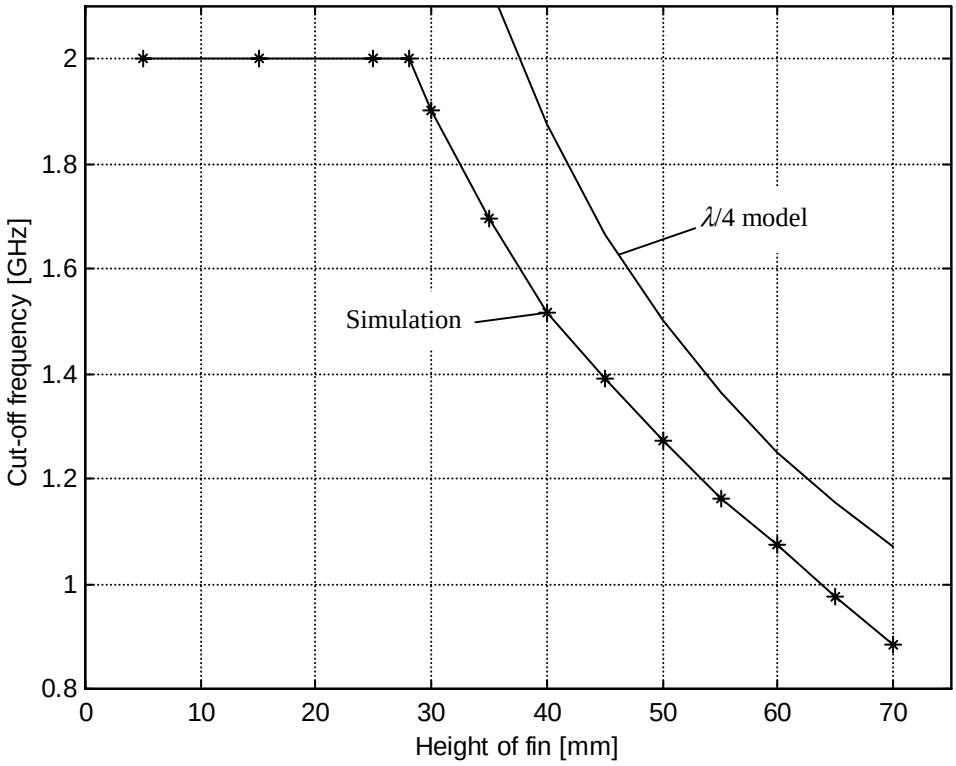

Figure 4.6 The cut-off frequency of the waveguide shown in Fig. 4.5 as simulated with HFSS. For a fin height ≤ 28 mm the TE_{10} mode, which can also exist because the electric field is perpendicular to the fin, is the lowest mode with a cut-off frequency of 2 GHz. The resonant frequency estimated based on a $\lambda/4$ stripline structure is also shown. This frequency is 17…34% higher than the cut-off frequency resulting from the simulations.

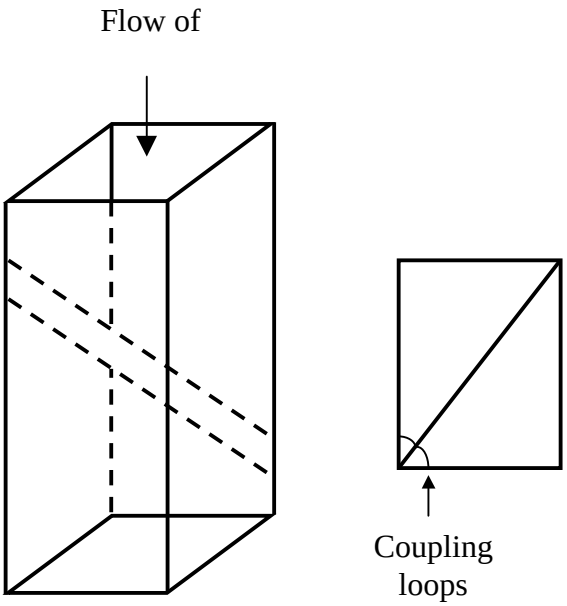

Figure 4.7 A resonator sensor in a rectangular pipe formed by a strip attached diagonally between corners of the pipe [Tiuri et al., 1986]. The resonant frequency is below the cut-off frequency of the pipe, because the strip is longer than the width of the broader wall.

sensors, the density of the flow will be modulated by the revolutions of the screw. This modulation provides variations in the measured signal, which helps finding the time delay accurately from the calculated cross correlation. However, the periodicity of the variations causes ambiguity in the cross correlation. If the time it takes for the flow to travel the distance between the strips is Δt and the period of the modulations is T, peaks will be found in the cross correlation at Δt, $\Delta t \pm T$, $\Delta t \pm 2T$,… . To avoid confusion between peaks, the distance between the strips should, if possible, be chosen so that $\Delta t << T$.

Figure 4.7 shows a sensor formed by a strip that is shorted in both ends. The strip will therefore be half a wavelength long at the first resonance. It may be just mounted diagonally between two opposite corners of the pipe, or the other point of attachment may in addition be displaced in the direction of the flow to make the strip even longer, as shown in Fig. 4.7. Because the cut-off wavelength of the rectangular pipe is twice the width of the broad wall, and the strip is always longer than the broad wall, the resonant frequency is below the cut-off.

The strip resonator in Fig. 4.7 has a more even distribution of sensitivity in the cross section of the pipe than the sensor in Figs. 4.4 and 4.5, which has a more profound field maximum at the end of the strip.

Helical Resonator Sensor

If the centre conductor of a coaxial line is a helix instead of straight wire, the waves will travel slower in the line. When the turns of the helix are loose enough to keep

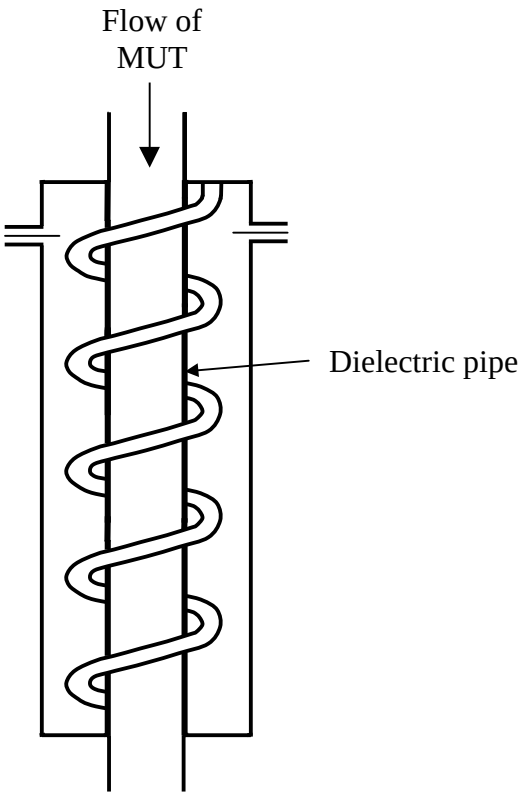

Figure 4.8 A helical resonator sensor that has been made in an enlargement of the pipe. This type of sensor has an exceptionally low first resonant frequency compared to the outer dimensions, and several harmonic resonances can be used for measuring the permittivity of the MUT as a function of frequency.

the capacitive coupling between the turns low, the current runs along the helical wire. The length of the wire will therefore determine the phase shift. A resonator made of a helix inside a cavity such that one end is shorted and the other end is open, as shown in Figure 4.8, will have a low first resonant frequency compared to the size. Such a sensor may in practice have up to ten usable harmonic resonances below the frequency, where it starts to leak. These frequencies provide the possibility of measuring the permittivity of the MUT as a function of frequency. The helical resonator has an even field distribution inside the helix, where the MUT is flowing. For more details see [Meyer, 1981], or [Nyfors and Vainikainen, 1989a].

Resonator Sensors Based on Waveguide with Low Cut-Off Frequency

If a section of the pipe has a lower cut-off frequency than the rest of the pipe, this section may serve as a resonator below cut-off. The nonintrusive sensor, which was described above, actually falls into this category, but there are also waveguide structures with the same outer diameter as the pipe, but which still have a lower cut-off frequency. Especially TE_{nml} resonance modes with $l = 0$ ($f_r = f_c$) are favourable, because they can exist in open-ended structures.

The best known waveguide type, which has a lower cut-off frequency than the basic rectangular or cylindrical waveguide, is the ridged waveguide. As discussed

above, the stripline resonator in a rectangular pipe can be regarded as belonging to this group. Another case is the sectorial waveguide with a sector angle of 2π, which is described in Ch. 5. Sensors based on these are studied in more detail in Ch. 6.

4.3 Resonator Sensors with End Grids

Instead of designing the resonator sensor to operate below the cut-off frequency of the pipe so that the pipe confines the energy of the sensor, a section of the pipe can be turned into a cavity resonator by isolating the section with end grids, which will act as shorts. The basic principle is shown in Fig. 4.9. A cavity with shorted ends can support all TE_{nml} and TM_{nml} modes with $l \geq 1$, but only TM_{nml} modes with $l = 0$ ($f_r = f_c$). From Eq. (3.48) it is clear that the resonant frequency of any mode with $l \geq 1$ is higher than the cut-off frequency of the corresponding waveguide mode. Because the lowest cut-off frequency in a rectangular waveguide is that of the TE_{10} mode and in a circular waveguide that of the TE_{11} mode, the resonant frequency of any mode, the lowest TM_{nm0} mode included, will be higher than the lowest cut-off frequency of the pipe. The pipe will therefore provide no isolation, and the end grids must provide all the isolation needed to achieve an acceptable radiation quality factor.

Regardless of the exact design of the end grids, they consist of holes of various cross sections. Because the grids have a finite length in the axial direction, the holes can be regarded as waveguides below cut-off. The improvement of the isolation as a function of the length of the grids (length of the waveguides) can therefore be directly

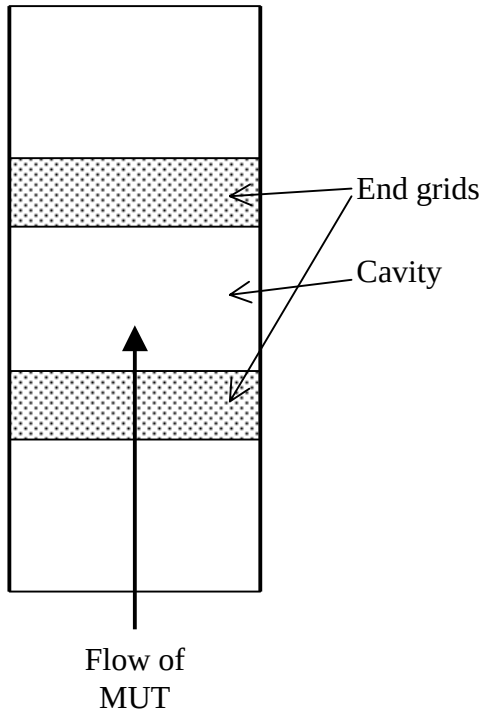

Figure 4.9 A section of the pipe is isolated into a cavity resonator by shorting end grids that stop the microwaves from escaping but allow the flow of MUT to pass relatively unhindered.

calculated from Eq. (4.10), when the cut-off frequency of the holes is known. To achieve a given Q_{rad} with loose grids (large holes) therefore requires longer grids than if dense grids are used. The end grids should preferably be as dense as possible to distort the used resonance mode as little as possible. At the same time they should obstruct the flow as little as possible not to cause a too high pressure drop or a risk of congestion. To minimize the production cost of the sensor, the end grids should also be as short as possible. The problem of optimizing the design will be studied in detail in Ch. 7, where also some realized examples will be presented.

The MFI WaterCut sensor made by Roxar is an example of a commercial resonator sensor based on end grids [Gaisford et al., 1992].

4.4 Fringing Field Resonator Sensors

The resonator sensors that operate below the cut-off frequency, or are confined between end grids, typically measure the whole flow of the MUT. If the flow is homogeneous enough such that measuring the whole flow is not necessary, fringing field resonator sensors can also be used. In these sensors the radiation leakage is kept low enough by designing the structure such that only a fringing field protrudes into the pipe to be influenced by the permittivity of the MUT. Consequently most of the energy is outside the MUT.

Several types of designs are possible for realizing fringing field resonator sensors. For example the open-ended coaxial structure in Fig. 2.4 turns into a resonator, when a short or open circuit (e.g. a gap in the centre conductor providing at the same time the open circuit and capacitive coupling for measuring the reflection coefficient) is applied at some distance behind the open end. The dielectric ring in Fig. 2.3 can also be used as a resonator, if the couplings are made loose enough. Other possibilities are cavity or coaxial resonators on the outside of the pipe. In these one or several slots in the common wall allow the field to fringe into the pipe. The slots must have dielectric windows that prevent the MUT from entering into the resonator.

Because only a small part of the energy in a fringing field resonator sensor is in contact with the MUT, the sensitivity is lower than in sensors that are filled with the MUT. Because of the low sensitivity, they can tolerate higher losses in the MUT, but they are less well suited for detecting very small changes in the permittivity of the MUT.

4.5 Summary

When a resonator sensor is implemented in a pipe, the structure must allow the flow to pass relatively unhindered, and at the same time prevent the energy from escaping. These features can be achieved based on mainly three different principles. The first principle is to use a resonant frequency that is below the cut-off frequency of the pipe, in which case the pipe prevents the energy from escaping. The second principle is to isolate a section of the pipe with grids, in which case the holes in the grids are waveguides below cut-off. The third principle is to have a basically non-radiating resonator structure outside the pipe, and allow only a small part of the energy to fringe into the pipe, e.g. through a slot.

5 SECTORIAL AND SEMISECTORIAL WAVEGUIDES

5.1 Introduction

If a resonator cavity in a pipe is isolated with end grids made of radial plates, the holes in the grids are sectors. For example if the number of plates is four, the sector angle is $\pi/2$ (see Fig. 7.1). If a smaller pipe is mounted in the centre so that the plates are between the outer surface of the smaller pipe and the inner surface of the larger pipe, the holes are what will here be called semisectors. A semisector is therefore the part of a sector between two circles of different radius.

To provide enough isolation, an end grid must in practice have a finite thickness, i.e. length of plates. The holes then form pieces of sectorial, or semisectorial and circular waveguides. The thickness of the grid, i.e. length of the waveguides, affects the attenuation below cut-off.

To be able to design the end grids (length, sector angle, ratio of radii for semisectorial grids), and the CFR sensor (Ch. 6) and the downhole watercut sensor (Ch. 7), which are also based on sectorial and semisectorial waveguides, one must know the wave modes in such waveguides. The circular waveguide in the centre of the semisectorial grid is well known. The semisectorial waveguides have been briefly described by F. Lin and A.S. Omar, who present two sets of graphs for the lowest TE mode, and the same for the lowest TM mode [Lin and Omar, 1989]. One set gives the cut-off wavenumber as a function of the sector angle for various ratios of radii, and the other as a function of the ratio of radii for various sector angles. A theoretical derivation of the mode functions is given in [Felsen and Marcuvitz, 1994]. For the work in this thesis more detailed information is needed, and also knowledge about the higher modes. The waveguide modes in sectorial and semisectorial waveguides are therefore derived and analyzed here. The derivation follows the same pattern as presented for ordinary circularly cylindrical waveguides in the textbooks, e.g. [Collin, 1966], [Ramo et al., 1984], and [Pozar, 1998], but with other boundary conditions.

5.2 Sectorial Waveguides

For the derivation of the waveguide modes cylindrical co-ordinates (ρ, φ, z) will be used as shown in Fig. 5.1. The angle of the sector is φ_0 and the radius of the sector is a. Metal walls are where $\rho = a$ (for all φ), $\varphi = 0$ (for all ρ), and $\varphi = \varphi_0$ (for all ρ).

5.2.1 TM Modes in Sectorial Waveguides

For TM modes the axial magnetic field is zero ($H_z = 0$). The waveguide modes can be derived from the transversal Helmoltz's equation for the axial electric field E_z:

$$\nabla_T^2 E_z(\rho,\varphi) + k_c^2 E_z(\rho,\varphi) = 0 \qquad (5.1)$$

where ∇_T is the transversal Laplacean operator and k_c is the cut-off wave number. Eq. (5.1) can be solved by separating

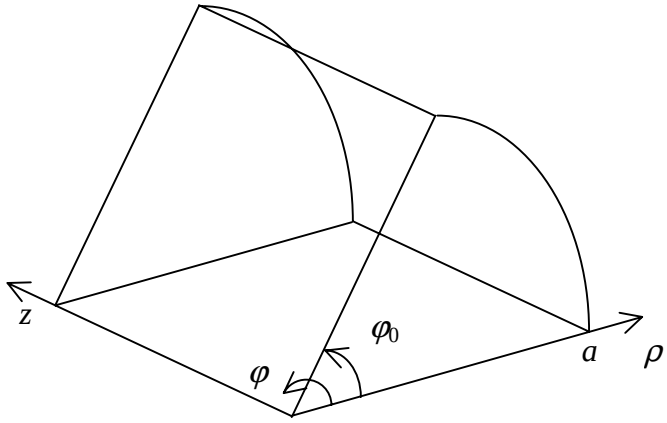

Figure 5.1 The sectorial waveguide in cylindrical co-ordinates.

$$E_z(\rho,\varphi) = P(\rho)\,\Phi(\varphi) \tag{5.2}$$

which leads to two differential equations:

$$\frac{1}{P(\rho)}\left\{\rho\left[\rho P'(\rho)\right]' + k_c^2\rho^2 P(\rho)\right\} = -\frac{\Phi''(\varphi)}{\Phi'(\varphi)} = \nu^2 \tag{5.3}$$

The solutions to (5.3) are known to be

$$\begin{aligned}\Phi(\varphi) &= A\cos\nu\varphi + B\sin\nu\varphi \\ P(\rho) &= C\,J_\nu(k_c\rho) + D\,Y_\nu(k_c\rho)\end{aligned} \tag{5.4}$$

where J_ν and Y_ν are Bessel functions of the first and second kind and order ν. This is the standard solution for a circularly cylindrical waveguide, see e.g. p.108 in [Collin, 1966]. Because the functions must always obtain finite values, it follows that $D = 0$, because $Y_\nu(x) \xrightarrow{x\to 0} -\infty$. If the boundary condition of the sectorial waveguide that $E_z = 0$ on all metal walls is now applied, the flat walls give

$$\begin{aligned}&E_z(\varphi = 0) = 0 \quad \Rightarrow A = 0 \\ &E_z(\varphi = \varphi_0) = 0 \quad \Rightarrow \sin\nu\varphi_0 = 0 \quad \Rightarrow \nu\varphi_0 = n\pi \quad \Rightarrow \nu = \frac{n\pi}{\varphi_0}\end{aligned} \tag{5.5}$$

where n is an integer: n = 1, 2, 3, ... Also n = 0 fulfils the boundary condition, but leads to zero fields and is therefore an unphysical solution. Now ν is not necessarily an integer, as one is used to from the solutions of wave modes in ordinary circular waveguides. On the curved wall the boundary condition gives

$$\begin{aligned}&E_z(\rho = a) = 0 \quad \Rightarrow J_\nu(k_c a) = 0 \\ &\Rightarrow k_c a = p_{\nu m}\end{aligned} \tag{5.6}$$

where $p_{\nu m}$ is the m:th zero of the Bessel function (i.e. m is an integer, m = 1, 2, 3, ...) of the first kind and order ν. The cut-off wave number is now

$$k_{c,\nu m} = \frac{p_{\nu m}}{a} \tag{5.7}$$

and the cut-off frequency is

$$f_{c,\nu m} = \frac{c\, p_{\nu m}}{2\pi a} \tag{5.8}$$

The field equations for the $\mathrm{TM}_{\nu m}$ modes in a sectorial waveguide have the same shape as in an ordinary circular waveguide, but with the values for ν and $p_{\nu m}$ from above:

$$\begin{aligned}
E_z &= E_0 J_\nu\left(\frac{p_{\nu m}\rho}{a}\right)\cdot \sin\nu\varphi \cdot \exp\{-j\beta_{\nu m} z\} \\
E_\rho &= \frac{-j\beta_{\nu m} p_{\nu m}}{a k_{c,\nu m}^2} E_0 J_\nu'\left(\frac{p_{\nu m}\rho}{a}\right)\cdot \sin\nu\varphi \cdot \exp\{-j\beta_{\nu m} z\} \\
E_\varphi &= \frac{-j\nu\beta_{\nu m}}{\rho k_{c,\nu m}^2} E_0 J_\nu\left(\frac{p_{\nu m}\rho}{a}\right)\cdot \cos\nu\varphi \cdot \exp\{-j\beta_{\nu m} z\} \\
H_z &= 0 \\
H_\rho &= -\frac{E_\varphi}{Z_{e,\nu m}} \\
H_\varphi &= \frac{E_\rho}{Z_{e,\nu m}}
\end{aligned} \tag{5.9}$$

where

$$\begin{aligned}
\beta_{\nu m} &= \sqrt{k^2 - \left(\frac{p_{\nu m}}{a}\right)^2} \\
k &= \frac{2\pi f}{c} \\
Z_{e,\nu m} &= \frac{\beta_{\nu m}}{k} Z_w \\
Z_w &= \sqrt{\frac{\mu_r}{\varepsilon_r}}
\end{aligned} \tag{5.10}$$

5.2.2 TE Modes in Sectorial Waveguides

For TE modes the axial electric field is zero (E_z = 0). The waveguide modes can be derived from the transversal Helmoltz's equation for the axial magnetic field H_z:

$$\nabla_{\mathrm{T}}^2 H_z(\rho,\varphi) + k_c^2 H_z(\rho,\varphi) = 0 \tag{5.11}$$

This is the same differential equation for H_z as Eq. (5.1) for E_z. The solutions are therefore also the same:

$$\begin{aligned} H_z &= P(\rho)\Phi(\varphi) \\ \Phi(\varphi) &= A\cos\nu\varphi + B\sin\nu\varphi \\ P(\rho) &= C\,J_\nu(k_c\rho) + D\,Y_\nu(k_c\rho) \end{aligned} \tag{5.12}$$

The boundary condition is that the tangential electric field is zero on the metal walls. Before it can be applied, the transverse electric field must be calculated:

$$E_T = \hat{\mathbf{u}}_z \times \nabla_{\mathrm{T}} H_z(\rho,\varphi) \tag{5.13}$$

where

$$\begin{aligned} \nabla_{\mathrm{T}} H_z(\rho,\varphi) &= \hat{\mathbf{u}}_\rho \frac{\partial H_z}{\partial \rho} + \hat{\mathbf{u}}_\varphi \frac{1}{\rho}\frac{\partial H_z}{\partial \varphi} \\ \frac{\partial H_z}{\partial \rho} &= \Phi(\varphi)\left[Ck_c J_\nu'(k_c\rho) + Dk_c Y_\nu'(k_c\rho)\right] \\ \frac{\partial H_z}{\partial \varphi} &= P(\rho)\left(-A\nu\sin\nu\varphi + B\nu\cos\nu\varphi\right) \end{aligned} \tag{5.14}$$

The transverse electric field is now

$$E_T = -\hat{\mathbf{u}}_\varphi \frac{\partial H_z}{\partial \rho} + \hat{\mathbf{u}}_\rho \frac{1}{\rho}\frac{\partial H_z}{\partial \varphi} \tag{5.15}$$

Again $D = 0$ because the fields must receive finite values. Applying the boundary condition on the flat walls, i.e. $E_\rho = 0$, ($\varphi = 0$, $\varphi = \varphi_0$), gives

$$\begin{aligned} &E_\rho(\varphi = 0) = 0 \quad \Rightarrow B = 0 \\ &E_\rho(\varphi = \varphi_0) = 0 \quad \Rightarrow \sin\nu\varphi_0 = 0 \quad \Rightarrow \nu\varphi_0 = n\pi \quad \Rightarrow \nu = \frac{n\pi}{\varphi_0} \end{aligned} \tag{5.16}$$

where n is an integer: $n = 0, 1, 2, 3, \ldots$. This time $n = 0$ is also a possible solution. Again ν does not have to be an integer. On the curved wall the boundary condition gives

$$\begin{aligned} &E_\varphi(\rho = a) = 0 \quad \Rightarrow J_\nu'(k_c a) = 0 \\ &\Rightarrow k_c a = p_{\nu m}' \end{aligned} \tag{5.17}$$

where $p'_{\nu m}$ is the *m*:th zero of the derivative of the Bessel function (i.e. *m* is an integer, *m* = 1, 2, 3, ...) of the first kind and order ν. The cut-off frequency for the $TE_{\nu m}$ mode in a sectorial waveguide is now

$$f_c = \frac{c\,p'_{\nu m}}{2\pi a} \tag{5.18}$$

The field equations for the $TE_{\nu m}$ modes in a sectorial waveguide have the same shape as in an ordinary circular waveguide, but with the values for ν and $p'_{\nu m}$ from above:

$$\begin{aligned}
H_z &= H_0 J_\nu\left(\frac{p'_{\nu m}\rho}{a}\right)\cdot\cos\nu\varphi\cdot\exp\{-j\beta_{\nu m}z\}\\
H_\rho &= \frac{-j\beta_{\nu m}p'_{\nu m}}{ak^2_{c,\nu m}}H_0 J'_\nu\left(\frac{p'_{\nu m}\rho}{a}\right)\cdot\cos\nu\varphi\cdot\exp\{-j\beta_{\nu m}z\}\\
H_\varphi &= \frac{j\nu\beta_{\nu m}}{\rho k^2_{c,\nu m}}H_0 J_\nu\left(\frac{p'_{\nu m}\rho}{a}\right)\cdot\sin\nu\varphi\cdot\exp\{-j\beta_{\nu m}z\}\\
E_z &= 0\\
E_\rho &= Z_{h,\nu m}H_\varphi\\
E_\varphi &= -Z_{h,\nu m}H_\rho
\end{aligned} \tag{5.19}$$

where

$$\begin{aligned}
\beta_{\nu m} &= \sqrt{k^2-\left(\frac{p'_{\nu m}}{a}\right)^2}\\
Z_{h,\nu m} &= \frac{k}{\beta_{\nu m}}Z_w
\end{aligned} \tag{5.20}$$

The values for *k* and Z_w are given by Eq. (5.10).

5.2.3 Values of $p_{\nu m}$ and $p'_{\nu m}$ for Waveguide Modes in Sectorial Waveguides

Because ν depends on the sector angle φ_0 for all $n \neq 0$, the values of $p_{\nu m}$ and $p'_{\nu m}$ will also depend on the sector angle. No comprehensive table of values can therefore be given, but typical and useful examples. Table 5.1 gives $p_{\nu m}$ and $p'_{\nu m}$ values for ν values corresponding to cases, where the sector angle is an even fraction of 2π (i.e. the cylinder has been divided into an even number of sectors) and *n* = 1, or an arbitrary sector when *n* = 0. For $n \geq 2$, ν can be calculated from Eq. (5.5) or (5.16) and $p_{\nu m}$ and $p'_{\nu m}$ looked up in Table 5.1 ignoring the two first columns, or approximately from the graphs in Figure 5.2, or calculated using the approximate polynomials given by Eq. (5.21) and Table 5.3. Table 5.2 gives the values for ordinary circular waveguides for comparison. It is interesting to note that for a sector with $\varphi_0 = 2\pi$, which is a

Table 5.1 Values of $p_{\nu m}$ and $p'_{\nu m}$ in sectorial waveguides for various values of ν. The given φ_0 and corresponding number of sectors in a circle are valid only if $n = 1$, see Eqs. (5.5) and (5.16). The values were calculated with *Matlab* and checked using tables in [Abramowitz and Stegun, 1972].

No. of sectors in a circle when $n = 1$	φ_0	ν	$\mathrm{TM}_{\nu m}$			$\mathrm{TE}_{\nu m}$		
			$p_{\nu 1}$	$p_{\nu 2}$	$p_{\nu 3}$	$p'_{\nu 1}$	$p'_{\nu 2}$	$p'_{\nu 3}$
Any ($n = 0$)	Any	0	-	-	-	3.832	7.016	10.174
1	2π	0.5	π	2π	3π	1.1656	4.604	7.790
2	π	1	3.832	7.016	10.174	1.8412	5.331	8.536
4	$\pi/2$	2	5.135	8.417	11.620	3.054	6.706	9.970
6	$\pi/3$	3	6.380	9.761	13.015	4.201	8.015	11.346
8	$\pi/4$	4	7.588	11.065	14.372	5.318	9.282	12.682

Table 5.2 Values for p_{nm} and p'_{nm} for ordinary circular waveguide, e.g. [Collin, 1966].

n	TM_{nm}			TE_{nm}		
	p_{n1}	p_{n2}	p_{n3}	p'_{n1}	p'_{n2}	p'_{n3}
0	2.405	5.520	8.654	3.832	7.016	10.174
1	3.832	7.016	10.174	1.8412	5.331	8.536
2	5.135	8.417	11.620	3.054	6.706	9.970

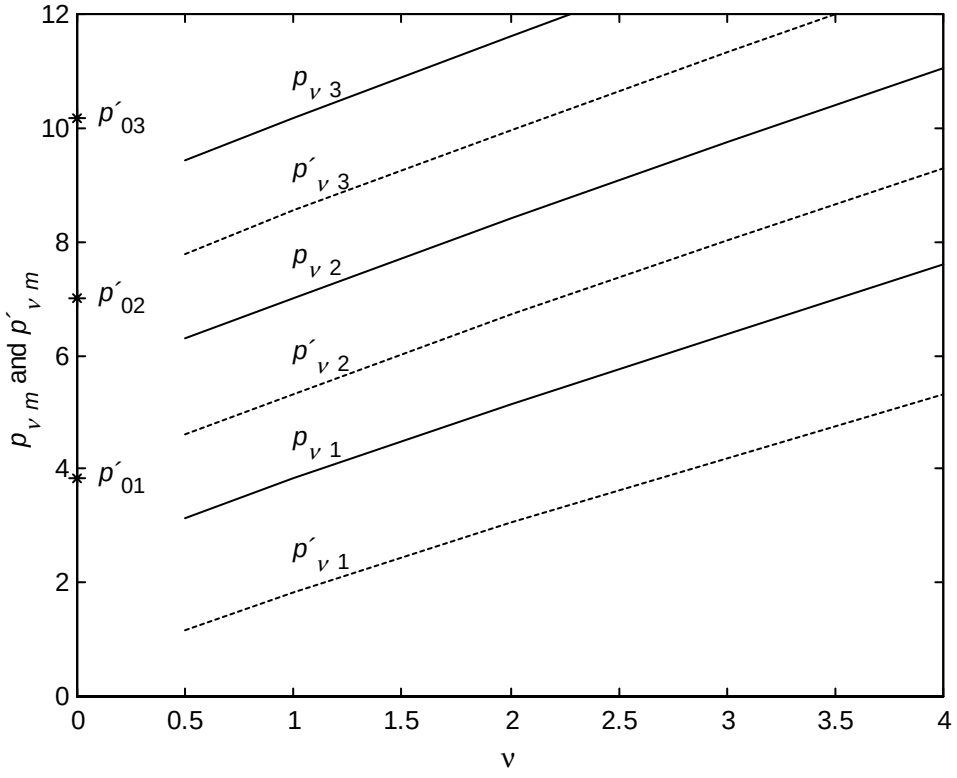

Figure 5.2 Values of $p_{\nu m}$ and $p'_{\nu m}$ in sectorial waveguides for arbitrary values of ν. The values with first index "0" correspond to $n = 0$. The graphs are based on Table 5.1. Approximations for the graphs are given by Eq. (5.21) and Table 5.3.

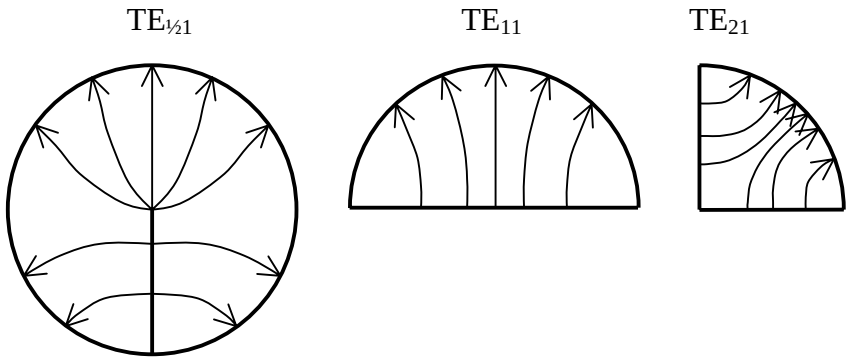

Figure 5.3 A qualitative representation of the electric field of three special cases of the same mode $\left(p'_{\nu 1},\, n=1\right)$ for $\varphi_0 = 2\pi$, π, and $\pi/2$.

cylindrical waveguide with a fin stretching from the wall to the centre of the waveguide, the lowest cut-off frequency is lower than in the waveguide without the fin. The cut-off frequency of $TE_{½1}$ in the waveguide with the fin is 63.3 % of the cut-off frequency of TE_{11} in the ordinary waveguide. For a sector with $\varphi_0 = \pi$, i.e. semicircularly cylindrical waveguide, the cut-off frequency is the same as in the full waveguide and the lowest mode is TE_{11} in both cases. The mode in the semicircular waveguide is half of the mode in the circular waveguide cut along the symmetry plane perpendicular to the electric field. One can think of $TE_{½1}$ in the waveguide with the fin as being formed from TE_{11} in the semicircular waveguide by stretching it over 2π, indeed any mode with $p'_{\nu 1}$ stretched or squeezed to occupy φ_0. Because there is a stepless transition, when φ_0 is changed, modes with the same n and m values should be regarded as the same mode even though the index ν changes with φ_0. Figure 5.3 shows qualitatively the shape of the electric field of $TE_{½1}$ in a waveguide with a fin, TE_{11} in a semicircular waveguide and TE_{21} in a $\pi/2$ sector, all which are special cases of the same mode for different φ_0.

Approximate polynomials of the form

$$p = a + b\nu + c\nu^2 \tag{5.21}$$

have been fitted to the values in Table 5.1 using the command *polyfit* in the program *Matlab*. The values for a, b, and c are given in Table 5.3. The largest deviations

Table 5.3 The constants for the polynomials of the form given by Eq. (5.21) approximating the p values in sectorial waveguide. The polynomials are valid up to $\nu = 4$.

	a	b	c
$p_{\nu 1}$	2.4579	1.3936	-0.0280
$p_{\nu 2}$	5.5508	1.4868	-0.0272
$p_{\nu 3}$	8.6732	1.5211	-0.0242
$p'_{\nu 1}$	0.5218	1.3330	-0.0339
$p'_{\nu 2}$	3.8811	1.4732	-0.0309
$p'_{\nu 3}$	7.0415	1.5170	-0.0269

between the polynomials and the values in Table 5.1 is 1.22 % (for $p'_{1/21}$) and 1.1 % (for p'_{11}). The mean deviation (i.e. the arithmetic mean of the deviations) is 0.15 %.

5.3 Semisectorial Waveguides

For the derivation of the waveguide modes in semisectorial waveguides the same cylindrical co-ordinates (ρ, φ, z) will be used as for sectorial waveguides. A picture of a semisectorial waveguide is shown in Fig. 5.4. The sector angle is φ_0, the outer (larger) radius is a, and the inner (smaller) radius is b. Metal walls are where $\rho = a$ (for all φ), $\rho = b$ (for all φ), $\varphi = 0$ (for all ρ), and $\varphi = \varphi_0$ (for all ρ).

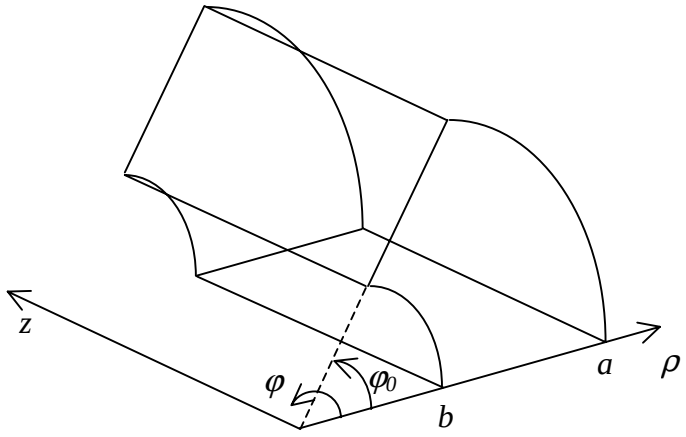

Figure 5.4 A semisectorial waveguide in cylindrical co-ordinates.

5.3.1 TM Modes in Semisectorial Waveguides

Solving the wave modes in semisectorial waveguides follows the same path as for sectorial waveguides. The difference comes in, when applying the boundary conditions. The general solution given in Eqs.(5.2) and (5.4) for the axial electric field E_z therefore applies also to semisectorial waveguides:

$$E_z(\rho,\varphi) = P(\rho)\,\Phi(\varphi) \tag{5.22}$$

$$\begin{aligned} \Phi(\varphi) &= A\cos\nu\varphi + B\sin\nu\varphi \\ P(\rho) &= C\,J_\nu(k_c\rho) + D\,Y_\nu(k_c\rho) \end{aligned} \tag{5.23}$$

In this case, however, $D \neq 0$ because the waveguide does not extend to $\rho = 0$. The fact that Y_ν approaches infinity, when the argument approaches zero, is therefore no problem for the semisectorial waveguides, as it was for the sectorial waveguides. The boundary condition for the semisectorial waveguide is that $E_z = 0$ on all metal walls. Applied on the flat walls it gives exactly as for sectorial waveguide that

$$E_z(\varphi = 0) = 0 \quad \Rightarrow A = 0$$
$$E_z(\varphi = \varphi_0) = 0 \quad \Rightarrow \sin \nu\varphi_0 = 0 \quad \Rightarrow \nu\varphi_0 = n\pi \quad \Rightarrow \nu = \frac{n\pi}{\varphi_0} \tag{5.24}$$

where n is an integer: n = 1, 2, 3, ... Also n = 0 fulfils the boundary condition, but leads to zero fields and is therefore an unphysical solution. Again ν is not necessarily an integer. On the curved walls the boundary condition is

$$E_z(\rho = a, b) = 0 \tag{5.25}$$

which leads to

$$\begin{aligned} C J_\nu(k_c a) + D Y_\nu(k_c a) &= 0 \\ C J_\nu(k_c b) + D Y_\nu(k_c b) &= 0 \end{aligned} \tag{5.26}$$

This system of equations can not be solved in closed form, except in the special case, when ν = ½ (see Sec. 5.3.3). By slight manipulation (5.26) turns into

$$\frac{J_\nu(k_c a)}{J_\nu(k_c b)} \cdot \frac{Y_\nu(k_c b)}{Y_\nu(k_c a)} - 1 = 0 \tag{5.27}$$

which can be solved numerically. Again there is an infinite number of solutions $p_{\nu m} = k_c a$ for any ratio of the radii $r = b/a$. This time $p_{\nu m}$ denotes the m:th solution to (5.27) and is generally not equal to a zero of any specific Bessel function. From (5.26):

$$s = \frac{D}{C} = -\frac{J_\nu(p_{\nu m})}{Y_\nu(p_{\nu m})} \tag{5.28}$$

The field equations for the $\mathrm{TM}_{\nu m}$ modes in semisectorial waveguides are now

$$\begin{aligned} E_z &= E_0 \left[J_\nu\left(\frac{p_{\nu m}\rho}{a}\right) + s Y_\nu\left(\frac{p_{\nu m}\rho}{a}\right) \right] \cdot \sin \nu\varphi \cdot \exp\{-j\beta_{\nu m} z\} \\ E_\rho &= \frac{-j\beta_{\nu m} p_{\nu m}}{a k_{c,\nu m}^2} E_0 \left[J_\nu'\left(\frac{p_{\nu m}\rho}{a}\right) + s Y_\nu'\left(\frac{p_{\nu m}\rho}{a}\right) \right] \cdot \sin \nu\varphi \cdot \exp\{-j\beta_{\nu m} z\} \\ E_\varphi &= \frac{-j\nu\beta_{\nu m}}{\rho k_{c,\nu m}^2} E_0 \left[J_\nu\left(\frac{p_{\nu m}\rho}{a}\right) + s Y_\nu\left(\frac{p_{\nu m}\rho}{a}\right) \right] \cdot \cos \nu\varphi \cdot \exp\{-j\beta_{\nu m} z\} \\ H_z &= 0 \\ H_\rho &= -\frac{E_\varphi}{Z_{e,\nu m}} \\ H_\varphi &= \frac{E_\rho}{Z_{e,\nu m}} \end{aligned} \tag{5.29}$$

The values of β_{vm}, k, $Z_{e,vm}$, and Z_w are given by Eq. (5.10).

5.3.2 TE Modes in Semisectorial Waveguides

Solving the TE modes in semisectorial waveguides follows the same path as for sectorial waveguides. The solution for E_T is given by Eqs. (5.14) and (5.15):

$$\begin{aligned} E_T &= -\hat{\mathbf{u}}_\varphi \frac{\partial H_z}{\partial \rho} + \hat{\mathbf{u}}_\rho \frac{1}{\rho} \frac{\partial H_z}{\partial \varphi} \\ \frac{\partial H_z}{\partial \rho} &= \Phi(\varphi)\left[Ck_c J_\nu'(k_c\rho) + Dk_c Y_\nu'(k_c\rho)\right] \\ \frac{\partial H_z}{\partial \varphi} &= P(\rho)\left(-A\nu \sin\nu\varphi + B\nu\cos\nu\varphi\right) \end{aligned} \tag{5.30}$$

The boundary condition on the flat walls is $E_\rho(\varphi = 0,\ \varphi = \varphi_0) = 0$, which gives

$$\begin{aligned} &E_\rho(\varphi = 0) = 0 \quad \Rightarrow B = 0 \\ &E_\rho(\varphi = \varphi_0) = 0 \quad \Rightarrow \sin\nu\varphi_0 = 0 \quad \Rightarrow \nu\varphi_0 = n\pi \quad \Rightarrow \nu = \frac{n\pi}{\varphi_0} \end{aligned} \tag{5.31}$$

where n is an integer: n = 0, 1, 2, 3, ... This time n = 0 is also a solution, corresponding to modes with fields without dependence on φ. Because always $\nu = 0$ when n = 0, independent of φ_0, the wave mode solution, including the cut-off frequency, is also independent of the sector angle φ_0.

On the curved walls the boundary condition is

$$E_\varphi(\rho = a,\ b) = 0 \tag{5.32}$$

which applied on (5.30) gives

$$\begin{aligned} &CJ_\nu'(k_c a) + DY_\nu'(k_c a) = 0 \\ &CJ_\nu'(k_c b) + DY_\nu'(k_c b) = 0 \end{aligned} \tag{5.33}$$

Eq. (5.33) can not be solved in closed form. By slight manipulation it turns into

$$\frac{J_\nu'(k_c a)}{J_\nu'(k_c b)} \cdot \frac{Y_\nu'(k_c b)}{Y_\nu'(k_c a)} - 1 = 0 \tag{5.34}$$

which can be solved numerically. Again there is an infinite number of solutions $p'_{\nu m} = k_c a$ for any ratio of the radii $r = b/a$. This time $p'_{\nu m}$ denotes the m:th solution to (5.34) and is generally not equal to a zero of a derivative of any specific Bessel function. When the solution $p'_{\nu m}$ has been found, $s = D/C$ is found by solving (5.33):

$$s = -\frac{J'_\nu(p'_{\nu m})}{Y'_\nu(p'_{\nu m})} \tag{5.35}$$

The field equations for the $TE_{\nu m}$ modes in semisectorial waveguides are now:

$$\begin{aligned}
H_z &= H_0\left[J_\nu\left(\frac{p'_{\nu m}\rho}{a}\right) + sY_\nu\left(\frac{p'_{\nu m}\rho}{a}\right)\right]\cdot\cos\nu\varphi\cdot\exp\{-j\beta_{\nu m}z\}\\
H_\rho &= \frac{-j\beta_{\nu m}p'_{\nu m}}{ak^2_{c,\nu m}}H_0\left[J'_\nu\left(\frac{p'_{\nu m}\rho}{a}\right) + sY'_\nu\left(\frac{p'_{\nu m}\rho}{a}\right)\right]\cdot\cos\nu\varphi\cdot\exp\{-j\beta_{\nu m}z\}\\
H_\varphi &= \frac{j\nu\beta_{\nu m}}{\rho k^2_{c,\nu m}}H_0\left[J_\nu\left(\frac{p'_{\nu m}\rho}{a}\right) + sY_\nu\left(\frac{p'_{\nu m}\rho}{a}\right)\right]\cdot\sin\nu\varphi\cdot\exp\{-j\beta_{\nu m}z\}\\
E_z &= 0\\
E_\rho &= Z_{h,\nu m}H_\varphi\\
E_\varphi &= -Z_{h,\nu m}H_\rho
\end{aligned} \tag{5.36}$$

where k and Z_w are given by Eq. (5.10), and $\beta_{\nu m}$ and $Z_{h,\nu m}$ are given by Eq. (5.20).

5.3.3 Values for $p_{\nu m}$ and $p'_{\nu m}$ for Waveguide Modes in Semisectorial Waveguides

As for sectorial waveguides, $p_{\nu m}$ and $p'_{\nu m}$ depend on the sector angle φ_0, for all $n \neq 0$. For semisectorial waveguides they also depend on the ratio of radii $r = b/a$, i.e. the problem has got one more dimension. Actually sectorial waveguides are a special case of semisectorial waveguides with $r = 0$. No comprehensive table of values can be given, but typical and useful examples. The tables below give $p_{\nu m}$ and $p'_{\nu m}$ values for different values of r. Each table is for one value of ν, corresponding to one line in Table 5.1. The first line ($r = 0$) in each table is therefore the same as one line in Table 5.1. For $n = 0$ (only TE modes) the values are valid for any φ_0. For $n = 1$, the ν values correspond to cases, where the sector angle is an even fraction of 2π (i.e. the cylinder has been divided into an even number of sectors: 1, 2, 4, 6, or 8). For modes with $n \geq 2$, ν can be calculated from (5.24) or (5.31) and $p_{\nu m}$ and $p'_{\nu m}$ looked up in Tables 5.4-5.9, or approximately from the graphs in Figs. 5.5 - 5.10, or calculated using the approximate polynomials given by (5.41) and Table 5.10. It is also possible to solve (5.27) or (5.34) using a mathematical computer program, as was done in this work.

For some special cases of $\nu = l + ½$, where l is an integer, there may be exact solutions to (5.27). For example from Ch. 11 in [Arfken, 1970]:

$$\begin{aligned}
J_{l+½}(x) &= \sqrt{\frac{2x}{\pi}}\,j_l(x)\\
Y_{l+½}(x) &= \sqrt{\frac{2x}{\pi}}\,y_l(x)
\end{aligned} \tag{5.37}$$

where *j* and *y* are so called spherical Bessel functions of the first and second kind. For integer order they have exact representations given by trigonometric functions. For example for $l = 0$ [Arfken, 1970]:

$$j_0(x) = \frac{\sin x}{x}$$
$$y_0(x) = -\frac{\cos x}{x} \tag{5.38}$$

If Eqs. (5.37) and (5.38) are substituted into Eq. (5.27), the result is

$$\frac{\tan k_c a}{\tan k_c b} - 1 = 0 \tag{5.39}$$

The solutions to this equation are

$$p_{½m} = k_c a = \frac{m\pi a}{a-b} = \frac{m\pi}{1-r} \tag{5.40}$$

For *j* and *y* for higher values of *l*, see e.g. [Arfken, 1970]. Exact solutions to (5.27) may be found also for these special cases, which correspond to ν = integer + ½.

It is worth noting that because sectorial waveguides are special cases of semisectorial waveguides, when $r \to 0$, the $p_{\nu m}$ and $p'_{\nu m}$ values approach those given for sectorial waveguides. Because these are the zeros of J_ν and J'_ν, also $s \to 0$. This means that there is a stepless transition from sectorial to semisectorial modes. In the discussion on sectorial waveguides, all modes with the same *n* and *m* values were called the same mode, because of the stepless transition with changing φ_0. Because the transition now is stepless both as a function of φ_0 and *r*, all sectorial and semisectorial modes with the same *n* and *m* values can be regarded as the same mode.

The $p_{\nu m}$ and $p'_{\nu m}$ values for the semisectorial waveguides have been solved numerically from (5.27) and (5.34) in the program *Maple V* using the command *fsolve*. As a check about 20 % of the values have also been solved by numerical iteration in *Matlab*, which gave exactly the same results.

To help obtaining approximate *p* values as a function of *r* for the values of ν and *m* used in Tables 5.4 – 5.9, polynomials of the 5th degree have been fitted to the calculated points. The graphs in Figs. 5.5 – 5.10 are given by these polynomials. As can be seen, the fit is not perfect, but good enough for many purposes. Especially a hump that is not real can be seen for low values of *r*, and ν = 2, 3, and 4. The largest deviations between the polynomials and the solved points are seen in p'_{43}, where three points deviate by 1.5 %, 1.2 %, and 1.1 %, and in p'_{33}, where one point deviates by 1.3 %. All other points deviate <1 %.

If *p* values are needed for other values of ν than 0, ½, 1, 2, 3, and 4, they can be approximately interpolated from Figs. 5.5 – 5.10 or Tables 5.4 – 5.9, or they can be solved numerically from Eqs. (5.27) or (5.34).

Table 5.4 Values of p' for TE modes in semisectorial waveguides for $\nu = 0$ ($n = 0$). The sector angle φ_0 may obtain any value. The values were calculated with *Maple*.

r	TE_{0m}		
	p'_{01}	p'_{02}	p'_{03}
0.00	3.832	7.016	10.174
0.10	3.941	7.331	10.748
0.20	4.236	8.055	11.926
0.30	4.706	9.104	13.553
0.40	5.391	10.558	15.766
0.50	6.393	12.625	18.889
0.60	7.930	15.747	23.588
0.70	10.522	20.969	31.433
0.80	15.737	31.431	47.134

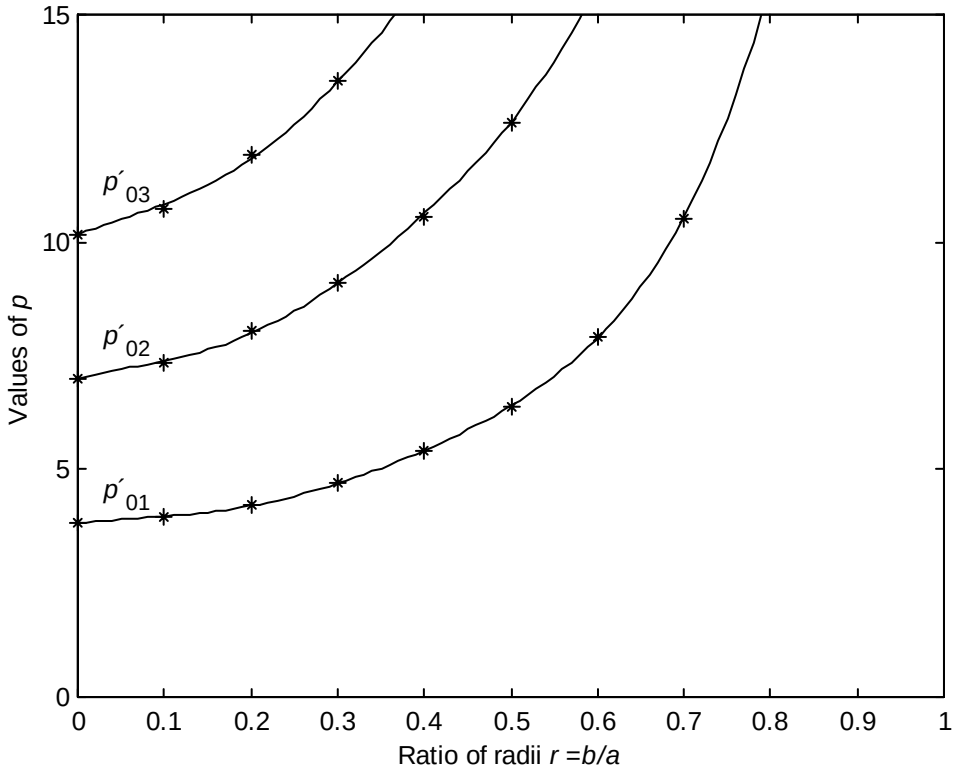

Figure 5.5 Values of p' for TE modes in semisectorial waveguides for $\nu = 0$ ($n = 0$, the sector angle φ_0 may obtain any value) from Table 5.4. The graphs are given by the polynomials in Eq. (5.41) and Table 5.10. The asterisk denotes solved values.

Table 5.5 Values of p and p' for TM and TE modes in semisectorial waveguides for $\nu = 0.5$. The values for the TE modes were calculated with *Maple*, and the values for the TM modes from Eq. (5.40).

r	$\mathrm{TM}_{1/2m}$			$\mathrm{TE}_{1/2m}$		
	$p_{1/2,1}$	$p_{1/2,2}$	$p_{1/2,3}$	$p'_{1/2,1}$	$p'_{1/2,2}$	$p'_{1/2,3}$
0.00	π	2π	3π	1.1656	4.604	7.790
0.10	3.491	6.981	10.472	1.0140	4.316	7.557
0.20	3.927	7.854	11.781	0.8973	4.429	8.149
0.30	4.488	8.976	13.464	0.8074	4.816	9.155
0.40	5.236	10.472	15.708	0.7366	5.459	10.589
0.50	6.283	12.566	18.850	0.6792	6.436	12.645
0.60	7.854	15.708	23.562	0.6316	7.958	15.761
0.70	10.472	20.944	31.416	0.5913	10.539	20.978
0.80	15.708	31.416	47.124	0.5567	15.748	31.436
0.90				0.5266		
0.99				0.5025		

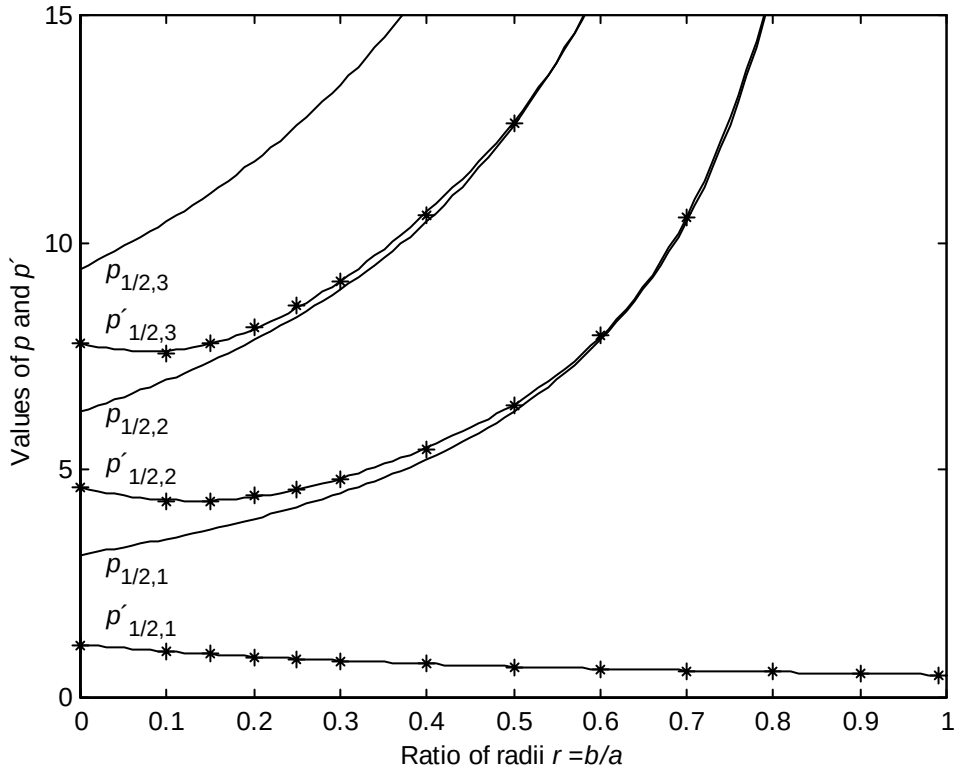

Figure 5.6 Values of p and p' for $\nu = ½$ from Table 5.5 for TM and TE modes in semisectorial waveguides. The graphs for the TE modes are given by the polynomials in Eq. (5.41) and Table 5.10, and the graphs for the TM modes are given by the exact equation (5.40). The asterisks denote solved values.

Table 5.6 Values of p and p' for TM and TE modes in semisectorial waveguides for $\nu = 1$. The values were calculated with *Maple*.

r	TM_{1m}			TE_{1m}		
	p_{11}	p_{12}	p_{13}	p'_{11}	p'_{12}	p'_{13}
0.00	3.832	7.016	10.174	1.8412	5.331	8.536
0.10	3.941	7.331	10.748	1.8035	5.137	8.199
0.20	4.236	8.055	11.926	1.7051	4.961	8.433
0.30	4.706	9.104	13.553	1.5821	5.137	9.308
0.40	5.391	10.558	15.766	1.4618	5.659	10.683
0.50	6.393	12.625	18.889	1.3547	6.565	12.706
0.60	7.930	15.747	23.588	1.2621	8.041	15.801
0.70	10.522	20.969	31.433	1.1824	10.592	21.004
0.80	15.737	31.431	47.134	1.1134	15.778	31.451
0.90				1.0531		
0.99				1.0050		

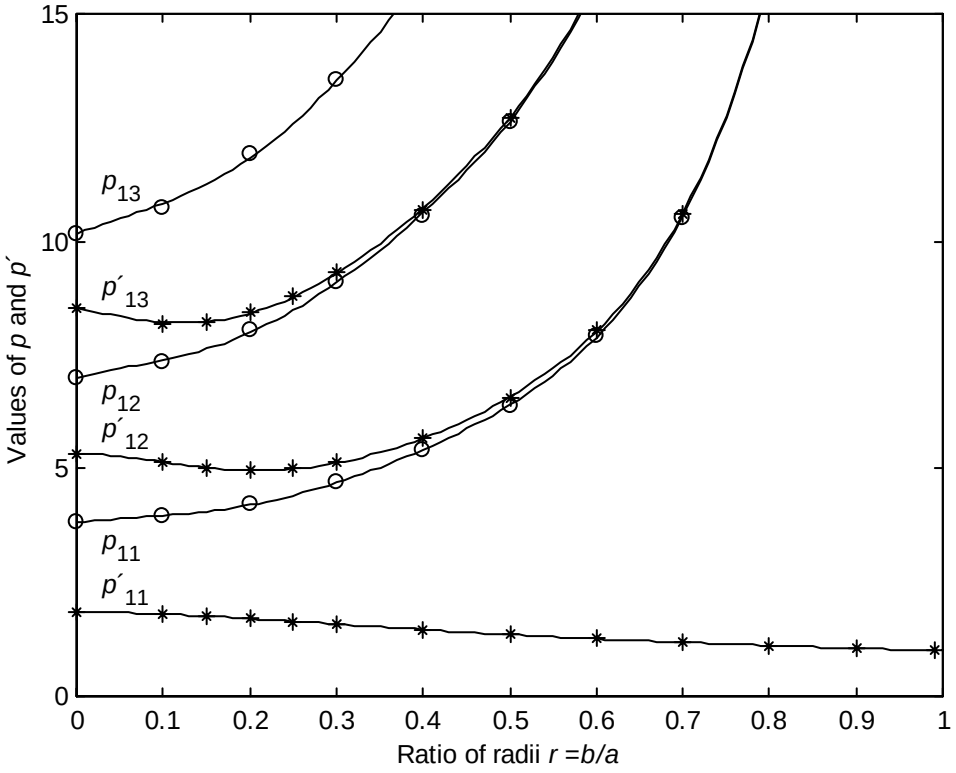

Figure 5.7 Values of p and p' for $\nu = 1$ from Table 5.6 for TM and TE modes in semisectorial waveguides. The graphs are given by the polynomials in Eq. (5.41) and Table 5.10. The asterisks and the rings denote solved values.

Table 5.7 Values of p and p' for TM and TE modes in semisectorial waveguides for $\nu = 2$. The values were calculated with *Maple*.

r	TM_{2m}			TE_{2m}		
	p_{21}	p_{22}	p_{23}	p'_{21}	p'_{22}	p'_{23}
0.00	5.135	8.417	11.620	3.054	6.706	9.970
0.10	5.142	8.457	11.738	3.053	6.687	9.887
0.20	5.222	8.804	12.494	3.035	6.495	9.549
0.30	5.470	9.600	13.905	2.968	6.274	9.918
0.40	5.966	10.894	15.999	2.842	6.416	11.056
0.50	6.814	12.856	19.046	2.681	7.063	12.949
0.60	8.227	15.904	23.694	2.516	8.367	15.961
0.70	10.720	21.071	31.501	2.363	10.799	21.106
0.80	15.855	31.490	47.174	2.226	15.898	31.510
0.90				2.106		
0.99				2.010		

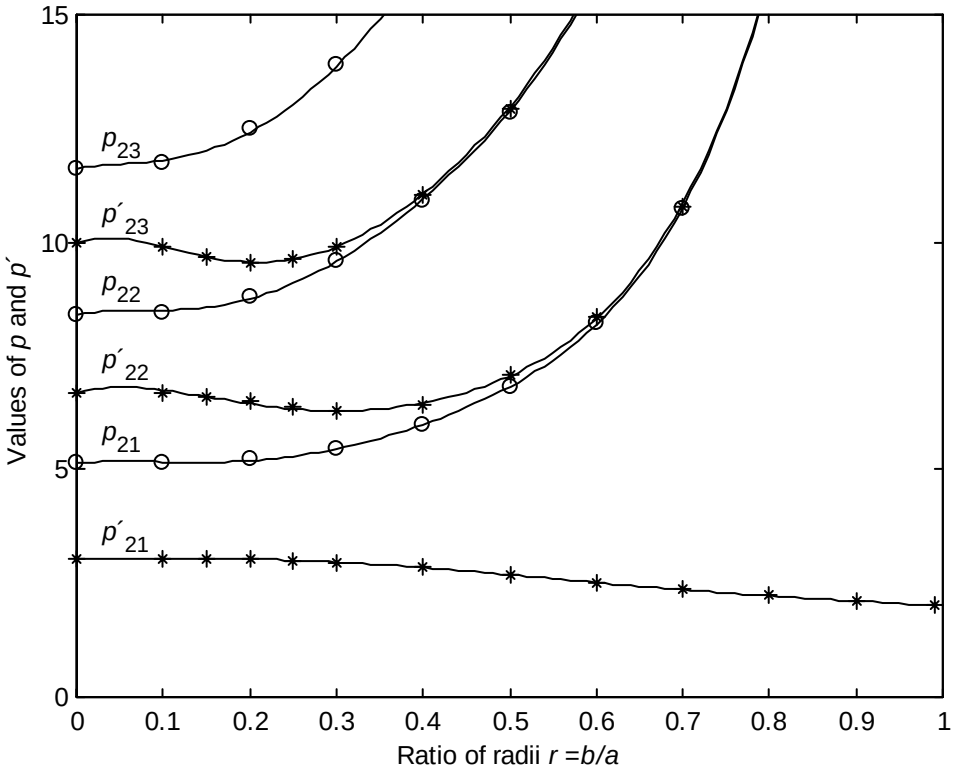

Figure 5.8 Values of p and p' for $\nu = 2$ from Table 5.7 for TM and TE modes in semisectorial waveguides. The graphs are given by the polynomials in Eq. (5.41) and Table 5.10. The asterisks and the rings denote solved values.

Table 5.8 Values of p and p' for TM and TE modes in semisectorial waveguides for $\nu = 3$. The values were calculated with *Maple*.

r	TM_{3m}			TE_{3m}		
	p_{31}	p_{32}	p_{33}	p'_{31}	p'_{32}	p'_{33}
0.00	6.380	9.761	13.015	4.201	8.015	11.346
0.10	6.380	9.764	13.030	4.201	8.014	11.338
0.20	6.394	9.874	13.381	4.199	7.964	11.106
0.30	6.494	10.371	14.477	4.180	7.721	10.920
0.40	6.780	11.435	16.380	4.108	7.535	11.666
0.50	7.458	13.232	19.304	3.958	7.840	13.347
0.60	8.699	16.161	23.868	3.754	8.889	16.226
0.70	11.041	21.239	31.614	3.540	11.136	21.276
0.80	16.050	31.589	47.240	3.339	16.096	31.610
0.90				3.159		
0.99				3.015		

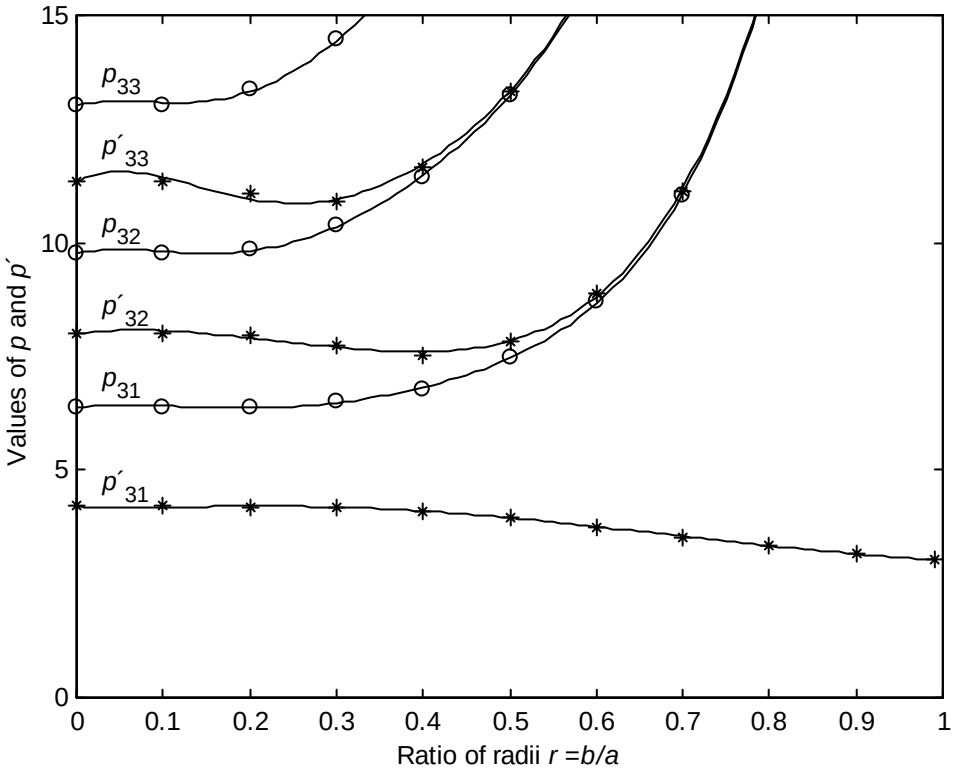

Figure 5.9 Values of p and p' for $\nu = 3$ from Table 5.8 for TM and TE modes in semisectorial waveguides. The graphs are given by the polynomials in Eq. (5.41) and Table 5.10. The asterisks and the rings denote solved values.

Table 5.9 Values of p and p' for TM and TE modes in semisectorial waveguides for $\nu = 4$. The values were calculated with *Maple*.

r	TM_{4m}			TE_{4m}		
	p_{41}	p_{42}	p_{43}	p'_{41}	p'_{42}	p'_{43}
0.00	7.588	11.065	14.372	5.318	9.282	12.682
0.10	7.588	11.065	14.374	5.317	9.282	12.681
0.20	7.590	11.091	14.497	5.317	9.273	12.610
0.30	7.623	11.348	15.245	5.313	9.152	12.241
0.40	7.790	12.152	16.901	5.282	8.852	12.501
0.50	8.267	13.742	19.662	5.175	8.836	13.892
0.60	9.317	16.515	24.110	4.970	9.582	16.590
0.70	11.476	21.472	31.771	4.711	11.594	21.512
0.80	16.318	31.727	47.332	4.451	16.369	31.748
0.90				4.212		
0.99				4.020		

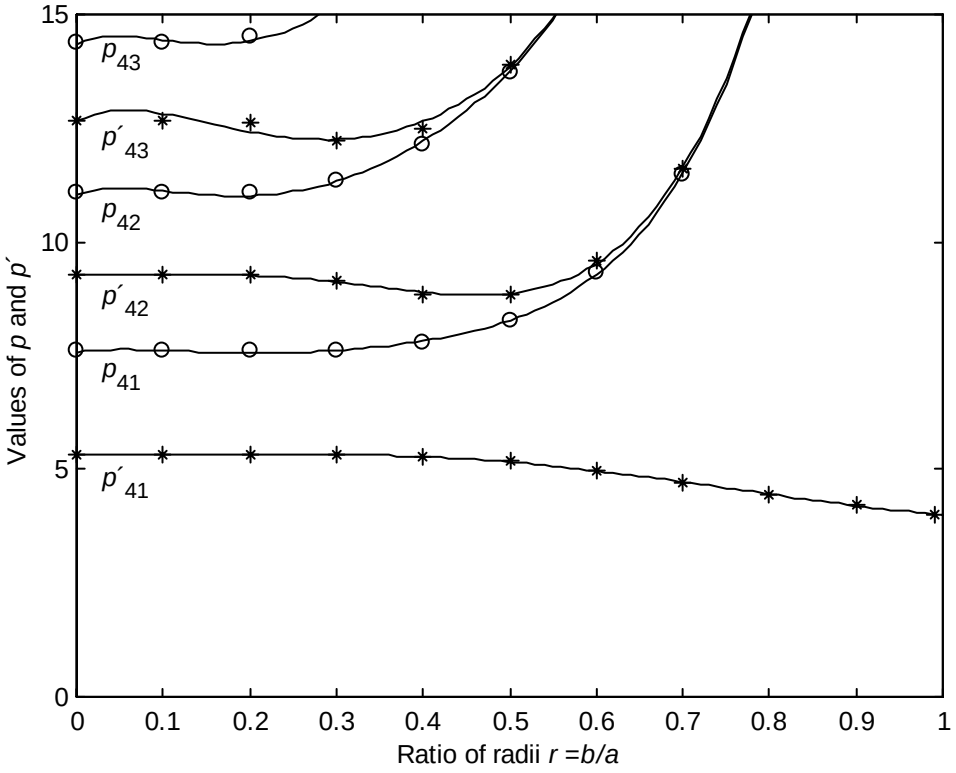

Figure 5.10 Values of p and p' for $\nu = 4$ from Table 5.9 for TM and TE modes in semisectorial waveguides. The graphs are given by the polynomials in Eq. (5.41) and Table 5.10. The asterisks and the rings denote solved values.

The fitted polynomials are of the form

$$p = a + br + cr^2 + dr^3 + er^4 + fr^5 \qquad (5.41)$$

The values of the constants are given in Table 5.10 together with information on the largest and the mean deviation between the polynomials and the solved points. The polynomials are valid within the range of r values in Tables 5.4 – 5.9, i.e. $0 \le r \le 1$ for

Table 5.10a The values of the constants for the polynomials given by Eq. (5.41) approximating the $p'_{\nu m}$ values as a function of r for the $TE_{\nu m}$ modes in semisectorial waveguides. *dev* is the mean deviation between the polynomial and the solved points in %, and *DE* is the maximum deviation in %. See the limitations of validity in the text.

ν	*m*	*a*	*b*	*c*	*d*	*e*	*f*	*dev*	*DE*
0	1	3.8258	2.2190	-18.4344	124.7267	-235.4021	166.2821	0.37	0.69
0	2	7.0031	5.0608	-31.5679	232.0675	-449.9913	323.6859	0.40	0.77
0	3	10.1542	8.6492	-46.9061	341.2466	-663.9598	480.0321	0.41	0.80
½	1	1.1657	-1.7351	2.3644	-2.1955	1.1584	-0.2579	0.01	0.03
½	2	4.5971	-3.3865	1.9980	83.7038	-193.5305	149.4963	0.32	0.67
½	3	7.7734	-3.5513	11.2061	128.5329	-331.8755	272.9520	0.40	0.94
1	1	1.8412	0.1122	-5.9066	11.4074	-9.3110	2.8576	0.03	0.08
1	2	5.3289	0.5806	-42.7088	214.3737	-352.0887	219.0243	0.17	0.42
1	3	8.5283	-3.3756	-15.4337	226.6582	-465.2449	335.7024	0.27	0.55
2	1	3.0527	-0.0135	1.5285	-12.6944	16.9224	-6.8010	0.11	0.26
2	2	6.6935	5.2107	-66.6865	229.7466	-325.1189	193.0019	0.43	0.89
2	3	9.9667	7.2979	-125.9934	546.1984	-850.4198	503.5797	0.13	0.32
3	1	4.2036	-0.5705	6.5129	-22.0742	22.3624	-7.4328	0.12	0.22
3	2	8.0027	2.6295	-26.0537	69.0398	-101.5909	88.2372	0.48	0.96
3	3	11.3242	10.5995	-140.4011	528.0736	-772.4738	450.6731	0.49	1.30
4	1	5.3224	-0.6332	5.8051	-14.9819	9.8821	-1.3839	0.18	0.31
4	2	9.2774	-0.0716	5.8720	-33.6643	16.7978	41.9231	0.28	0.71
4	3	12.6503	9.0704	-104.9654	358.7643	-509.5047	317.3718	0.65	1.49

Table 5.10b The values of the constants for the polynomials given by Eq. (5.41) approximating the $p_{\nu m}$ values as a function of r for the $TM_{\nu m}$ modes in semisectorial waveguides.

ν	*m*	*a*	*b*	*c*	*d*	*e*	*f*	*dev*	*DE*
½	*m*	Equation (5.40)							
1	1	3.8258	2.2190	-18.4344	124.7267	-235.4021	166.2821	0.37	0.69
1	2	7.0031	5.0608	-31.5679	232.0675	-449.9913	323.6859	0.40	0.77
1	3	10.1542	8.6492	-46.9061	341.2466	-663.9598	480.0321	0.41	0.81
2	1	5.1292	2.2059	-31.7659	158.9642	-271.7745	180.7051	0.30	0.54
2	2	8.4066	3.2939	-48.2309	294.5516	-531.1946	360.3205	0.32	0.54
2	3	11.6034	3.8866	-49.7598	377.7850	-722.7681	509.3590	0.35	0.60
3	1	6.3726	2.5746	-34.8753	152.3067	-253.3392	170.0321	0.33	0.67
3	2	9.7499	4.9455	-73.5484	356.3934	-594.2279	384.1026	0.30	0.54
3	3	13.0016	5.5561	-89.0212	497.3303	-868.0012	572.6603	0.28	0.50
4	1	7.5814	2.2048	-29.2508	125.9388	-219.2279	155.6410	0.27	0.53
4	2	11.0507	5.7777	-80.1037	350.4768	-566.4190	365.8013	0.34	0.67
4	3	14.3560	7.9462	-119.2441	569.3872	-939.3969	598.6538	0.29	0.54

$p'_{\nu 1}(\nu \neq 0)$, and $0 \leq r \leq 0.8$ for all other wave modes. For large values of r, the limiting values given in Sec. 5.4.2 can be used. It should also be mentioned that

$$p'_{0m} = p_{1m} \tag{5.42}$$

Because the TE_{0m} modes exist independent of φ_0, they also exist at the values of φ_0 for which the TM_{1m} modes exist. In these cases the TE_{0m} and TM_{1m} modes are degenerate modes. Eq. (5.24) gives that $\nu = 1$, i.e. the modes are degenerate, for $\varphi_0 = \pi$ & $n = 1$, and $\varphi_0 = 2\pi$ & $n = 2$.

5.4 Discussion on Sectorial and Semisectorial Waveguides

5.4.1 Field Distribution and $f_c(r)$ of the Waveguide Modes

The distribution of the fields of the waveguide modes in sectorial waveguides shows some interesting features. Intuitively one would expect the fields to occupy the wider space closer to the periphery and escape from the tip, especially for narrow sector angles. This is also the case for most of the modes, as can be seen by considering that the narrower the sector becomes, the larger becomes ν. It is also large for large values of n, which correspond to cases where the basic field pattern (of a wave mode with $n = 1$) repeats n times over the sector, so that one pattern occupies only a narrow sector. From Eqs. (5.9) and (5.19) it is seen that the field distribution along ρ is then

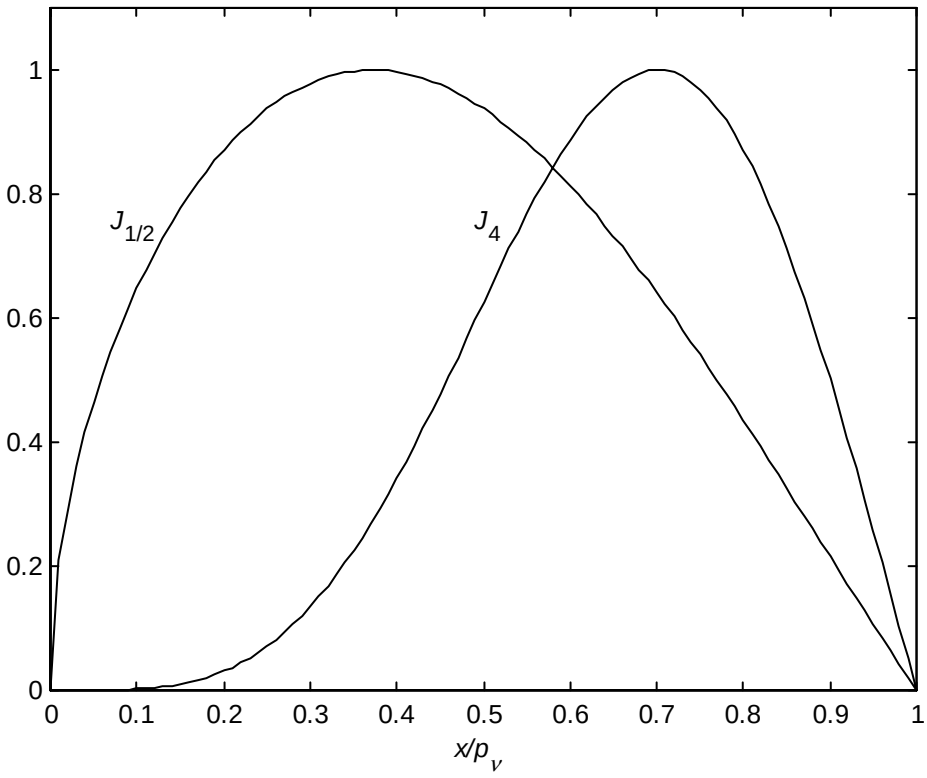

Figure 5.11 $J_{½}$ and J_4 from 0 to their first zero (p), normalized so that the maximum value is 1.The figure illustrates that modes with $n \neq 0$ have little energy in the tip of the sector in a narrow sectorial waveguide.

described by Bessel functions of high order or their derivatives. The higher the order of a Bessel function, the slower the function rises in the beginning. This also applies to its derivative, which for a Bessel function of order ν is a linear combination of the Bessel functions of order $\nu + 1$ and $\nu - 1$:

$$J'_\nu = \frac{1}{2}\left(J_{\nu-1} - J_{\nu+1}\right) \tag{5.43}$$

As an example Figure 5.11 shows $J_{½}$ and J_4 from 0 to their first zero, normalized so that the maximum value is 1. J_4 clearly rises slower than $J_{½}$. This means that the larger ν becomes, the more the fields are concentrated close to the periphery and the less in the centre tip of the sector.

Because the wave modes have little energy in the tip of a narrow sector, it is no surprise that cutting the tip off and turning the waveguide into a semisectorial waveguide, has little effect on the cut-off frequencies of the modes as long as r is small. This is seen in Fig. 5.10 ($\nu = 4$), where the graphs have a longer horizontal part in the beginning, than the graphs in Fig. 5.6 ($\nu = ½$).

Taking a closer look at Eqs. (5.9) and (5.19), reveals that E_φ and H_ρ of the TM modes and H_φ and E_ρ of the TE modes also depend on $1/\rho$, which goes to infinity, when $\rho \to 0$. However, for $\nu > 1$ ($\varphi < \pi$, $n \geq 1$) $J_\nu(\rho)$ decreases faster than $1/\rho$ increases, when $\rho \to 0$. Therefore the discussion above holds and all fields are zero in the tip of a sector, when the sector angle is smaller than π. On the other hand, for large sectors ($\varphi > \pi$) the field strength is theoretically infinite at the sector tip for modes with $n = 1$.

There is one exception to the discussion above, the TE_{0m} modes. These modes have a field structure that is independent on φ, i.e. they have circular symmetry. They also exist in circular waveguides. In a narrow sectorial waveguide the fields look like a piece of cake cut out of the fields in a circular waveguide. The electric field lines extend from one flat wall to the other, and the magnetic field lines are loops in the axial/radial plane. The axial magnetic field H_z has a maximum in the tip of the sector. Therefore these modes are affected by increasing r already from 0. In Fig. 5.5 there is no horizontal part in the graphs at small values of r.

5.4.2 Limiting Values for Semisectorial Waveguide Modes

It was mentioned above that sectorial waveguides are special cases of semisectorial waveguides ($r = 0$). Therefore the solutions of Eqs. (5.27) and (5.34) approach the solutions of Eqs. (5.6) and (5.17), when $r \to 0$.

When $r \to 1$, the semisectorial waveguide turns into a low rectangular waveguide that is bent. When the radius of curvature is large compared to the height of this waveguide, the fact that the waveguide is bent has no effect on the cut-off frequency. The cut-off frequency of a semisectorial waveguide is therefore expected to approach that of a rectangular waveguide with the broad wall equal to the length of the arc of the sector

$$A = \varphi_0 a \tag{5.44}$$

and the narrow wall equal to the difference in radii

$$B = a - b \tag{5.45}$$

The cut-off wave number in a rectangular waveguide is (both TE and TM modes):

$$k_{cr} = \sqrt{\left(\frac{n\pi}{A}\right)^2 + \left(\frac{m\pi}{B}\right)^2} \tag{5.46}$$

The lowest mode in a rectangular waveguide is TE_{10}. For the rectangular waveguide being the limit for a semisectorial waveguide with $\varphi_0 = 2\pi$ the limiting value

$$k_{cr}(\mathrm{TE}_{10}) = \frac{\pi}{\varphi_0 a} = \frac{1}{2a} \tag{5.47}$$

is obtained. From Tables 5.4 - 5.9 it can be seen that the lowest semisectorial mode is $TE_{½1}$, and from Table 5.5 that the limiting value is: $p'_{½1} \xrightarrow{r\to 1} 0.5$. This then gives for k_c

$$k_c(\mathrm{TE}_{½1}) = \frac{p'_{½1}}{a} = \frac{0.5}{a} \tag{5.48}$$

Equation (5.48) gave the same result as (5.47), as expected. It is, however, interesting to note that the rectangular mode and the semisectorial mode have different m indexes ($m = 0$ for the rectangular mode and $m = 1$ for the semisectorial mode). When looking at Fig. 5.3, it is easy to understand that when r increases, the electrical field lines will extend from the inner curved surface to the outer. At the limit the field will lack structure in the radial direction and therefore naturally turn into the rectangular mode with $m = 0$.

Studying Tables 5.4 - 5.9 again shows that generally for $m = 1$, $\nu \neq 0$:

$$p'_{\nu 1} \xrightarrow{r\to 1} \nu \tag{5.49}$$

thus giving

$$k_c(\mathrm{TE}_{\nu 1}) \xrightarrow{r\to 1} \frac{n\pi}{\varphi_0 a} \tag{5.50}$$

which is the same as for the rectangular modes with $m = 0$. From Tables 5.5 – 5.9 it is seen that the $p'_{\nu 1}$ ($\nu \neq 0$) values are monotonously falling with increasing r. The lowest cut-off frequency in a semisectorial waveguide is therefore lower than in the sectorial waveguide with the same sector angle, except for narrow angles and small r, when TE_{01} is the lowest mode and increasing with r. This will be studied further in Ch. 7, when dealing with end grids of cavity resonators.

The cut-off frequency of the semisectorial TE modes with $m \geq 2$, or $m = 1$ and $\nu = 0$, and all TM modes goes to infinity at the limit, just as the rectangular modes with $m \geq 1$. A comparison of results given by Eq. (5.46) and the values in Tables 5.4 – 5.9 of the modes mentioned above shows that for large values of r, the semisectorial modes approach the respective rectangular modes, as expected. The cut-off wave numbers are then solely determined by m, r and a, independent on ν, but such that the m value is higher by 1 for the semisectorial TE modes, except for modes with $\nu = 0$. The fact that the semisectorial TE modes have an m value higher by 1, can be understood so that when r goes from 0 to 1, they loose one period of the structure of the field in the direction of ρ, as was seen in the discussion of $TE_{½1}$. This does not apply to TE_{0m} modes, because they have no electric field perpendicular to the curved walls.

6 CYLINDRICAL FIN RESONATOR SENSOR

6.1 Introduction

In Ch. 4 it was shown that a resonator sensor for measuring a flow of material (MUT) in a pipe can be realized with an open structure and still be nonradiating, when the resonant frequency is below the cut-off frequency of the pipe. In Ch.5 it was shown that a sectorial waveguide with a sector angle of 2π, i.e. a cylindrical pipe with a fin extending from the wall to the centreline, has a cut-off frequency, which is lower than the cut-off frequency of the pipe without the fin. Mounting a fin to the wall of the pipe therefore provides a simple and convenient means of implementing a microwave sensor, which will here be called a cylindrical fin resonator (CFR) sensor, in a pipe. The advantages are minimal obstruction to the flow and low manufacturing cost. The CFR sensor was developed by the author at Roxar [Nyfors and Bringsvor, 1998]. This chapter is devoted to the design of CFR sensors.

6.2 Resonance Modes in CFR Sensors

A CFR sensor, with the fin extending from the wall to the centre of the pipe, is a piece of sectorial waveguide with a sector angle of 2π, and open ends. The resonance modes are based on the waveguide modes. The cut-off frequencies in vacuum of the $TM_{\nu m}$ and $TE_{\nu m}$ modes in a sectorial waveguide are given by Eqs. (5.8) and (5.18):

$$\text{TM:} \quad f_{c,\nu m} = \frac{c\, p_{\nu m}}{2\pi a} \tag{6.1}$$

$$\text{TE:} \quad f_{c,\nu m} = \frac{c\, p'_{\nu m}}{2\pi a} \tag{6.2}$$

where c is the speed of light and a is the radius of the pipe. The p-values are given by Table 5.1, and ν by Eq. (5.5) or (5.16):

$$\nu = \frac{n\pi}{\varphi_0} \tag{6.3}$$

Because $\varphi_0 = 2\pi$ in this case, and the possible values of n are n = 1, 2, 3, … for the TM modes, and n = 0, 1, 2, … for the TE modes, possible values of ν are ν = ½, 1, 1½, … for the TM modes, and ν = 0, ½, 1, … for the TE modes. Eqs. (6.1) and (6.2) also apply for the cut-off frequencies of the pipe outside the fin (ordinary cylindrical waveguide), but with the values for p_{nm} or p'_{nm} from Table 5.2. The lowest mode in the cylindrical waveguide is the TE_{11} mode with $p'_{11} = 1.841$, which also exists in the sectorial waveguide. Expressing the cut-off frequencies of the modes in the sectorial waveguide (the pipe with the fin) relative to that of the TE_{11} mode gives: $TE_{½1}$(63.3%), TE_{11}(100%), $TE_{3/2,1}$(132.8%), TE_{21}(165.9%), and $TM_{½1}$(170.6%).

The resonant frequency in the CFR sensor of a resonance mode that is based on one of the waveguide modes, is given by Eq. (3.50):

$$f_{r,vml} = \frac{c}{2}\left[\left(\frac{p}{\pi a}\right)^2 + \left(\frac{l}{L}\right)^2\right]^{1/2} \tag{6.4}$$

where p stands for p_{vm} or p'_{vm}. Because of the open ends, TE_{vml} modes with $l \geq 0$ and TM_{vml} modes with $l \geq 1$ are supported, as described in Sec. 3.3. The lowest resonance mode is therefore $TE_{½10}$, with a resonant frequency that is independent of the length of the fin. Because of the fringing field in the open ends, the resonant frequency will, however, be slightly dependent of the length of the fin. This will be treated in more detail in Sec. 6.4.2. Figure 6.1 shows the order of the resonances as a function of the length of the fin. The end effects have not been taken into account and the frequencies are normalized to the cut-off frequency of the pipe without the fin (TE_{11}). The modes TE_{11} and TE_{21} also exist in the pipe without the fin. They are therefore not reflected from the ends of the fin and have no resonance modes with $l \geq 1$. All modes with a relative resonant frequency $f_r > 1$ (see Fig. 6.1) will have a poor quality factor, because the pipe provides no isolation. The quality factor depends on how well the resonance mode couples to modes in the pipe.

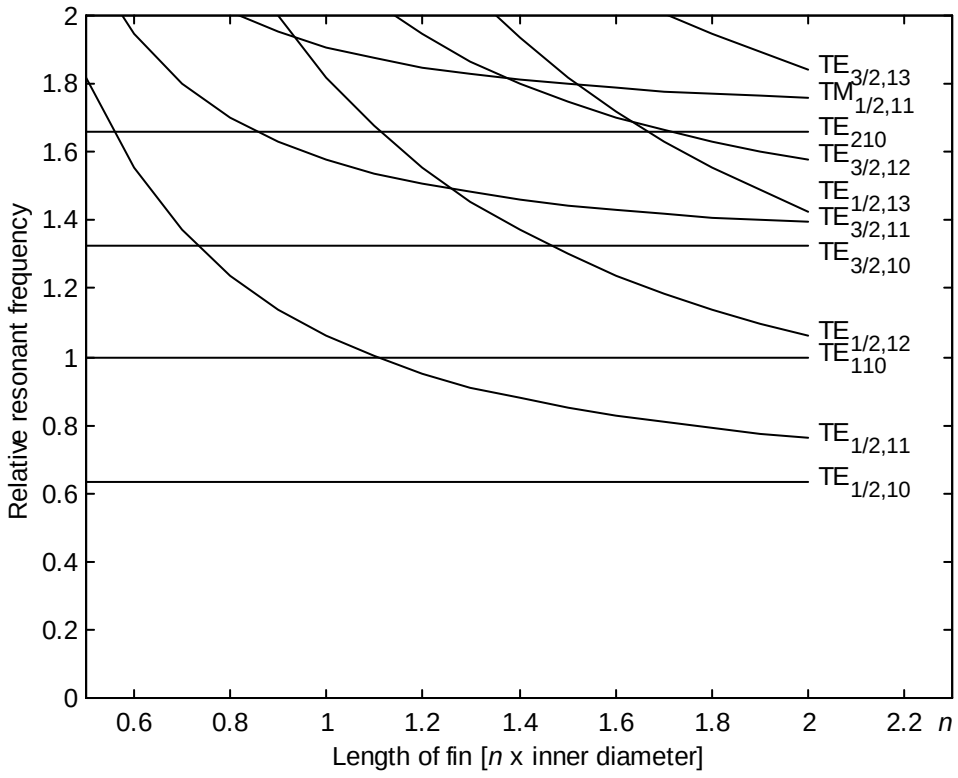

Figure 6.1 The order of the resonances in a CFR sensor as a function of the length of the fin. The resonant frequencies are normalized to the cut-off frequency of the pipe without the fin (TE_{11}). The end effects have not been taken into account. Modes are shown up to index $l = 3$.

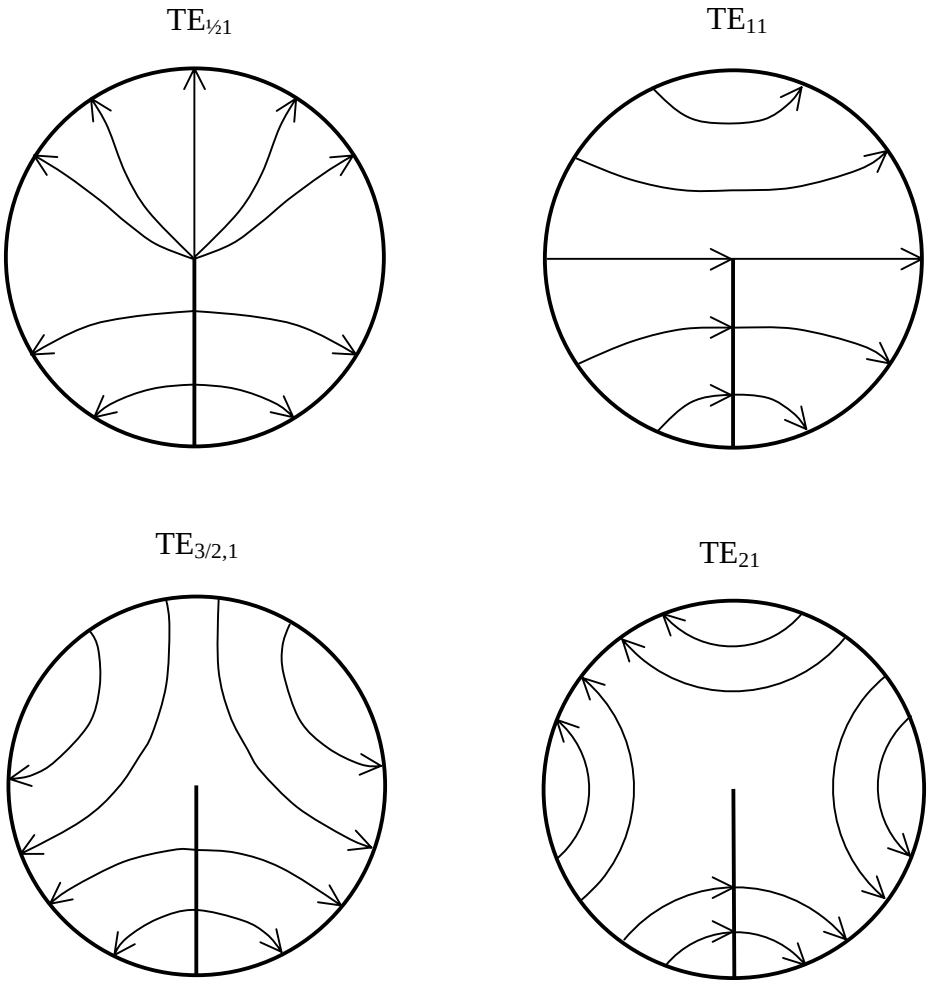

Figure 6.2 The electric field configuration of the lowest modes in a sectorial waveguide with a sector angle of 2π. The modes TE_{11} and TE_{21} also exist in an ordinary cylindrical waveguide without the fin.

The only mode that in practice can be used for measuring purposes is the $TE_{½10}$. To avoid confusion of modes and influence of other modes on $TE_{½10}$, when the MUT is lossy and the peaks broad, it is desirable to have an as large distance to the next mode as possible. From Fig. 6.1 it can be seen that the fin should be shorter than 1.1 inner diameters. The next resonance mode is then TE_{110}, which sees both the sensor and the pipe outside the fin as a single long resonator. It has a resonant frequency 1.58 times the frequency of $TE_{½10}$. Figure 6.2 shows qualitatively the cross section of the electric field configuration of the modes $TE_{½1}$, TE_{11}, $TE_{3/2,1}$, and TE_{21}.

6.3 Type and Location of Coupling Probes

Two probes are used because the power transmission method of measuring the resonant frequency of the sensor is preferred (see Sec. 3.5). This is because of the broad bandwidth required with completely filled sensors, and the desire to be able to use FSA electronics (see Sec. 6.8.2) in low-cost versions of the sensor.

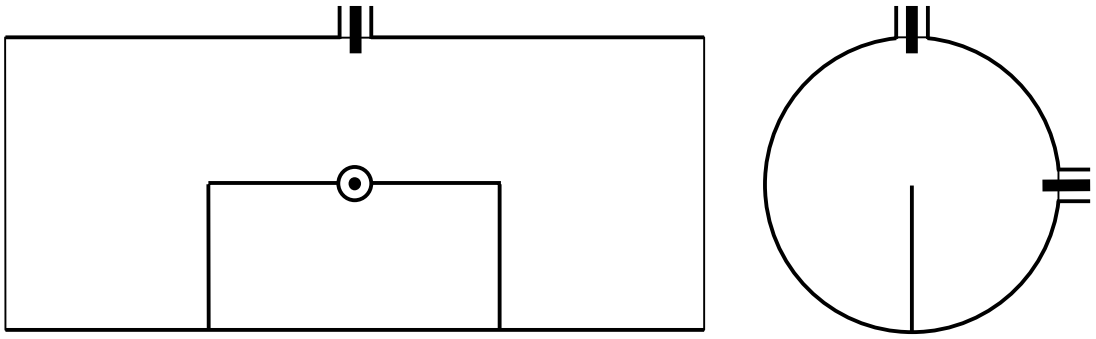

Figure 6.3 A probe configuration that gives good coupling to the $TE_{½10}$ mode, but prevents coupling to the next two modes (TE_{110} and $TE_{½11}$) in a CFR sensor. The resulting frequency response has a good separation between the used mode and other modes.

The used resonance mode ($TE_{½10}$) has an electric field with a strong radial component at the wall. It is therefore convenient to use coupling probes of the electric type (see Sec. 3.7.3), because they are mechanically easier to implement than coupling loops, and also easier to simulate (with HFSS, see Sec. 6.4) for finding the optimal design.

The field distribution of $TE_{½10}$ is even along the length axis of the fin. The coupling is therefore not critical to the axial location of the probes. Of the next two modes, $TE_{½11}$ has field maxima in both ends of the fin and a null in the middle. Locating at least one of the probes in the null in the middle therefore avoids coupling to $TE_{½11}$. The other of the next two modes, TE_{110}, also has an even distribution along the length axis, but a null along a line opposite to the fin. Locating at least one of the probes in the null that is opposite to the fin therefore avoids coupling to TE_{110}. Locating the probes as shown in Fig. 6.3 avoids coupling to both TE_{110} and $TE_{½11}$, and gives good coupling to $TE_{½10}$. A disadvantage is that the probes have different strength of coupling. Generally, in cases of very strong asymmetry of coupling, the resonance peak becomes both broad and low. Broad because one probe leaks, and low, because the other probe has loose coupling, as is seen from Eqs. (3.27b) and (3.14) with a large Q_{e1} and a small Q_{e2}. With the configuration of Fig. 6.3 the probe opposite to the fin is located in the field maximum, whereas (5.19) gives the relative field strength at the location of the other probe as $\sin(\pi/4) = 0.707$. This difference is so small that it has no effect on the performance of the sensor. It only makes the analysis of the simulated result (see below) slightly more complicated.

6.4 The Size and Shape of the Fin

The waveguide modes can be exactly solved, when the fin extends from the wall to the centreline of the pipe, but not for other heights of the fin. It is also difficult to calculate the end effects at the open ends, the effect of other shapes than straight ends, and the effect of the length and thickness of the fin. The effect of the shape of the probes on the frequency response and the height of the resonance peak are also difficult to calculate. These design parameters have therefore been simulated with the

Hewlett-Packard HFSS (High Frequency Structure Simulator) software, version 5.1 for PC.

6.4.1 The Height of the Fin

To find out the cut-off frequency as a function of the height of the fin for the mode that is called $TE_{½1}$, when the fin extends to the centre of the pipe, a waveguide model was simulated with HFSS. The waveguide model had an inner diameter of 50 mm and a length of 150 mm. The cylindrical pipe was divided into segments of 15^{o}. A fin was attached to the wall and the height of the fin was varied in consecutive simulations.

The length of the waveguide model was also varied to check that the chosen length did not influence the results. This check confirmed that the length had no influence on the deduced cut-off frequency.

The results of the simulations are shown in Figure 6.4. The asterisks are simulated points and the rings are exactly calculated results for the cylindrical waveguide without the fin, and the $TE_{½1}$ mode for a fin extending to the centre of the pipe. It can be seen that there is a good agreement between the simulated and the calculated results.

The results are in accordance with the general properties of standard ridged waveguides, where the ridge (or two oppositely mounted ridges) is used to lower the cut-off frequency and increase the bandwidth.

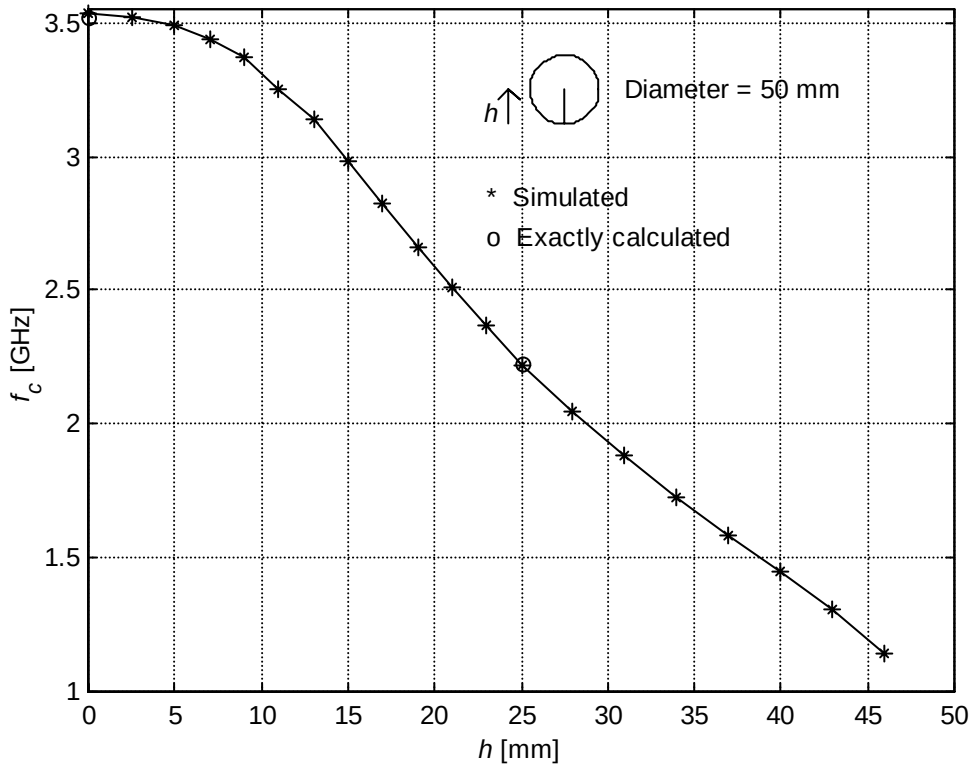

Figure 6.4 Simulations with HFSS and calculations of the cut-off frequency of a cylindrical waveguide with a fin of varying height.

It is often desirable to have as little intrusive parts in the sensor as possible. To minimize the intrusivity of the fin, a low fin can be used. However, as is seen in Fig. 6.4, the cut-off frequency (and hence also the resonant frequency) increases fast as the height of the fin is decreased from reaching to the centreline, while the cut-off frequency of the pipe is unchanged. Even though a probe configuration is used that does not couple to TE_{110}, the frequency response will be poorer because of the closer distance to the next peaks. Because of the lower isolation provided by the pipe outside the fin, the sensor will also be more sensitive to things outside the section with the fin. (Definition of terminology: The sensor consists of a piece of *sensor pipe* with a fin mounted to the wall. The fin may be shorter than the sensor pipe. For measuring a flow of MUT the sensor is mounted in series with, i.e. between flanged ends of, a *process pipe*). For example, if a sensor is mounted on a process pipe with a diameter slightly different from that of the sensor pipe, e.g. because of a different pressure rating, this will slightly affect the resonant frequency. To keep this effect below a limit, the sensor pipe has to be made longer with a lower fin, i.e. the total length of the sensor will have to be increased.

Using a fin that extends past the centreline increases the distance to TE_{110}, thus improving the frequency response. The frequency also becomes lower, which may be desirable. The main disadvantage is that the electric field energy becomes more concentrated in the narrow gap between the edge of the fin and the wall of the sensor pipe. The sensitivity therefore becomes more unevenly distributed over the cross section of the sensor. For most applications a fin extending to the centreline seems to be a good compromise.

6.4.2 The Length of the Fin

Based on the simple theory of a sensor with exactly located open ends, the resonant frequency of the $TE_{½10}$ mode is independent of the length of the fin. In practice the fringing field at the ends of the fin can be expected to cause some change in the resonant frequency, especially for short fins, when a substantial part of the energy is in the fringing field. To study this effect, a sensor model, which consisted of an open-ended sensor pipe section with probes and a fin, was simulated with HFSS. The length of the pipe was 150 mm, and the diameter 50 mm. The pipe was divided in segments of 15^o. The probes were located as indicated in Fig. 6.3, and the open ends of the pipe were defined as radiation boundaries. The fin extended to the centreline, and the length was varied in consecutive simulations from 7.5 mm to 75 mm.

The results of the simulations are shown in Fig. 6.5. Compared to the distance in cut-off frequency between the waveguide modes $TE_{½1}$ (2.226 GHz) and TE_{11} (3.516 GHz), the effect of the length of the fin is small. Whereas the cut-off frequency of $TE_{½1}$ is 63.3% of the cut-off frequency of TE_{11}, the resonant frequency is 68.5% for a fin length of 7.5 mm, 64.5% for 50 mm, and 63.9% for 75 mm.

A sensor with a fin that is 25 mm high and 7.5 mm long resembles the sensor in Fig. 4.4, except that the sensor pipe in Fig. 4.4. is rectangular. The field configuration resulting from the simulation also strongly resembles that of a transversal quasi-TEM mode. The electric field is similar to that shown in Fig. 6.2 for $TE_{½1}$, and the magnetic field lines are loops around the fin, similar to the magnetic field around the centre conductor in a $\lambda/4$ coaxial resonator. As for the sensor in Fig. 4.4, the coaxial model does not give the resonant frequency accurately. A $\lambda/4$

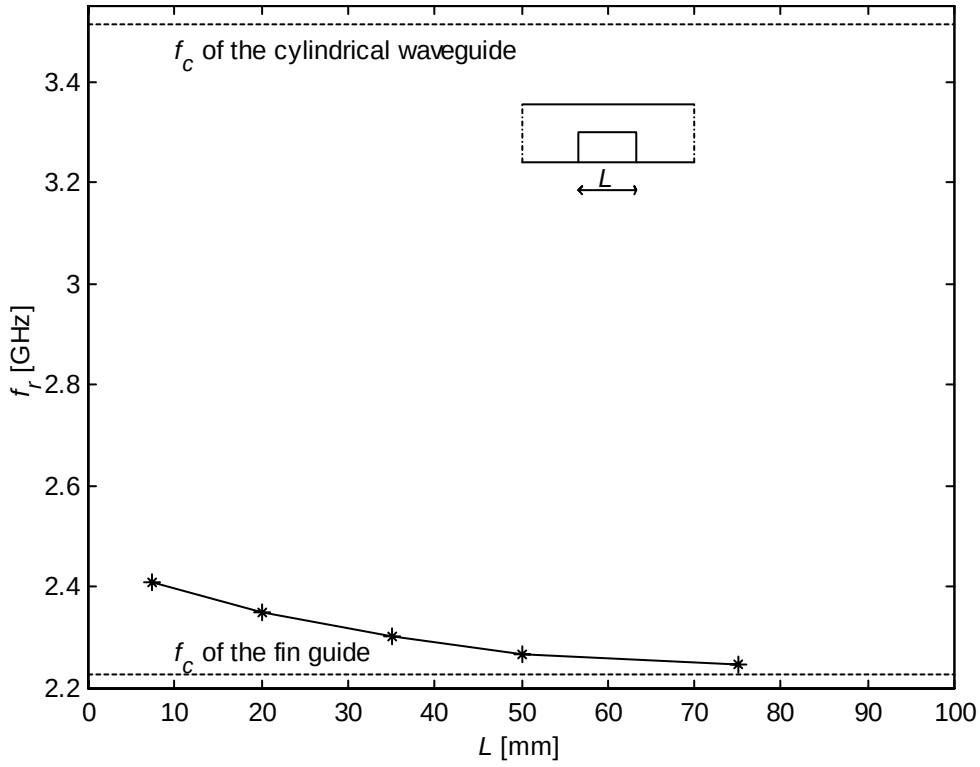

Figure 6.5 The resonant frequency of a CFR sensor as a function of the length of the fin. The data are the results from simulations with HFSS. The diameter of the pipe is 50 mm and the height of the fin is 25 mm.

resonator that is 25 mm long, would have a resonant frequency of 3 GHz, which is 32.3% higher than the 2.267 GHz resulting from the simulation.

Considering that the length of the fin has a relatively small effect on the resonant frequency, mainly other factors than the resonant frequency determine the choice of the length of the fin. As was mentioned in Sec. 6.2, the length should be shorter than 1.1 pipe inner diameters in order to achieve the largest possible distance to the other modes. The simulations show that this distance becomes slightly smaller for even shorter fins, but more important, the sensor becomes shorter, such that the instantaneous volume of MUT affecting the measurement result is smaller. A longer fin results in averaging over a larger volume, making the sensor less sensitive to inhomogeneities. It therefore seems that a fin length of 1 pipe diameter (50 mm in the case of the simulations) is a good choice.

6.4.3 The Shape of the Ends of the Fin

In applications, where the MUT contains solid components, a slanting front edge of the fin may be desirable. The slanting edge can to some extent prevent clogging by guiding the solid particles past the fin. In other applications, where various kinds of build-up is a problem, the pipe system is sometimes cleaned with piston like tools called pigs. Such a pig can not pass a CFR sensor with fixed intrusive parts. Part of a solution may be a retractable, spring-loaded fin with slanting ends.

To study the effect on the resonant frequency of slanting fin ends, simulations were performed with HFSS. The same model was used as for the study of the length of the fin, but with variously shaped fins. The results are shown in Fig. 6.6. Generally, slanting ends increase the resonant frequency. The increase is larger for short fins than for long fins. For example, with a 20 mm long fin with straight ends, the resonant frequency is 2.352 GHz. If both ends are extended 15 mm at the base, such that the base is 50 mm long, the resonant frequency is 2.550 GHz (72.5% of TE_{11}). If only one end is slanting, the resonant frequency is 2.428 GHz. For a 50 mm long fin with straight ends the resonant frequency is 2.267 GHz. If the base is extended between 5 … 25 mm in one end, the resonant frequency is 2.292 … 2.342 GHz. For an extension of 30 mm, the frequency seems to have decreased again to 2.334 GHz. The results for the 50 mm long fin are shown also in Fig. 6.7. The cornered shape of the graph is probably caused by the limited accuracy of the simulated resonant frequency.

Slanting ends increase the mean length and decrease the mean height of the fin. Increasing the length should decrease the frequency, whereas decreasing the height should increase the frequency. The fin that is 20 mm at the top and 35 mm at the base has a mean height of 19.6 mm, whereas the fin that is 50 mm at the base has a mean height of 17.5 mm. From the data presented in Fig. 6.4, the corresponding resonant frequencies (ignoring the effect of the length of the fin) should be 2.616 GHz and 2.782 GHz. The actual simulated frequencies are much lower (2.428 GHz vs. 2.550 GHz). Clearly neither the change in the mean length nor the mean height of the fin can directly explain the small changes in resonant frequency, which are predicted by the simulations to result from the slanting ends. This indicates that the slanting ends should only be regarded as affecting the fringing fields at the ends.

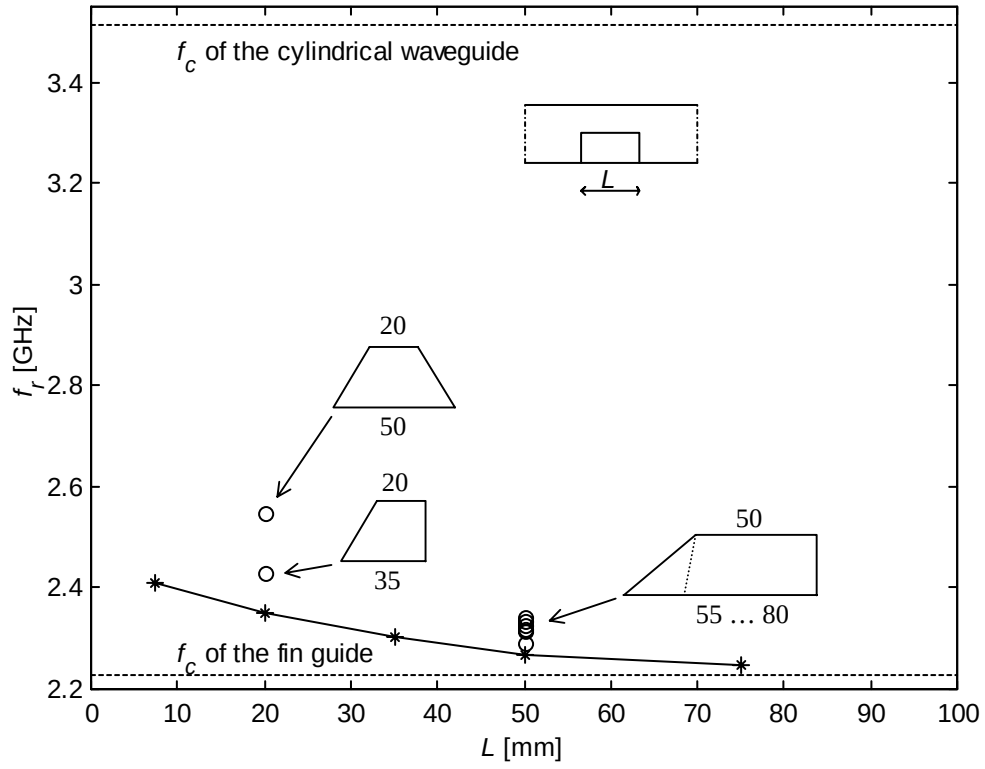

Figure 6.6 The increase in resonant frequency of a CFR sensor caused by slanting end(s) on the fin, compared to the distance in cut-off frequency of the waveguide modes $TE_{½1}$ and TE_{11}, and the increase in resonant frequency caused by the finite length of the fin.

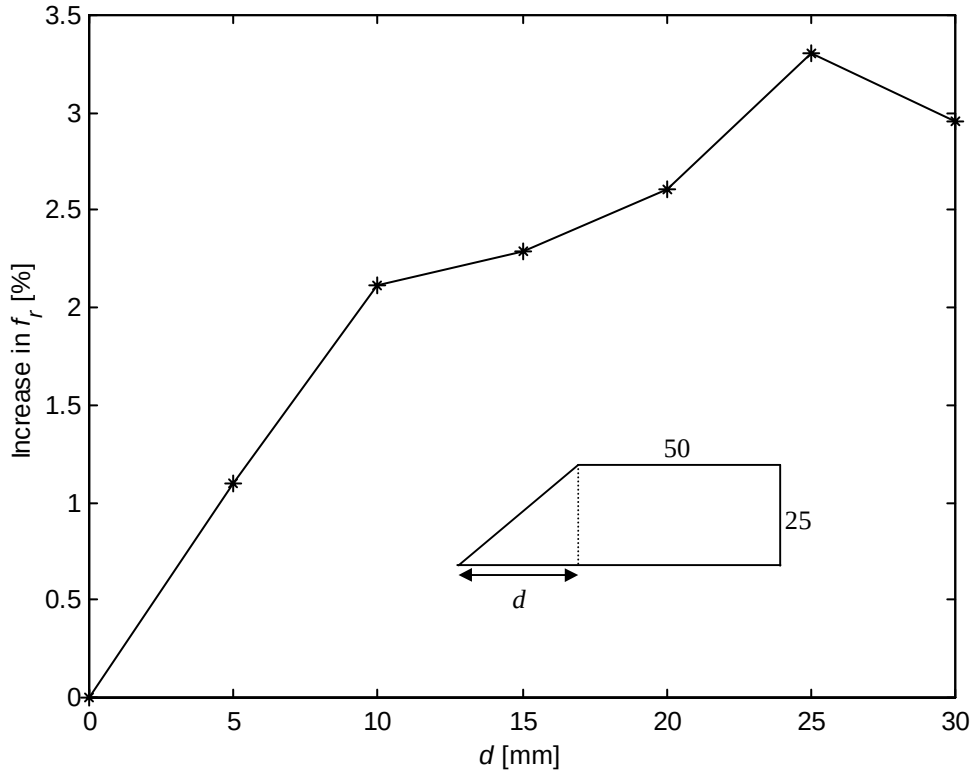

Figure 6.7 The increase in resonant frequency of a CFR sensor caused by one slanting end on the fin. The data were simulated with HFSS

The increase in resonant frequency that is caused by one or two slanting ends is small compared to the distance to TE_{11}, especially for a fin that is 50 mm long at the top. Using a fin with a slanting end facing the flow, which contains solid particles, or with both ends slanting to let cleaning tools pass both ways, is therefore feasible in applications, where this design is mechanically desirable.

A sensor with a fin with one slanting end was built. The inner diameter of the sensor was D_p = 590.54 mm (D_p = 24", with the pressure rating Sch. 20), the straight part of the fin was $L = 1D_p$, and the height of the fin and the length of the slanting section were $h = d = 0.5D_p$. The theoretical cut-off frequency for the pipe with the fin is 188.5 MHz. Taking into account that the finite length of the fin is predicted to cause a 1.9% increase in the resonant frequency compared to the cut-off frequency (Fig. 6.5), and the slanting end a 3.3% increase (Fig. 6.7), the theoretical resonant frequency is 198.4 MHz. The measured resonant frequency was 200.3 MHz, which confirms that the simulation results are at least of the right order of magnitude.

6.4.4 The Thickness of the Fin, a Wedge-Shaped Fin, and a Pointed Fin Edge

So far the fin has been regarded as infinitely thin, but in reality it must have a finite thickness. The optimal thickness is a compromise between high physical strength and minimal obstruction to the flow. In designing a CFR sensor it is important to know the influence of the thickness on the resonant frequency. This effect was therefore simulated with HFSS. The model was a piece of waveguide with a fin extending to the

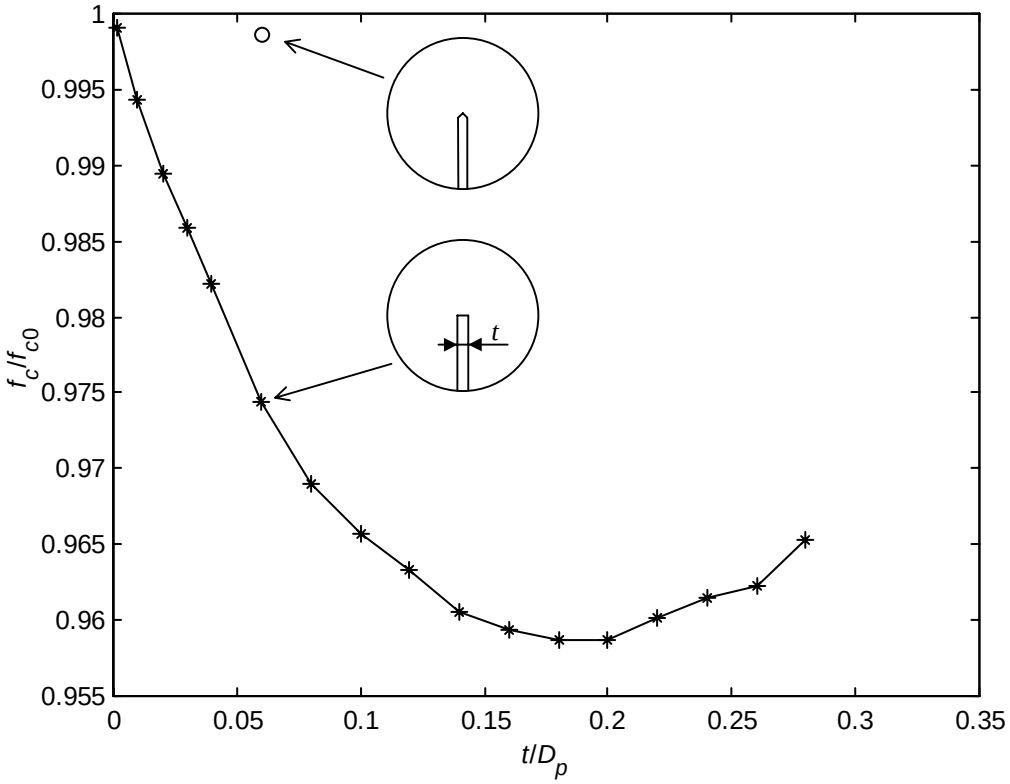

Figure 6.8 The effect of the thickness of the fin on the cut-off frequency of a cylindrical waveguide with a fin that extends to the centre. The graph is the result of simulations with HFSS. One simulation with a wedge-shaped edge is also shown ($\alpha = 90^o$).

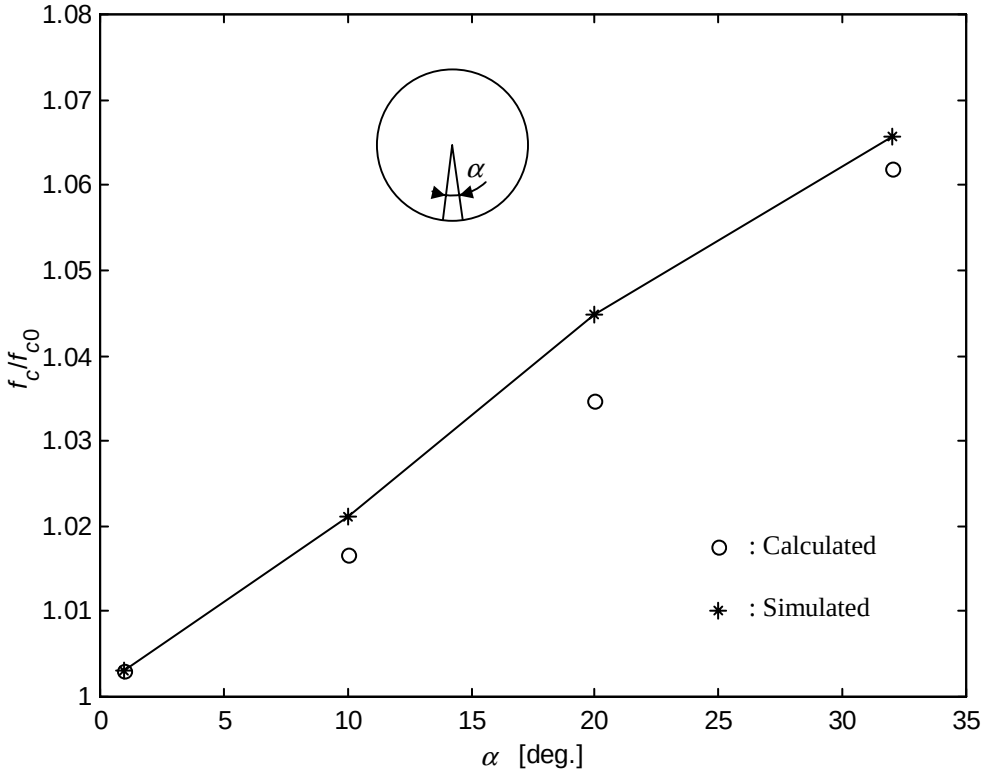

Figure 6.9 The effect of the wedge angle on the cut-off frequency, when the fin is wedge-shaped. The waveguide is circularly cylindrical and the fin extends to the centreline.

centre of the pipe. The ends were defined as ports and the cut-off frequency was derived from S_{21}. The results are shown in Fig. 6.8. It is seen that the cut-off frequency first decreases with increasing thickness, and then increases again. This was expected from the known general behaviour of ridged waveguides. The maximum effect is 4.1% of the cut-off frequency of a pipe with an infinitely thin fin, and occurs roughly for a fin thickness of $t = 0.19D_p$.

If the fin is shaped like a wedge instead of having a uniform thickness, the effect is that the sector angle becomes smaller, which should lead to a higher cut-off frequency. Figure 6.9 shows that this is indeed the case. Both simulated and calculated results are shown. The calculations were performed with (5.16)…(5.18). The agreement is seen to be satisfactory for practical purposes.

The most practical shape is a fin with a uniform thickness and a wedge-shaped edge. One such case was simulated, with a fin thickness of $t = 0.06D_p$ (t = 3 mm, D_p = 50 mm) and a wedge angle of $\alpha = 90^o$ (see inset in Fig. 6.8). In this case the effects of the wedge and the fin thickness nearly cancelled out each other, and resulted in $f_c = 0.9986f_{c0}$, where f_{c0} is the limiting cut-off frequency, when $t \to 0$.

6.5 The Size and Shape of the Probes

The most important feature of the probes is their ability to couple power to the sensor, i.e. the height of resonance peak obtained with a particular design. Of interest is also the mechanical design, with emphasis on ruggedness, low intrusivity, and easy assembly with no need for tuning.

As was concluded in Sec. 6.3, suitable probes for the CFR sensor are those of the electric type because of the strong radial electric field at the wall, and because magnetic coupling loops are mechanically more complicated. The electric type probes have a coaxial structure, with the centre conductor protruding into the sensor like a small monopole antenna (Figs. 3.4a and 6.10). Simulations with HFSS were carried

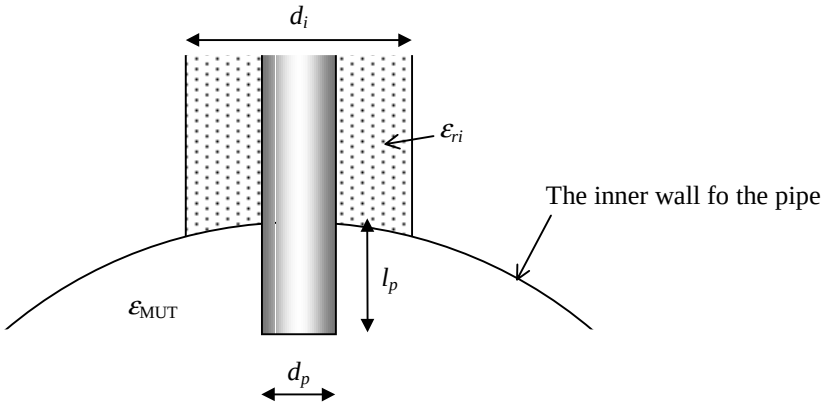

Figure 6.10 The coupling probes of the electric type (that couples to the electric field) have a coaxial structure, with the centre conductor protruding into the resonator like a small monopole antenna. The strength of the coupling depends on the intrusion l_p, the diameter of the pin d_p, the diameter d_i and permittivity ε_{ri} of the dielectric, and the permittivity of the MUT $\varepsilon_{\mathrm{MUT}}$. The internal structure of the probe has been simplified in the figure.

out to find out the dependence of the power coupling ability on the intrusion, the diameter of the pin, the diameter and permittivity of the dielectric material, and the permittivity of the MUT.

6.5.1 Predicting the Height of the Resonance Peak

The height of the resonance peak, i.e. the maximum power transmission coefficient, depends in addition to the design of the probes, on the permittivity of the MUT and the losses in the resonator. The height of the peak will therefore vary with the measurement situation. It is important to be able to predict the height of the peak in the specified range of measurement conditions for an application, but exact calculation is difficult (see Ch. 7 in [Collin, 1991]). Simulations were therefore performed with HFSS to get directly applicable results. The goal with the simulations was to find out the approximate dependence of the coupling on the design parameters to be able to approximately predict the height of the peak for given dielectric properties of the MUT. It is also important to be able to predict the effect of a change of an existing design, instead of using the trial and error method with prototypes. Such a change may become necessary e.g., when a sensor is used in a new application with a MUT with different dielectric properties.

If the two probes of a CFR sensor are identical, they will have unequal coupling because the relative field strength of the resonance mode is different at the locations of the probes, with the probe configuration shown in Fig. 6.3. This asymmetry of coupling could be eliminated by designing the probes unequal. The probe opposite to the fin could for example be made slightly shorter than the other one. However, the asymmetry of coupling is so small that it does not affect the performance of the sensor negatively, and based on manufacturing considerations it is desirable to have identical parts in the probes. In the discussion below, the probes will therefore be assumed to be identical.

Because of the asymmetry of coupling, two different external quality factors must be used. From Eq. (3.27b) the power transmission coefficient at the resonant frequency is then given by

$$a_r = \frac{4Q_l^2}{Q_{e1}Q_{e2}} \tag{6.5}$$

Assuming that the pipe (sensor + process pipe) continues far enough outside the fin in both directions for the sensor to be practically non-radiating, $Q_{\text{rad}} \approx \infty$. From (3.14) the loaded quality factor Q_l is then:

$$\frac{1}{Q_l} = \frac{1}{Q_d} + \frac{1}{Q_m} + \frac{1}{Q_{e1}} + \frac{1}{Q_{e2}} \tag{6.6}$$

In practice the loss in the metal parts will also be negligible compared to the other losses, when the sensor is filled with a MUT. The peak height a_r will therefore only depend on the dielectric loss in the MUT, represented by Q_d, and the coupling losses represented by Q_{e1} and Q_{e2}. In interpreting the results from the simulations the focus has therefore been on obtaining Q_{e1} and Q_{e2} as a function of the design parameters and

the properties of the MUT. Figure 6.11 gives the peak height calculated from (6.5) and (6.6) as a function of Q_d, Q_{e1} and Q_{e2}, assuming that $Q_{e1} = Q_{e2}$. For cases when $Q_{e1} \neq Q_{e2}$, see Sec. 6.5.3 and Fig. 6.19 for a correction.

The Effect of the Real Part of the Permittivity of the MUT ($\varepsilon'_{\mathrm{MUT}}$) on the Coupling ($Q_{\mathrm{ext}}$)

Generally the permittivity in various regions in a medium affects the distribution of an applied electric field such that, qualitatively speaking, the field is attracted to regions with a higher permittivity. It is therefore natural to expect that the fringing field of an electric probe, with which the probe couples to the resonant modes in the cavity, is affected by both the permittivity of the dielectric material of the probe (ε_{ri}) and the permittivity of the MUT ($\varepsilon_{\mathrm{MUT}}$). More specifically, Q_{ext} can be expected to decrease with increasing $\varepsilon_{\mathrm{MUT}}$, and increase with increasing ε_{ri}.

The dependence of Q_{ext} on ε_{ri} and $\varepsilon_{\mathrm{MUT}}$ can be expected to be independent of the design of the cavity. A simple rectangular cavity resonator model (Fig. 6.12) was therefore simulated with the HFSS. The rectangular shape was chosen because of the shorter simulation times than for cylindrical geometries. Two probes were used. They were moved 15 mm towards opposite ends to reduce the direct coupling. The length of the probe structure outside the sensor was 11.9 mm. The simulations were

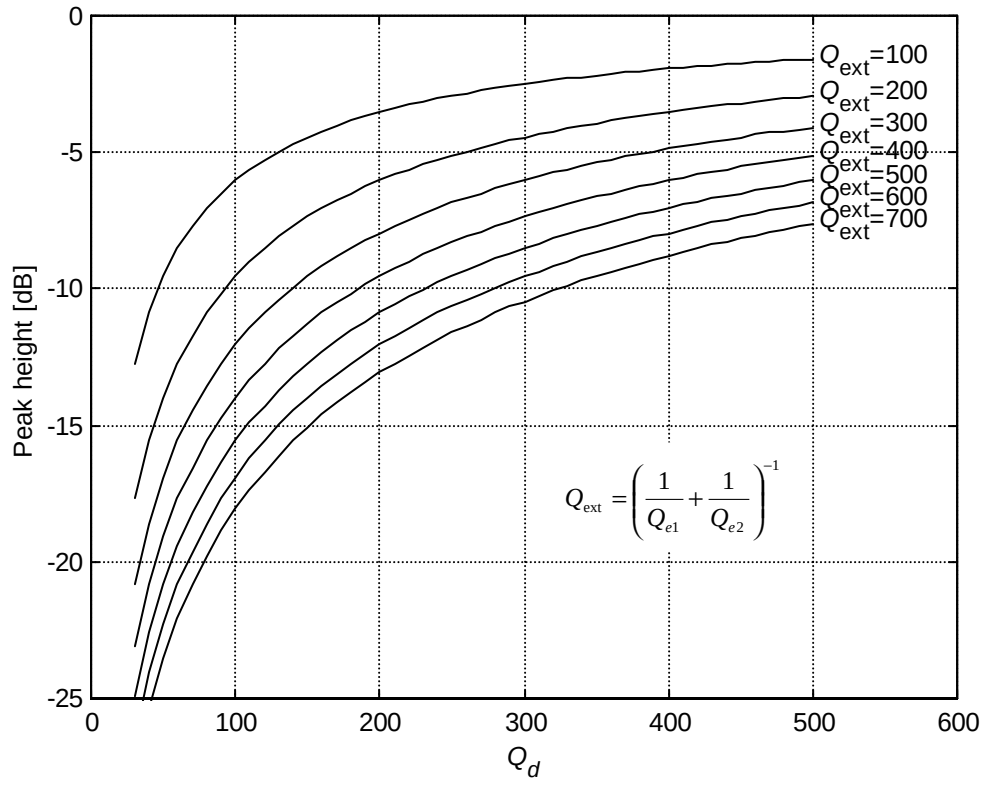

Figure 6.11 The height of the resonance peak as a function of the dielectric loss in the MUT and the loss due to coupling to the measurement circuit, assuming that the radiation and metal losses are negligible. The graphs were calculated from Eqs. (6.5) and (6.6) assuming that $Q_{e1} = Q_{e2}$.

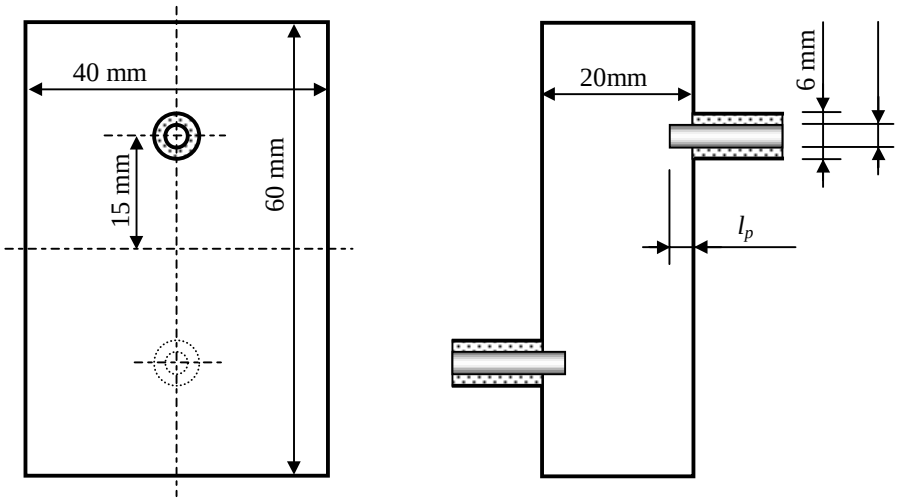

Figure 6.12 The rectangular cavity resonator that was used in the simulations with HFSS to study the effect of ε_{ri} and ε_{MUT} on Q_{ext} as a function of l_p.

performed with three different values for the intrusion (l_p = 1, 2, and 3 mm) to study, whether the influence of ε_{ri} and ε_{MUT} on Q_{ext} depends on the relative dimensions of the probes.

Simulations were performed with a matrix of permittivities: ε_{ri} = 1, 3.25, and 4.8, and ε_{MUT} = 1, 2.18, 4.8, and 10. The values were chosen because the permittivity of PEEK, which is a plastic material that is used as the dielectric material in MFI low-pressure probes, is 3.25, the permittivity of the glass/ceramic material used in MFI high-pressure probes is 4.8, and the permittivity of diesel fuel is 2.18. Because 12 different combinations of permittivities were simulated for 3 different intrusions, 36 simulations were performed.

From the S parameters (i.e. the scattering matrix) resulting from the simulations f_r and Q_{ext} were calculated with the method described in Sec. 6.5.2. While performing these simulations it became evident that the accuracy of the simulated resonant frequency is high already after a small number of iterations, while a larger number of iterations is required to achieve the same accuracy for Q_{ext}. After studying the converging of the results for Q_{ext} as a function of the number of iterations and the convergence parameter ΔS (a parameter given by HFSS that is a measure of the change in the results compared to the previous iteration) it was decided to use the criteria $\Delta S < 0.005$, or maximum 8 iterations, for all simulations with the rectangular resonator. With these criteria the values for Q_{ext} are estimated to have converged to within 1.5% of the final values. The accuracy of the simulated results is studied further in Ch. 8.

The results for Q_{ext} as a function of ε_{ri}, ε_{MUT}, and l_p are shown in Fig. 6.13. They confirm the general anticipations above: The coupling improves, when ε_{MUT} increases. Also longer probes, and probes with a lower ε_{ri}, give better coupling. It is also seen that the relative dependence on ε_{MUT} is almost the same independent of l_p. Only a small "saturation" can be perceived for low values of Q_{ext}, and possibly also for high values.

From the slope of the graphs in Fig. 6.13, an approximate model can be made for predicting Q_{ext} as a function of ε_{MUT} from one known value, which has e.g. been measured or simulated for a sensor filled with oil with WC = 0%:

$$Q_{ext2} = Q_{ext1}\left(\frac{\varepsilon_{MUT2}}{\varepsilon_{MUT1}}\right)^{-0.4} \tag{6.7}$$

The value of the exponent was derived by manually fitting the model to the results in Fig. 6.13 to get a best fit ignoring the "saturation" at high and low values of Q_{ext}. The quality of the fit is illustrated in Fig. 6.14, which shows the relative deviation between the simulated values and values predicted with model (6.7) from the simulated values for ε_{MUT} = 2.18. The deviation is generally less than 15% (less than 11% for ε_{MUT} > 2.18), except for two points (22.8% and 35.5%), which correspond to air-filled probes, ε_{MUT} = 10, and l_p = 3 mm and 2 mm respectively. Because air-filled probes are not practical, the large deviation of these two points is not important. The maximum effect on the power transmission coefficient of a 15% error in the predicted Q_{ext} is 1.4 dB, and 1.0 dB for 11%.

The dependence of Q_{ext} on ε_{MUT} was verified by measurement. A CFR sensor (D_p = 50.8 mm, d_p = 8 mm, d_i = 17.5 mm, l_p = 7.5 mm, ε_{ri} = 3.25) and an end cross sensor (see Ch. 7) of the same size, with magnetic coupling loops in PEEK

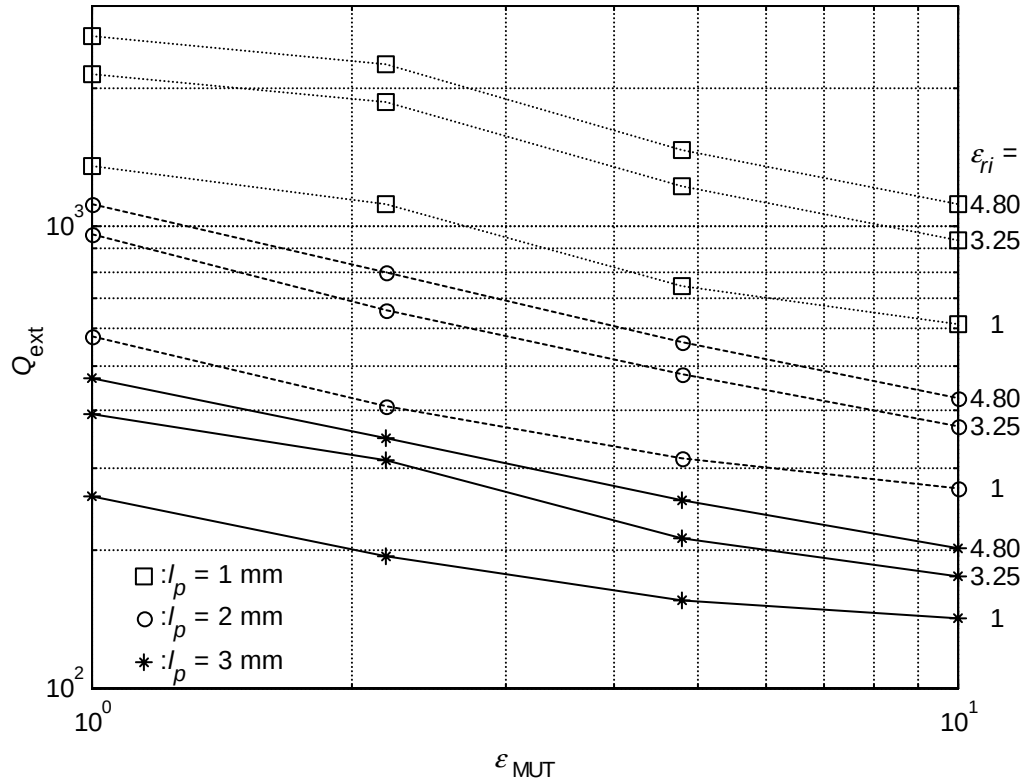

Figure 6.13 The external quality factor as a function of the intrusion, the permittivity of the dielectric material in the probes, and the permittivity of the MUT. The data were simulated with HFSS for the model resonator in Fig. 6.12.

enclosures, were measured in a test loop with crude oil with varying *WC*. For the CFR sensor Q_{ext} was calculated from the measured a_r, Q_l and f_r using (3.32) and (6.13), assuming R_e = 1.75. For the end cross sensor Q_{ext} was calculated from (3.29) and (3.14). The results of two runs are shown in Fig. 6.15 together with model (6.7). In one run the salinity of the water was S = 5%, and in the other freshwater was used. The results for the CFR sensor from both runs obey model (6.7) for $\varepsilon_{MUT} \geq 2.18$ (i.e. $WC \geq 0\%$), even though the losses in the MUT were much higher for S = 5%. The measurement in air (ε_{MUT} = 1), however, deviates considerably from model (6.7), when compared to the other measurement points. The reason for the deviation could not be found.

The results for the end cross sensor show that the coupling decreases with increasing ε_{MUT}. This is probably a result of two factors: The coupling loops couple via the magnetic field and are therefore not affected by the permittivities in the same way as electric probes, and the loops are surrounded by a sheath of PEEK, which creates a contrast towards the MUT at higher watercut. Also for the end cross sensor the measurement in air does not seem to fit into the series of measurements in oil at various watercut.

As a consequence of the different behaviour of Q_{ext} as a function of ε_{MUT} the peak height decreases faster as a function of ε_{MUT} in end cross sensors than in CFR sensors. Smaller variations in the peak height is an advantage, when simple electronics is used for measuring the sensor. Figure 6.16 shows the measured peak height from the loop tests. In the CFR sensor the peak height decreases only 0.7 dB in

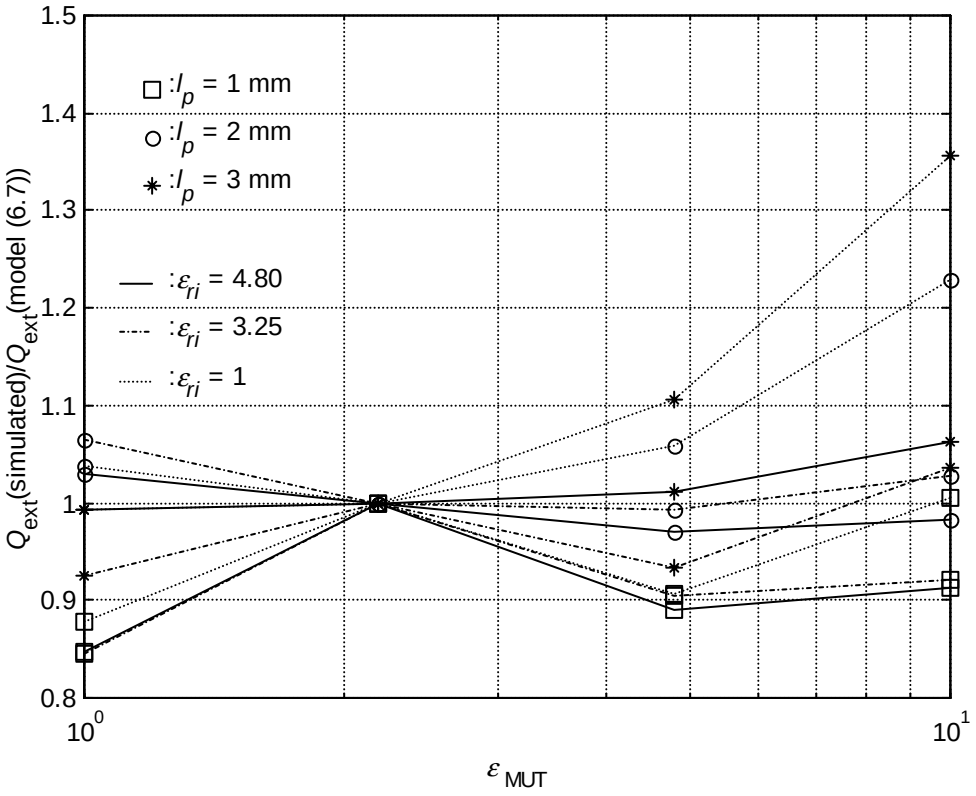

Figure 6.14 The difference between the simulated values of Q_{ext} as a function of ε_{MUT}, and values predicted by (6.7) from the simulated values for ε_{MUT} = 2.18

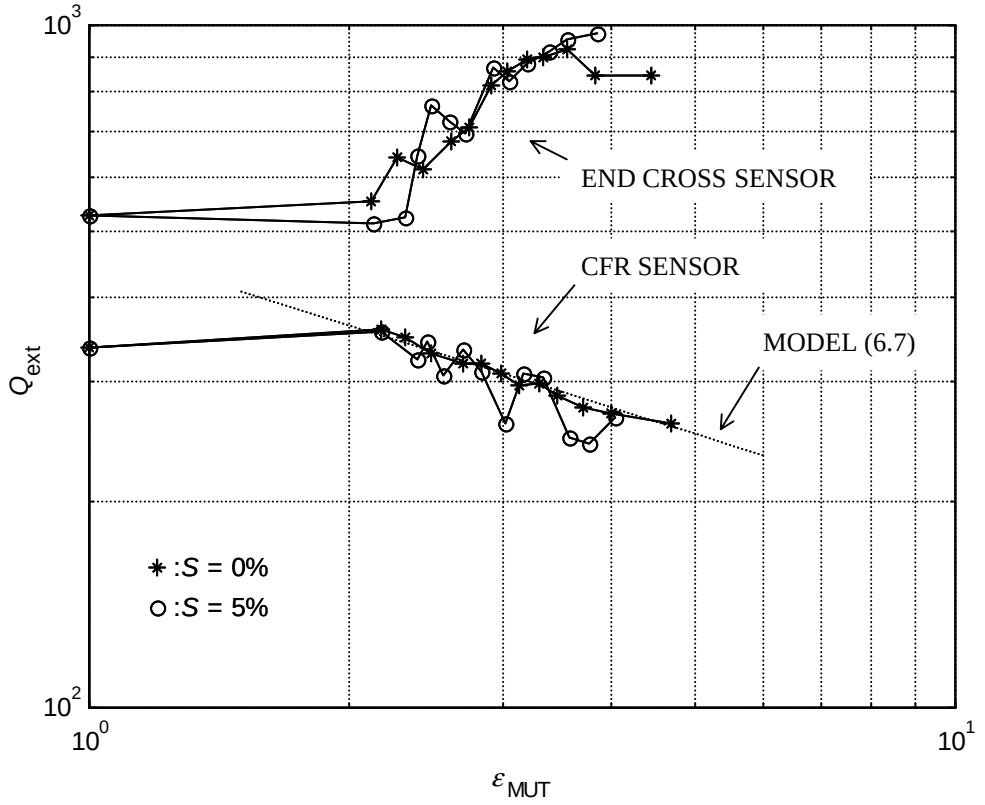

Figure 6.15 Results from a loop test, where a CFR sensor and an end cross sensor were compared. Crude oil and water with two different salinities (S) were used. The graphs show the Q_{ext} values derived from the measurements.

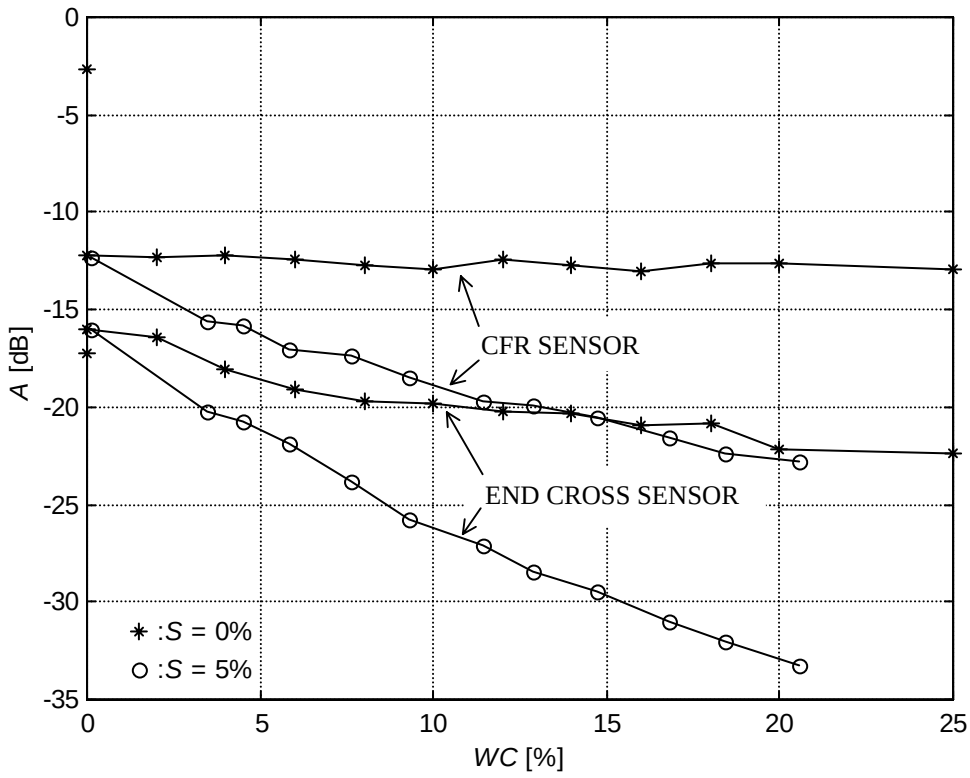

Figure 6.16 The peak height (maximum power transmission coefficient) measured with a CFR sensor and an end cross sensor in a test loop. The two isolated points on the y-axis are measurements in air (CFR: -2.6 dB, end cross s.: -17.2 dB).

the range WC = 0…25%, when S = 0%, whereas in the end cross sensor the decrease is 6.3 dB. For S = 5%, the numbers are 10.6 dB and 17.2 dB respectively (WC = 0…20.5%). The peak heights measured with the empty sensors are also shown. For the CFR sensor the relation between the peak heights in air and oil obey (6.5) and (6.6), when Q_d for the oil is added. In the end cross sensor the peak height in air is anomalously low, and Q_l actually increases from air to oil, even though Q_{ext} is roughly unchanged, Q_m has decreased according to (3.39), and Q_d has been added. Mathematically this is impossible. The reason for the anomaly is most probably an interfering resonance internally in the probes, of which a distortion in the peak shape also bears witness.

As a conclusion, for a CFR sensor Eq. (6.7) can be used to predict Q_{ext} as a function of ε_{MUT}, from one known value. Care must be taken when $\varepsilon_{\text{MUT}} < 2.18$.

The Effect of the Imaginary Part of the Permittivity of the MUT ($\varepsilon''_{\text{MUT}}$) on the Coupling ($Q_{ext}$)

In the previous section it was qualitatively explained how the real part of the permittivity of the MUT might affect the coupling, based on the boundary conditions for the electric field at the interface between the MUT and the dielectric material in the probes. Based on the same discussion the imaginary part is not expected to considerably affect the coupling. A series of 24 simulations were performed for a

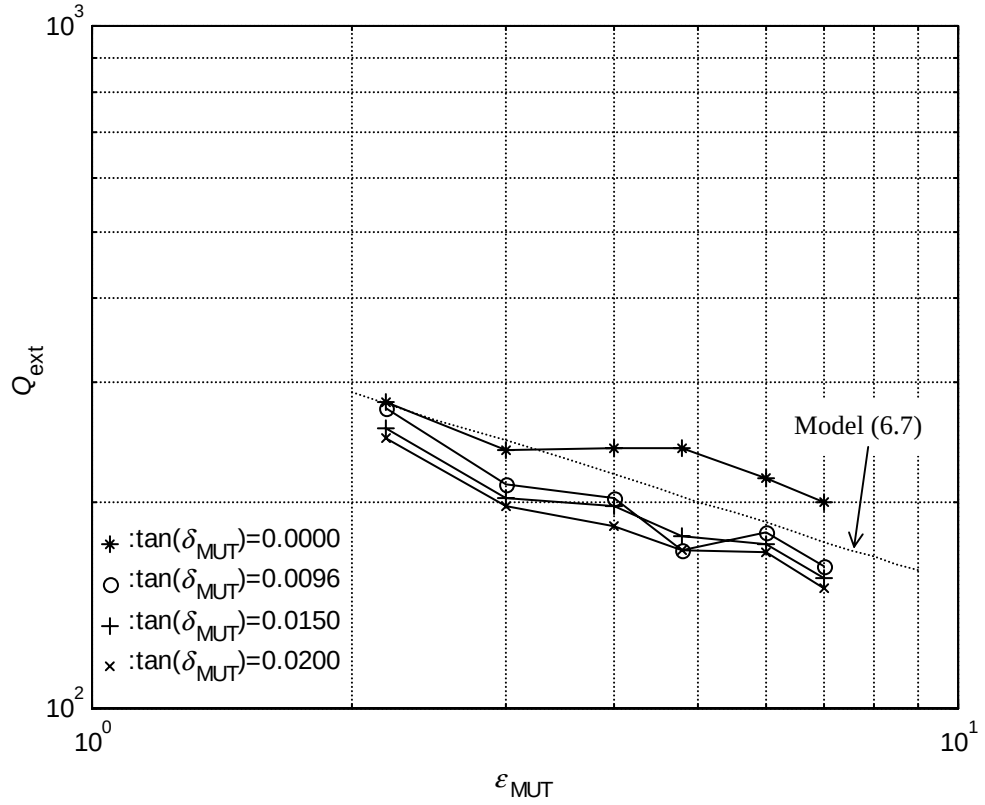

Figure 6.17 The external quality factor as a function of the permittivity of the MUT for various values of the loss tangent. The values were simulated with HFSS for a CFR model with D_p = 50.8 mm, d_p = 8 mm, d_i = 17.5 mm, l_p = 6 mm, and ε_{ri} = 3.25.

model of the CFR sensor with the purpose to verify this assumption. The results are shown in Fig. 6.17, where $\tan(\delta_{\mathrm{MUT}}) = \varepsilon''_{\mathrm{MUT}} / \varepsilon'_{\mathrm{MUT}}$. They indicate that there is a difference between the cases of small losses (equivalent to the losses of pure diesel fuel) compared to no losses, but a further increase in the losses has only a minor effect on the coupling. This situation seems fairly unlikely, especially as the no-loss graph deviates from model (6.7). Looking at the graphs for freshwater and water with S = 5% in Fig. 6.15, does not reveal any difference in the coupling in the two cases, even though there is a large difference in the loss factor. The simulations were performed before the poor accuracy of the simulations of Q_{ext} for a small number of iterations was detected. The results may therefore not have converged well enough. A series of new simulations was therefore performed with the intention to achieve a higher accuracy, but the problem tended to diverge after the 5th iteration in HFSS.

If $\tan(\delta_{\mathrm{MUT}})$ has an effect on Q_{ext}, the phenomenon can be assumed to be independent of the shape of the resonator. A series of 4 simulations was therefore performed with the rectangular resonator shown in Fig. 6.12, using the same criteria for high accuracy as above: $\Delta S < 0.005$, or maximum 8 iterations. The conditions were: ε_{ri} = 3.25, $\varepsilon'_{\mathrm{MUT}} = 4.8$, and $\tan\delta_{\mathrm{MUT}} =$ 0, 0.0096, 0.015, and 0.02. The results were: Q_{ext} = 211.8, 223.3, 226.8, and 226.4 respectively, i.e. no dependence on the losses was found. It therefore seems likely that the losses in the MUT has at most a negligible effect on the coupling and can in practice be ignored, especially as compared to the large effect on the peak height through Q_d.

6.5.2 Deriving Q_{e1} and Q_{e2} from the Simulations

The HFSS produces the S parameters (i.e. the scattering matrix) for the simulated object at a set of discrete frequencies defined by the user. To get the resonant frequency and the set of quality factors, the theoretical resonance curve must be fitted to the simulated points. Because separate values are needed for Q_{e1} and Q_{e2}, and the transmission curve (3.27) only contains information about their product, the reflection curve (3.24) must be fitted separately to S_{11} and S_{22}.

The results of a simulation consists of a 2x2 matrix of S parameters for each frequency point. These matrices were exported to Matlab, where the fitting was done. The backslash operator was used to fit a ”linear-in-the-parameters” regression model to the simulated points. The inverse of the transmission coefficient for the probe (transmission coefficient = 1 - reflection coefficient) was used as the regression model, i.e. the real resonance curve (3.24) was fitted to the simulated points:

$$\frac{1}{1-\left|S_{nn}\right|^2} = \frac{1}{4\dfrac{Q_l}{Q_{un}}\left(1-\dfrac{Q_l}{Q_{un}}\right)} + \frac{Q_l^2}{4\dfrac{Q_l}{Q_{un}}\left(1-\dfrac{Q_l}{Q_{un}}\right)}\left(\frac{f}{f_r}-\frac{f_r}{f}\right)^2 \qquad (6.8)$$

$$Y_n = a_{0n} + a_{1n}\cdot\left(\frac{f}{f_r}-\frac{f_r}{f}\right)^2$$

where n is 1 or 2. Note that the unloaded quality factors are different when fitting S_{11} and S_{22}, because Eq. (3.24) assumes that the resonator has only one coupling probe,

whereas the simulations were done for a resonator with two probes. Therefore the coupling loss due to the other probe is included in the unloaded quality factor.

The fitting was done iteratively such that the resonant frequency f_r was given manually before Matlab performed the fitting. The simulated points and the fitted model were then plotted to show the quality of fit. This process was repeated until a visually judged good fit was achieved. The obtained value for Q_{ext} was not very sensitive to the used value for f_r such that the fitting method being partly manual is not expected to have contributed significantly to the error of Q_{ext}. Figure 6.13 shows a typical example of the obtained plots. When the best fit had been obtained, Q_l and Q_{un} were calculated from a_{0n} and a_{1n}. Note that both fittings give a value for Q_l. Ideally the values should be identical and they are therefore not denoted as separate below. In practice the difference between the two values is almost always <3%, and usually <1%. The largest relative errors seemed to occur, when measurement of high loss samples was simulated, and the loaded quality factor was low. By solving from (6.8) the equations for deriving Q_l and Q_{un} from the simulations are obtained:

$$\begin{aligned} Q_l &= \sqrt{\frac{a_1}{a_0}} \\ Q_{un} &= \frac{2Q_l}{1+\sqrt{1-\frac{1}{a_{0n}}}} \end{aligned} \tag{6.9}$$

and from these Q_{e1}, Q_{e2}, and Q_u are given by

$$\begin{aligned} Q_{e1} &= \left(\frac{1}{Q_l}-\frac{1}{Q_{u1}}\right)^{-1} \\ Q_{e2} &= \left(\frac{1}{Q_l}-\frac{1}{Q_{u2}}\right)^{-1} \\ Q_u &= \left(\frac{1}{Q_l}-\frac{1}{Q_{e1}}-\frac{1}{Q_{e2}}\right)^{-1} \end{aligned} \tag{6.10}$$

The resonance curves (3.24) and (3.27) are known to describe the resonance peak accurately only close to the resonant frequency. Far from the resonance, at the flanks of the peak, other effects like direct capacitive coupling between the probes, and other resonance modes affect the frequency response of the resonator. It is therefore important to choose the spacing between the frequency points for the simulation such that at least three points are between approximately the –6 dB points. This was also seen in practice. When a larger number of points was chosen such that some lay farther from the resonant frequency than specified above, or the spacing between the points was too lage, the quality of the fit became poor especially for the points closest to the peak.

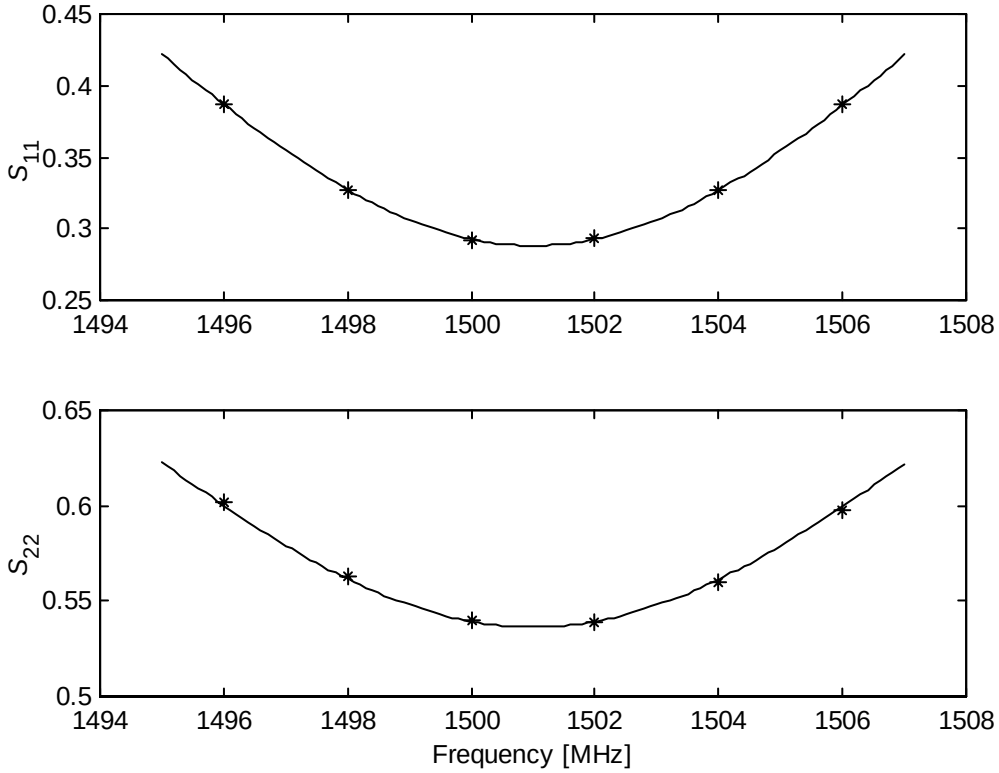

Figure 6.13 An example of the plots produced by the fitting routine written for Matlab. The plots show the simulated points (*) and the fitted curves (-). In the simulated situation the sensor is filled with diesel fuel (assumption: $\varepsilon'_{\mathrm{MUT}} = 2.18, \tan\delta_{\mathrm{MUT}} = 0.0096$), d_i = 17.5 mm, d_p = 8 mm, l_p = 7.5 mm, and ε_{ri} = 3.25. The sensor diameter is D_p = 50.8 mm, and the fin length and height are L = 50 mm and h = 25.4 mm.

6.5.3 The Ratio Q_{e1}/Q_{e2}

The ratio of the two external quality factors is primarily determined by the ratio of the electric field of the resonance mode at the locations of the probes. From (5.36) the ratio of the field strengths at the locations of the probes in Fig. 6.3 is:

$$\frac{E_1}{E_2} = \frac{1}{\sin(\pi/2)} = 1.4142 \tag{6.11}$$

Because the voltage that the field of a resonance mode excites into a cable through a probe must be directly proportional to the field strength at the location of the probe, and the external quality factor is proportional to the power, the ratio can be expected to be

$$R_e = \frac{Q_{e1}}{Q_{e2}} = \left(\frac{E_1}{E_2}\right)^2 = 2 \tag{6.12}$$

Because of the finite intrusion and diameter of the probes, and the distorting effect of the holes in the metal wall, the effective ratio may be different and slightly dependent

on the dimensions of the probes, especially the intrusion. The ratio can, however, be expected to be constant enough that the exact ratio is not needed for prediction of the peak height and width in practice. If that is true, the results from the simulations can be reported in terms of only one external quality factor and the peak height predicted from (3.27a) instead of (3.27b). Two different choices for the quality factor are possible: From (6.5) and (3.27):

$$\frac{4Q_l^2}{Q_{e1}Q_{e2}} = \frac{Q_l^2}{Q_e^2} \Rightarrow Q_e = \frac{\sqrt{Q_{e1}Q_{e2}}}{2} \tag{6.13}$$

or from (6.6):

$$Q_{\text{ext}} = \left(\frac{1}{Q_{e1}} + \frac{1}{Q_{e2}} \right)^{-1} \tag{6.14}$$

Here Q_{ext} is the real external quality factor, but Q_e gives the product of Q_{e1} and Q_{e2} correctly. When using Q_e in (6.6), Q_l will be slightly in error, and therefore the peak height calculated from (3.27a) will also be slightly in error. Of the same reason the predicted peak width will also be in error. When using Q_{ext} in (6.6), Q_l will be right, and hence also the peak width, but when used in (3.27a) the peak height will be in error.

The relative difference between the results of (6.13) and (6.14) is only a function of the ratio R_e:

$$\frac{Q_e}{Q_{\text{ext}}} = \frac{1}{2}\left(\sqrt{R_e} + \frac{1}{\sqrt{R_e}} \right) \tag{6.15}$$

To be able to decide whether to use Q_e, Q_{ext}, or Q_{e1} and Q_{e2}, the errors that are introduced by using one of the alternatives must first be studied in more detail. Calculating the peak height from (3.27a) by using Q_{ext}, and comparing to the exact result from (6.5), the relative error is seen to be

$$K_{\text{ext}} = \frac{a_r(Q_{\text{ext}})}{a_r(Q_{e1}, Q_{e2})} = \left(\frac{Q_e}{Q_{\text{ext}}} \right)^2 \tag{6.16}$$

In the same way the error in using Q_e is easily shown to be

$$K_e = \frac{a_r(Q_e)}{a_r(Q_{e1}, Q_{e2})} = \left(\frac{Q_{\text{ext}} + Q_u}{Q_e + Q_u} \right)^2 \cdot \left(\frac{Q_e}{Q_{\text{ext}}} \right)^2 \tag{6.17}$$

From (6.17) and (6.16) it is seen that K_e is closer to 1 than K_{ext}. For $Q_u << Q_e \& Q_{\text{ext}}$, K_e is close to 1, and for $Q_u >> Q_e \& Q_{\text{ext}}$, $K_e \approx K_{\text{ext}}$. The error when using Q_e is smaller than when using Q_{ext}, but varying with Q_u. On the other hand, from (6.15) and (6.16) it is seen that K_{ext} is only dependent on R_e. If R_e is reasonably constant for the sensor

design, the error is constant and easily corrected. Because using Q_{ext} also gives the right peak width, Q_{ext} is preferable to Q_e.

The correction factor expressed in dB that should be added to a peak height value that has been calculated from (3.27a) using Q_{ext}, is given by (6.15) and (6.16):

$$\Delta A_r = -10 \cdot \log_{10}\left[\frac{1}{4}\left(R_e + 2 + \frac{1}{R_e}\right)\right] \tag{6.18}$$

Figure 6.19 shows the correction factor ΔA_r as a function of R_e. If the peak height has been calculated from (3.27a) using Q_{ext} and converted to dB, and e.g. $R_e = 2 \Rightarrow 0.51$ dB should be subtracted from the calculated peak height to get the right value.

Expressing the results from the simulations in the form of Q_{ext} is practical only if the ratio R_e is constant enough that the same correction factor can be used for all results. Studying the results shows that in a set of 76 simulations of probe coupling that was performed, R_e was in the range $1.30 < R_e < 2.01$, and the mean value was 1.63. In the last set of 42 simulations, where the probe dimensions were those chosen for the prototype, the values were in the range $1.41 < R_e < 1.97$, with a mean of 1.75. Eq. (6.18) gives ΔA_r = -0.074 dB for R_e = 1.30, ΔA_r = -0.23 dB for R_e = 1.7, and ΔA_r = -0.52 dB for R_e = 2.01. If ΔA_r = -0.3 dB is used, the maximum error will be 0.23 dB, which is small for all practical purposes.

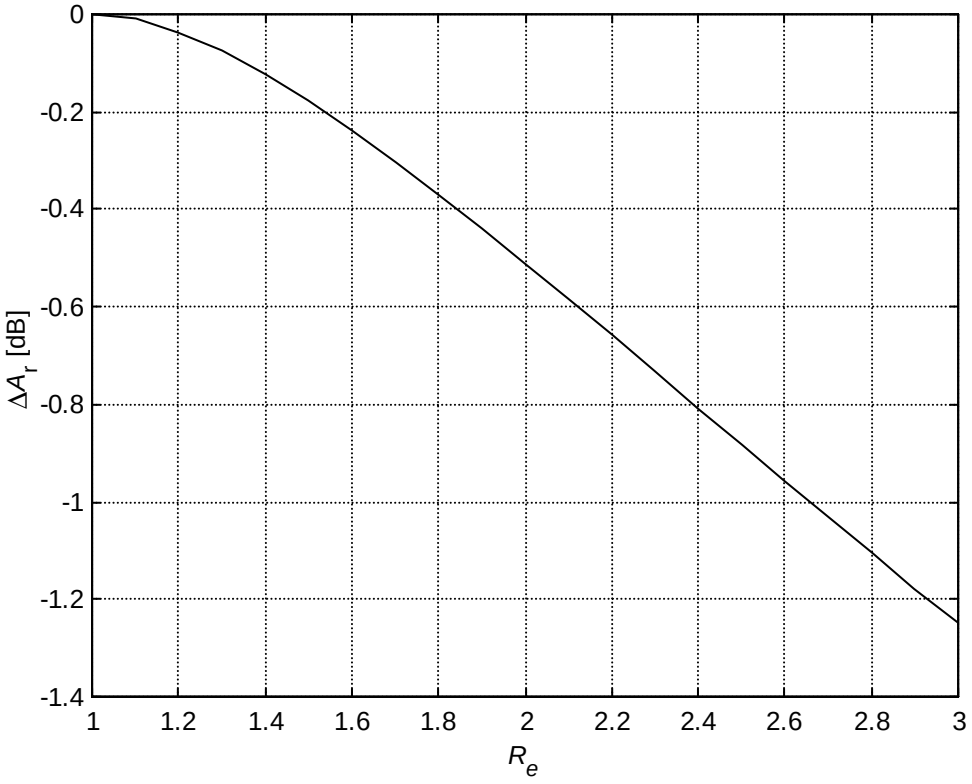

Figure 6.19 The correction factor ΔA_r as a function of R_e, as given by Eq. (6.18), i.e. the difference between the peak height predicted by Eq. (3.27b) and Eq. (3.27a), when $Q_{e1} \neq Q_{e2}$.

6.5.4 Simulation Results in Terms of Q_{ext} as a Function of the Shape of the Probes

Based on practical considerations and the results from the simulations of the effect of the shape of the fin, the CFR sensor for the simulations of the shape of the probes was chosen to have an inner diameter of 50.8 mm, and a fin that was 50 mm long and 25.4 mm high. The sensor model was 150 mm long and terminated with radiation surfaces. The metal parts were defined to be perfect conductors. When the sensor was filled with a lossless MUT, the radiation from the open ends gave the model sensor an unloaded quality factor of roughly $600< Q_u <1200$, depending on the permittivity of the MUT. High permittivity values correspond to low values of Q_u.

Because of the large number of variables that affect the coupling, it is in practice impossible to make simulations with a tight spacing of all possible combinations of values. Likewise it is difficult to present the results in such a way that the external quality factors could be readily obtained from one table or graph for any situation of interest. The goal with the simulations was therefore first to find a design that seemed to be at least acceptable for standard applications. Then a set of simulations was performed to find out the sensitivity of the coupling to variation of each parameter, so that some optimization could be performed. A summary of the results is given below.

The Intrusion of the Probes

The intrusion (l_p) of the probes is one of the most important factors that determine the strength of the coupling (Q_{ext}). To determine the sensitivity of the coupling to the intrusion, simulations were performed both for the rectangular resonator shown in Fig. 6.12, and for the CFR sensor. The results obtained for the rectangular resonator (criteria: $\Delta S < 0.005$, or maximum 8 iterations) are shown in Fig. 6.20. The relative change in Q_{ext} caused by a change in l_p (i.e. the slope of the graphs) is seen to be more or less independent of ε_{ri} and ε_{MUT} for all the plotted cases. The slope is also almost independent of l_p, except for a slight steepening for small values of l_p.

For the CFR sensor simulations were performed with probes of various diameters, with various dielectric materials in the probes, and with various properties of the MUT. The results are summerized in Figure 6.21. Also here the slope steepens for small values of l_p, but it also seems to steepen for high values of Q_{ext}, such that the slope is the same for a specific value of Q_{ext} for all simulated cases. No such dependence of the slope on Q_{ext} is seen in Fig. 6.20. This contradiction may be caused by the poorer accuracy of the simulations for the CFR sensor, because of fewer iterations performed by HFSS, but it may also be caused by the different dimensions of the probes.

The radiating properties of antennas in general are related to the size of the radiating structures measured in wavelengths. The coupling provided by a probe can therefore also be expected to be related to the size of the probe relative to the wavelength. Fig. 6.22 shows the results for both the rectangular resonator and the CFR sensor plotted with the intrusion given in wavelengths. The slope is indeed the same in both sets of simulations, except for the steepening of the slope for high Q_{ext} values for the CFR sensor. For practical sensor applications of measuring mixtures of oil and water the range $Q_{\text{ext}} < 1000$ is the most interesting. In this range the slope can

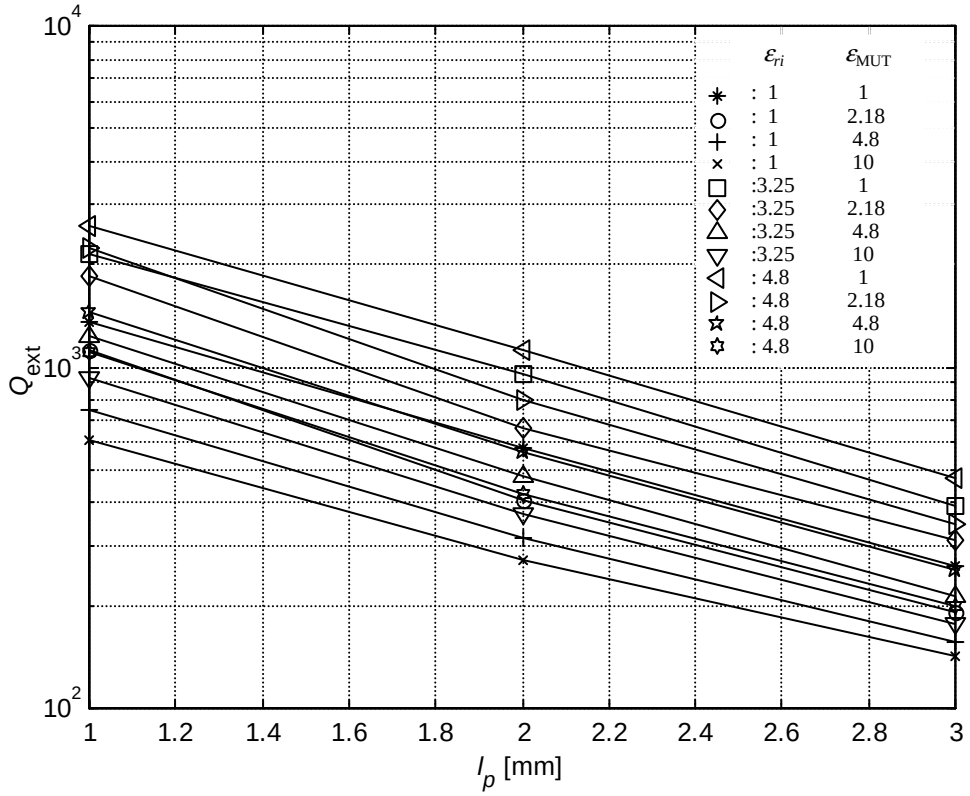

Figure 6.20 The dependence of the coupling on the intrusion of the probes in the rectangular resonator in Fig. 6.12. The graphs are based on the same simulation results as Fig. 6.13.

be considered to be constant, leading to a model for predicting the effect on Q_{ext} of changing l_p:

$$Q_{ext2} = Q_{ext1} \cdot 10^{-22.4(l_{p2}-l_{p1})/\lambda} \tag{6.19}$$

where λ is the wavelength of a plane wave in the MUT (which is constant in a completely filled resonator). The value of the constant (-22.4) was derived by manually fitting the model to the data in Fig.6.22.

A CFR sensor (D_p = 50.8 mm, d_p = 8 mm, d_i = 17.5 mm, ε_{ri} = 3.25) was measured with two sets of probes with different intrusion: l_{p1} = 6 mm and l_{p2} = 7.5 mm. The measurements were performed with the sensor filled both with air and diesel. The measured external quality factors were Q_{ext1} = 595.8 and Q_{ext2} = 351.6 in air, and Q_{ext1} = 623.9 and Q_{ext2} = 375.9 in diesel. The values are higher than the simulated (graph D in Fig. 6.21) of reasons that are not completely known but probably related to the poor convergence of the simulations, and the values in diesel are not lower than the values in air as predicted by the simulations. The latter effect is also seen in Fig. 6.15. The measurements give Q_{ext1}/Q_{ext2} = 1.69 in air, and Q_{ext1}/Q_{ext2} = 1.66 in diesel, while model (6.19) predicts Q_{ext1}/Q_{ext2} = 1.82. The difference of 7.7% or 9.6% respectively is satisfactory for practical purposes.

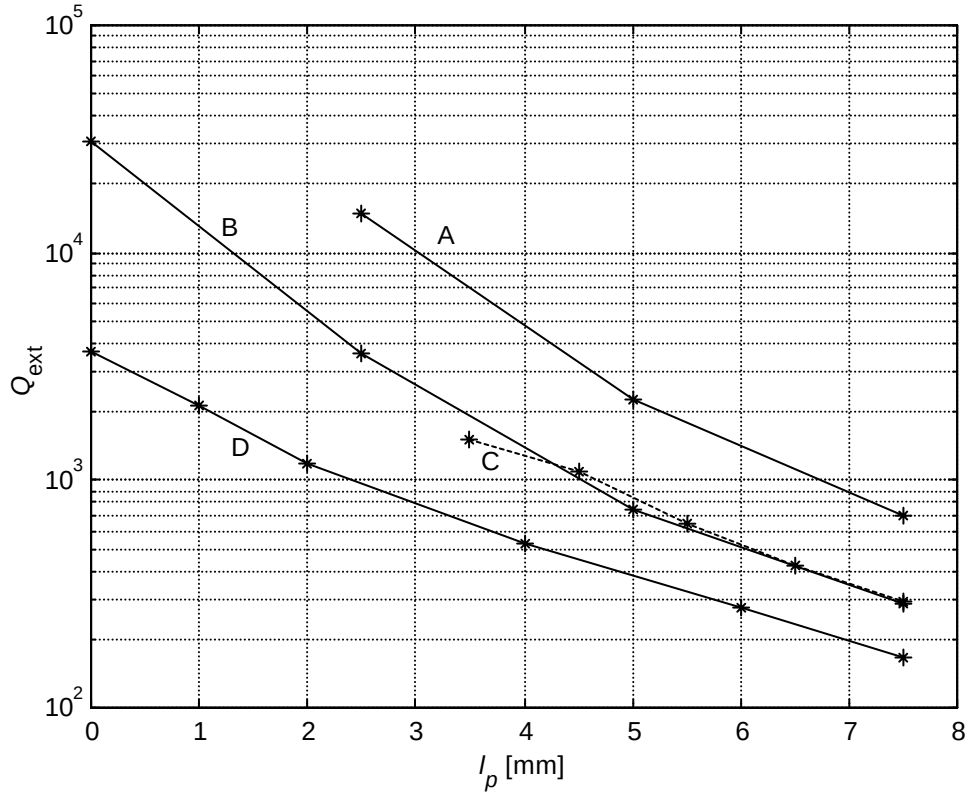

Figure 6.21 The external quality factor Q_{ext}, as defined in (6.14), of a CFR sensor as a function of the probe intrusion l_p. The data are the results of simulations with HFSS. A: d_p = 2 mm, d_i = 4.6 mm, ε_{ri} = 1, B: d_p = 4.34 mm, d_i = 10 mm, ε_{ri} = 1, C: d_p = 7.5 mm, d_i = 13.5 mm, ε_{ri} = 3.25 (=PEEK), and D: d_p = 8 mm, d_i = 17.5 mm, ε_{ri} = 3.25, ε_{MUT} = 2.18, $\tan(\delta_{MUT})$ = 0.0096 (MUT = diesel fuel).

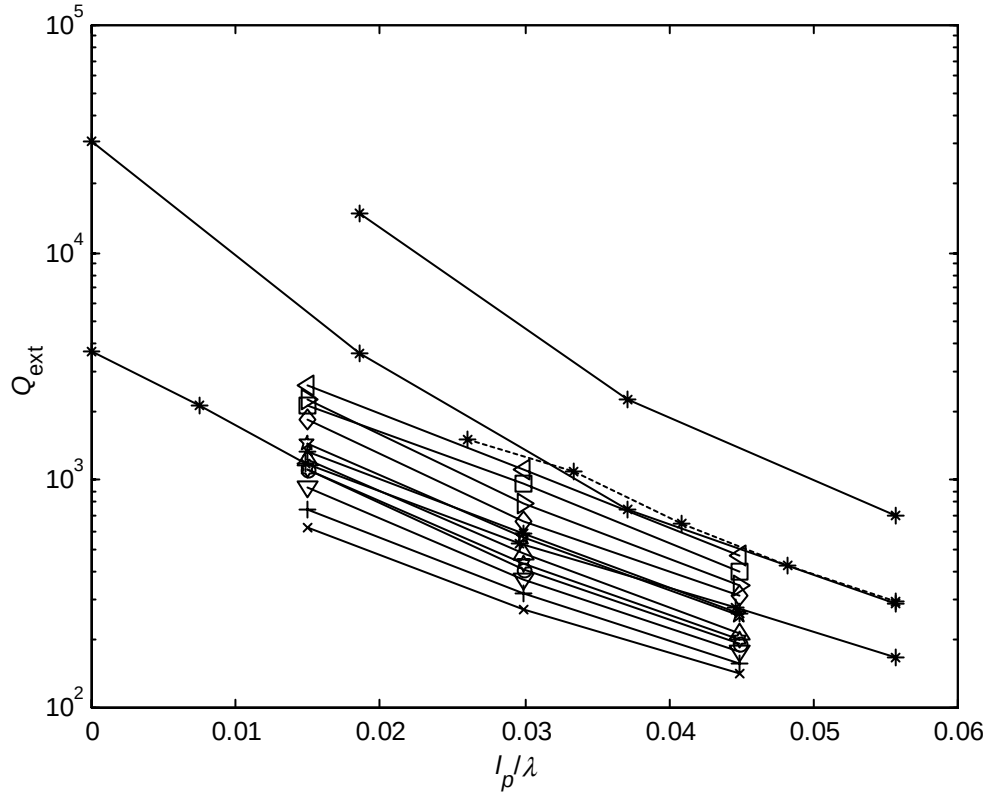

Figure 6.22 The data from Figs. 6.20 and 6.21 combined, with l_p given in wavelengths.

The Permittivity of the Dielectric Material in the Probes (ε_{ri})

The permittivity of the dielectric in the probes (ε_{ri}) affects the coupling of the same reasons as the permittivity of the MUT (see Sec. 6.5.1). This effect can be seen in Fig. 6.13, which shows the simulation results for the rectangular resonator shown in Fig. 6.12. A series of simulations was also performed for the CFR sensor with the purpose of finding out how the choice of the dielectric material affects the coupling. The results for both the rectangular resonator and the CFR sensor are summarized in Fig. 6.23, which shows that the local slope of the graphs is the same for both resonators, but the slope changes with ε_{ri}.

The most interesting materials for the sensors, which are made by Roxar, are PEEK with $\varepsilon_{ri} = 3.25$, and a ceramic reinforced glass with $\varepsilon_{ri} = 4.8$. Figure 6.24 shows the ratio of the simulation results for Q_{ext} for these two cases based on the data shown in Fig. 6.23. No systematic dependence on ε_{MUT}, l_p, or resonator type can be seen. The arithmetic mean of the data points in Fig. 6.24 is $Q_{\text{ext}}(4.8)/Q_{\text{ext}}(3.25) = 1.1824$, which can be used as a model. If other materials are used, an estimate of the effect on the coupling of the choice of material can be derived from Fig. 6.23.

The permittivity of the MUT and the dielectric in the probes can be expected to affect the coupling mainly because of the effect the contrast in permittivity has on the fringing field. This is confirmed by the data for the rectangular resonator in Figs. 6.13 and 6.23, which show that e.g. the cases with $\varepsilon_{ri} = 1$ & $\varepsilon_{\text{MUT}} = 1$, and $\varepsilon_{ri} = 4.8$ & $\varepsilon_{\text{MUT}} = 4.8$, have roughly the same Q_{ext}. Fig. 6.23 shows a larger deviation between

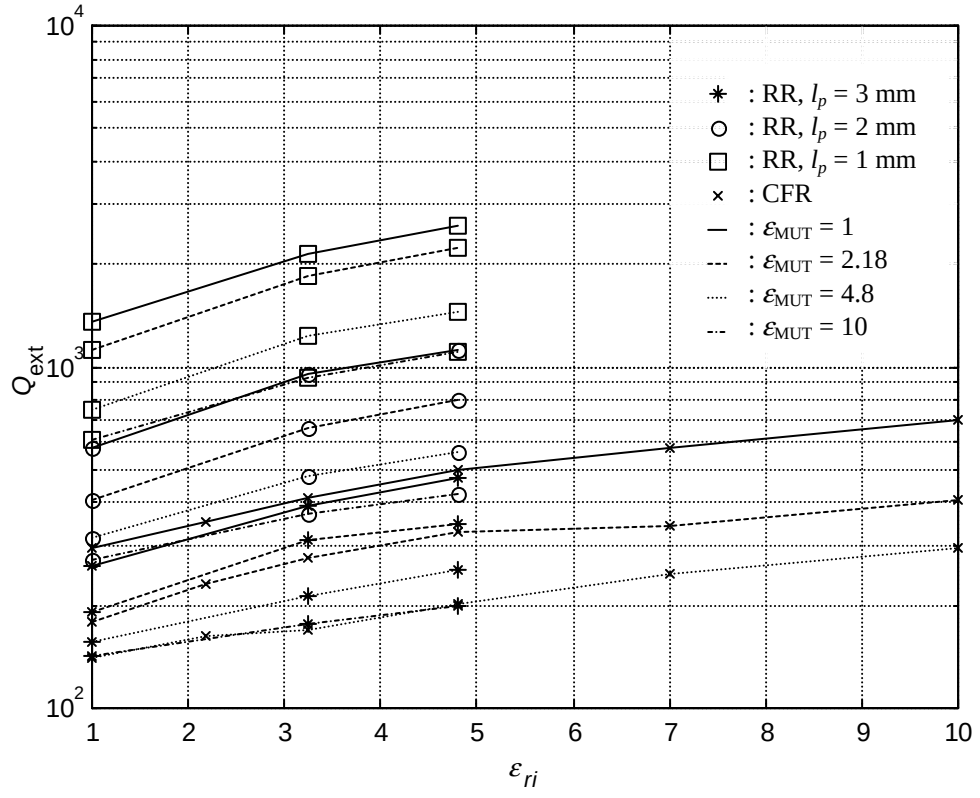

Figure 6.23 The external quality factor as a function of the permittivity of the dielectric in the probes. The graphs are simulation results for the rectangular resonator (RR) shown in Fig. 6.12, and the CFR sensor ($D_p = 50.8$ mm, $d_p = 8$ mm, $d_i = 17.5$ mm, $l_p = 6$ mm).

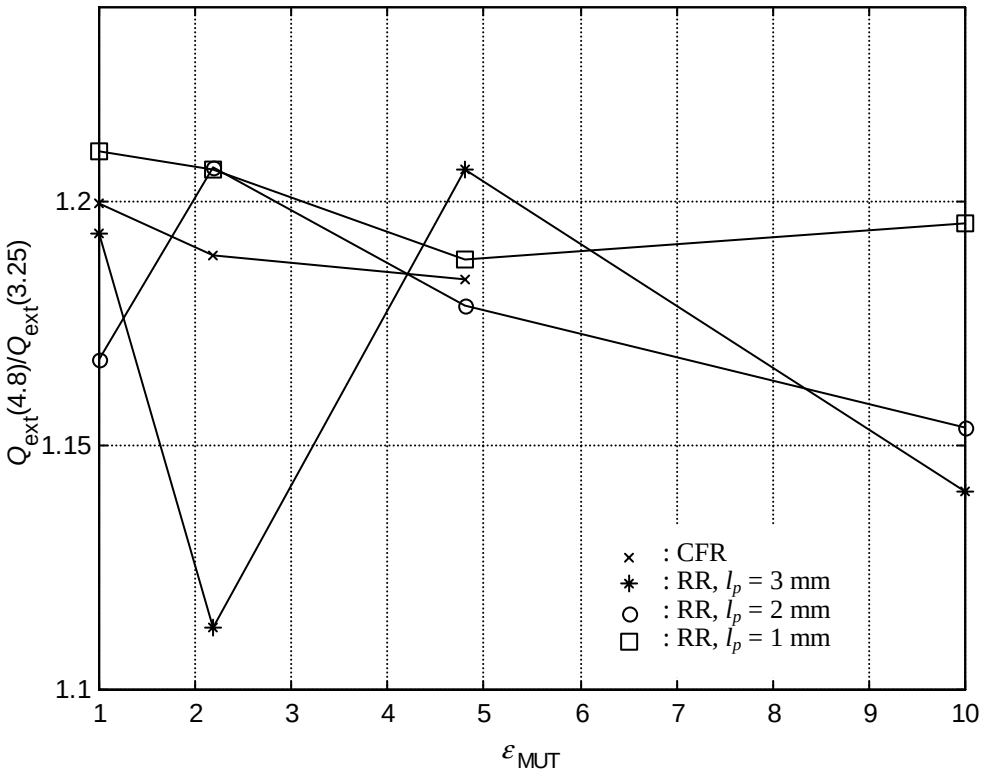

Figure 6.24 The ratio of the external quality factor of sensors with ε_{ri} = 4.8 to sensors with ε_{ri} = 3.25. The graphs are based on the same data as Fig. 6.23.

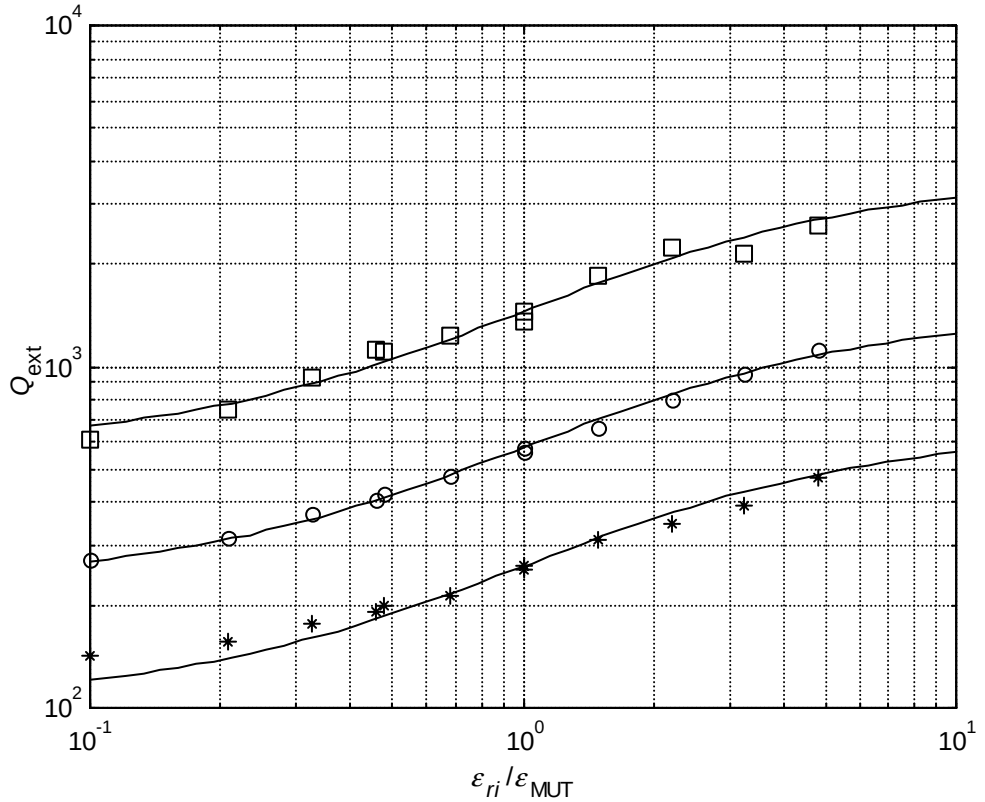

Figure 6.25 The coupling as a function of the ratio of the permittivities of the dielectric material in the probes and the MUT. For an explanation of the symbols, see Fig. 6.24.

these cases for the CFR sensor, but this is probably caused by poorer accuracy. Fig. 6.25 shows the simulation data for the rectangular resonator plotted as a function of the ratio

$$r_\varepsilon = \frac{\varepsilon_{ri}}{\varepsilon_{\mathrm{MUT}}} \tag{6.20}$$

The figure shows that all data points for a specific value of l_p fall roughly on the same curve. The model that has been fitted to the points in the figure is

$$Q_{\mathrm{ext}} = Q_{\mathrm{ext1}} \cdot 10^{A \cdot \tanh\left(B \cdot \lg r_\varepsilon\right)} \tag{6.21}$$

where A = 0.4, B = 1.2, and Q_{ext1} is the value of Q_{ext} for r_ε = 1. The points deviate from the model significantly only for the smallest values of Q_{ext}.

The Probe Diameters

Both the diameter of the centre pin (d_p) and the diameter of the dielectric (d_i) affect the coupling. Some examples of the effect of various diameters is seen in Fig. 6.21, which shows the simulation data for the CFR sensor, but to get a better means to predict the effect of the choice of the diameters, simulations were performed with the rectangular resonator in Fig. 6.12, with l_p = 3 mm, ε_{ri} = 3.25, $\varepsilon_{\mathrm{MUT}}$ = 1, d_p = 2, 3, and 4 mm, and d_p/d_i = 0.4, 0.5, and 0.67. The results are shown in Fig. 6.26. Again the graphs are almost straight lines, so that a simple model can be used in practice:

$$Q_{\mathrm{ext}2} = Q_{\mathrm{ext1}} \left(\frac{d_{p2}}{d_{p1}} \right)^{-1.8} \cdot 10^{+1.5\left(r_{d2} - r_{d1}\right)} \tag{6.22a}$$

where

$$r_d = \frac{d_p}{d_i} \tag{6.22b}$$

The error of the model is expected to grow outside the range shown in Fig. 6.26. If the same data is plotted against d_i, it appears that the diameter of the dielectric strongly affects the coupling, while the diameter of the centre pin has no influence. This is probably approximately true only for the narrow range of aspect ratios used in the simulations, because from practice it is known not to be generally true. Because both thin and long probes, and short and wide probes are of interest in various applications, a new series of simulations was performed for a larger range of d_p/d_i, and for other aspect ratios of the probes (l_p/d_i = 0.1, 0.5, and 2.0), varying the diameter of the centre pin. The results are shown in Fig. 6.27. They confirm that there is an intermediate range, where the coupling is not sensitive to the diameter of the centre pin, but they also confirm the practical experience that very thin pins provide less coupling than

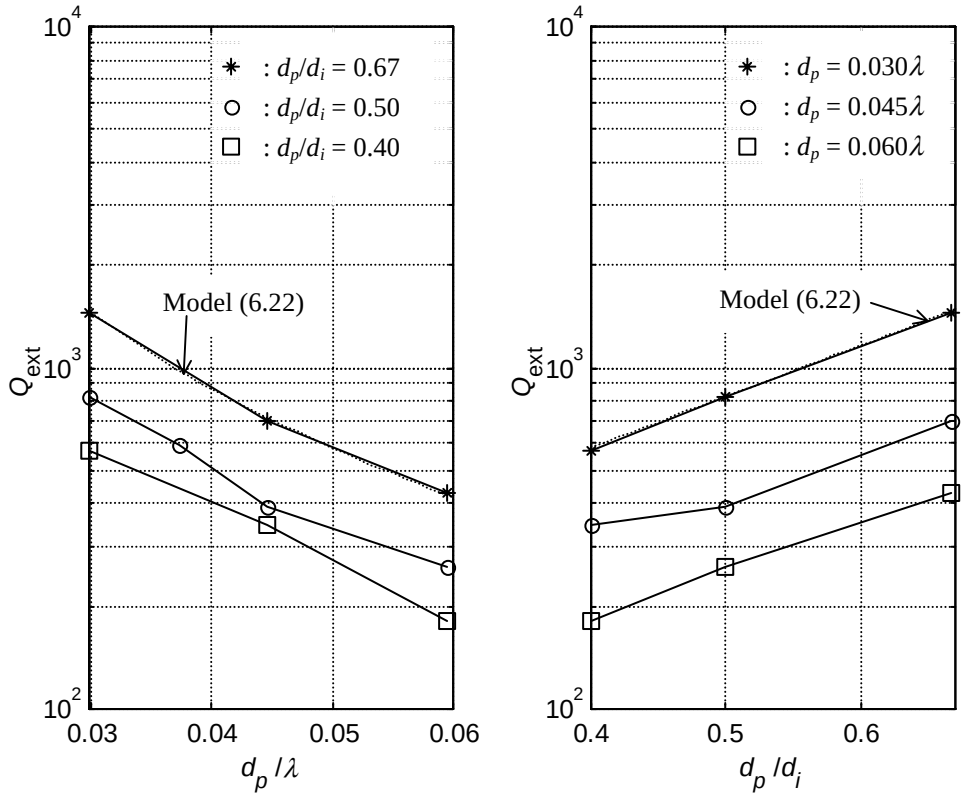

Figure 6.26 The dependence of the coupling on the diameter of the centre pin and the dielectric in the probes. The data are results of simulations with HFSS of the rectangular resonator in Fig. 6.12, with l_p = 3 mm.

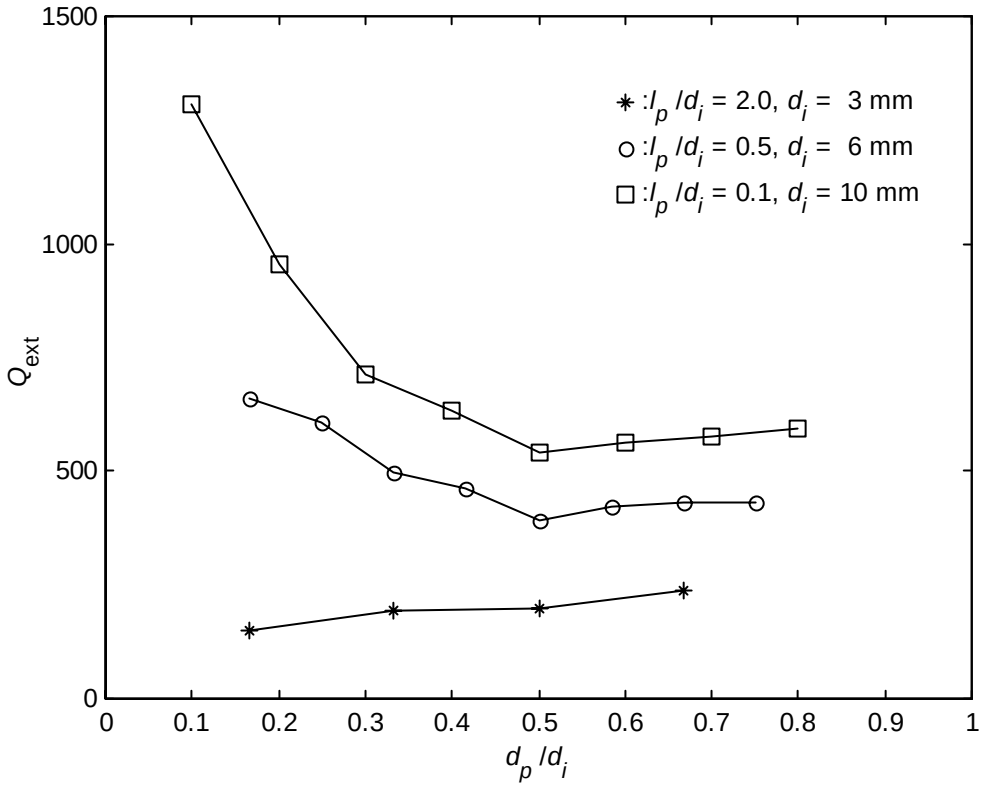

Figure 6.27 The coupling as a function of the diameter of the centre pin for probes of various aspect ratios. The data are the result of simulations of the rectangular resonator in Fig 6.12.

slightly thicker ones, and the intuitive conclusion that the same applies to a narrow gap around the centre pin. An exception is the long and thin probe, which seems to provide more coupling the narrower it is. Based on experience the author would regard this result as dubious, possibly caused by poor accuracy of the simulations as a result of the small dimensions ($d_p \geq 0.5$ mm).

If models (6.19) and (6.22) are used to predict the simulation results for the long ($l_p/d_i = 2$) and the short ($l_p/d_i = 0.1$) probes from the probes with $l_p/d_i = 0.5$, the models tend to underestimate Q_{ext} for the long probes, and overestimate for the short probes. Care should therefore be taken, when using the models to estimate the coupling provided by probes with extreme aspect ratios.

The results have also been influenced by impedance mismatch, because in most of the cases the impedance of the probes differs from 50Ω, but this is also the case in practice. With the used permittivity for the dielectric ($\varepsilon_{ri} = 3.25$), the impedance is 50Ω, when $d_p/d_i = 0.222$. As a consequence, however, the coupling is also influenced by the length of the section inside the probe, with an impedance other than 50Ω. In practice this section is kept as short as possible to avoid ripple in the frequency response. In the simulated model this section was 11.9 mm long, which is within practical limits.

It can be concluded that the intrusion of the centre pin and the diameter of the dielectric are the design parameters that have the largest influence on the coupling. For a fixed diameter of the dielectric, a centre pin with a diameter that is roughly half of the diameter of the dielectric seems to give the optimal coupling.

6.5.5 Conclusions

The influence on the height of the resonance peak, i.e. the maximum of the power transmission coefficient, of the various design parameters of the probes of a CFR resonator sensor have been studied both by simulation using HFSS, and by measurement of prototypes. Especially the intrusion, the diameter of the centre pin and the dielectric, and the permittivity of the dielectric have been studied. Based on the results it is recommended that the probes of a 2" sensor have the following properties: $d_p = 8$ mm, $d_i = 17.5$ mm, $l_p = 7.5$ mm, and $\varepsilon_{ri} = 3.25\ldots4.8$. For sensors of other sizes the dimensions of the probes should be directly scaled.

The whole frequency response was simulated for a sensor with the pipe diameter $D_p = 50.8$ mm, length of fin $L = 50$ mm, height of fin $h = 25.4$ mm, $d_p = 8$ mm, $d_i = 17.5$ mm, $l_p = 7.5$ mm, and $\varepsilon_{ri} = 3.25$. The metal parts were assumed to be perfect conductors. Simulations were performed both for an empty sensor and a sensor filled with diesel fuel ($\varepsilon_r' = 2.18$, $\tan\delta = 0.0096$). The empty sensor was also simulated with $l_p = 6$ mm. The results are shown in Fig. 6.28.

A sensor with the same dimensions as the simulated sensor was built and measured in the laboratory. Two sets of probes were made, with $l_p = 6$ mm and 7.5 mm respectively. The measured frequency responses of the sensor filled with diesel is shown in Fig. 6.29.

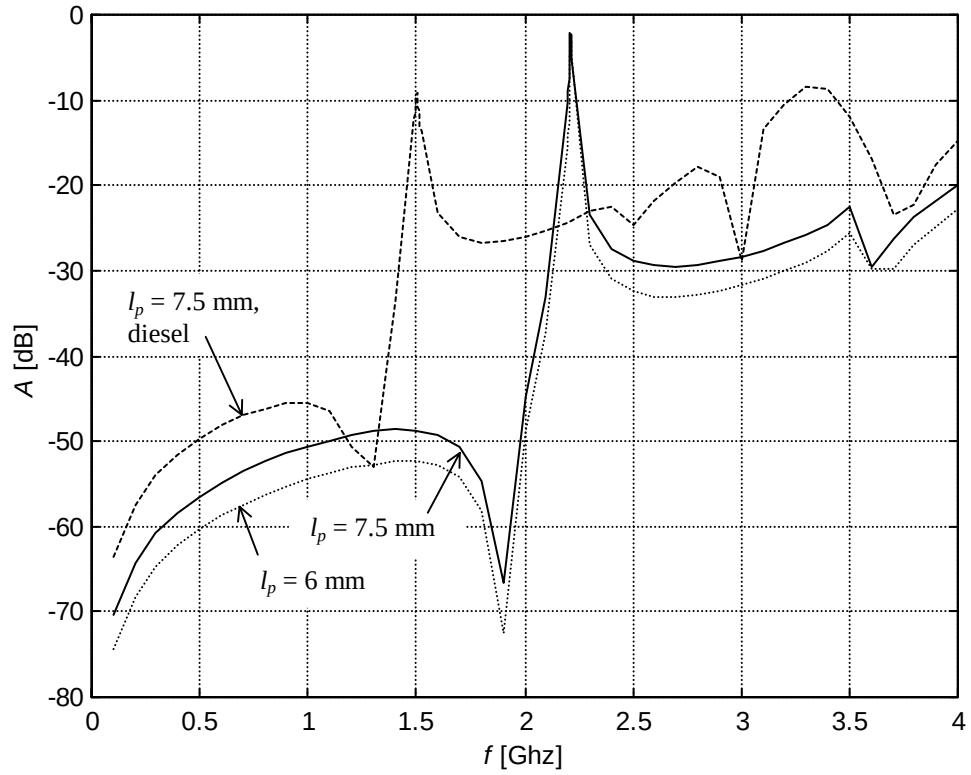

Figure 6.28 The simulated frequency response of a CFR sensor filled with diesel or air. See the text for details.

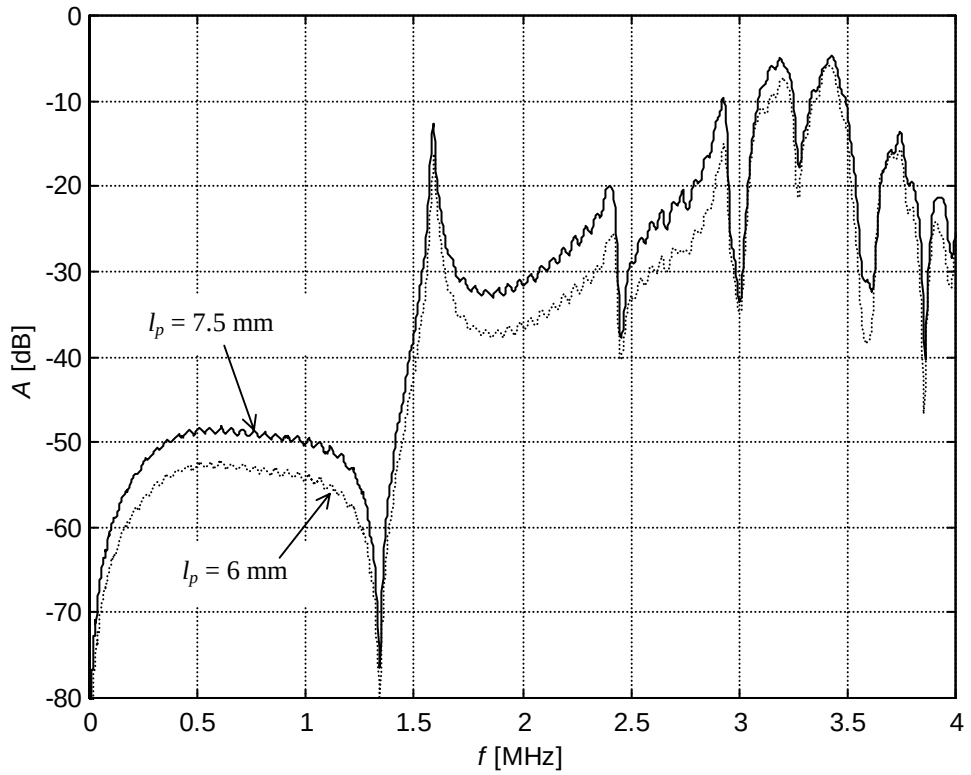

Figure 6.29 The measured frequency response of the CFR sensor prototype filled with diesel. See the text for details.

6.6 The Length of the Sensor

A CFR sensor will have flanges at the ends and be installed as a part of the process pipe. In practice there is then the possibility that the inner diameter of the process pipe is slightly different from that of the sensor pipe, e.g. because of corrosion, different pressure ratings, or the tolerances. In some instances it may even be desirable to mount e.g. a 2” sensor on a 3” process pipe, or vice versa. Because the inner diameter is the most important factor determining the resonant frequency of a CFR sensor, and the fringing field extends a distance outside the ends of the fin, the different diameter of the process pipe can be expected affect the resonant frequency, if the distance from the end of the fin to the start of the process pipe is short..

6.6.1 The Effect on the Resonant Frequency of a Process Pipe with a Different Diameter than the Sensor Pipe

To investigate the effect on the resonant frequency of a difference in the diameter of the process and the sensor pipes, a series of measurements were made. A CFR sensor with an inner diameter of 52.5 mm, and a 50 mm long fin that extended to the centre line of the pipe, was used. The sensor body was 60 mm long, i.e. the sensor pipe extended only 5 mm outside the ends of the fin. The resonant frequency of the empty sensor was f_{r0} = 2198.4 MHz, when mounted on a process pipe with the same inner diameter.

In the first test flanged sections of pipe were mounted on both ends of the sensor. The pipe sections were 100 mm long, i.e. long enough to be practically nonradiating and therefore appear infinitely long. The inner diameter of the pipe sections was 53.8 mm, i.e. the radius was 0.65 mm larger than in the sensor. When the pipe sections were mounted concentrically with the sensor, the resonant frequency was 2.3 MHz lower than f_{r0}. When the pipe sections were mounted 0.65 mm off-centred such that the pipe wall was continuous (without a step in radius) on one side, and with a 1.3 mm step on the opposite side, the resonant frequency varied in the range 0.88…3.66 MHz lower than f_{r0}. The resonant frequency was highest, when the step was on the side opposite to the fin, and lowest, when the step was on the side of the attachment of the fin.

Larger changes in diameter were tested next. The results of the measurements are shown in Figure 6.30. First one of the pipe sections was replaced by another section, with an inner diameter of 77 mm (length = 195 mm). A varying number of 5 mm thick rings, with a hole equal to the inner diameter of the sensor pipe, were inserted between the sensor and the pipe section so that the distance from the fin to the location of the change in diameter, i.e. the length of the sensor, varied. The resonant frequency was recorded as a function of the distance to the change of diameter in the range 5 mm to 55 mm, in steps of 5 mm. The measurements were then repeated with another pipe section, with an inner diameter of 41.3 mm. Finally the pipe sections on both sides of the sensor were replaced by sections, with an inner diameter of 77 mm, and an equal number of rings were inserted on both sides between the sensor and the pipe sections.

From the results in Fig.6.30 one can conclude that an increase in diameter causes a reduction in the resonant frequency, while a reduction in diameter causes an increase in the resonant frequency. When similar changes in diameter occur on both

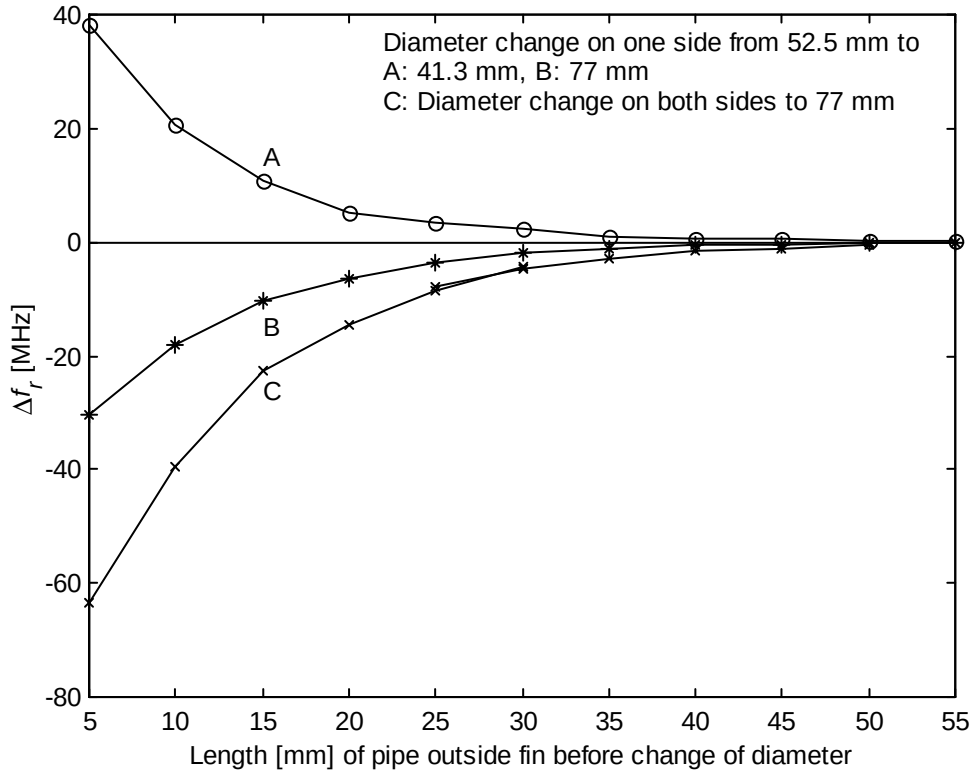

Figure 6.30 The measured change in resonant frequency, when a CFR sensor of varying length is mounted on a process pipe, with a diameter different from that of the sensor pipe.

sides of the sensor, the change in the resonant frequency is twise that of a change of diameter on just one side of the sensor. The maximum effect that was measured was 2.9% of the frequency of the empty sensor (change to 77 mm on both sides of the sensor at a distance of 5 mm). One can also conclude that when the distance from the end of the fin to the start of the process pipe is larger than roughly 50 mm (≈ 1 inner diameter), the diameter of the process pipe does not affect the resonant frequency.

The measurements were made with a Hewlett Packard 8753D network analyzer. The frequency response was first measured up to 4 GHz and then zoomed in on the resonance peak and Q_l automatically displayed. The quality factor stayed unchanged during the measurements, indicating that radiation from the pipe sections was very low and did not affect the measurements. The frequency response was essentially uninfluenced by the sections of larger or smaller diameter, with the exception of a low extra peak that emerged at roughly 2.4 GHz, with the 77 mm sections and a distance of 5…15 mm from the fin to the process pipe. This extra peak was most probably the TE_{111} resonance in the 77 mm pipe sections. This peak was always much lower than the $TE_{½10}$ peak and would not complicate the use of the sensor, regardless of the used measurement method.

6.6.2 The Effect of Nonconducting Gaskets

In conjunction with the measurements that were described in Sec. 6.6.1, measurements were also made with electrically nonconducting fibre gaskets inserted at various locations between the sensor, rings, and pipe sections. The insertion of the

gaskets had no detectable effect on the frequency response, independent of the location of the gaskets. A CFR sensor can therefore be made at least as short as the one used in the measurements (1.2 inner diameters), without that special requirements have to be put on the quality of the gaskets.

6.6.3 Radiation as a Function of the Length of the Sensor

If a CFR sensor is to be used without being mounted on a pipe, and for testing and calibration purposes in the laboratory, low radiation from the ends of the sensor is important. This matter was theoretically discussed in Sec. 4.2.1.

In conjunction with the measurements that were described in Secs. 6.6.1 and 6.6.2, the sensor was also measured without the other pipe section, i.e. with just the rings at one end. From these data Q_u was calculated using (3.32), assuming $R_e = 1.75$. From the measurements with the 77 mm pipe sections and the maximum number of rings the metal quality factor was calculated using (3.33) (assuming $Q_{\text{rad}} = \infty$), which gave $Q_m = 652.2$. Then Q_{rad} was calculated from (3.13) (assuming $Q_d = \infty$) for the measurements without the other pipe section. The obtained values for Q_{rad} were then divided by 2 to correspond to a sensor that radiates equally from both ends. The results are shown in Figure 6.31, which also shows simulations made with HFSS, and

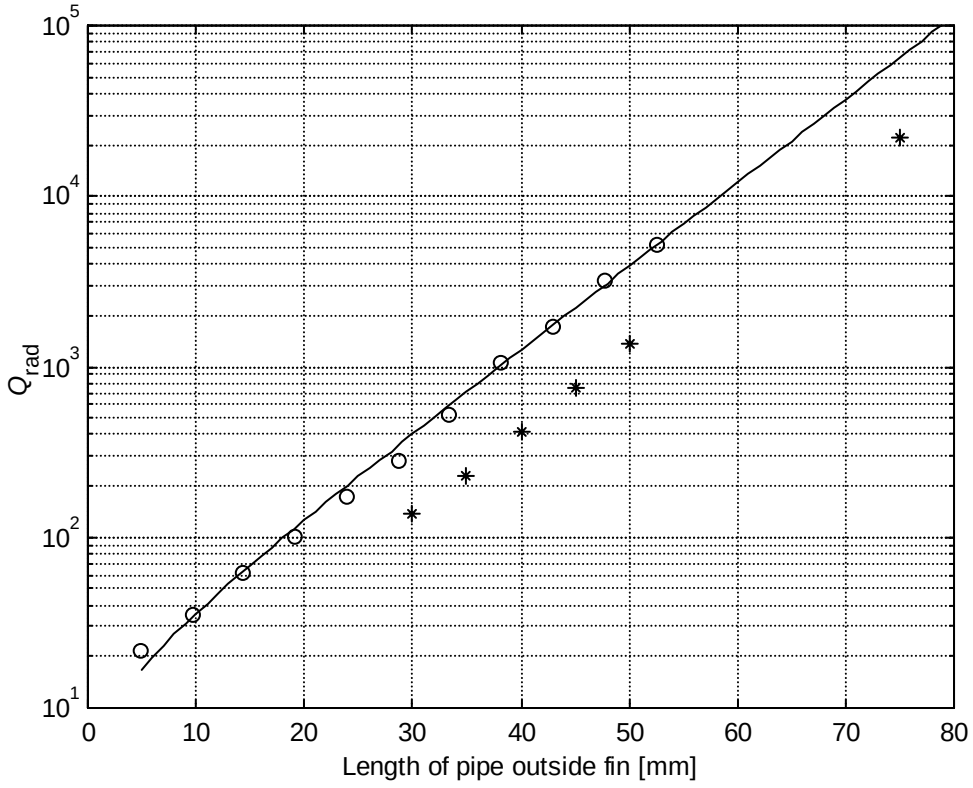

Figure 6.31 The radiation quality factor Q_{rad} of a CFR sensor with an inner diameter of 50 mm. The rings are measurements, the asterisks are simulations with HFSS, and the graph is calculated from Eq. (4.10) assuming $Q_{\text{rad0}} = 28$. The calculations fit the simulated data assuming $Q_{\text{rad0}} = 9.4$.

calculations based on Eq. (4.10). Equation (4.10) contains the unknown factor Q_{rad0}. The fit between the calculations and the measurements that is shown in Fig 6.31 was obtained for $Q_{rad0} = 28$. To fit the simulations $Q_{rad0} = 9.4$ had to be assumed. The fact that a lower value of Q_{rad0} fits the simulated data than the measured data is probably partly explained by the fact that the model in the simulations was terminated by radiation surfaces (i.e. absorbing boundary conditions), which do not reflect anything, whereas an open waveguide end has a finite reflection coefficient. In practice it has been observed that an absorbing body located at the open end of a sensor affects the loaded quality factor and peak height (see Sec. 6.6.4). The lower value of Q_{rad0} in the simulations is probably partly explained also by poor convergence of the simulations. It has been observed that the peak gets narrower, and consequentially the quality factors increase, when a larger number of iterations is used in HFSS to improve the accuracy. Note that the slope is the same in all data, which confirms the validity of Eq. (4.10).

6.6.4 The Distance to Resonating or Absorbing Structures in the Pipe

Above it was concluded that the size of the process pipe has no influence on the resonant frequency, when the distance from the fin to the start of the process pipe is at least $1D_p$. However, resonating or absorbing structures may have some effect on the quality factor even at the distance of $1D_p$. This was realized, when a thermowell was mounted on a 2" CFR sensor so that the distance from the nearest point of the thermowell to the fin was $1D_p$. While the thermowell was being screwed in place, the resonance peak was at times slightly distorted ($\Delta f < 0.2\%$, $\Delta A <$ a few dB). When the thermowell was tightened, the interference disappeared and the resonant frequency was exactly the same as before the thermowell was mounted. The thermowell probably came into resonance close to the resonant frequency of the sensor for some conditions of imperfect shorting through the threads.

A similar effect was experienced, when two CFR sensors (of different length) were mounted together such that the distance between the nearest points of the fins was $1.1D_p$. A clear coupling between the resonance modes of the two sensors was noted. Because the resonant frequencies were slightly different, the peaks appeared to be double. When the sensors were turned so that the fins became orthogonal, the fields also became orthogonal, and the interference disappeared.

When the 24" sensor with a slanting fin end that was described in Sec. 6.4.3 was measured with open ends in the laboratory, the peak height was notably sensitive to an absorbing object held close to the open end. For example a persons leg caused a change of the peak height of a few dB, while the resonant frequency was unaffected.

Based on earlier experience the results reported in this Section were not totally unexpected, but may be difficult to deduce theoretically.

6.6.5 Conclusions

Because the frequency response was good in all the measured cases and the gaskets had no effect on the performance of the sensor, it can be concluded that a CFR sensor can be made at least as short as the sensor that was used in the measurements described in Secs. 6.6.1 and 6.6.2 ($1.2D_p$), even if the diameter of the process pipe

differs from that of the sensor pipe. The resonant frequency was, however, influenced by the diameter of the process pipe and the precision of mounting, when the sensor was short. A short sensor must therefore be calibrated on the site after installation, and recalibrated after each time it has been demounted e.g. for the purpose of service. Alternatively restrictions can be put on the diameter of the process pipe and the precision of mounting, depending on the specified accuracy requirements for the application.

If the length of the sensor pipe outside the fin is made at least equal to $1D_p$, the process pipe has no effect on the operation of the sensor and $Q_{\text{rad}} \approx 4000$, at least for sensors with straight fin edges. It can then be calibrated before shipment and needs no further calibration after installation. On the other hand a long sensor is more expensive to produce and bulkier and heavier to handle during manufacturing and calibration, but is easier to test and calibrate in the laboratory, because it requires no extra end pieces to limit the radiation.

Short sensors (e.g. *length of fin* = $1D_p$, *length of sensor* = $1.2D_p$) seem to be the right solution for applications, where the required accuracy is low and the price of the meter is important, whereas long sensors (e.g. *length of fin* = $1D_p$, *length of sensor* = $3D_p$) should be used in other cases.

6.7 Sensitivity to Contamination

In many applications of microwave resonator sensors some kind of contamination may occur. For example, when the humidity sensor that is described in Ch. 7 is used in a veneer dryer, vaporized resin may condence on the walls and mix with dust to form a layer on the walls of the sensor. In the petroleum industry scale (mainly calcium carbonate or barium sulphate) or wax may sometimes grow on the walls of the pipes, including the sensors. In such cases the sensor should preferably be as little sensitive to the contamination as possible. If thick layers of contamination build up, any sensor will be affected. The question of minimizing the sensitivity to contamination is a question of maximizing the cleaning interval.

In a microwave resonator sensor the electric field is affected by the permittivity of the material in the sensor. The sensitivity distribution is therefore identical to the distribution of the electric field. The TE_{011} mode (see Sec. 3.7.1) that is used in the humidity sensor (Ch. 7) has zero electric field on all walls. This feature makes it extra well suited for use where contamination may occur. The TM_{010} mode (see Sec. 3.7.2) that is used in the so-called end grid sensor (Ch. 7) also has zero electric field on the cylindrical walls, but the electric field lines terminate on the flat ends. In the end grid sensor the flat ends have been replaced by grids to allow the flow to pass. The exact design of the grids may vary between sensors (see Ch. 7), because different features (e.g. short grids, loose grids, clean frequency response, ease of production) have been given priority, but the grids are always designed to give minimum blockage. They will therefore be composed of structures resembling knife blades across the pipe. The electric field lines terminate on the edges of these blades, where ”hot spots” are created. These sensors are therefore sensitive to contamination on the end grids, but less sensitive to contamination on the walls. In the CFR sensor the electric field lines emanate from the fin and terminate on the wall. The maximum sensitivity is in the centre of the sensor, with a ”hot spot” on the edge of the fin. The

CFR sensor is therefore sensitive to contamination on the fin, but also to some degree to contamination on the wall.

6.7.1 The Relative Sensitivity to Contamination of a CFR Sensor and an End Grid Sensor

The relative sensitivity to contamination of the end grid sensor and the CFR sensor is of particular interest. Comparison is, however, made difficult because the contamination is unlikely to form a uniform layer on all structures. Will there for example be more build up on the walls or on the fin or the grid structures? It seems unlikely that contamination will build up on the edge of the fin, but what about the trailing edges of the grid structures? To get at least an indication of the relative sensitivity a test was made with two sensors. One was a 2” end grid sensor, with end grids designed as simple crosses. The other was a 2” CFR sensor. Both sensors were first filled with motor oil. The sensors were then emptied and the resonant frequency was measured with a network analyzer as a function of time, while the oil slowly ran down the structures. The test was performed with the sensors first in a vertical position and then repeated with the sensors in a horizontal position. The CFR sensor was tested twice in the horizontal position, once with the fin standing upright, and once with the fin hanging down from the top. The test with the sensors in a vertical position was also performed with an emulsion containing 35% water (by weight). The emulsion has a higher permittivity and a lower viscosity than pure motor oil, and therefore had a larger effect that lasted longer. The results are shown in Fig. 6.32.

The Test Results

The results with the sensors in a horizontal position show that the CFR sensor is sensitive to drops hanging from the edge of the fin, when the fin hangs from the top. The steps in the graphs were caused by drops first accumulating on the edge of the fin and then falling off. With the fin standing upright, the CFR sensor is first less affected but eventually shows a larger effect than the end cross sensor. The larger effect in the end is caused by the larger sensitivity to contamination on the walls, in this case particularly the oil accumulating on the lower side of the sensor.

The tests with the sensors in a vertical position show a larger effect in the end cross sensor than in the CFR sensor. The steps in the graph for the end cross sensor are caused by drops accumulating on and falling off the edges of the upper end cross. The graph for the CFR sensor also displays some small steps. They are caused by drops hanging from the end of the fin, where the sensitivity is lower than on the axial edge of the fin. Clearly the sensitivity to contamination on the edges of the crosses in the end cross sensor caused a larger effect in this test than the sensitivity to contamination on the wall in the CFR sensor.

6.7.2 Conclusions

The tests confirm that the end cross sensor is sensitive to contamination on the end crosses but not on the wall, whereas the CFR sensor is sensitive on the edge of the fin

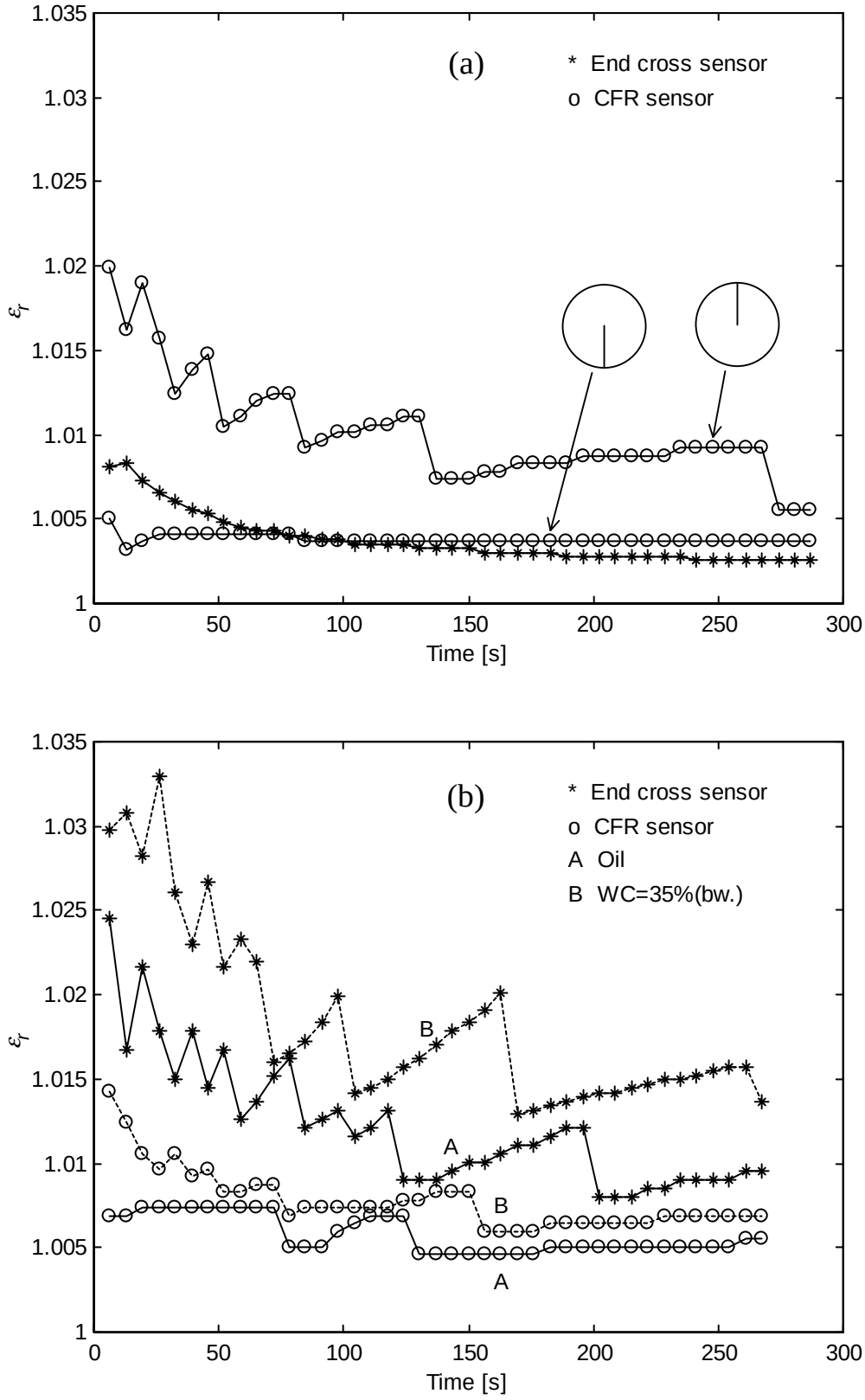

Figure 6.32 Measurements illustrating the relative sensitivity to a layer of contamination that is coating the metal parts of a sensor. The sensors were first filled with motor oil, and after they were emptied, the resonant frequency was measured with a network analyzer as a function of time. The sensors were held in a horizontal (a) and vertical (b) position. ε_r is the effective permittivity: $\varepsilon_r = (f_{r0}/f_r)^2$.

and also to some degree on the wall. Which sensor is less affected in practice depends on where the contamination builds up in the specific application. Intuitively it seems more likely that the contamination builds up on the trailing edges of the end grids, which are perpendicular to the flow, than on the axial edge of the fin, which is parallel to the flow. It is, however, uncertain how well the tests reflect the relative importance of contamination on the walls and the edges. There seem therefore not to be a clear answer to the question, which type of sensor is less sensitive to contamination.

The error in e.g. the deduced watercut that is caused by contamination depends on the relative permittivity of the contamination and the MUT. If the permittivities are equal, the error is zero. If the permittivity of the contamination is higher than the permittivity of the MUT, the watercut will be too high, and in the opposite situation, too low.

6.8 Sensitivity to Corrosion and Erosion

If the dimensions of a sensor change as a consequence of corrosion or erosion, the resonant frequency will also change. If the sensor is not recalibrated, the deduced results (e.g. watercut) will be in error. It is impossible to know exactly how the dimensions would change in practice, but an indication of the relative sensitivity to such changes of dimensions in a CFR sensor and an end cross sensor can be gained by assuming that all metal surfaces are eroded/corroded equally.

The sensitivity can be calculated from the results reported in Sec. 6.4. Here a 2” CFR, with a fin thickness of t = 3 mm, will be studied as an example. If it is assumed that all metal surfaces are eroded/corroded by 0.5 mm, the diameter will increase by 1mm. Eq. (6.4) then gives that the change of the resonant frequency is Δf_D = –2%. From Fig. 6.4, a reduction of the fin height by 0.5 mm causes an increase of the frequency of Δf_h = 1.65%. From Fig. (6.8), a reduction in the fin thickness from 3 mm to 2 mm causes an increase of the frequency of Δf_t = 0.8%. The sum of theses effects gives: Δf_{CFR} = 0.45%. In an end cross sensor only the change in diameter causes a change in frequency, hence Δf_{EC} = –2%. It is known that a 1% absolute change in the watercut causes roughly a –1.5% change in the frequency. In the above studied example the errors in the deduced watercut for the two sensors would therefore be: $\Delta WC_{\mathrm{CFR}} = -0.3\%_{wc}$ ($\%_{wc}$ stands for 1 %-unit of watercut) and $\Delta WC_{\mathrm{EC}} = 1.3\%_{wc}$ for a corrosion/erosion of 0.5 mm on all surfaces. If the axial edge of the fin in a CFR sensor is wedge shaped, the thickness of the fin has practically no effect on the frequency (see Fig. 6.8). In that case the error is $\Delta WC_{\mathrm{CFR}} = 0.23\%_{wc}$ (for 0.5mm). In practice the truth is probably somewhere between these two values, which means that a CFR sensor is less sensitive to erosion and corrosion than an end cross sensor.

6.9 The CFR Sensor as a Low-Cost Watercut Sensor

In the petroleum industry and related areas the measurement of the water content of oil, i.e. the watercut, is an important measurement problem. In some cases a high accuracy ($\leq 0.1\%_{wc}$) or resolution ($\leq 0.01\%_{wc}$) are needed, but in many cases a lower price is more important than a high accuracy or resolution. Because of its simple

mechanical structure the CFR sensor provides a good basis for developing a watercut meter version that can be sold to a lower price than the standard version.

In a low-cost meter the manufacturing cost of every component is important. Therefore the electronics must also be simple and not contain expensive parts. The author and his team at Roxar have developed a low-cost watercut meter based on the CFR sensor and the feedback self-oscillating amplifier method of measuring the resonant frequency [Nyfors and Bringsvor, 1998]. Because the used method of measuring the resonant frequency puts particular requirements on the frequency response of the sensor, the low-cost watercut concept will be briefly discussed below, even though matters related to a specific product and the methods of measuring the resonant frequency are outside the scope of this thesis.

6.9.1 Low-Cost Sensor

The fin structure is simpler and less expensive to produce than the end grids of the end grid sensor that is described in Ch. 7. It can also be produced with the wire cutting technique without welding the fin. This method produces a high quality finish and tight tolerances. Especially in the case of small sensors (up to about 4") the sensor body can be machined from one piece, in which case no welding is used in the production of the sensor. This is a strong sales argument in the offshore business, where all welding has to be performed in accordance with specific procedures, which must be adjusted to the customer's requirements and checked and approved by the customer in a time-consuming and tedious process.

The electric type probes are also mechanically simpler than the magnetic type loop probes that are used in the end grid sensor. Because of the lower accuracy requirements for a low-cost meter, the sensor can be made short, despite of the possible influence that a slightly different diameter of the pipe would have on the resonant frequency (see Sec. 6.6.1). For example, a CFR sensor for a low-cost watercut meter can be made 1.2 D_p long and without own flanges. Instead it is squeezed between the flanges of the surrounding pipe with through bolts.

6.9.2 The Feedback Self-Oscillating Amplifier (FSA) Method of Measuring f_r

Basics of the FSA Method

The most frequently used methods of measuring the resonant frequency of a resonator sensor are based on performing a frequency sweep measuring the frequency response that is shown in Fig. 3.1 (reflection coefficient) or 3.2 (transmission coefficient) [Nyfors and Vainikainen, 1989a], [Vainikainen, 1991], [Okamura, Miyagaki, and Ma, 1998]. The signal is generated by a VCO (voltage controlled oscillator) and the amplitude is measured and the frequency is counted in a number of points. The resonant frequency is determined from a curve fitted to the measurement points. The curve fitting may vary in complexity depending on the required accuracy. In the simplest case only the –3 dB points are measured and the resonant frequency taken to be the mean value. The sweep methods are limited in speed, because of the time it takes to perform a frequency sweep and to count the frequency with the required accuracy in the required number of points. The sweep methods are also limited in

range by the frequency range of the used VCO, but they have the potentiality of providing a high accuracy, only dependent on the number of measurement points and the accuracy of the measurements of amplitude and frequency. The accuracy may be limited by the time it takes to perform one measurement of resonant frequency compared to the time scale of the changes in the resonant frequency.

The FSA method of measuring resonant frequency is a so-called active method, where the resonator sensor is an active part of the measurement system. The method has long been known as a fast and simple method of measuring the resonant frequency in narrowband applications [Nyfors and Vainikainen, 1989a, p.171]. In this thesis the use of the method in broadband applications is studied.

The FSA electronics consists of an amplifier, which may internally consist of a chain of amplifiers, with feedback through the sensor (Fig. 6.33). If the gain of the amplifier at a certain frequency is higher than the attenuation in the sensor and the cables, there will be net amplification of a signal for each revolution in the circuit. This condition leads to oscillation. The amplifier is driven further into saturation until the gain balances the attenuation. The sensor acts like a filter such that the net gain will normally be grater than 1 (unsaturated amplifier) only at the resonance peak. However, just as described in Sec. 3.3 for microwave resonators, the phase condition must also be fulfilled before the oscillation can start. The total phase change of a signal during one revolution in the circuit must be

$$\Delta\phi_t = n \cdot 2\pi \tag{6.23}$$

where n is an integer. This means that the circuit can oscillate only on certain discrete frequencies. Generally it will not oscillate on the exact resonant frequency but on the nearest frequency, where both the phase and the net gain conditions are fulfilled. The distance between the frequencies, where the phase condition is fulfilled, determines the resolution of the measurement of the resonant frequency. This distance depends on n, i.e. the length of the cables. The longer the cables, the more closely spaced are these frequencies.

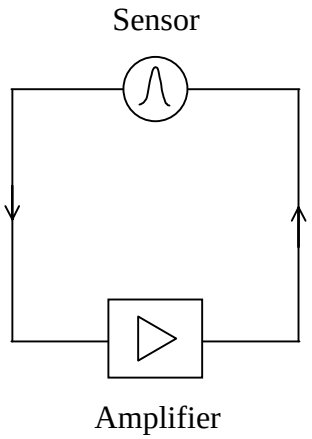

Figure 6.33 The FSA method of measuring resonant frequency. A signal is amplified in the amplifier and attenuated in the sensor. If the gain is larger than the attenuation at a frequency, where also the phase condition is fulfilled, the circuit will start to oscillate. The sensor acts like a filter such that oscillation is possible only close to the resonant frequency.

Resolution

If only the phase shift in the cables is taken into account, the resolution, i.e. the distance between the frequencies where the phase condition is fulfilled, is

$$\Delta f = \frac{(n+1)c}{l\sqrt{\varepsilon'_{rc}}} - \frac{n \cdot c}{l\sqrt{\varepsilon'_{rc}}} = \frac{c}{l\sqrt{\varepsilon'_{rc}}} \tag{6.24}$$

where ε'_{rc} is the permittivity of the insulation and l is the total length of the cables. If 10 m long cables with $\varepsilon'_{rc} = 2.2$ are used, the resolution is then Δf = 10.1 MHz. The sensitivity of a 2" CFR sensor has been measured to be roughly 15 MHz/%$_{wc}$, where %$_{wc}$ stands for 1 %-unit of watercut. The definition of watercut is [Handbook of Multiphase Metering, 1995]

$$WC = \frac{V_{\text{water}} \cdot 100\%}{V_{\text{water}} + V_{\text{oil}}} \tag{6.25}$$

where V stands for volume. The resolution is therefore in this case

$$\Delta WC = \frac{10.1\text{MHz}}{15\text{MHz}/\%_{wc}} = 0.67\%_{wc} \tag{6.26}$$

So far only the phase shift in the cables was taken into account because it dominates, when the cables are long, and therefore gives a good but conservative estimate of the resolution. In reality the total phase shift is the sum of the phase shift in the cables, the sensor, and the electronics. The phase shift in the electronics is difficult to express accurately but in practice it is equivalent to a small extra length of cable. Compared to the total length of 20 m in this example, the effect is small.

The phase shift in the sensor is +90^o far below the resonant frequency, ±45^o at the –3 dB points, and –90^o far above the resonant frequency. This phase shift in the sensor effectively pushes the frequencies, where the phase condition is fulfilled, closer together in the vicinity of the resonant frequency. The resolution is therefore slightly better than estimated by (6.24), but depends on the width of the resonance peak. To estimate the typical effect on the resolution of the phase shift in the sensor, the total phase shift must be calculated. It is the sum of the phase shift in the cables and the sensor:

$$\Delta\phi_t = \Delta\phi_c + \Delta\phi_s \tag{6.27}$$

where the phase shift in the cables is

$$\Delta\phi_c = -\frac{2\pi \cdot l \cdot f\sqrt{\varepsilon'_{rc}}}{c} \tag{6.28}$$

and the phase shift in the sensor is given by (3.27a):

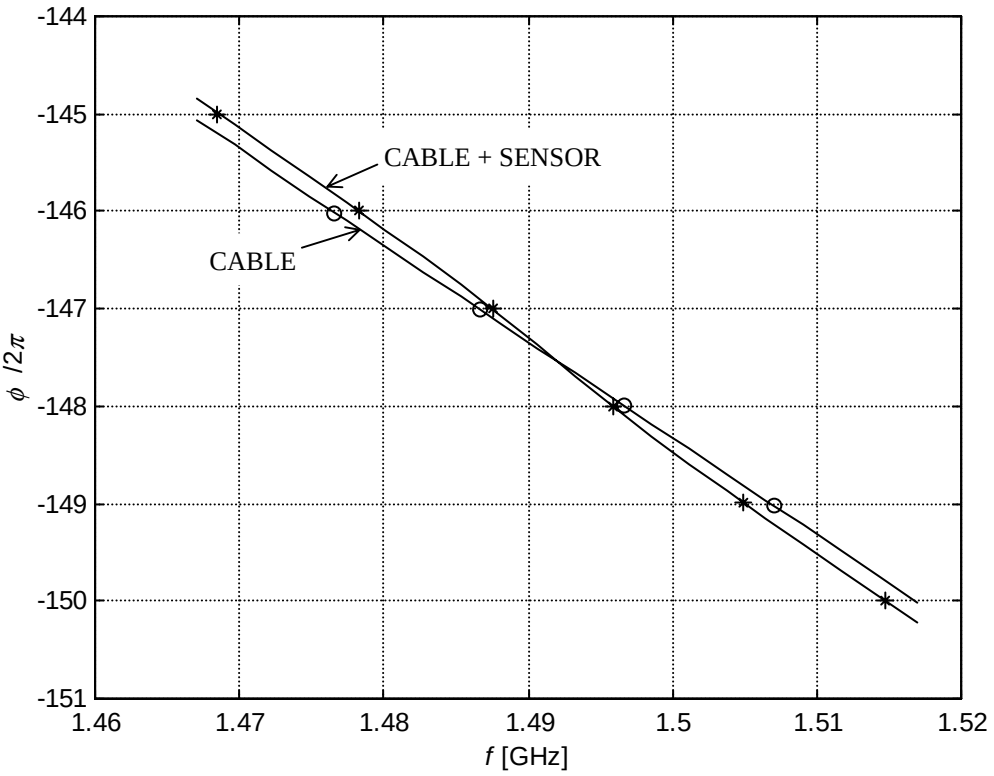

Figure 6.34 The phase shift in a 20 m long cable, and in the cable + sensor. The rings and the asterisks mark frequencies, where the phase shift is $n \cdot 2\pi$. The phase shift in the sensor improves the resolution of the FSA method from that given by (6.24). The chosen values correspond to a watercut of 0%.

$$\Delta\phi_s = -\arctan\left[Q_l \left(\frac{f}{f_r} - \frac{f_r}{f} \right) \right] \tag{6.29}$$

The effect on the resolution of the phase shift in the sensor is illustrated in Fig. 6.34. If the cables are 10 m long (total 20 m) and the peak narrow (WC = 0%), the resolution improves from 10.1 MHz to 8.3 MHz. For a peak corresponding to WC = 30% the resolution is 8.8 MHz. The corresponding resolution in WC is 0.55%$_{wc}$ and 0.59%$_{wc}$ respectively, compared to the 0.67%$_{wc}$ for the cable alone. These calculated results agree well with test results.

Implications of the Discrete Nature of the FSA Method

The fact that the FSA circuit can oscillate only on certain frequencies means that the measured watercut will jump in steps, when the real change in watercut is continuous. In the used example (2" sensor, 10 m cables) the step size is roughly 0.6%$_{wc}$, which means that the discretization error is ±0.3%$_{wc}$.

In designing a system based on the FSA method care must also be taken to match the frequency resolution Δf to the width B_{hp} of the resonance peak. If the peak is much narrower than Δf, the insertion loss may be too high at the nearest frequency,

where the phase condition is fulfilled, when the peak is in the middle between two such frequencies. A practical condition is

$$\Delta f \leq B_{hp} = \frac{f_r}{Q_l} \tag{6.30}$$

which means that it is enough to have a gain margin of 3 dB, i.e. 3 dB more gain in the amplifier than the insertion loss of the sensor+cables, over the whole measurement range. Note that the gain margin changes with the watercut, because the peak height and the frequency change and the gain depends on the frequency.

In a 2" CFR sensor the peak width is roughly in the range 13 … 30 MHz, depending on the type of oil, the *WC*, and the strength of the coupling. This is more than the resolution of 8.8 MHz that is achieved with 10 m long cables, which means that condition (6.30) is fulfilled. Figure 6.35 shows the calculated situation corresponding to *WC* = 0% and 20%. The horizontal lines depict a gain margin of 3 dB at the resonant frequency, and the asterisks are frequencies, where the phase condition is fulfilled. Oscillation is then possible at the frequencies marked with asterisks that are above the horizontal line. In practice the circuit will oscillate at the frequency with the highest gain margin.

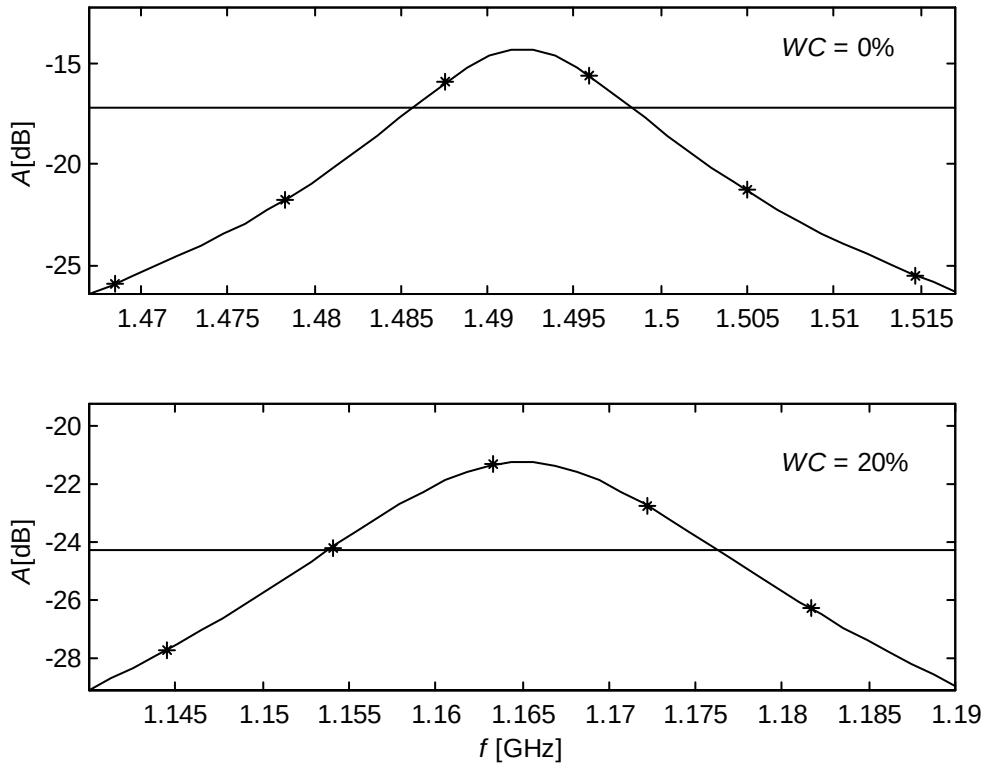

Figure 6.35 The resonance peak for a watercut of 0% and 20%. The asterisks show the frequencies, where the phase criterion for oscillation is fulfilled with 10 m long cables (calculated). The horizontal line depicts a gain margin of 3 dB at the resonant frequency. The resonant frequencies and peak widths correspond to measured values for motor oil and fresh water.

Matching the Frequency Responses of the Amplifier and the Sensor

Above it was assumed that the sensor has only one resonance peak, but in reality every microwave resonator has an infinite number of resonances. The FSA circuit will oscillate at the peak with the highest gain margin. It is therefore important to match the frequency response of the amplifier to the frequency response of the sensor so that this will always occur at the right peak. In a CFR sensor the used resonance is the one with the lowest frequency, and the next two resonance peaks have been eliminated by the choice of locations for the probes (see Sec. 6.3). By using an amplifier with a falling frequency response (i.e. higher frequency → lower gain) the risk of the circuit oscillating at the wrong frequency is therefore minimized. A falling frequency response is also motivated by the fact that the height of the peak generally falls, when the watercut increases and the resonant frequency decreases. On the other hand, a falling frequency response slightly favours oscillation frequencies on the lower side of the resonant frequency, leading to a small systematic error. In practice this error is negligible compared to the discretization error. In a tested circuit, consisting of three Hewlett-Packard MSA-0885 amplifiers in series, the gain dropped 20 dB/1 GHz, which is equal to 0.6 dB/30 MHz. With a resolution of 8.8 MHz and a peak width of 30 MHz this gives a systematic error of 0.55 MHz, corresponding to 0.04%$_{wc}$. If the resolution is 30 MHz, the systematic error is 0.9 MHz (0.06%$_{wc}$). With narrower peaks the error is smaller.

The higher the gain margin is the more noise the circuit creates. This noise easily leads to uncontrolled oscillations at low frequencies, where the gain is highest. To prevent this from happening the lowest part of the frequency response (below the lowest expected resonant frequency) of the electronics should be filtered out with a highpass filter. Practical tests have shown that enough filtering to allow at least 30 dB of gain margin is achieved by using small enough coupling capacitors between the amplifier stages. In the present design of the electronics 10 pF capacitors have been used.

6.10 Summary

A new type of microwave resonator sensor, the CFR sensor, has been developed for measurements in pipes. The CFR sensor is an application of sectorial waveguides, and is as a resonator based on the principle of isolation below cut-off. Various design aspects have been studied both using simulation tools and by measurements. The effects of the length, height, thickness, and shape of the fin have been studied. The effect on the frequency response of the location of the probes, and the effect on the coupling of the shape and size of the probes and the permittivity of the MUT and the dielectric material in the probes have also been studied. Various aspects related to the length of the sensor have been studied and recommendations given for alternative designs depending on the specifications. The sensitivity to contamination (scale and wax) has been studied in practical tests, and the sensitivity to corrosion and erosion has been studied theoretically. Here CFR sensors and end cross sensors were compared. A low-cost watercut meter for applications in the petroleum industry has been developed. It is based on a CFR sensor and simple FSA electronics. The advantages are low manufacturing cost, no welding needed, and minimal obstruction to the flow.

7 RESONATOR SENSORS WITH END GRIDS

7.1 Introduction

The method of implementing microwave cavity resonator sensors in pipes by isolating a section of the pipe with grids (see Fig. 4.9), has been widely used for measuring the material properties of materials flowing in pipes. The method was briefly discussed in Sec. 4.3. Three cases of end grid sensors are discussed in this chapter.

The first case is the MFI WaterCut sensor made by Roxar. A new type of end grid that was developed by the author is presented. Various design aspects of the end grids are discussed based on the theory presented in Ch. 4, and on measurements.

The second case is the MFI downhole watercut meter that is being developed at Roxar. The sensor for this meter was designed by the author. The design of the end grids and the sensor to match the spatial requirements in the annulus of an oil well are discussed, as well as the size, shape, and location of the probes from the point of view of creating a frequency response that is suitable for the FSA method of measuring resonant frequency.

The third case is a humidity sensor with a broad measurement range. It was designed to be used inside a veneer sheet dryer, where the temperature is high and the air contains dust and vaporized resin. It could also be used in other similar harsh environments. A general description of the design is given. This sensor was developed by the author and his collegues at the Radio Laboratory of the Helsinki University of Technology. It was successfully tested but never commercialized.

7.2 The MFI WaterCut Sensor

7.2.1 Basic Design

The WaterCut sensor is based on using the TM_{010} mode (see Sec. 3.7.2) in a cavity that is isolated by end grids in a cylindrical pipe. The length of the cavity is shorter than or equal to the radius of the pipe, which means that the used mode is the lowest one, with a relatively long distance to the next one (see Fig. 3.3). The sensor is always completely filled with the MUT, which means that all modes are moved by the same relative amount, when the watercut and thereby the permittivity of the MUT changes. Generally, when the watercut is high, the resonance peaks are low and broad and the right one may be difficult to identify if there are other peaks close to the used one, and especially in the presence of ripple. The long distance to the next mode therefore reduces the risk of confusion between peaks in the WaterCut sensor.

The end grids in the small dimensions (up to 4” in diameter) of the WaterCut sensor all used to be simple cross grids, i.e. made of two crossed plates, as shown in Fig. 7.1. The length of the grids (d_g) was designed to be equal to the inner diameter (D_p) of the pipe. Tests had shown this to be enough. Because there is a grid in both ends, the grids add totally $2D_p$ to the length of the sensor. In the small sensors this is of little importance, but in the large sensors the long grids add significantly to the manufacturing cost of the sensor. Star grids, consisting of four crossed plates (Fig 7.1), were therefore used in the larger dimensions. Because the holes in the star grids are smaller than in the cross grids, they were supposed to provide better isolation

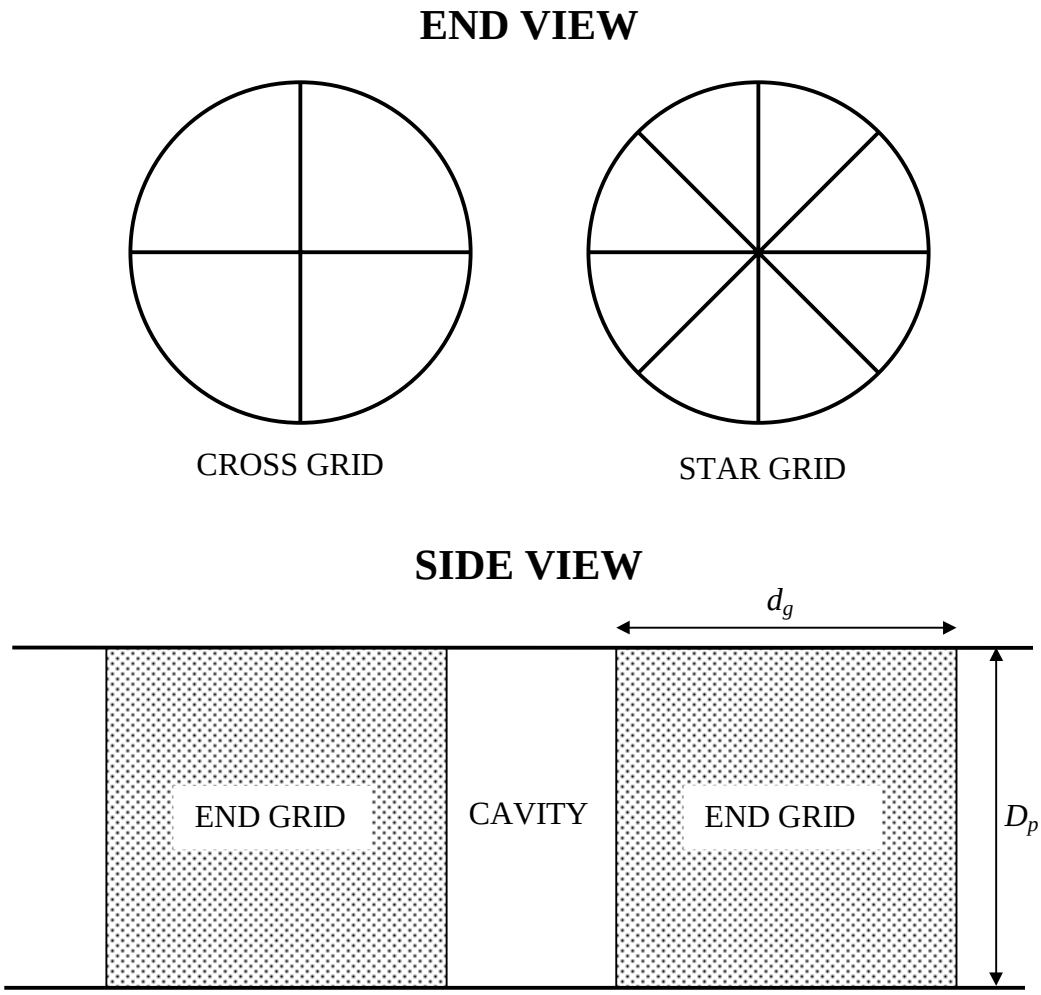

Figure 7.1 The basic design of the cross and star grids used in MFI WaterCut sensors.

allowing the star grids to be made shorter than the cross grids. They were designed to be half as long as the cross grids, i.e. $d_g = 0.5D_p$. In practice this length also turned out to be more or less enough, even though the frequency response did not quite seem to reflect the supposedly increased cut-off frequency of the grid.

It was not known how much more isolation could be achieved by further increasing the number of plates. The desire was, however, to make the grids as short as possible in order to minimize the manufacturing costs and the space taken by the sensor. The author's task became to study the existing design, if possible improve it, and to specify the length for each design to be used with the various dimensions of the WaterCut sensor. Because the relative isolation provided by different designs of grids was not known, the HFSS software had not yet been acquired, and building and measuring prototypes is expensive and gives only limited answers, the author started by analyzing the waveguide modes in the holes of the existing end grids. This resulted in the solutions for sectorial waveguides. Also semisectorial waveguides were studied, when the existing design was improved (see below). As a spin-off effect the author invented the CFR sensor. The waveguide mode solutions were presented in Ch. 5 and the CFR sensor in Ch. 6. The results for the end grids of the WaterCut sensor are presented below.

7.2.2 Relative Isolation Provided by Cross and Star Grids

The Theoretical Effect of the Length of the Grids

The holes in a cross grid are sectorial waveguides, with a sector angle $\varphi_0 = \pi/2$. From Eqs. (5.8) and (5.18), and Tab. 5.1, the lowest cut-off frequency in these waveguides is seen to be that of the mode TE_{21}. In this case the ratio between the cut-off frequency in the holes and the resonant frequency of the TM_{010} mode is given by the ratio of (5.18) to (3.50) with $l = 0$:

$$\frac{f_c(\mathrm{TE}_{21})}{f_r(\mathrm{TM}_{010})} = \frac{p'_{21}}{p_{01}} = \frac{3.054}{2.405} = 1.270 \tag{7.1}$$

Because the ratio is low, the grids have to be long to provide the necessary isolation. This had also been seen in practice and the grids were designed to be one inner diameter long. Equation (4.10) gives $Q_{\mathrm{rad}} = 1866 \cdot Q_{\mathrm{rad0}}$ for $d_g = D_p$.

In sensors larger than 4" star grids were used. Because the holes are smaller than in the cross grids, the cut-off frequency was assumed to be higher and they were designed to have a length of $d_g = 0.5D_p$. Because they are made with 4 crossed plates (8 sectors), the sector angle is $\varphi_0 = \pi/4$. The mode that was the lowest in the cross grids and called TE_{21} (in a sector with $\varphi_0 = \pi/2$), is called TE_{41} when $\varphi_0 = \pi/4$. It has $p'_{41} = 5.318$ and is not the lowest mode in a star grid. The lowest mode is the sectorial mode TE_{01}, with $p'_{01} = 3.832$, independent of the sector angle. It also exists in ordinary cylindrical waveguides. The electric field of this mode is tangential, i.e. perpendicular to the sector walls, which is the reason that the plates in a star or cross grid do not affect this mode. TE_{01} gives the ratio

$$\frac{f_c}{f_r} = \frac{3.832}{2.405} = 1.593 \tag{7.2}$$

In fact already a grid with 6 sectors would have the same cut-off frequency as the grid with 8 sectors (see Tab. 5.1).

The relative length of two grid types with different f_c/f_r ratio that give the same isolation can be calculated from (4.10). Assuming that Q_{rad0} is the same for both grid types, (4.10) gives

$$\frac{d_{g2}}{d_{g1}} = \sqrt{\frac{\left(\frac{f_{c1}}{f_r}\right)^2 - 1}{\left(\frac{f_{c2}}{f_r}\right)^2 - 1}} \tag{7.3}$$

From the f_c/f_r ratios calculated above, (7.3) gives that a star grid needs to be 0.716 times the length of a cross grid to provide the same isolation.

The surface currents are radial in the flat ends of a TM_{010} resonator. The radial structure of the cross and star grids should therefore provide a good short to the mode, leading to a high Q_{rad0}. The higher the number of legs in the star is, the higher can Q_{rad0} be expected to be. Taking this into account, the real length of a star grid that provides the same isolation as a cross grid is probably shorter than 0.716 times the length of the cross grid.

From (5.18) and Tab. 5.1 it can be concluded that the cut-off frequency of a star grid increases with the number of sectors only up to 6 sectors. Based on this information it does not seem possible to make significantly shorter grids by increasing the number of sectors in the grids past 6.

Measured Cut-Off Frequency of Cross and Star Grids

The author performed a series of simple tests to check the calculations and to find out the real cut-off frequency of the cross and star grids. The tests were performed with a network analyzer (NA) such that the microwave signal was fed into the sensor through one of the two probes. The signal was received in free space on the outside of the sensor with a short monopole antenna mounted on the cable connected to the input of the NA. The leakage was measured as a function of frequency with the antenna in various positions and at various distances from the sensor. A subjective estimate of the cut-off frequency was made from the printouts.

The first test was made with a 3" sensor (D_p = 97.5 mm) with cross grids. The calculated theoretical resonant frequency for a sensor with this diameter, perfect ends, and no influence from the probes, is f_{rt} = 2.356 GHz, whereas the measured resonant frequency was 2.160 GHz. The measured cut-off frequency of the grids was approximately 3.000 GHz. This gives the ratio f_c/f_{rt} = 1.273, which is close to the expected ratio of 1.27.

Another test was made with a 15" sensor (D_p = 381 mm, nominally a 16" sensor, with a high pressure rating) with star grids. The length of the grids was d_g = 203 mm. The calculated theoretical resonant frequency for a sensor with this diameter, perfect ends, and no influence from the probes, is f_{rt} = 603 MHz, whereas the measured resonant frequency was 550 MHz. The measured cut-off frequency was approximately 860 MHz, where a prominent peak in the leakage was observed. This gives the ratio f_c/f_{rt} = 1.43, which is somewhat lower than the expected ratio of 1.593, which would have given f_c = 960 MHz.

A qualitative explanation for the unexpectedly low cut-off frequency of the star grids and the observed peak can be obtained by considering transversal quasi-TEM modes in the grids. If two adjacent sectors are studied, the common wall forms the centre conductor of the TEM structure, and the other walls form the outer conductor. The TEM structure is shorted in one end by the sensor wall and in the other end by the welding in the centre of the star. A TEM structure that is shorted in both ends has a first resonance, when the structure is half a wavelength long. Because of the finite thickness of the plates in the grids and the welding in the centre point, the radius of the sectors was a = 170 mm. The approximate resonant frequency of this TEM structure is

$$f_r = \frac{c}{\lambda} = \frac{c}{2a} = \frac{3 \cdot 10^8}{2 \cdot 0.17} = 882\,\text{MHz} \qquad (7.4)$$

which is close to the observed cut-off frequency and peak of the star grids.

When a resonance is present in an end grid, energy can easily be conveyed through the grid by coupling to the resonance mode from the inside and escaping by radiation at the outside.

Simulated Isolation of Cross and Star Grids

The cut-off frequency of cross and star grids was calculated based on the assumption that the cut-off frequency of a grid is equal to the cut-off frequency of the holes in the grid. The discussion above, however, indicates that adjacent holes might together support resonant modes with a resonant frequency that is slightly lower than the cut-off frequency of the holes. To test the general efficiency of the grids and the explanation given above, the leakage through both a cross grid and a star grid was simulated with HFSS. The models for the grids consisted of a cylindrical waveguide with input and output ports at the ends, and with a single grid in the middle. The dimensions were: D_p = 50 mm, d_g = 50 mm, length of model = 150 mm, and thickness of the plates = 2 mm.

The result for the cross grid is shown in Fig. 7.2 together with the calculated below cut-off attenuation. The cut-off frequency was calculated assuming a = 24 mm

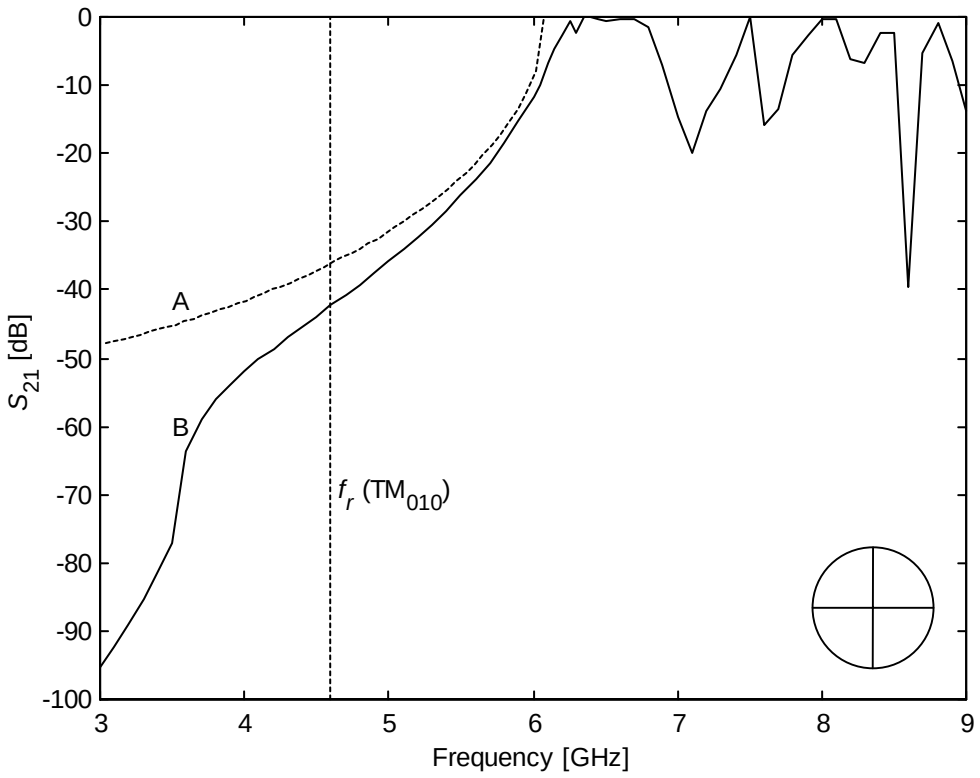

Figure 7.2 The isolation provided by a cross grid (4 sectors) with the dimensions d_g = D_p = 50 mm. The thickness of the plates = 2 mm. A: The attenuation below cut-off as calculated from (4.3). B: The result from the simulation with HFSS.

to compensate for the plate thickness, giving f_c = 6.08 GHz. The attenuation was calculated from (4.3).

The cross grid is seen to perform well compared to the calculated result. The simulated isolation is slightly better than the calculated because of the inefficiency in coupling from the waveguide to the holes in the grid. This is the phenomenon accounted for by Q_{rad0}. The effect of the cut-off frequency of the pipe at 3.52 GHz is also seen, giving extra attenuation on frequencies lower than that.

The result of the simulation of the star grid is shown in Fig. 7.3. The calculated cut-off frequency is 7.32 GHz. The star grid is seen to perform well at the resonant frequency of the sensor, providing considerably more isolation than calculated with (4.3). This fact is probably due to the higher Q_{rad0}, as explained above.

The isolation resulting from the simulations at the theoretical resonant frequency (4.593 GHz) is -79.7 dB for the star grid, and -42.5 dB for the cross grid. The isolation provided by the star grid is roughly double (in dB), which explains why the star grids can be made only half as long as the cross grids despite of the relatively small difference in cut-off frequency.

A strong resonance-like feature is seen at 7.1 GHz, corresponding to the ratio f_c/f_{rt} = 1.54, which is somewhat lower than the calculated ratio of 1.593 for TE_{01}, and higher than the measured ratio of 1.43, or the predicted ratio of 1.46 for the quasi-TEM resonance. The electric field configuration that was displayed by the HFSS for the simulation at 7.1 GHz resembles that of TE_{01}, not the TEM mode. The exact

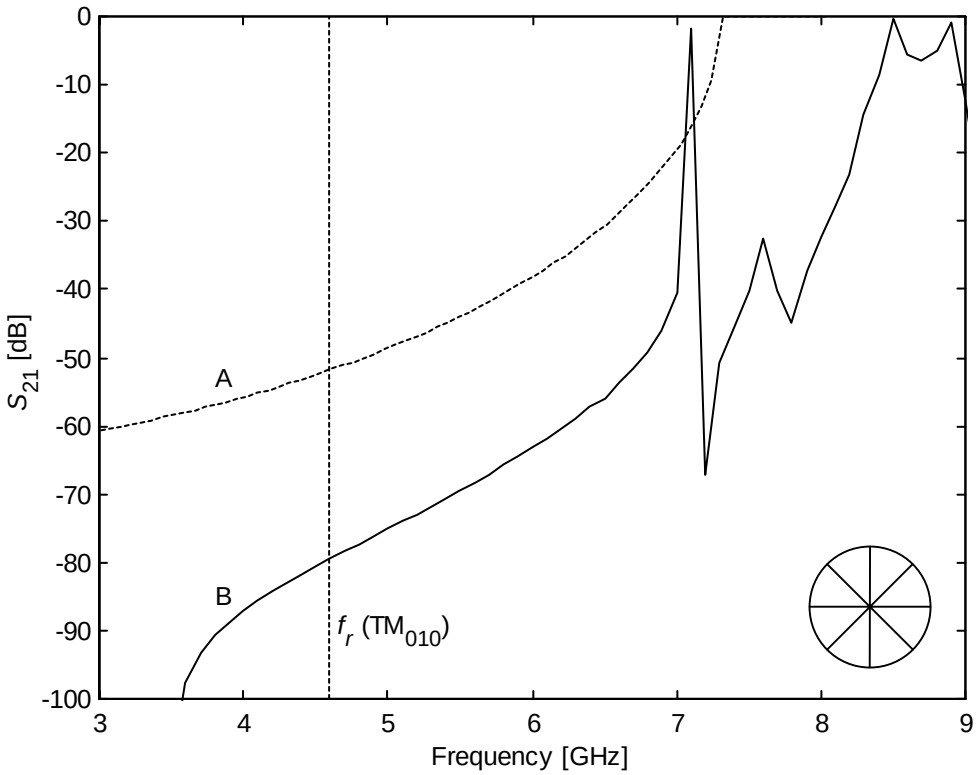

Figure 7.3 The isolation provided by a star grid (8 sectors) with the dimensions $d_g = D_p$ = 50 mm. The thickness of the plates = 2 mm. A: The attenuation below cut-off as calculated from (4.3). B: The result from the simulation with HFSS.

nature of the resonance phenomenon and the possible existence of the TEM mode therefore remain obscure.

To avoid interference from things outside the sensor, e.g. caused by reflections from the thermowell, it is desirable to have a high cut-off frequency in the grids in addition to a high isolation at the resonant frequency. Otherwise extra peaks might appear inside the sweep window and be mistaken for the resonance peak, especially in the presence of ripple.

Conclusions

The cross grid provides a simple and satisfactory solution for sensors of small diameter, where the grids can be made long enough without high extra costs. However, the low cut-off frequency constitutes a risk for interference from e.g. the thermowell, which is normally mounted quite close to the sensor.

The star grid has a cut-off frequency that is lower than originally anticipated, and only slightly higher than that of the cross grid. The isolation efficiency is, however, good at the resonant frequency. Increasing the number of sectors further does not increase the cut-off frequency, because the lowest mode is only dependent on the diameter of the pipe, when the number of sectors is 6 or higher. Increasing the number of sectors might improve the isolation efficiency because of an increase in Q_{rad0}. For the large sensors a more efficient end grid design, with a higher cut-off frequency, is needed so that the grids can be made shorter than the star grids and the risk of interference be avoided.

7.2.3 Improved End Grid Design – The Ring Grid

The main problem with the star grid is the TE_{01} mode that is independent of the sector angle, and possibly the transversal quasi-TEM mode resonance in the legs of the star. If the diameter of the grid is maintained equal to the pipe diameter, the cut-off frequency of TE_{01} in the grid can only be increased by turning the sectors into semisectors. The author has therefore designed a new grid – the ring grid, which is shown in Fig. 7.4. The ring grid has a ring in the centre making the holes semisectorial waveguides. This also makes the legs of the star shorter, thereby pushing the resonant frequency of the possible TEM resonance upwards. The ring grid can therefore be expected to give a high isolation efficiency, and remove the TEM resonance and the risk of interference in the sweep window.

Optimization of the Ratio $r = b/a$ and the Number of Sectors in a Ring Grid

In choosing the ratio of radii $r = b/a$ for the ring grid, the cut-off frequency in the centre hole and the semisectors, as well as the resonant frequency of the TEM resonance in the legs, should be taken into account. The wall thickness of the ring and the legs can be forgotten. In reality the finite thickness will further improve the efficiency of the grid. Figure 7.5 shows the relative cut-off frequency of the centre hole and the semisectors, and the resonant frequency of the TEM mode, as a function of r in a ring grid with 8 sectors. It is seen that the optimal choice for r is in the

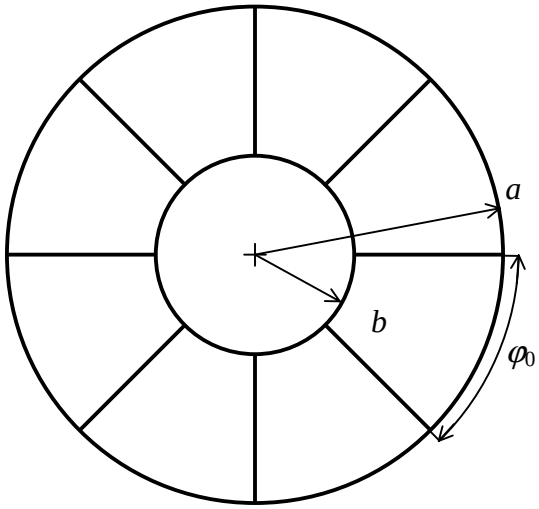

Figure 7.4 The basic design of a ring grid with 8 sectors. The semisectors have a higher cut-off frequency than the sectors in a star grid, thereby allowing the grid to be made shorter. The legs are also shorter than in a star grid, thus pushing the TEM resonance further away from the resonant frequency of the sensor.

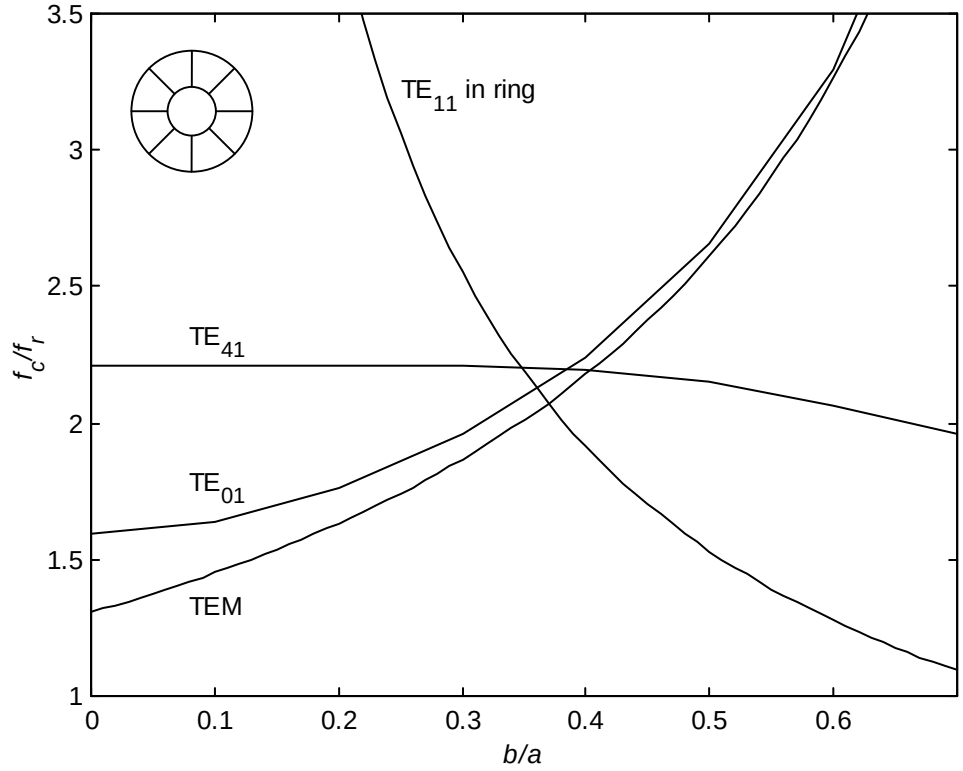

Figure 7.5 A comparison of the cut-off frequency of the semisectors and the centre hole relative to the theoretical resonant frequency of the sensor. The graphs are for a ring grid with 8 sectors. The quasi-TEM resonance in the legs of the star is also shown. A value of $b/a \approx 0.37$ gives optimal performance.

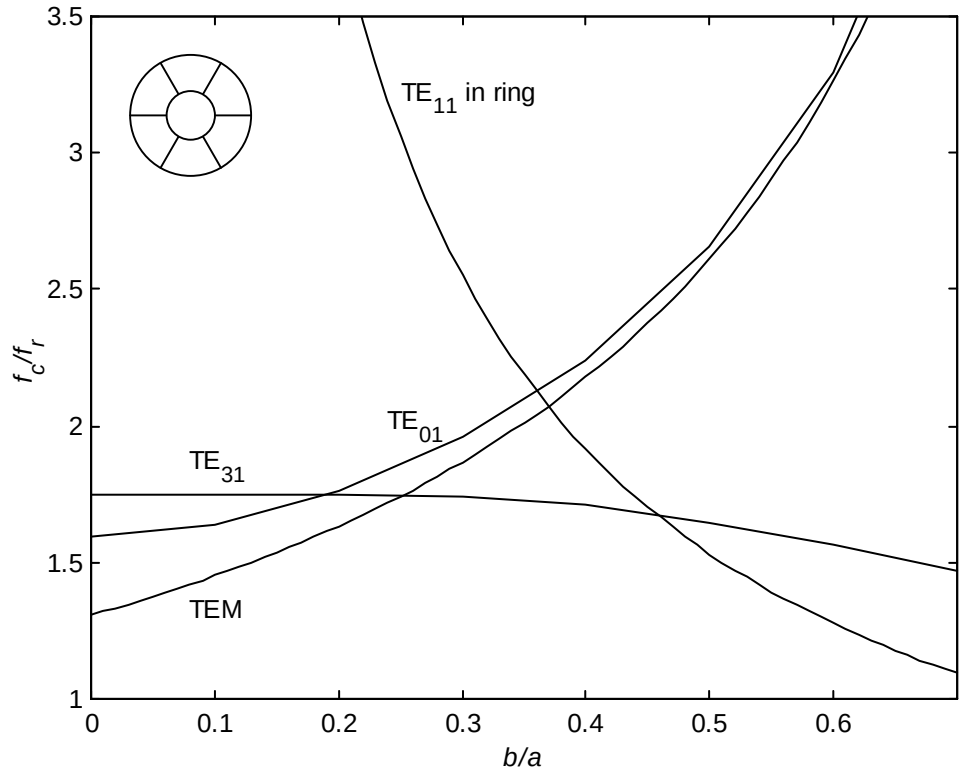

Figure 7.6 A comparison of the cut-off frequency of the semisectors and the centre hole relative to the theoretical resonant frequency of the sensor. The graphs are for a ring grid with 6 sectors. The quasi-TEM resonance in the legs of the star is also shown. A value of $b/a \approx 0.25$ gives optimal performance.

vicinity of 0.37, which gives a ratio $f_c/f_{rt} = 2.07$ for the grid. If the thickness of the ring is taken into account, the optimal value for r in the semisectors is slightly higher. In practice $r = 0.4$ can be recommended, when b is the outer radius of the ring.

If more than 8 sectors would be used, only the cut-off frequency of the $TE_{\nu 1}$ mode, where ν = 0.5*number of sectors, would increase. From Figure 7.5 it is seen that already for 8 sectors either the cut-off frequency of TE_{11} in the centre hole or TE_{01} in the semisectors is lower than that of TE_{41}. Increasing the number of sectors past 8 therefore does not bring any improvement to the lowest cut-off frequency of the grid.

Figure 7.6 shows the situation for a ring grid with 6 sectors. The optimal value for r is ≈ 0.25, which gives the ratio $f_c/f_{rt} = 1.74$. This is somewhat better than for a star grid with 8 sectors. A ring grid with 8 sectors is, however, significantly better.

In a cross grid the lowest mode is TE_{21}. The cut-off frequency of this mode would decrease if a ring would be used in the centre. Ring grids are therefore not recommended to be designed with only 4 sectors.

For optimal performance, ring grids with 8 sectors and r = 0.4 are recommended as the most efficient type of sectorial/semisectorial grid.

Simulated Isolation of a Ring Grid with 8 Sectors

The isolation of a ring grid was simulated with the HFSS in the same way as the cross and star grid. The same type of model was used: D_p = 50 mm, d_g = 50 mm, length of

model = 150 mm, thickness of plates and ring = 2 mm, b_o/a = 0.412 (b_o is the outer radius of the ring) and b_i/a = 0.372 (b_i is the inner radius of the ring), ports at the ends, and grid in the middle. The b/a values were chosen to be the same as in the prototype described below. With the given dimensions the cut-off frequency in the centre hole is 9.5 GHz, and 10.06 GHz in the semisectors.

S_{21} was simulated as a function of frequency. The result is shown in Fig. 7.7a together with the calculated attenuation based on the lowest cut-off frequency. The ring grid is seen to perform well. The effective cut-off frequency seems to be roughly 10.5 GHz and only a few small peaks are seen in the graph. The peaks are so small that they have no practical effect on the isolation. They may be caused by HFSS. When visualized by HFSS, the field configuration at the frequencies of the peaks looked exactly like outside the peaks. Based on these results it seems feasible to make the ring grids considerably shorter than the star grids.

If the isolation would be purely caused by attenuation below cut-off, the isolation expressed in dB would be directly proportional to the length of the grid. However, because of Q_{rad0} the situation is not quite that simple. A new simulation was therefore made with $d_g = 0.25D_p$. The result of this simulation is shown in fig. 7.7b. The graph of the isolation looks much like for the longer grid, except that the isolation has decreased. The graph again contains some small peaks, which are partly at different frequencies than for the longer grid. Again they may be caused by the HFSS.

At the theoretical resonant frequency (f_{rt} = 4.593 GHz) the isolation given by the simulation is -34.9 dB, whereas the theoretical attenuation below cut-off as given by (4.3) is -18.9 dB. The difference (-16.0 dB) comes mainly from the inefficiency with which the exciting mode launches the waveguide modes in the grid holes, and the fact that already a grid made of thin wires would provide some isolation, as taken into account by Q_{rad0}. In this simulation the waveguide was excited by the dominant mode, i.e. the TE_{11} mode, whereas the TM_{010} mode is used in the resonator. Because of this, and the fact that the quality factors of a resonator also depend on the stored energy, which depends on e.g. the length of the cavity as is seen from (3.23), it is impossible to predict the exact values of Q_{rad} and Q_{rad0} from the simulations. To achieve this a whole sensor would have to be simulated.

It is also difficult to put an exact limit to Q_{rad} for a sensor. If only the influence on the peak is taken into account, a fairly low value (Qrad ≈ 300) could be tolerated before the radiation starts to affect the measurements of watercut. Another factor is the interference from objects outside the sensor. It is for example important to be able to measure and calibrate the sensor on the bench, without that e.g. a hand in front of an end grid disturbs the measurement. Here the CFR sensor described in Ch. 6 provides a good reference. In Sec. 6.6.1 it was shown that when the sensor (D_p = 52.5 mm) is surrounded by 40 mm long pipe sections, things at the outside affect the sensor very little, and when the pipe sections are 50 mm long, the sensitivity to the outside disappears completely. From Fig. 6.31 it is seen that these lengths correspond to Q_{rad} = 1200...4000. Q_{rad} values within this range, or higher, can therefore be considered acceptable for a sensor.

An indication of the radiation quality factors corresponding to the simulation of the ring grid can be obtained from (4.10). Because the simulation takes into account the coupling and the reflection from a thin grid, (4.10) gives "Q_{rad}", when Q_{rad0} = 1 is assumed:

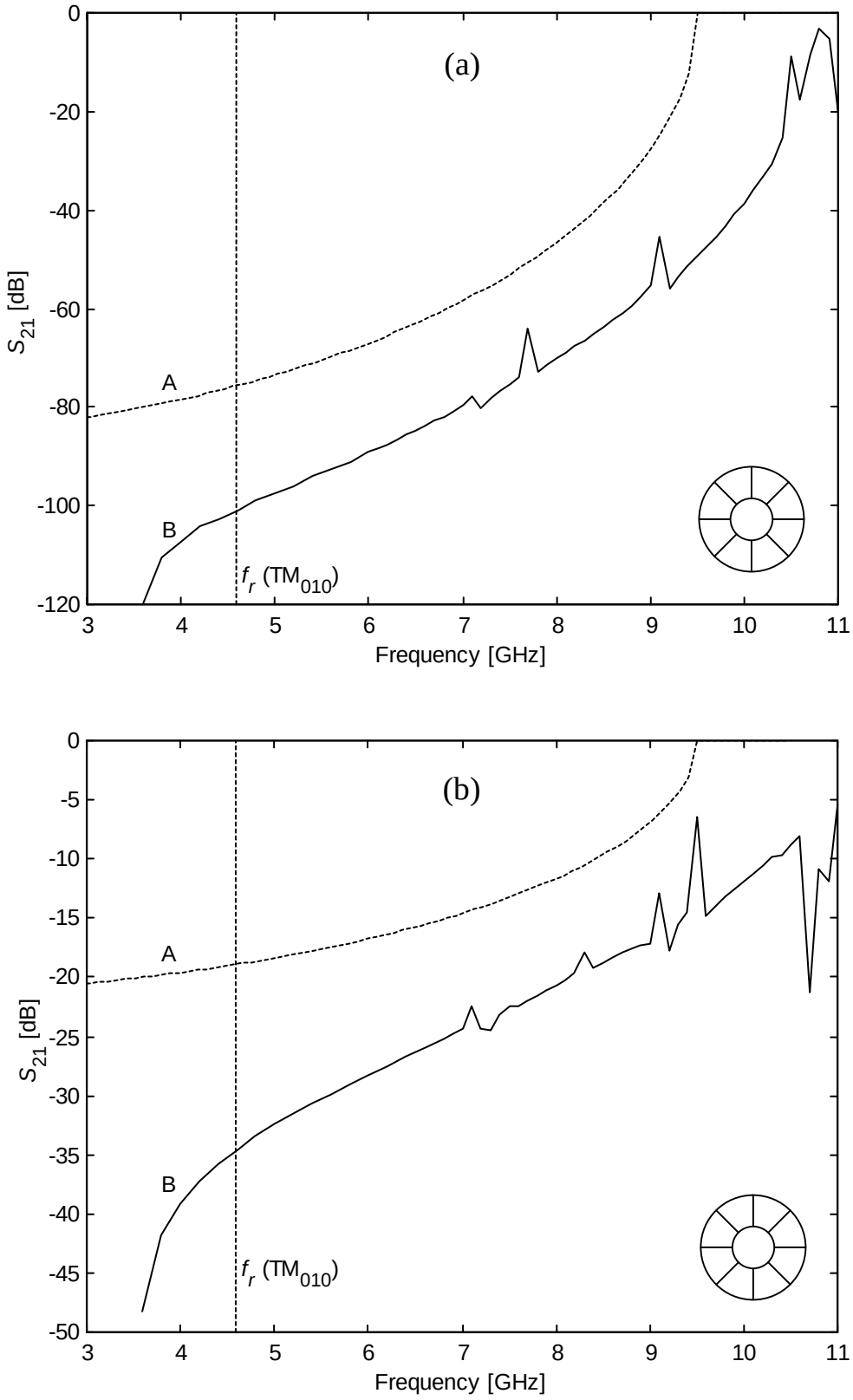

Figure 7.7 The isolation provided by a ring grid (8 sectors) with the dimensions $d_g = D_p = 50$ mm (a), and $d_g = 0.25D_p = 12.5$ mm (b), $b/a = 0.37...0.41$. The thickness of the plates and the ring = 2 mm. A: The attenuation below cut-off as calculated from (4.3). B: The result from the simulation with HFSS.

$$Q_{\text{rad}} = \frac{1}{10^{-34.9/10}} = 3090 \qquad (7.5)$$

In the same way "Q_{rad0}" is obtained from the difference between the calculated attenuation and the simulated isolation (-16.0 dB), which gives $Q_{\text{rad0}} = 39.8$. The value for Q_{rad} given by (7.5) is well within the acceptable range obtained for the CFR sensor.

Measurements of a Prototype Sensor with Ring Grids

A prototype sensor with ring grids was made from a piece of pipe. The dimensions were: D_p = 101.5 mm, b/a = 0.372…0.412 (as in the simulation model), length of cavity = 50 mm, and d_g = 48 mm. The resonant frequency and the quality factors of the sensor were measured, together with the relative radiation on the outside of the sensor. The radiation was measured in the same way as described in Sec. 7.2.2, except that the measurement was performed at two fixed positions at distances of 10 cm and 60 cm from the sensor. Thin slices were then cut from the ends of the sensor in steps of roughly $0.05D_p$ so that the measurements could be performed as a function of d_g.

Figure 7.8 shows the results for the resonant frequency f_r and the unloaded quality factor Q_u. The resonant frequency is seen to be almost unaffected by d_g. Q_u is also almost unchanged in the first few measurements. The first value was therefore taken as the metal quality factor Q_m. Q_{rad} was then calculated from (3.13) assuming $Q_d = 0$. The results for Q_{rad} are shown in fig. 7.9, together with a graph given by (4.10) fitted to the results. The best fit was obtained with f_c/f_{rt} = 1.95, and Q_{rad0} = 70. For $d_g = 0.25D_p$ the fitted graph gives Q_{rad} = 4280, which is a quite satisfactory value and slightly higher than indicated by the simulation.

The frequency ratio is slightly, but not significantly lower than the theoretical value of 2.07, considering that these values are quite sensitive to measurement errors. If the real peak height would be 0.15 dB higher than measured, the best fit would be obtained with f_c/f_{rt} = 2.07, and Q_{rad0} = 55. This would increase Q_{rad} to 4600.

The measured radiation was plotted as a function of frequency. Because of the large variations in the radiation level, and the unknown frequency response of the antenna, readings were taken from the printouts at one frequency only. A resonance peak at 2.8 GHz in the sensor was clearly distinguishable in the measured radiation. The readings were therefore taken at the top of this peak. No significant difference was detected between the measurements at the two different distances. Figure 7.10 shows the relative increase in the radiation compared to the level in the first measurement at $d_g = 0.475D_p$, corrected for the observed variation in the peak height in the sensor. The graph shows the expected increase calculated from (4.3). The best fit was obtained for f_c/f_{rt} = 2.15. This time the frequency ratio is slightly, but not significantly higher than the theoretical value of 2.07.

When the prototype was measured, qualitative observations of the sensitivity to the outside world were also done. The following observations were noted:

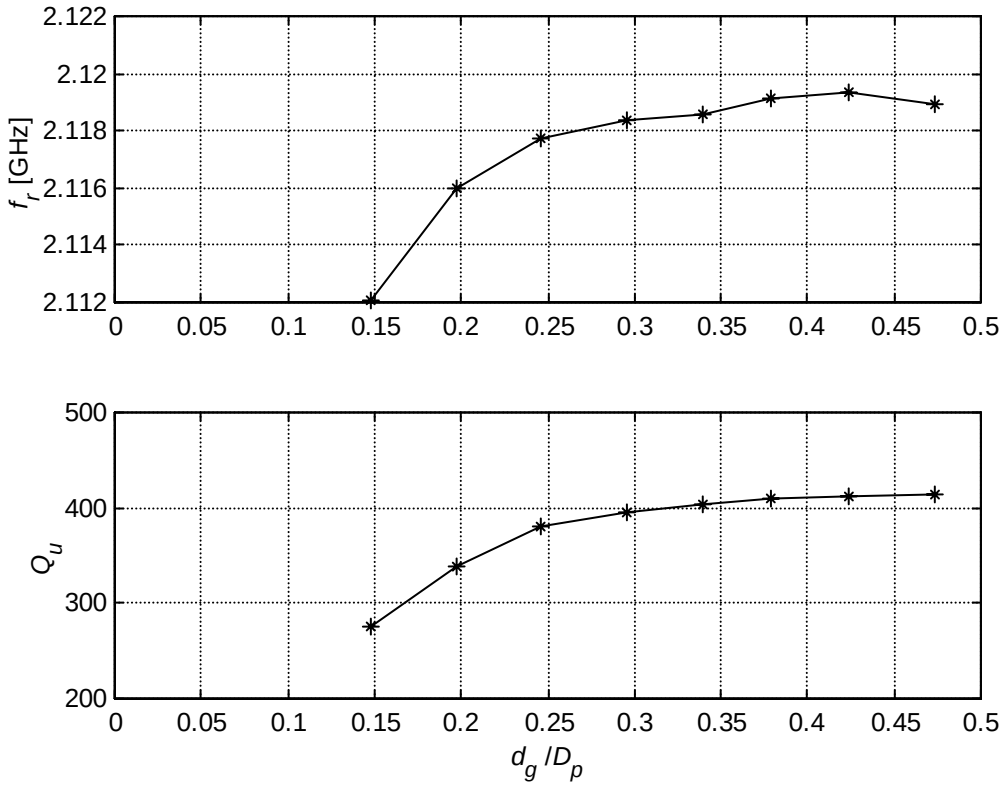

Figure 7.8 The measured resonant frequency and loaded quality factor of the prototype sensor with ring grids as a function of the length of the grids. The measurements were performed with a network analyzer .

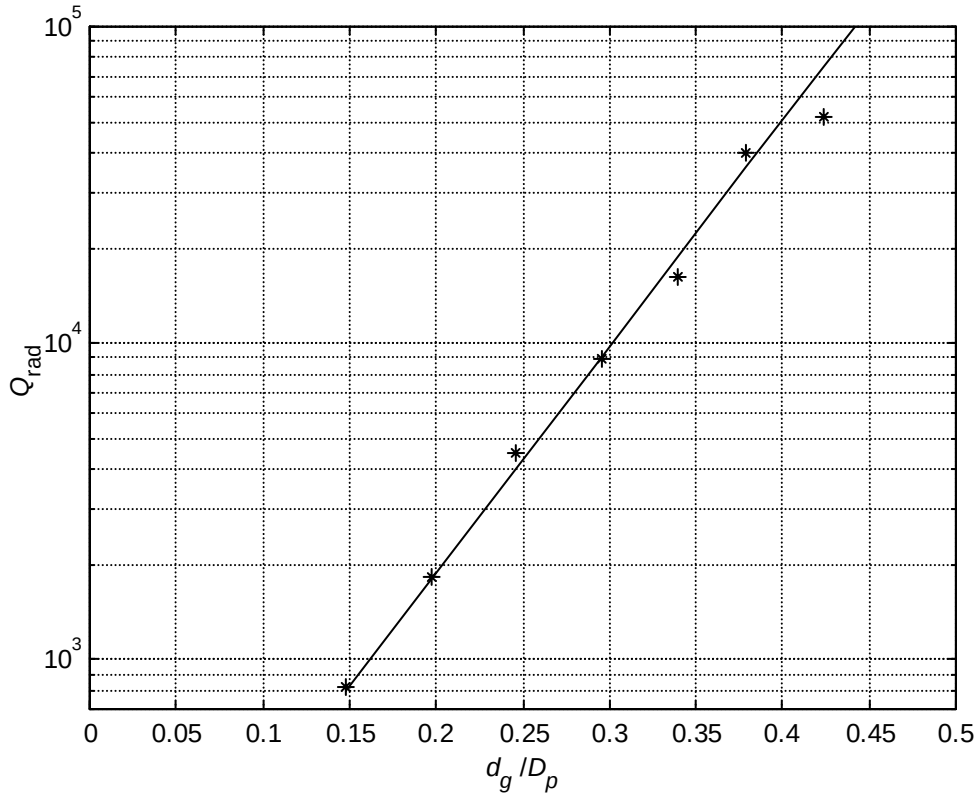

Figure 7.9 The radiation quality factor calculated from the measurements of the prototype sensor with ring grids. The graph was calculated with (4.10) assuming f_c/f_{rt} = 1.95, and Q_{rad0} = 70, which values gave the best fit.

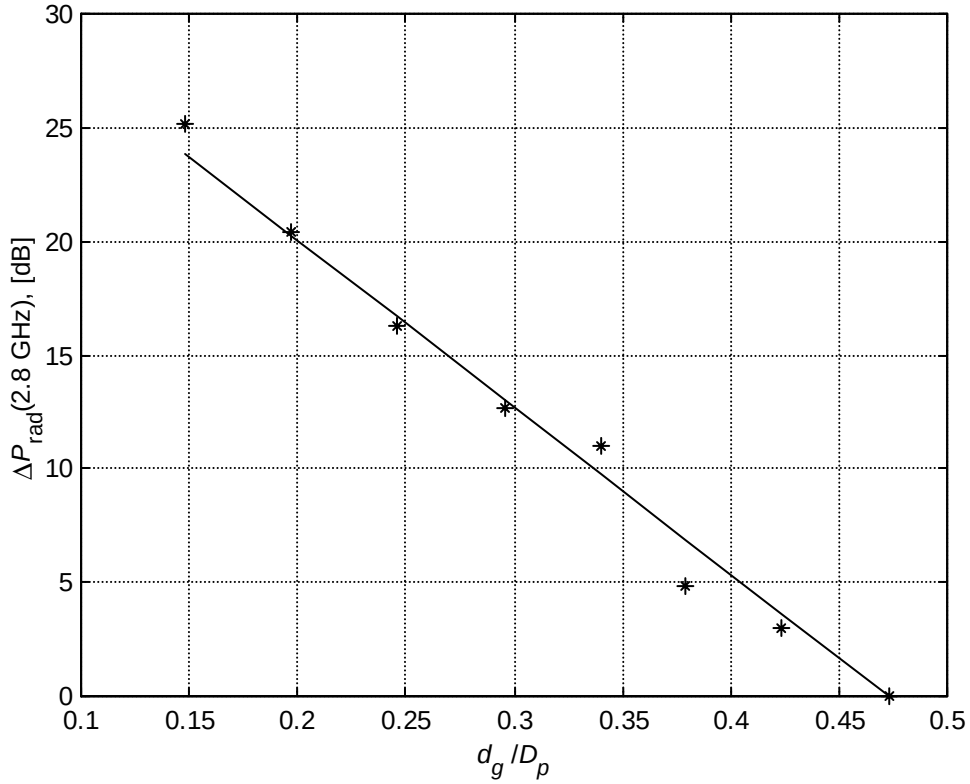

Figure 7.10 The measured increase in the radiation outside the sensor at 2.8 GHz, when the ring grids were cut shorter. The graph was calculated from (4.3). The best fit was obtained for $f_c/f_{rt} = 2.15$.

- $d_g \geq 0.296D_p$: The resonance peak was unaffected by a hand held in front of the grid.
- $d_g = 0.246D_p$: The height of the resonance peak dropped 1...2 dB, when a hand was held against the grid. The effect disappeared a very short distance away. With a metal plate the effect was negligible. The sensor performed well.
- $d_g = 0.197D_p$: The effect of the hand had increased: At a distance of 5 cm the hand caused no change of frequency, but a drop of 0.4 dB in power. Held right in front of the grid the hand caused a frequency shift of +0.35 MHz, and a drop in power of 4.1 dB. Metal plate: +0.35 MHz and -3 dB at 5 cm, and -2.65 MHz and -3.1 dB at 1 cm. The sensor was still usable as a sensor, but the accuracy and repeatability of measurements and calibration performed on the bench would be degraded.

The results from the measurements of the prototype confirm the results from the theoretical calculations and the simulations about the high f_c/f_{rt} ratio compared to cross and star grids. They also confirm the result from the simulations that ring grids, which are a quarter of a pipe diameter long, provide enough isolation for the resonance to be unaffected by radiation.

7.2.4 Conclusions

The end grids in a sensor have two purposes. First of all they shall prevent the energy at the resonant frequency from escaping through radiation. Secondly they shall prevent energy also at higher frequencies from escaping during a frequency sweep measurement. If energy can escape, it may become reflected and enter the cavity again and create spurious peaks. Especially when the watercut is high, these spurious peaks may enter the sweep window from the high end, while the right peak is low and broad, and may even have left the sweep window from the low end in the case of an out-of-range situation. It is therefore important that the isolation at the resonant frequency is high enough, the cut-off frequency of the grids is high, and the frequency response is clean without resonances. The isolation outside the resonance does not need to be so high, because the power is attenuated both in escaping and in penetrating back after reflection. Note that the frequency response of the grids is affected by the permittivity of the MUT in the same way as the resonator, because both the resonator and the holes in the grids are completely filled by the MUT.

Figure 7.11 shows the simulated results for cross, star, and ring grids of the same length, $d_g = D_p$. The ring grid has the best isolation and the cleanest response without resonances, and therefore has the best potential for making short grids. Figure 7.12 shows the simulated results for a cross grid with $d_g = D_p$, a star grid with $d_g = 0.5D_p$, and a ring grid with $d_g = 0.25D_p$, 8 sectors, and $b/a = 0.37...0.4$. With these d_g values the ring grid has the lowest isolation at the resonant frequency, but the isolation was proven good enough by the measurements of the prototype. Figure 7.8 shows that $d_g = 0.25D_p$ is a turning point - shorter grids start to become affected by radiation,

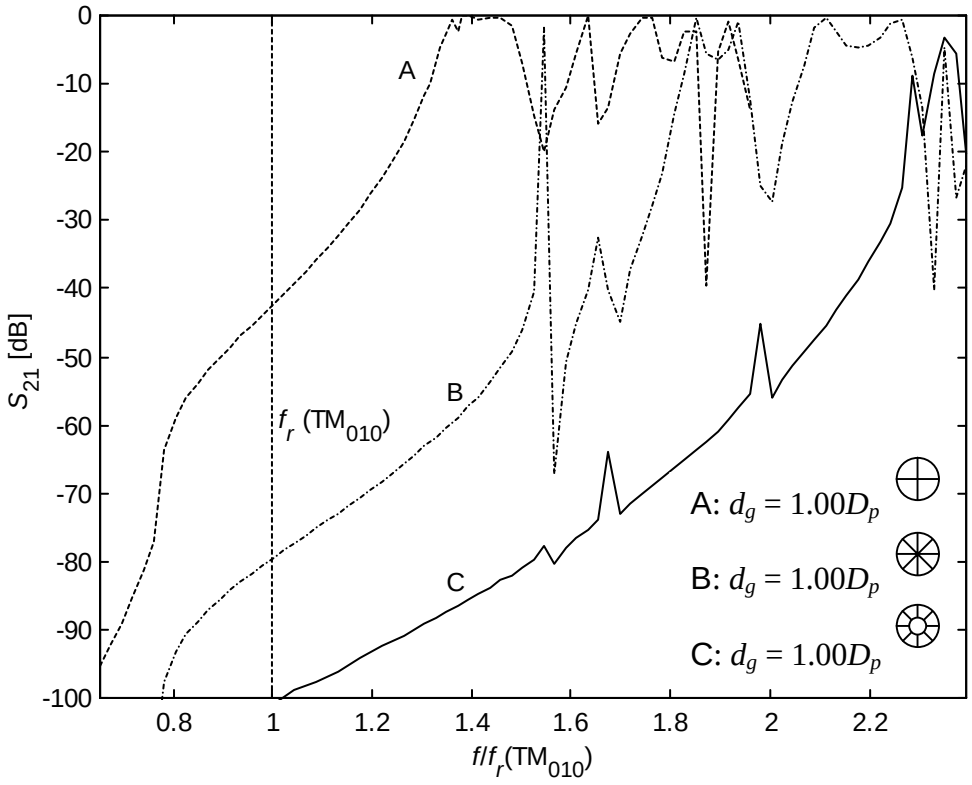

Figure 7.11 The simulated isolation of a cross grid, a star grid, and a ring grid of the same length.

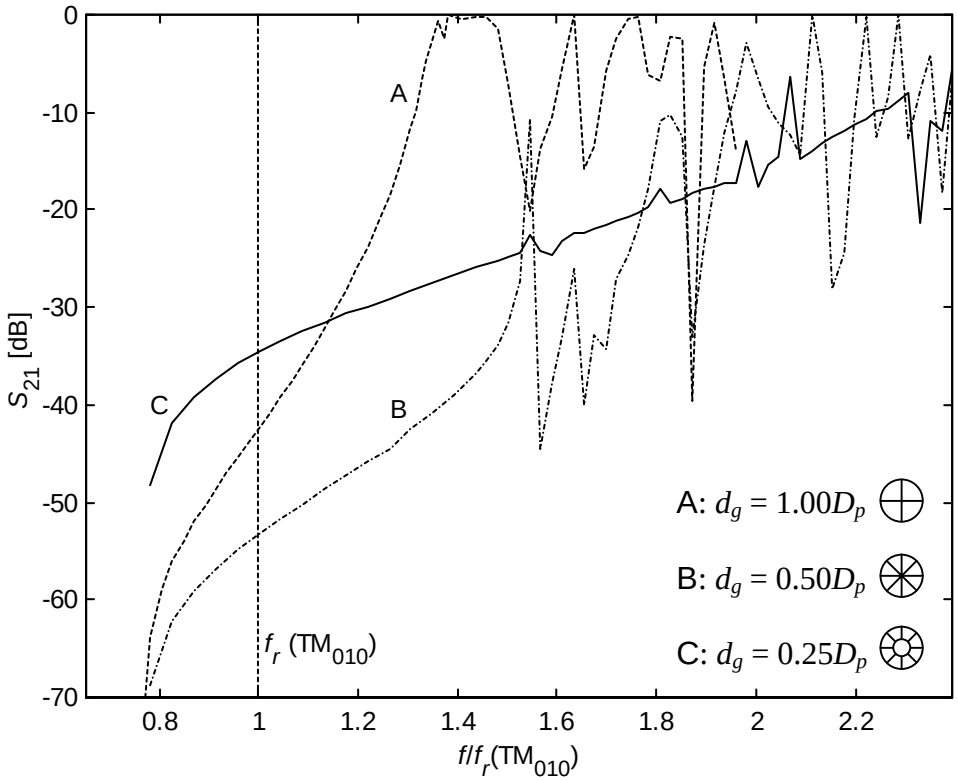

Figure 7.12 The simulated isolation of a cross grid, a star grid, and a ring grid. The lengths are those with which they have been used in various versions of the MFI WaterCut sensor.

longer are not. Figure 7.5 shows that increasing the number of sectors in a ring grid past 8 does not increase the cut-off frequency, whereas a slight increase in Q_{rad0} might be expected because of the denser structure. The small improvement in the minimum grid length would, however, be of little practical importance. Grids with more than 8 sectors are not recommended. Fig. 7.12 also shows that the frequency response of the ring grid is clean and the cut-off frequency high, whereas both the cross and the star grids have far lower cut-off frequencies and strong resonances.

Because the discussed structures do not obstruct the flow significantly, the pressure drop crated by the flow is small and does not affect the choice of end grid.

Based on the results above, cross grids with $d_g = D_p$ are recommended only for small sensors (2”), where the mechanically more complicated structure of the ring grids are difficult or expensive to manufacture. For larger sensors ring grids with $d_g = 0.25D_p$, 8 sectors, and $b/a = 0.37\ldots 0.4$ are recommended.

7.3 The MFI Downhole WaterCut Sensor

7.3.1 Introduction

The oil well technology is going in the direction of longer or multiple boreholes with production from many zones into the same main well. In order to optimise the production and the recovery this brings in the need to measure and control the

contribution from each zone separately. Currently permanent downhole instrumentation include temperature and pressure sensors. In addition such ”smart wells” would benefit largely from having watercut meters that measure the composition of the inflow from a zone. With these instruments in place, the operator would continuously know what is being produced from each zone, enabling him to optimise the well production. For the control of a well it is important to know how the watercut develops over time and with changing production rate, but especially important that a water breakthrough is detected.

Roxar has a development project going on with support from the Norwegian Research Council and the oil companies Elf Petroleum and Norsk Hydro. In this project a complete downhole watercut meter is being developed. The sensor for the downhole watercut meter will be described in this chapter. The sensor was developed by the author.

Compared to a topside meter, a downhole meter has to face entirely different environmental constraints. First of all the space available is small, and the temperature can be high. The highest temperature rating for current instruments is 180^{o}C. The pressure is also high, up to the order of 1000 bar, depending on the depth of the well. Furthermore the power available is limited. The high pressure is the easiest to overcome. It is merely a question of mechanical design. The high temperature, the low power available, and the limited space, all require that the amount of electronics put downhole be kept to an absolute minimum. Therefore the FSA method of measuring resonant frequency (see Sec. 6.9.2) was chosen as the operating principle for the electronics. The electronics will not be discussed further here, but the operating principle was mentioned because it must be taken into account in the design of the sensor because of the requirements put by the FSA method on the cleanness of the frequency response.

7.3.2 Geometrical Constraints

In an oil well the drilled hole is lined by a metal pipe called a casing or a liner (depending on dimension and location in the well) that is cemented in place. It will here mostly be called casing for simplicity. Inside the casing is the completion, which consists of another metal pipe, which is called the tubing, and the necessary safety valves and other equipment plus instrumentation. The space between the casing and the tubing is called the annulus. The produced fluids flow in the tubing to the surface.

In a producing zone of a smart well a length of the annulus is sealed off by packers. Inside this sealed off area the casing has been perforated for a certain distance by firing small shaped explosive charges. Through these perforations the fluids flow into the annulus. A distance away, inside the same sealed off area, is a valve, where the fluids flow into the tubing to be mixed with the main flow.

A watercut sensor for measuring the inflow from a zone must be located so that it can be passed by wireline tools, which are used for various interventions in the well, i.e. it must not obstruct the tubing. The only possibility is therefore to locate the sensor in the annulus between the perforations and the valve. The MFI WaterCut sensor has been designed to be mounted on the outside of the tubing. Two sensors will be mounted opposite to each other for detection of partial separation and for providing redundancy. The basic configuration is shown in Fig. 7.13, and a cross section showing the arrangement of the sensors in the annulus is shown in Fig. 7.14.

Oil wells come in various sizes. It has been decided that the watercut meter will be designed for the two most common sizes of smart wells: 4" tubing in 7" liner and $5^1/_2$" tubing in $9^5/_8$" casing. The latter alternative was chosen for the first prototype of the sensor, but the former has been chosen for the prototype of the meter. The difference between the sensors for the two sizes will only be the radius of curvature.

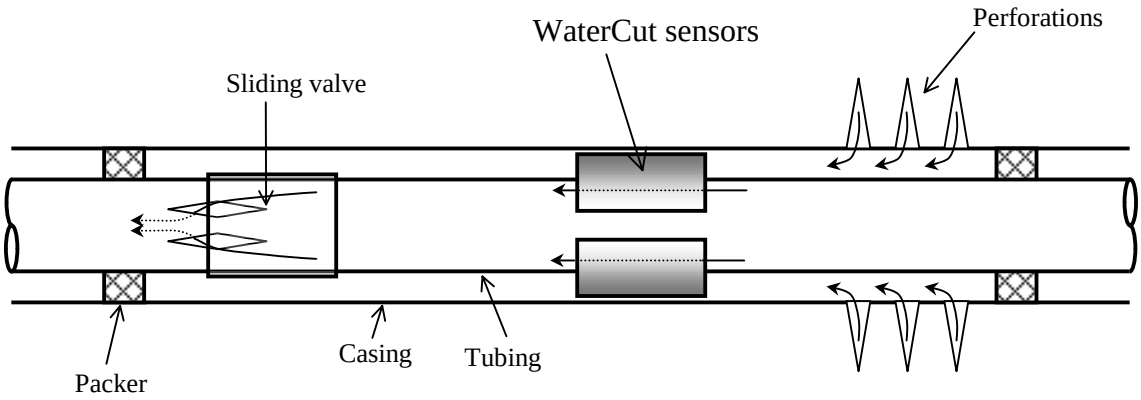

Figure 7.13 The basic arrangement of a production zone in a smart well that is equipped with two watercut sensors and a sliding valve for control of the inflow from the zone. The axial dimension has been reduced in the picture.

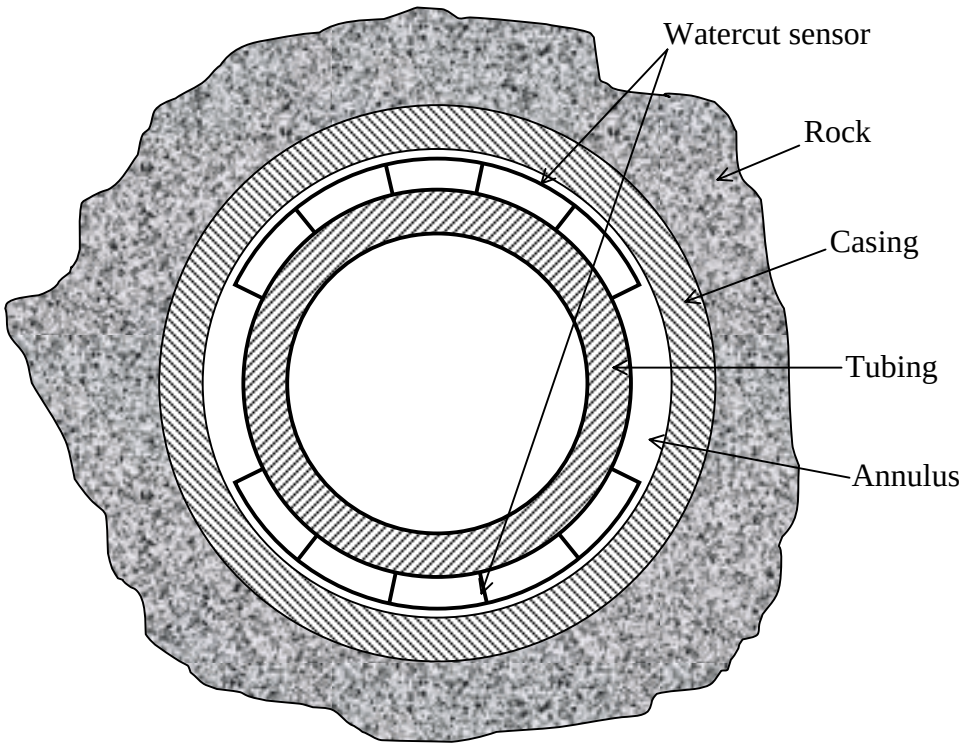

Figure 7.14 A cross section of an oil well showing the general outline of the watercut sensors mounted in the annulus.

7.3.3 Basic Design of the Sensor

Some of the design criteria for the sensor were that it should fit in the annulus, have some clearing to the casing (otherwise it would be impossible to install with the completion), cause as little pressure drop as possible, have a frequency response suitable for measurement with the FSA technique, and leave some space allowing cables and hydraulic pipes to pass on their way to gauges, valves, and watercut meters located at other producing zones deeper in the well.

The sensor that the author has designed to match the criteria is a semisectorial cavity sensor with a high b/a ratio. The ends are shorted by grids that allow the flow to pass through the sensor. The cylindrical walls are solid metal, and the end grids consist each of 4 evenly spaced radial/axial plates such that the openings in the ends are divided into 5 smaller holes.

The coupling probes are short pins that couple to the electric field. They are mounted on the concave wall for better protection during the completing of the well, when the tubing with the sensors mounted on is slided in place inside the casing. The distance from the top of the well to the location of the producing zone is typically several kilometres.

The enclosure for the electronics is a small pipe that is also mounted in the annulus a small distance downstream of the sensor.

7.3.4 Version #1 of the Sensor

The first version of the sensor (Fig. 7.15) was designed for a tubing pipe with an outer diameter of 5½" (140 mm). It has an axial length of 100 mm between the grids, a mean length of 150 mm in the perpendicular direction (i.e. the tangential direction), and an internal height of 10 mm. Hence the ratio of radii is b/a = 0.875. The grids are 50 mm long , i.e. $d_g = 0.33D_p$.

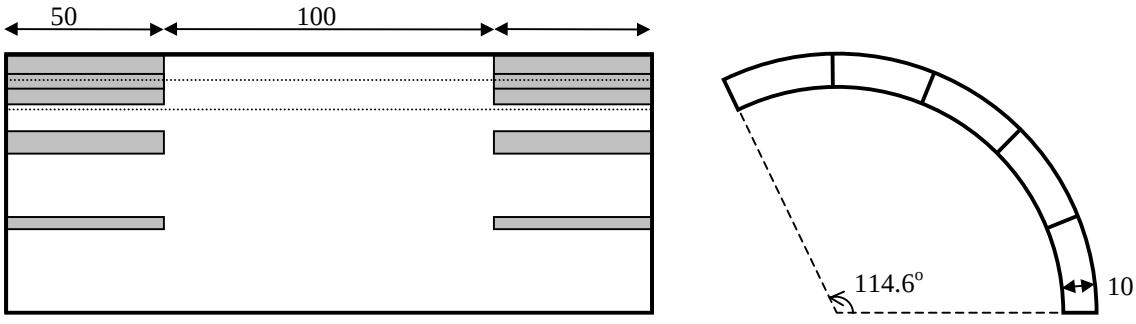

Figure 7.15 The basic design of version #1 of the sensor.

The Resonance Modes in the Sensor

Because the b/a ratio is high, the waveguide modes in the semisectorial waveguide resemble those in a low rectangular waveguide, with the broad side equal to the mean

arc of the sector (see Sec. 5.4.2). The sensor can therefore first be approximately analyzed as a rectangular cavity resonator, ignoring the curvature.

The resonant frequencies of the modes in a rectangular cavity are given by (3.49):

$$f_{r,nml} = \frac{c}{2}\left[\left(\frac{n}{A}\right)^2 + \left(\frac{m}{B}\right)^2 + \left(\frac{l}{L}\right)^2\right]^{1/2} \tag{7.6}$$

where A, B, and L denote the width, height and length of the rectangular resonator. Because the height B of the cavity is much smaller than the width A and the length L, the resonant frequencies of the modes with $m \geq 1$ will be much higher than those of the modes with $m = 0$. The lowest TE_{nm} waveguide mode in a rectangular waveguide is TE_{10}, and the lowest TM_{nm} mode is TM_{11}. Therefore all TM_{nml} resonant modes will have much higher resonant frequencies than the lowest TE_{nml} modes.

The resonant frequencies of the lowest modes are shown in Fig. 7.16 as a function of the width of the cavity. The resonant frequency of TM_{110} is 15.1 GHz, independent of A. The FSA method of measuring the resonant frequency requires that for the electronics always to lock to the right peak, there should be no other resonance peaks in the vicinity of the used peak (see Sec. 6.9.2). Figure 7.16 shows that the distance to the other modes decreases with increasing A. Hence, from this point of view only, a cavity with a width to length ratio of 1:1 would be optimal. However, achieving a high gain and a high reliability at high temperatures using currently available components becomes increasingly difficult with increasing frequency. Because also the resonant frequency of TE_{101} decreases with increasing A, a larger width to length ratio would therefore be preferable. The problem of the higher modes can be eliminated by properly locating the probes so that coupling to these modes is avoided. The first version of the sensor was therefore chosen to be 150 mm wide. The space that is left for cables and hydraulic pipes to pass the sensors would not be large enough, when two sensors are used, if the width would be significantly larger.

The electric field distribution of the modes with index values n, $l \leq 3$ are shown in Fig. 7.17. The crosses indicate probe locations. One has equal distance to the broad ends and is displaced 1/3 of the distance from the centre towards one short end, and the other one has equal distance to the short ends and is displaced 1/3 of the distance from the centre towards one broad end. In these positions at least one of the probes is always in a null of a mode with at least one even numbered index, or at least one index equal to 3, so avoiding coupling to these modes. This is also clearly seen in Fig. 7.17 from the fact that maximum one of the crosses is visible, except for TE_{101}. With the probes mounted in the indicated positions, a frequency response is achieved that is well suited for the FSA method.

The resonant frequencies were also calculated based on semisectorial resonant modes using the results from Ch. 5. The semisectorial resonator corresponding to the 150 mm x 10 mm x 100 mm rectangular resonator has the dimensions given above and in Fig. 7.15: $\varphi_0 = 114.6^o$, $b/a = 0.875$, $a = 80$ mm, and $L = 100$ mm. From the discussion in Ch. 5 it is evident that the TE_{vml} modes with $m \geq 2$, and all TM_{vml} modes, have much higher resonant frequencies than the TE_{vml} modes with $m = 1$ ($n \neq 0$). Thus the semisectorial modes with $m = 1$ correspond to the rectangular modes with

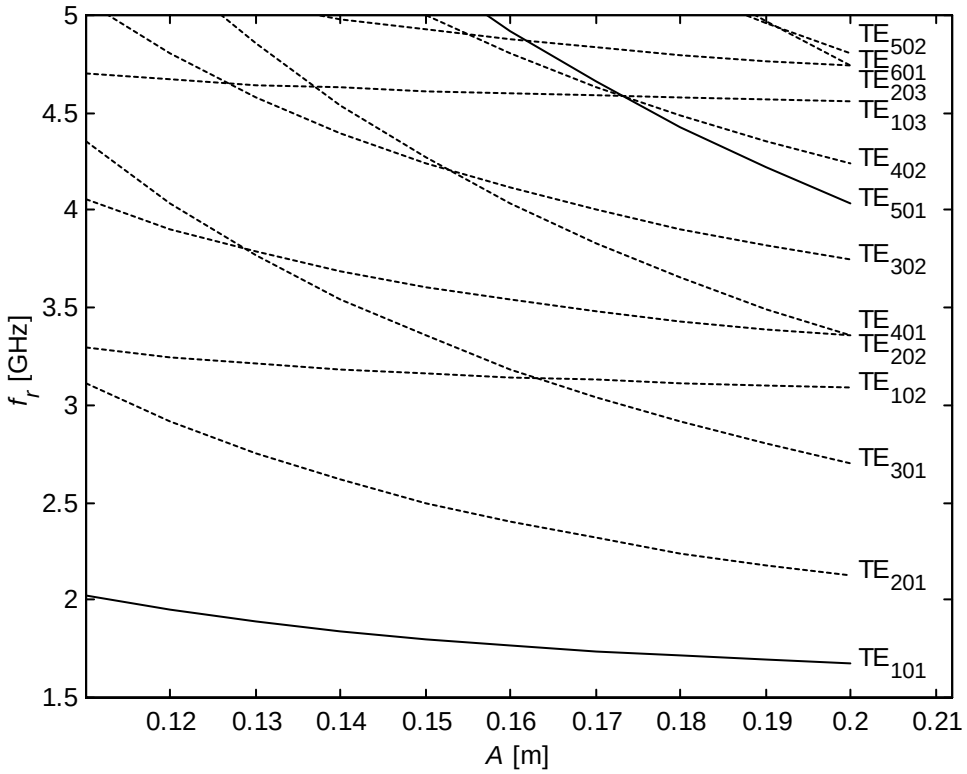

Figure 7.16 The resonant frequencies of the first 13 modes in a rectangular cavity as a function of A, when L = 100 mm, and B = 10 mm. The modes, to which coupling can be avoided with the probes located as shown in Fig. 7.17, are shown dashed.

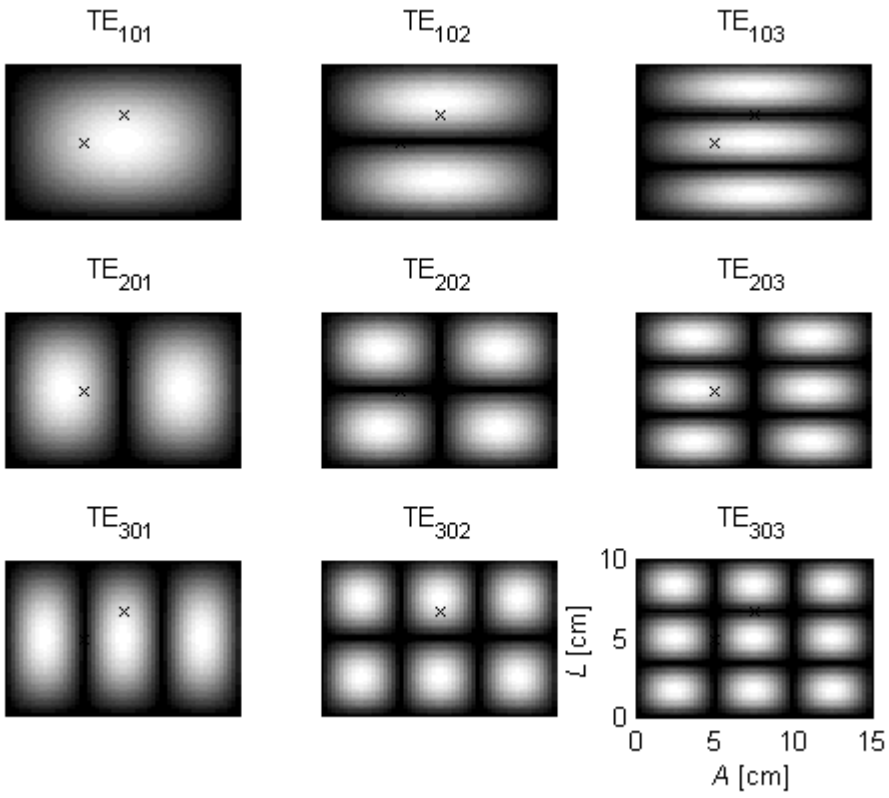

Figure 7.17 The distribution of the electric field of the modes with n, $l \leq 3$. The crosses indicate the positions of the probes that only couple to TE_{101} of the shown modes.

m = 0. The resonant frequencies of the TE_{vml} modes are given by (3.50) by substituting v for n:

$$f_{r,vml} = \frac{c}{2}\left[\left(\frac{p'_{vm}}{\pi a}\right)^2 + \left(\frac{l}{L}\right)^2\right]^{1/2} \tag{7.7}$$

The p values were calculated by solving (5.34) for the resonator with the given dimensions. The p values, the resulting resonant frequencies, and the corresponding resonant frequencies that were calculated using the rectangular resonator approximation are given in Table 7.1, together with measured values (see below). It is seen that the difference between the results of the exact and the approximate calculations of the resonant frequency is very small.

Prototype for Testing the Calculations

A prototype, with the nominal dimensions equal to those given above, was built for testing the calculations. The quality of the work was, however, not very high. The resulting frequency response was measured using a network analyzer and is shown in Fig. 7.18. It is seen that the coupling to the higher modes is much smaller than to the main mode, but not zero, as intended. The reason for the finite coupling is probably a combination of the the poor metal work and the perturbation of the electric field caused by the end grids and the probes.

The prototype was built so that the locations of the probes could be changed. In that way the coupling to the higher modes could be increased (see Fig. 7.20) and their resonant frequencies be derived accurately. The results are shown in Tab. 7.1. The measured resonant frequencies are 3.6…9.4% lower than the calculated. Due to the poor quality of the sensor, no absolute conclusions can be drawn from these deviations. It seems, however, that the deviation is proportional to l, which indicates that it is at least in part caused by the fringing field in the end grids. Because the exact resonant frequency of the sensor is not important for the application, the achieved accuracy is sufficient.

Simulation of the Frequency Response Using HFSS

A semisectorial sensor was simulated with HFSS for the purpose of optimising the design. By the time this was done, it had been decided that the first downhole watercut sensor was to be built for a 4” tubing, not 5½”. The mechanical design of the carrier (piece of ”tubing” with threads in the ends, with sensors, electronics, cables etc. mounted on) had been worked out, taking into account the space required by the probes on the concave side of the sensor. Maintaining the mean length of the arc, the simulated sensor was given the following dimensions: a = 72 mm, b = 62 mm, φ_0 = 128.3°, L = 100 mm. Table 7.1 shows the calculated resonant frequencies both for the 4” and the 5½” designs. In practice the resonant frequencies are the same.

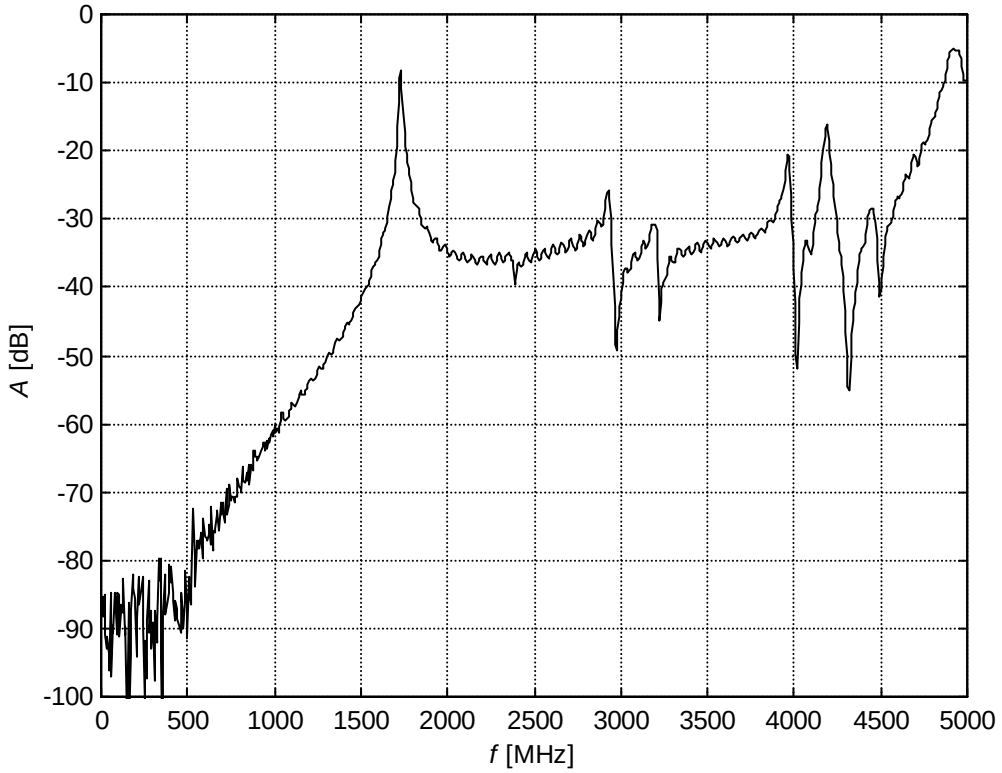

Figure 7.18 The measured frequency response of the prototype of version #1 of the downhole sensor for 5½" tubing.

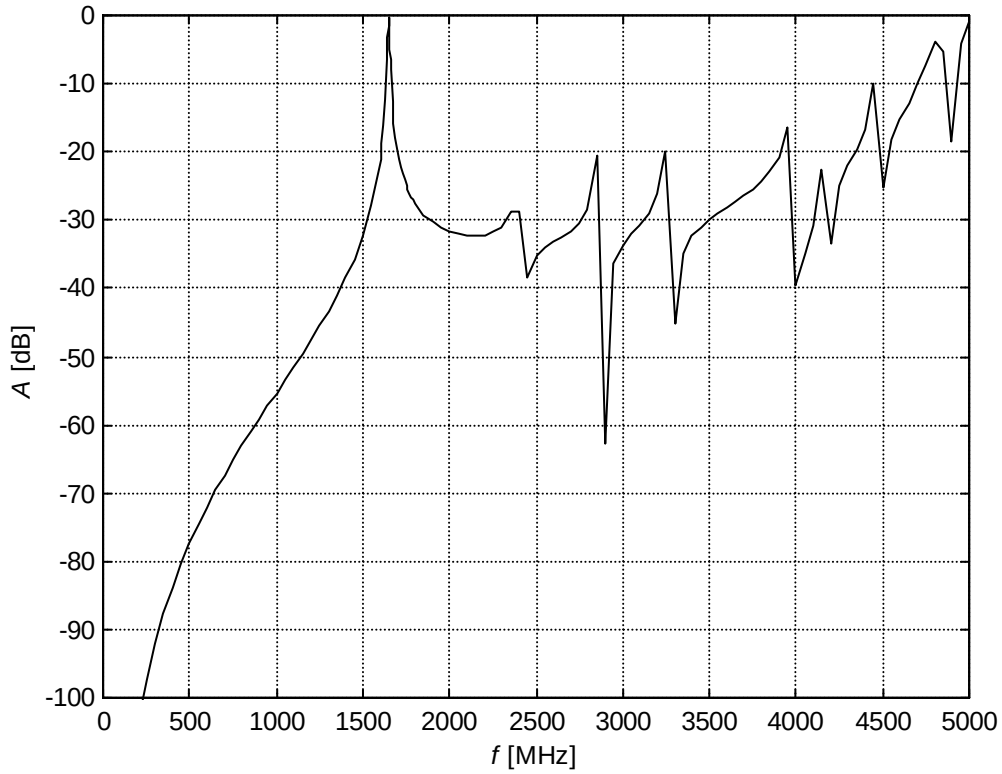

Figure 7.19 The frequency response of version #1 of the downhole sensor for 4" tubing as simulated with HFSS.

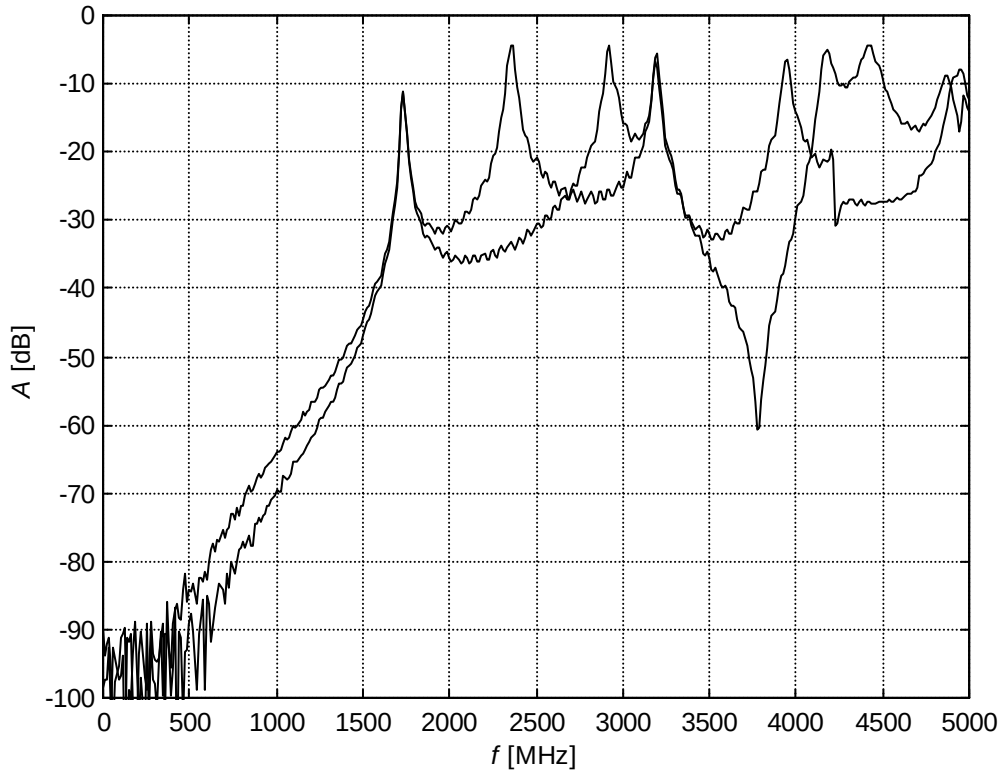

Figure 7.20 A superposition of two measurements of the frequency response of the prototype of version #1 of the downhole sensor for 5½" tubing. The probe locations have been varied to show all the modes of interest. Compare to Fig. 7.18, which was measured with the probes in the positions indicated in Fig. 7.17.

Table 7.1 Comparison of calculated and measured resonant frequencies for version #1 of the downhole sensor. The measurements were performed with a network analyzer using the prototype with a = 80 mm. For the semisectorial modes ν was calculated from (5.31), $p'_{\nu 1}$ was solved from (5.34), and f_r was calculated from (7.7). For the rectangular modes f_r was calculated from (7.6).

Calculated										Meas-ured	
Semisectorial cavity, L = 100 mm								Rectangular approximation 150x10x100			
Mode	n	a = 80 mm, φ_0 = 114.6°			a = 72 mm, φ_0 = 128.3°						
		ν	$p'_{\nu 1}$	f_r	ν	$p'_{\nu 1}$	f_r	Mode	f_r	f_r	Δ[%]
$TE_{\nu 11}$	1	1.571	1.677	1.803	1.403	1.509	1.803	TE_{101}	1.803	1.739	-3.6
$TE_{\nu 11}$	2	3.142	3.353	2.501	2.806	3.018	2.501	TE_{201}	2.500	2.375	-5.0
$TE_{\nu 12}$	1	1.571	1.677	3.163	1.403	1.509	3.162	TE_{102}	3.162	2.925	-7.5
$TE_{\nu 11}$	3	4.712	5.029	3.355	4.209	4.527	3.356	TE_{301}	3.354	3.198	-4.6
$TE_{\nu 12}$	2	3.142	3.353	3.606	2.806	3.018	3.606	TE_{202}	3.606	-	-
$TE_{\nu 12}$	3	4.712	5.029	4.244	4.209	4.527	4.244	TE_{302}	4.243	3.953	-6.8
$TE_{\nu 11}$	4	6.283	6.705	4.274	5.611	6.034	4.273	TE_{401}	4.272	4.075	-4.6
$TE_{\nu 13}$	1	1.571	1.677	4.610	1.403	1.509	4.610	TE_{103}	4.610	4.177	-9.4
$TE_{\nu 13}$	2	3.142	3.353	4.925	2.806	3.018	4.925	TE_{203}	4.924	-	-
$TE_{\nu 12}$	4	6.283	6.705	5.001	5.611	6.034	5.001	TE_{402}	5.000	-	-

A frequency span from 100 MHz to 5 GHz, with a step of 50 MHz, was used in the simulation. In the vicinity of the main resonance peak the step was decreased first to 10 MHz and then to 2 MHz. The resulting frequency response is shown in Fig. 7.19. The resonant frequency given by the simulation was f_r = 1.649 GHz, which is 8.5% lower than the calculated, and 5.2% lower than the measured. The deviations are probably due to the fringing field in the end grids and the inaccuracy of the dimensions of the built prototype. The overall similarity to the measured response is good.

7.3.5 Version #2 of the Sensor

The results obtained with version #1 were good, but there was a desire to further lower the resonant frequency in order to improve the gain margin of the FSA electronics. It was therefore decided to increase the length of the resonator but maintain the aspect ratio, i.e. L was increased from 100 mm to 225 mm. The locations of the probes were changed accordingly so as to maintain the same type of relation to the short and broad ends of the cavity (see Fig. 7.24).

Figure 7.21 shows the mode diagram as a function of L, and Table 7.2 shows the calculated resonant frequencies for L = 225 mm.

Simulation of the Frequency Response Using HFSS

A new simulation of the frequency response was performed after increasing the length of the sensor (a = 72 mm, φ_0 = 128.3°, L = 225 mm). The result is shown in Fig. 7.22. The modes were identified based on the electric field pattern visualized by HFSS. It clearly shows that the higher modes have been shifted relative to each other compared to the simulation in Fig. 7.19, even though the aspect ratio of the rectangular approximation was maintained. This is a further indication that the fringing field in

Table 7.2 The calculated and measured f_r for version #2 of the downhole sensor. For the semisectorial modes ν was calculated from (5.31), $p'_{\nu 1}$ was solved from (5.34), and f_r was calculated from (7.7). For the rectangular modes f_r was calculated from (7.6).

Calculated										Meas-ured	
Semisectorial cavity, L = 225 mm								Rectangular approximation 150x10x225			
Mode	n	a = 80 mm, φ_0 = 114.6°			a = 72 mm, φ_0 = 128.3°						
		ν	$p'_{\nu 1}$	f_r	ν	$p'_{\nu 1}$	f_r	Mode	f_r	f_r	Δ[%]
$TE_{\nu 11}$	1	1.571	1.677	1.203	1.403	1.509	1.202	TE_{101}	1.202	1.082	-1.75
$TE_{\nu 12}$	1	1.571	1.677	1.667	1.403	1.509	1.667	TE_{102}	1.667	-	-
$TE_{\nu 11}$	2	3.142	3.353	2.109	2.806	3.018	2.110	TE_{201}	2.108	-	-
$TE_{\nu 13}$	1	1.571	1.677	2.236	1.403	1.509	2.236	TE_{103}	2.236	-	-
$TE_{\nu 12}$	2	3.142	3.353	2.405	2.806	3.018	2.405	TE_{202}	2.404	-	-
$TE_{\nu 13}$	2	3.142	3.353	2.829	2.806	3.018	2.829	TE_{203}	2.828	-	-
$TE_{\nu 14}$	1	1.571	1.677	2.848	1.403	1.509	2.848	TE_{104}	2.848	-	-
$TE_{\nu 11}$	3	4.712	5.029	3.075	4.209	4.527	3.075	TE_{301}	3.073	-	-
$TE_{\nu 12}$	3	4.712	5.029	3.284	4.209	4.527	3.285	TE_{302}	3.283	-	-
$TE_{\nu 14}$	2	3.142	3.353	3.334	2.806	3.018	3.334	TE_{204}	3.333	-	-

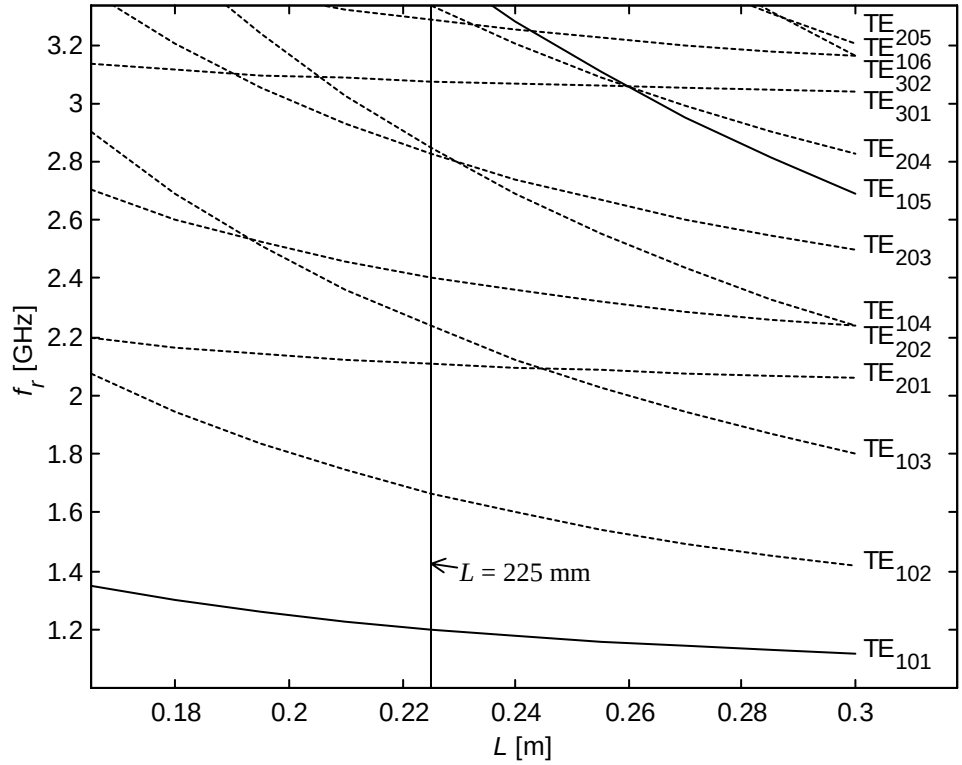

Figure 7.21 The resonant frequencies of the first 13 modes in a rectangular cavity as a function of L, when A = 150 mm, and B = 10 mm. The modes, to which coupling can be avoided with the probes located as shown in Fig. 7.17 (with A and L switched, n and l switched, and the scales multiplied by 1.5), are shown dashed.

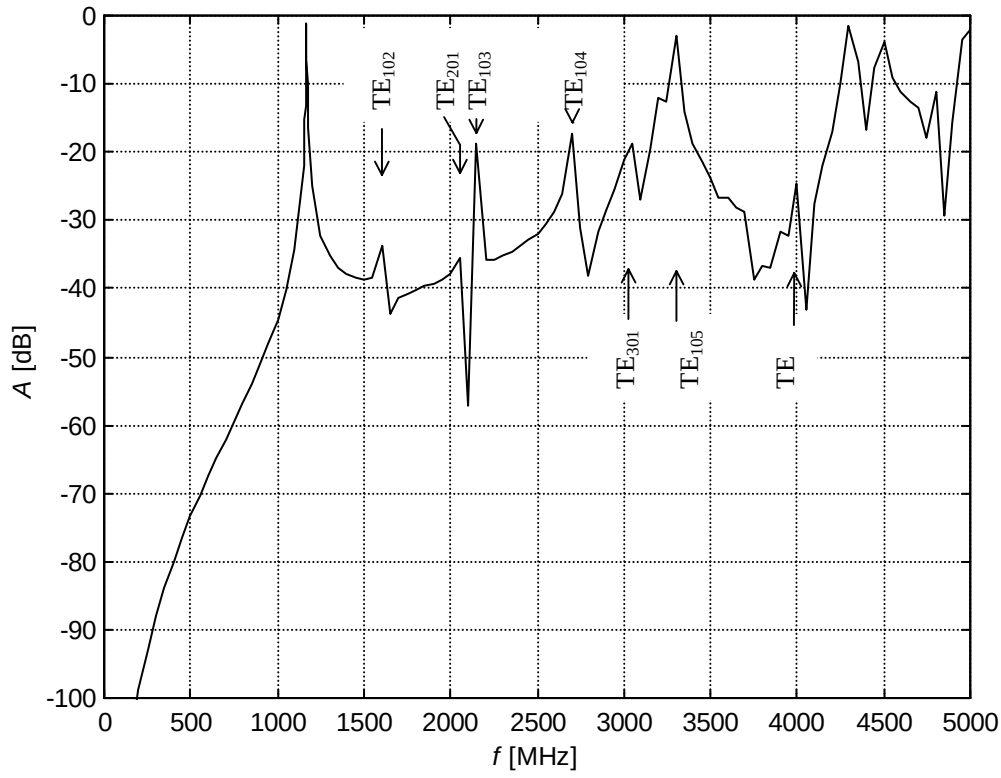

Figure 7.22 The simulated frequency response of version #2 of the downhole sensor for 4” tubing. The modes were identified based on the electric field pattern visualized by HFSS. The names of the modes refer to the rectangular cavity approximation.

the end grids influences the deviation between the theoretically calculated and the simulated resonant frequencies.

The simulation shows that the frequency response is well suited for measurement with the FSA method. It can, however, be further improved by optimising the locations of the probes. Before this was done, the probes were optimised to provide the desired coupling, because the size of the probes probably also influences the coupling to the higher modes.

Optimization of the Size and Shape of the Probes Using HFSS

The coupling probes are pins that couple to the electric field. When they are located as shown in Fig. 7.17, they have individual coupling quality factors (Q_{e1} and Q_{e2}) that are identical within the accuracy of the simulations of HFSS. The total quality factor Q_{ext}, as defined by (6.14), is therefore used below.

The external structure of the probes, which determines the coupling, is depicted in Fig. 7.23, with the important dimensions defined. All simulations have been performed with the sensor filled with air. The coupling in other situations can be calculated based on the discussion in Ch. 6.

Version #1 of the sensor (L = 100 mm), was simulated with probes with the following dimensions and permittivity: d_i = 10 mm, d_p = 4 mm, l_p = 6 mm, and ε_{ri} = 4.8. This gave the coupling Q_{ext} = 171.0.

Version #2 was first simulated with the same probes as version #1, resulting in the coupling Q_{ext} = 549.3. The decrease in the coupling is mainly due to the larger volume of the sensor, which leads to a lower energy density. When the diameter of the pin was increased to d_p = 6 mm, the coupling increased to Q_{ext} = 465.5. When the diameter of the insulator was also increased, to d_i = 12 mm, the coupling increased to Q_{ext} = 336.1. In these first three simulations of version #2 the location of probe P_1 (see Fig. 7.24) was erroneously put to z = –25 mm, while it should have been –37.5 mm (=

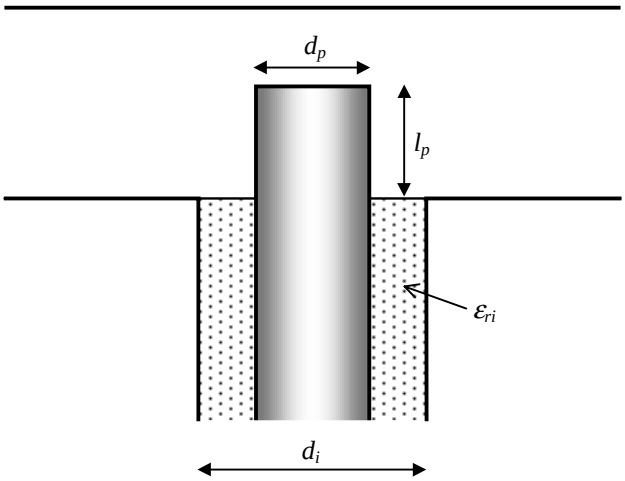

Figure 7.23 The shape of the external part of the probes, with definition of the notations.

225 mm/6). When this was corrected, the coupling slightly decreased to Q_{ext} = 361.1. This coupling was considered satisfactory, and the probes were therefore designed with the following dimensions and permittivity: d_i = 12 mm, d_p = 6 mm, l_p = 6 mm, and ε_{ri} = 4.8. The simulation in Fig. 7.22 was performed with these probes.

Optimization of the Locations of the Probes Using HFSS

As is seen from the frequency response in Fig. 7.22, the coupling to the modes that are shown dashed in Fig. 7.21 (modes with at least one even numbered index, or one index equal to 3) is not zero, as it would theoretically be, if the probes and the end grids would not perturb the electric field pattern. HFSS was used for optimising the locations of the probes so as to minimize the coupling to the next three modes (TE_{102}, TE_{201}, and TE_{103}). These modes were given the highest priority, because they are closest to the used resonance mode. The coupling to the higher modes can also be expected to decrease, when the locations are optimised for the mentioned modes.

Using the cylindrical co-ordinate system defined in Fig. 7.24, the starting point for the optimization was: P_1: z_1 = –37.5 mm, $\varphi_1 = 0^o$, and P_2: z_2 = 0 mm, $\varphi_2 = 21.4^o$ (= $128.3^o/6$). By studying which of the probes that was supposed to be in the null of a mode, and which of the co-ordinates of the probe that moves it relative to the null, it could be concluded that the following co-ordinates should be the subject of optimisation: z_2 for the coupling to TE_{102}, φ_1 for the coupling to TE_{201}, and z_1 for the coupling to TE_{103}. After a few manual iterations the following co-ordinates were found to significantly decrease the coupling to the mentioned modes: z_1 = –38.2 mm (Δz_1 = –0.7 mm), $\varphi_1 = 2^o$ ($\Delta\varphi_1 = 2^o$), z_2 = –1.5 mm (Δz_2 = –1.5 mm), $\varphi_2 = 21.4^o$.

The whole frequency response was simulated again with the new probe co-ordinates. The result is shown in Fig. 7.25. It can be concluded that the frequency

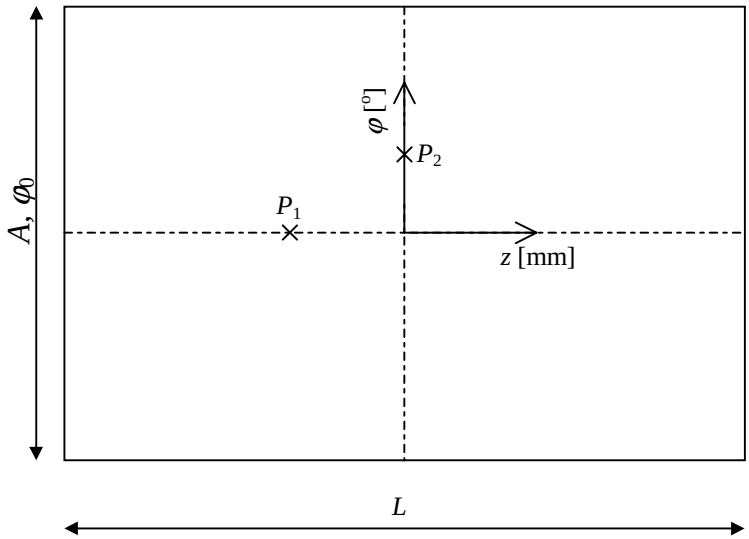

Figure 7.24 The cylindrical co-ordinate system for expressing the locations of the probes, with the theoretical locations (i.e. excluding the disturbing influence of the probes and the end grids) marked. Note that the sensor is shown in a flat 2-dimensional projection.

response has been significantly improved by the optimization of the probe locations and is well suited for measurement using the FSA method.

Measurements of the Prototype of Version #2 of the Sensor

A sensor with the dimensions given above was built. Because of the geometrical constraints that limit the maximum protrusion of the probes on the concave outside of the sensor, the probes had a 90^o bend such that a high-temperature coaxial cable was attached to the side of the pill-shaped rear part of the probes. The outer diameter of the cable was 3 mm, the sheath was made of a high-grade steel, and the dielectric was a ceramic powder. Because of the large diameter of the centre pin of a probe, and the closeness of the rear end of the outer conductor, there was a relatively large capacitance from the rear end of the pin to the rear end of the outer conductor. This shunt capacitance provides a shortcut to ground, which limits the coupling. The simulations, which gave a coupling of $Q_{ext} = 361.1$ (see above), were performed with straight probes for simplicity. To explore the influence of the shunt capacitance two sets of probes were made, which had a slightly different distance from the rear end of the pin to the outer conductor. The measured coupling was $Q_{ext} = 498.4$ for the probes with the shorter distance, and $Q_{ext} = 307.3$ for the probes with the larger distance. The results show that the capacitance strongly influences the coupling, and the probe design with the larger distance was adopted. The results reported below were measured with these probes.

The probes were produced so that a ceramic reinforced glass ($\varepsilon_{ri} = 4.8$) was cast between the centre conductor and the outer conductor, and the steel sheath of the cable was EB (electron beam) welded to the outer conductor of the probe. The probes are therefore perfectly watertight and pressure resistant. Because of the materials the probes and the sensor can also stand the specified temperature of 180^oC, and far beyond.

Figure 7.26 shows the measured frequency response, with the sensor filled with air. Comparison to Fig. 7.25 shows that the simulation has predicted the general shape of the frequency response well, especially considering that the resolution of the simulated response is 50 MHz outside the main resonance peak, while it is 6.2 MHz in the whole measured response. Figure 7.26 also shows that the optimization of the probe locations was less successful than expected. The reason is probably a combination of the production tolerances, and the limited accuracy of the simulations. The result is, however, acceptable. Because the peaks of TE_{102}, TE_{201}, and TE_{103} are much lower than the main peak, there is no risk for confusion of peaks, when the FSA method is used for measuring the resonant frequency.

The measured resonant frequency was 1183.9 MHz, while the simulated was 1169 MHz, and the calculated 1202 MHz. Hence the real resonant frequency deviated from the calculated by –1.51% and from the simulation by 1.27%.

The sensor was measured filled with static emulsions of motor oil and water, with a salinity of $S = 3\%$. The measured frequency responses are shown in Fig. 7.27, the peak height in Fig. 7.28, and the coupling (Q_{ext}) in Fig. 7.29. Fig. 7.27 shows that the peak is clearly defined for all the measured cases, and Fig. 7.29 shows that the coupling obeys model (6.7) relatively well. Now also the coupling measured in air fits the model better than was the case with the CFR sensor (see Fig. 6.15).

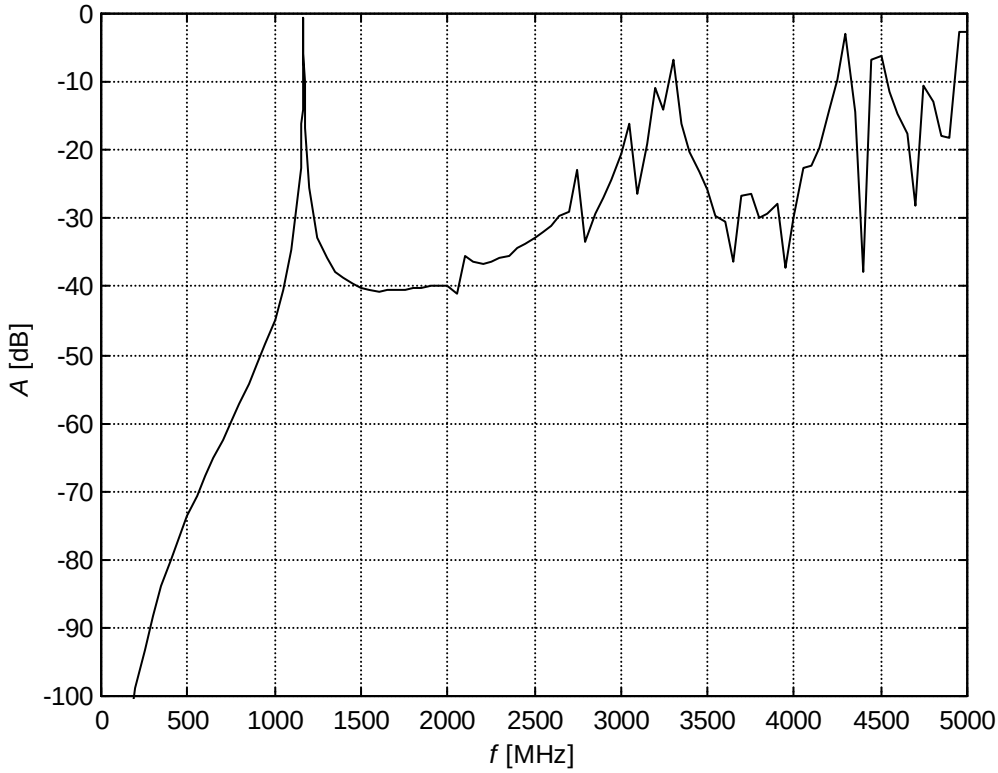

Figure 7.25 The simulated frequency response after optimization of the probe locations. Compare to Fig. 7.22.

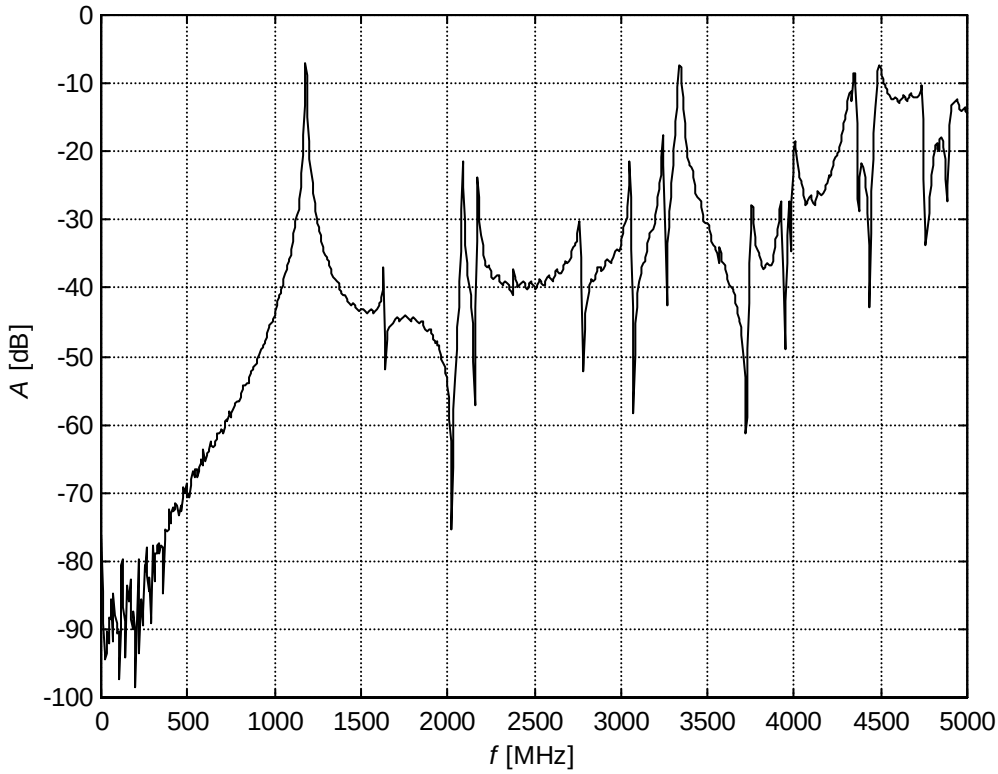

Figure 7.26 The measured frequency response of the prototype of version #2 of the downhole sensor for 4” tubing. The sensor was filled with air.

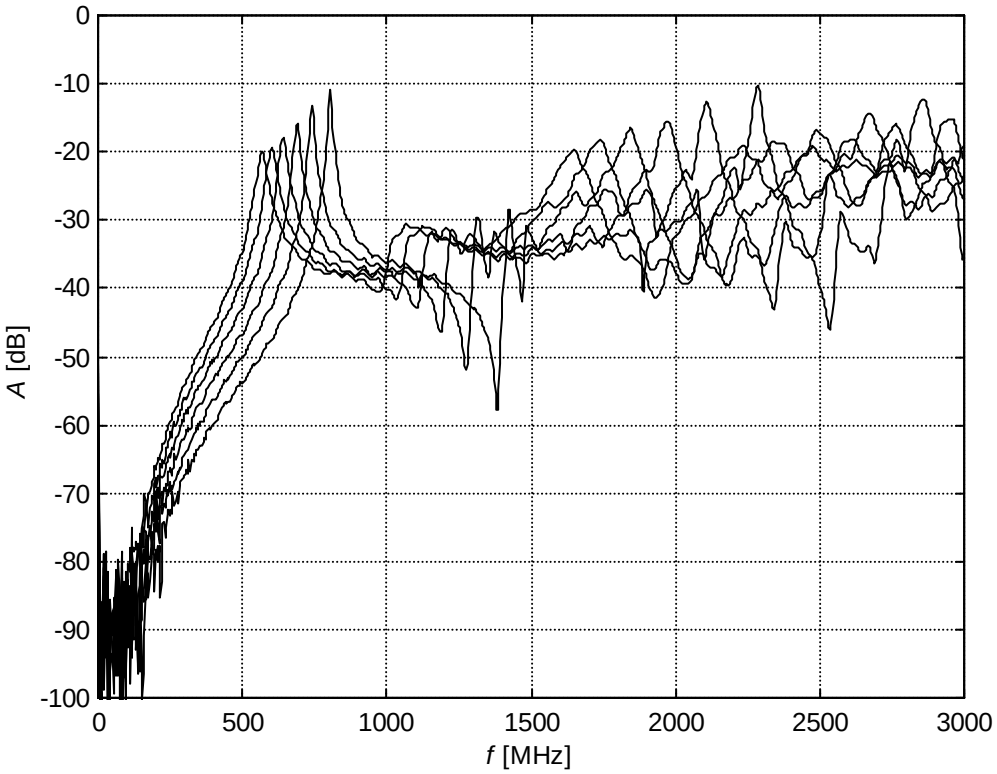

Figure 7.27 The measured frequency response of the prototype of version #2 of the downhole sensor, when it was filled with various mixtures of motor oil and water (S = 3%).

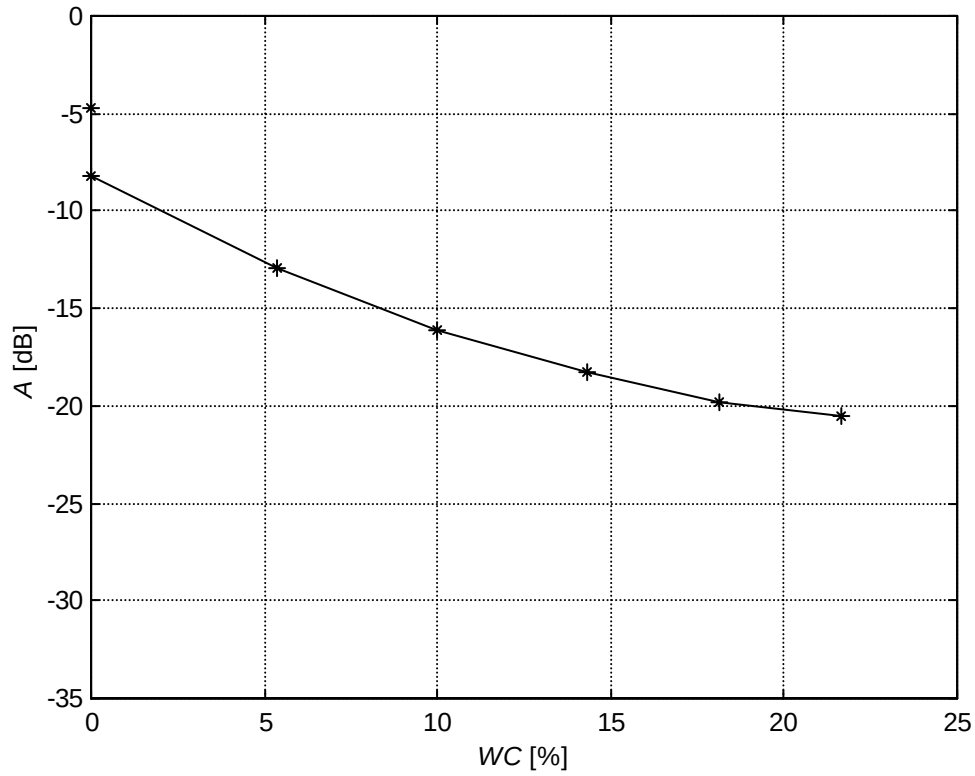

Figure 7.28 The measured peak height of the prototype of version #2 of the downhole sensor, when it was filled with various mixtures of motor oil and water (S = 3%). The single point on the y-axis (−4.7 dB) was measured for the empty sensor.

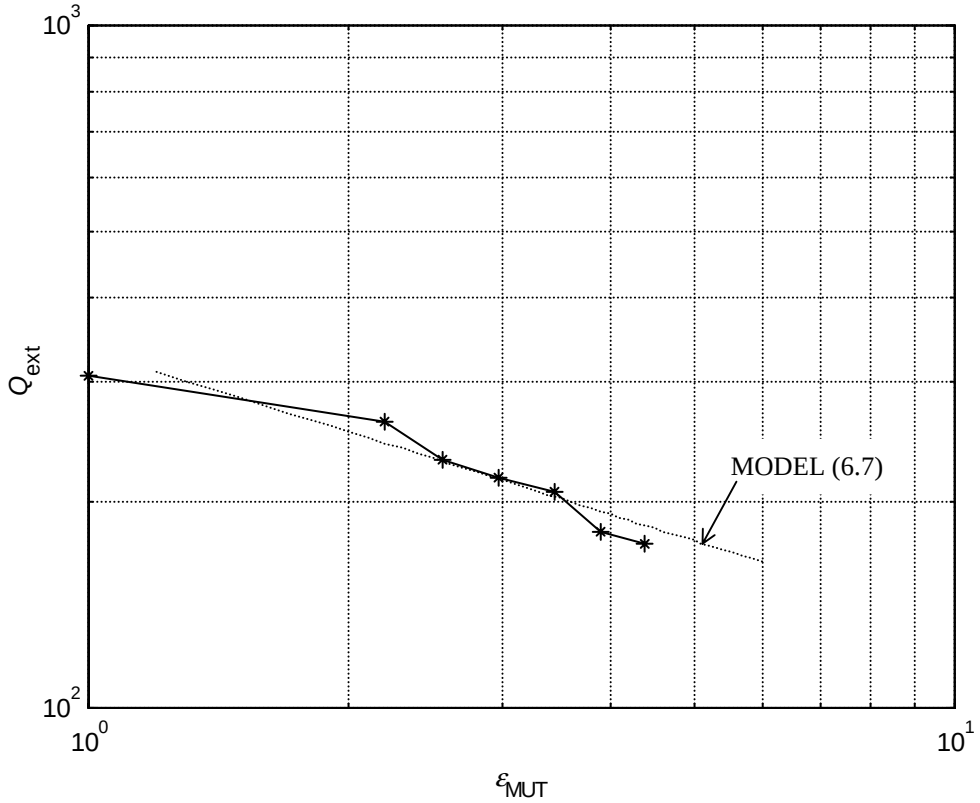

Figure 7.29 The coupling (Q_{ext}) calculated from the measurements of the prototype of version #2 of the downhole sensor, when it was filled with various mixtures of motor oil and water (S = 3%).

7.3.6 The Length of the End Grids

The length of the end grids was first designed to be d_g = 50 mm, because this was expected to be enough. The simulations of the sensor gave an ”infinitely high” radiation quality factor, indicating that the expectation was right. Because the value of Q_{rad0} is not known, an exact calculation of Q_{rad} can not be performed. An estimation of the efficiency of the grids will be performed here by comparing to the grids studied in Sec. 7.2.

The grids of the downhole sensor consist each of 4 evenly spaced radial/axial plates such that the openings in the ends are divided into 5 smaller holes (see Fig. 7.15). The size of the holes is consequentially: φ_0 = 25.7°, b/a = 0.861, a = 72 mm. The lowest mode is the semisectorial mode $TE_{\nu 1}$, with ν = 7.013. This has the p value $p'_{\nu 1}$ = 7.541. Eq. (5.18) now gives f_c = 5.001 GHz. Using the rectangular approximation, the holes are waveguides with the dimensions: A = 30 mm, B = 10 mm. This gives f_c = 5.000 GHz, which is practically the same result. The ratio to the theoretical resonant frequency is now

$$\frac{f_c}{f_{rt}} = \frac{5.001}{1.202} = 4.160 \qquad (7.8)$$

Equation (4.3) gives that the below-cut-off attenuation is –44.1 dB, and (4.10) that the radiation quality factor is

$$Q_{\mathrm{rad}} = 25975 Q_{\mathrm{rad0}} \tag{7.9}$$

Taking into account that probably $Q_{\mathrm{rad0}} >> 1$, the calculations support the result from the simulations that Q_{rad} is very high.

The measurements of the sensor with ring grids (see Sec. 7.2.3) gave $Q_{\mathrm{rad}} = 4280$ for $d_g = 0.25 D_p$, which was observed to be enough and therefore chosen as the design length. Assuming that $Q_{\mathrm{rad0}} = 1$, and solving (4.10) for d_g, gives that the same degree of isolation would be achieved in the downhole sensor with $d_g = 41.1$ mm. If $Q_{\mathrm{rad0}} = 10$ is assumed, the result is $d_g = 29.8$ mm, and if $Q_{\mathrm{rad0}} = 20$ is assumed, the result is $d_g = 26.4$ mm. Because Q_{rad0} is not yet known, and the space in the axial direction is not limited, it was decided to maintain $d_g = 50$ mm.

7.4 A Humidity Sensor for Harsh Environments

7.4.1 Introduction

The humidity of the air is an important control parameter in many industrial processes, and needs therefore to be measured. In some cases, such as dryers and ovens, the environmental conditions are harsh for conventional measuring methods. For example in a dryer for veneer sheets the temperature is typically 170$^{\mathrm{o}}$C and the air contains dust and vaporized resin. In addition the humidity may be high, up to the order of 1 kg of water vapour per 1 kg of dry air. Conventional humidity sensors incorporating materials such as metal oxide ceramics [Seiyama et al., 1983], organic polymers [Inami et al., 1985], and thin films [Jachowicz and Senturia, 1981] etc. encounter problems with the operating range of humidity, high ambient temperature, long period of operation, dust, oil vapours, or organic vapours etc. Therefore the author and his colleagues at the Radio Laboratory of the Helsinki University of Technology developed a microwave humidity meter for harsh environmental conditions [Vainikainen et al., 1986], [Toropainen et al., 1987]. The electronics of the meter was further developed by Toropainen [Toropainen, 1989]. The sensor of this meter will be briefly described here.

7.4.2 The Design of the Humidity Sensor

The humidity sensor is a cylindrical cavity resonator with end grids, as shown in Fig. 7.30. It is designed to be mounted in the open space inside an oven or a drier. The end grids allow the air to pass freely through the sensor. It operates on the TE_{011} mode (see Fig. 3.3 and Sec. 3.7.1), which has an electric field that is zero on all walls. Because the permittivity affects the resonant frequency through the electric field only, the sensor is insensitive to a thin layer of contamination (e.g. condensed resin and dust) on the walls. The reflection coefficient S_{11} is measured as a function of frequency. The sensor was designed for a frequency of 9.5 GHz (TE_{011}).

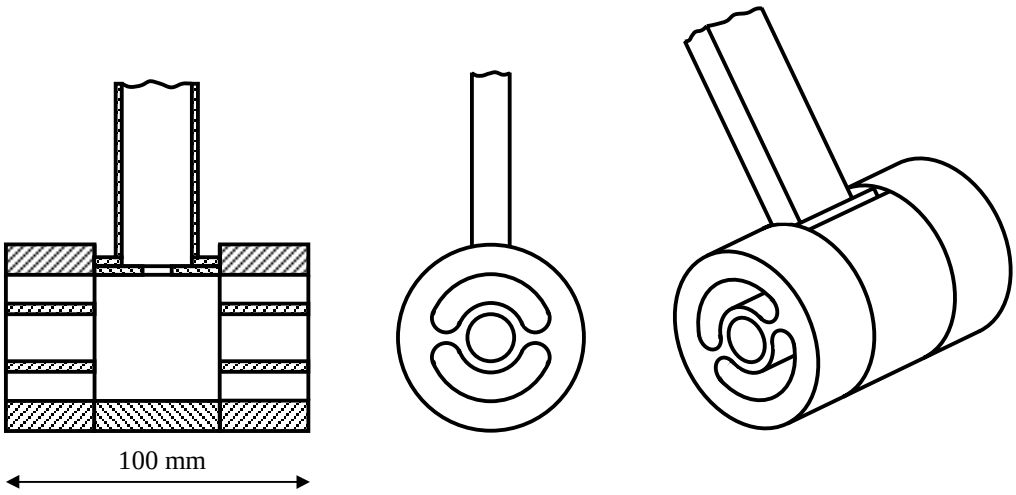

Figure 7.30 The microwave humidity sensor for harsh environments. The sensor is a cavity resonator operating on TE_{011}. The resonant frequency is 9.5 GHz and the signal is coupled to the cavity through an iris. S_{11} is measured as a function of frequency.

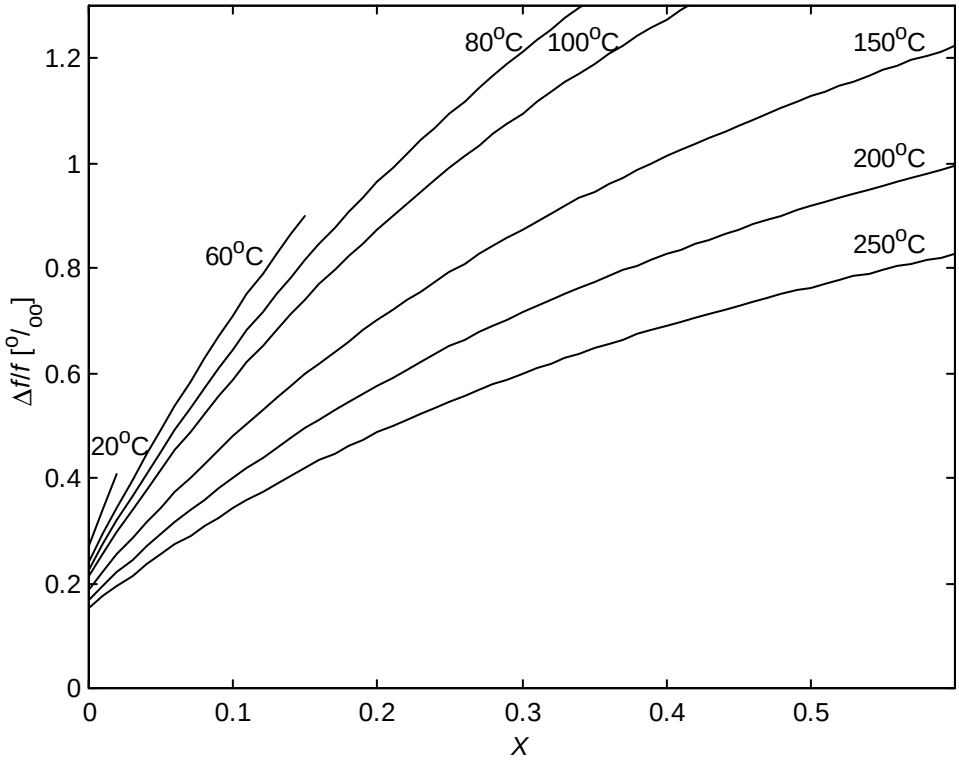

Figure 7.31 The negative relative frequency change as a function of humidity ratio (X is the ratio of the mass of the water vapour to the mass of the dry air), and temperature in a microwave cavity resonator. The graphs are based on (7.10), with p_{tot} = 0.1013 MPa.

A similar sensor operating on TE_{011} has been reported used for the measurement of the refractive index (th esquare root of the permittivity) of the atmosphere [Crain and Deam, 1952]. For that application the resonant mode was chosen because of the high Q_u, allowing the measurement of the resonant frequency with a high accuracy. Another related sensor has been reported used for the measurement of the density of hydrogen in both liquid, two-phase, and gaseous phase [Wenger and Smetana, 1972]. That sensor also operated on TE_{011}, but differed from the current design by having longer end ”grids”, with a ring in the centre and four radial legs, like a ring grid with four sectors. The legs were used mainly for holding the ring in place and were therefore limited to the outward facing part of the grids. The section of the grid that faced the cavity only consisted of the centre pipe, thus forming a coaxial section.

Because of the all-metal structure the humidity sensor can withstand high temperatures. The effect of the thermal expansion on the resonant frequency is, however, large compared to the effect of the humidity in the air. The temperature of the sensor must therefore be measured and compensated for. Preferably a material with an as small thermal expansion coefficient as possible should be used. The prototype of the sensor was built using a metal alloy called invar, which has a thermal expansion coefficient that is near zero in a temperature range around room temperature. Outside this range the coefficient grows, but stays low compared to that of most other metals.

7.4.3 The Method of Coupling

The signal is fed through a rectangular waveguide and coupled to the cavity through a magnetic aperture (see Fig. 3.4d) in the shorted end of the waveguide. The waveguide is oriented with the broad side parallel to the axis of the cylindrical cavity so that the aperture couples to the axial magnetic field at the wall. Because the TM_{nml} modes have no axial magnetic field, the aperture only couples to the TE_{nml} modes, thus avoiding coupling to TM_{111}, which is a degenerate mode to TE_{011}. Only one coupling is used because the resonant frequency is deduced from the reflection coefficient.

7.4.4 The End Grids

The structure of the end grids is shown in Fig. 7.30. They are ring grids with only two sectors, $b/a = 0.54$, and $d_g = 0.7D_p$. The sectorial holes are rounded at the ends, which makes the calculation of the cut-off frequency using semisectorial waveguide modes inaccurate. For the sake of simplicity the rectangular waveguide approximation is therefore used here to estimate the cut-off frequency of the grids.

The mean width of the waveguide is $A = 44.5$ mm, giving a cut-off frequency for TE_{10} of $f_c = 3.4$ GHz. Hence, the cut-off frequency in the grids is far lower than the resonant frequency of the TE_{011} mode, i.e. the isolation is completely based on Q_{rad0}. This is possible because the coupling from the TE_{011} mode in the cavity to the TE_{n0} modes in the grids is low, because their electric fields are orthogonal (tangential in the cavity, and radial in the grids). The first mode in the grids with a tangential electric field component is TE_{01}. It has a cut-off frequency of $f_c = 15.8$ GHz, which gives $f_c/f_r = 1.66$, which is somewhat higher than the value 1.593 given by (7.2) for the star

grids. Because the grids are also longer than the star grids (d_g = 0.7D_p compared to 0.5D_p for star grids), neither the modes with other than a purely radial electric field do significantly affect the resonance. The end grids in the hydrogen sensor that was mentioned above [Wenger and Smetana, 1972], are based on nearly the same principle. The TE_{011} mode does not couple to the coaxial TEM mode in the grids because of orthogonal electric fields.

The frequency change over the whole measurement range of humidity is small (see below). The requirements on the purity of the frequency response are therefore low. Because the coupling method only couples to TE_{nml} modes, and the grids are tight enough for TE_{011}, there are therefore no problems in identifying the right peak under any measurement conditions.

Measuring small changes of the resonant frequency with a high accuracy requires that the peak is clean and narrow, i.e. that Q_l is high. The measured loaded quality factor of the cavity was Q_l = 1240, and the calculated unloaded quality factor was Q_u = 1590, which gives Q_{ext} = 5633. It was assumed that most of the losses were due to the poor conductivity in the metal, and the sensor was therefore silver plated. After the plating the values were Q_l = 3000 and Q_u = 6418. The conductivity of silver is known to be $\sigma_{Ag} = 6.173*10^7$, but that of invar is not known to the author. The material resembles stainless steel, which has $\sigma_{ss} = 1.1*10^6$. Using these values in (3.34) gives Q_{rad} = 12059 for the radiation quality factor. Testing other values for the conductivity of invar gives $\sigma_{invar} = 0.5...3*10^6 \Rightarrow Q_{rad}$ = 9173...45420. It can be concluded that even though the radiation quality factor is not known exactly, the end grids are very tight, despite of the low cut-off frequency.

7.4.5 The Dielectric Properties of Humid Air

The measurement of humidity with a microwave resonator is based on the dependence of the permittivity of air on the humidity. The negative relative frequency change expressed in ppm is known to be [Smith, 1967]:

$$\frac{\Delta f}{f_0} = \frac{p_{tot}}{2T} \frac{1}{1 + X\dfrac{R_W}{R_L}} \left[1.57 + 1.35X \frac{R_W}{R_L} \left(1 + \frac{5580}{T} \right) \right] \qquad (7.10)$$

where p_{tot} is the total absolute pressure in N/m^2 (= Pa), R_W/R_L is the ratio of the gas constants of water vapour and dry air = 1.608, X is the moisture ratio of the air (the mass of the water vapour to the mass of the dry air), and T is the temperature in ^oK. Note that only the plane numbers without the units should be inserted in the equation. Figure 7.31 shows graphs calculated using (7.10) for typical measurement conditions. The changes in the resonant frequency are seen to be in the range up to 12.35 MHz (= 1.3 $^o/_{oo}$ of 9.5 GHz).

7.4.6 Practical Tests with the Prototype of the Meter

The prototype of the electronics had a resolution of $\Delta f/f_0$ = 0.002 $^o/_{oo}$, and the measurement time was 50 ms per point, which made fast dynamic measurements

possible. The sensor was equipped with two temperature sensors (Pt100), one measuring the temperature of the sensor body, and the other measuring the temperature of the air.

The prototype of the meter was mounted in a veneer sheet dryer and tested continuously for 8 weeks. The temperature was typically 170^{o}C, and the humidity ratio varied in the range X = 0.025…0.7. The reference humidity was measured with a classical psychrometer, i.e. the dry/wet temperature method. The correlation was good: R^2 = 0.9954. Most of the scatter is believed to have been caused by the reference method. The sensor got a thin layer of contamination during the test that was detected mainly as a change of colour. This contamination caused no detectable drift during the test period, even though the meter was never cleaned or recalibrated. Fast changes in temperature caused problems as expected, because of the large mass of the sensor, and hence long time constant for temperature changes. These situations could easily be detected from the difference in the readings of the two temperature sensors.

The test showed that the meter could withstand the conditions in the dryer and measure the humidity over the whole range of conditions occurring during the test. The test was considered successful.

7.4.7 Conclusions

The performance of the meter satisfied the requirements of the applications that it was intended for in terms of accuracy, speed of measurement, measurement range, and immunity to high temperatures and contamination. It was never commercialized, however, because of the high price of the components. With the technology of today it would be possible to realize the meter to a significantly lower cost.

8 ACCURACY OF RESULTS OF SIMULATION WITH HFSS

8.1 Introduction

Studying the accuracy of the results of the simulations with HFSS on a theoretical basis by studying the finite element method is outside the scope of this thesis. However, because simulation results have been used extensively throughout the thesis, the matter of accuracy is important. In some cases comments on the accuracy have been made in the thesis at the places where the results have been presented. In this chapter a summary is presented of the experiences and observations related to the accuracy that were made from the roughly 370 cases that were simulated. The only purpose with the presentation is to provide the reader with a basis for evaluating the reliability of the simulation results presented in the thesis. It should be noted that all simulations were performed with the Hewlett-Packard HFSS version 5.1 for PC, and no conclusions can be drawn about the accuracy of similar simulations performed with newer or older versions of the software.

Indications of the accuracy have been acquired in several ways:

- Simulation results have been compared to exactly calculated results, where possible.
- Simulation results have been compared to measurements.
- The variation of the simulation results as a function of the number of iterations and the convergence of the solution have been studied.
- The behaviour of the simulated frequency response in the vicinity of the cut-off singularity has been studied.
- The smoothness of graphs of simulated data points has been studied.

8.2 Comparison of Simulated Results to Calculated and Measured Results

8.2.1 Broadband Frequency Response

HFSS solves the simulation problem in an iterative process. First the volume of the simulated structure is divided into tetrahedron-shaped elements. Then a solution for the fields is calculated, and the *S* parameters are calculated based on the field solution. Next the model is refined by decreasing the size of the elements in places, where the solution indicates a high field strength. Then a new solution is calculated, and so forth. The convergence of the results is indicated by the parameter ΔS that is calculated by HFSS based on the changes in the *S* parameters from the previous to the last iteration.

The iteration process is performed at a single frequency. If a frequency range has been defined, the iteration is by default performed at the highest frequency, but can be defined otherwise by the user. Then the solutions at the other frequency points are calculated using the same tetrahedron model. If the iteration is performed at a frequency close to a resonant frequency, the refinement of the tetrahedron model will reflect the field pattern of that resonance mode. It may therefore be expected that the accuracy of the results for other resonances, with different field patterns, is poorer. In the few cases, where the frequency response was simulated over a broad range and the iteration was performed close to the main resonance, the results show that HFSS has

predicted the presence and the frequencies of the other resonances fairly well, also far from the iteration frequency. One example is shown in Figs. 6.28 and 6.29, where the simulated and measured responses of the CFR sensor are presented. It should be noted that the spacing of the frequency points (i.e. the frequency resolution) is 2.5 MHz in the measured response and 100 MHz in the simulated response, except close to the main resonant frequency, where it is 2 MHz. The most significant difference between the results is at the frequencies below the main resonance. The simulation predicts an upward sloping response before the antiresonance, where the measurements show an almost flat level. The resonant frequencies can not be compared because the simulation was performed for an infinitely thin fin, and the permittivity of the sample of diesel was not verified.

Another example is shown in Figs. 7.22, 7.25, and 7.26, where the simulated and measured responses of the downhole sensor are shown. The frequency resolution of the measurements is 6.25 MHz, and that of the simulations is 50 MHz, and 2 MHz close to the resonant frequency. In the simulation the metal parts were defined as perfectly conducting, which explains the higher resonance peak. The similarity of the responses is good taking into account the difference in resolution. However, the optimization of the location of the probes, which was performed to eliminate the coupling to the next three modes, more or less failed. The result may have been better if a larger number of iterations would have been used, resulting in smaller tetrahedrons.

Looking at the frequency responses in a narrow bandwidth, the shape of the top of the resonance peak always agreed well with the theoretical shape defined by (3.27). An example is given in Fig. 6.13.

HFSS also provides another possibility to simulate a frequency response, the so-called "fast frequency sweep". In this case the solution derived at the frequency, where the iteration was performed, is directly used to generate the *S* parameters at the other frequencies. This method generates a frequency response much faster than by calculating a new solution for each frequency point. The fast frequency sweep was tested by simulating a piece of rectangular waveguide. The iteration was performed above the cut-off frequency and the frequency sweep was extended below the cut-off. In this case HFSS displayed a perturbation in the vicinity of the cut-off frequency, but failed to predict the cut-off of the power transmission below this frequency. Based on this test the fast frequency sweep method was rejected and not further used in the reported work.

8.2.2 Cut-Off Frequency, Resonant Frequency, and Quality Factor

In a few cases the simulated results can be directly compared to calculated or measured results. In the latter case also measurement and machining errors will be included in the observed deviation between the results. Here simulation results that were used in the thesis are studied as examples illustrating the general accuracy level of the results. The dependence of the accuracy on the number of iterations and related matters are studied in Sec. 8.3.

From the simulations of the cut-off frequency of a cylindrical waveguide as a function of the height of the fin (see Fig. 6.4), two points can be compared to theory. These are the points with the fin extending to the centre of the waveguide, and without

the fin (h = 0). In these cases the simulated cut-off frequency deviates from the calculated by –0.25% and 0.47% respectively.

In the case of a wedge-shaped fin, all the simulated points can be compared to theory. Figure 6.9, shows that the largest deviation in the predicted effect of α is 0.95%. When the graphs were plotted, however, the systematic difference was removed by only plotting the effect of a change in α. When the absolute values are compared, the simulated value for $\alpha = 1^o$ is 1.6% lower than the calculated value. The deviation for other values of α are smaller. The systematic deviation is partly caused by the software bug described below. Another reason may be the finite sector angle used (15^o) in drawing the cylinder.

A sensor was simulated with exactly the same dimensions as the measured sensor only in the case of version #2 of the downhole sensor. As reported in Sec. 7.3.5, the simulated resonant frequency was 1.27% lower than the measured.

The used version of HFSS (5.1 for PC) contains a software bug, which usually (but not always) causes the data in the exported S parameter matrix to be shifted downwards in frequency by one frequency step. The error caused by the bug was considered insignificant for practical purposes, and was therefore not corrected. The step size used, when simulating resonances, was usually 2 or 3 MHz, which means that the reported resonant frequencies have been underestimated by maximum 0.3%. In the case of cut-off frequencies, the error is probably smaller than 0.5% (see Fig. 8.1).

The simulation results for the external quality factor seem to be more variable than those for the frequency. Fortunately the exact value of Q_{ext} is less important than that of f_r. In practice Q_{ext} only affects the peak height as shown in Fig. 6.11. The sensitivity varies, but generally a 10% change in Q_{ext} leads to a 0.4…0.8 dB change in the peak height in the range of interest (roughly: $100 < Q_{ext} < 700$). A difference of a few dB between the predicted and the measured peak height does not affect the performance of the sensor, as long as the peak height is within the dynamic range of the electronics.

CFR sensors with the same dimensions (except fin thickness), including two different values of probe intrusion (l_p), were both simulated and measured filled with diesel fuel (see Sec. 6.5.4). The simulated Q_{ext} was 56% lower than the measured in both cases. This is partly explained by the fact that l_p for the two probe sets in the measured sensor turned out to be 5.7 mm and 7.2 mm, instead of 6 mm and 7.5 mm as designed. The probe tips also had a rounded edge, while they were simulated with a sharp edge. Other reasons may be: General inaccuracy of the simulations, that the problem had not converged enough (see Sec. 8.3), or the same unknown phenomenon that caused the deviation from model (6.7) in going from measuring air to measuring diesel fuel in Fig. 6.15.

For the downhole sensor the simulated and measured values of Q_{ext} show a closer agreement than for the CFR sensor (see Sec. 7.3.5) but the shunt capacitance that was not included in the simulated model, affected the results. The simulated value was 17.5% higher and 27.5% lower than those measured with the smaller and larger shunt capacitances respectively.

The error caused by the process of retrieving Q_{ext} from the simulated S parameters is small, even though the resonant frequency is fitted manually (see Sec. 6.5.2). Because the shape of the resonance peak from the simulations agrees well with the theoretical shape, the resonant frequency can be fitted with a high precision. Tests have shown that even when the value of f_r clearly can be seen to be too small or too

large, the value of Q_{ext} differs less than 1.5% from the value obtained for the optimal fit.

8.3 The Variation of the Results with the Number of Iterations and the Degree of Convergence

The degree of convergence is indicated in HFSS by the parameter ΔS that is calculated from the changes in the S parameters from the previous iteration to the last. The changes are larger if the iteration is performed at a frequency close to the resonant frequency, and thus indicating poorer convergence, than if it is performed further away from the peak. The results for f_r and Q_{ext} do not, however, depend much on how close to the resonant frequency the iteration is performed. Therefore ΔS does not necessarily give a true indication of the quality of the simulation result. This is illustrated in Tab. 8.1, which shows the results from two simulations of the same case of the rectangular resonator described in Sec. 6.5.1. In Simulation 1 the problem does not seem to converge as judged from ΔS, whereas the situation looks better for Simulation 2. The results for f_r and Q_{ext} after 8 iterations are, however, nearly the same: Simulation 1: f_r = 4394.96 MHz and Q_{ext} = 245.1, and Simulation 2: f_r = 4393.20 MHz and Q_{ext} = 239.1. In HFSS the default criterion for good convergence is $\Delta S \leq 0.01$.

Two tests were performed to investigate the dependence of the results for f_r and Q_{ext} on ΔS and the number of iterations. In both cases the rectangular resonator (Sec. 6.5.1) was simulated but with different probe dimensions. The simulations were performed at points 17.9 dB and 15.2 dB below the peak maximum respectively. The results are shown in Tab. 8.2. They show that the resonant frequency is much less dependent on good convergence than the quality factor. While f_r has changed by 0.02% and 0.007% from the 4th to the 7th iteration, Q_{ext} has changed by 27.5% and 24.7%. After the 7th iteration the default criterion $\Delta S \leq 0.01$ is fulfilled in both cases, and Q_{ext} has changed by 1.4% and 0.1% from the 6th to the 7th iteration. It therefore seems that the criterion $\Delta S \leq 0.01$ can be used also in simulations of f_r and Q_{ext} as long as the iteration frequency is located above the resonant frequency, where the

Table 8.1 The ΔS parameter as a function of the number of iterations for two simulations of the same case of the rectangular resonator in Fig. 6.12, performed at two different frequencies. In Simulation 1 and 2 the iteration was performed at a frequency, where the power transmission coefficient was respectively 2.05 dB and 6.94 dB lower than at the resonant frequency. n is the number of iterations.

n	ΔS	
	Simulation 1	Simulation 2
2	0.09	0.095
3	0.047	0.052
4	0.158	0.084
5	0.116	0.076
6	0.152	0.043
7	0.066	0.0243
8	0.162	0.0295

Table 8.2 The results from two simulations of the rectangular resonator (Sec.6.5.1) illustrating the dependence of f_r and Q_{ext} on ΔS and the number of iterations (n).

n	Simulation A			Simulation B		
	ΔS	f_r	Q_{ext}	ΔS	f_r	Q_{ext}
4	0.056	4494.96	1057	0.200	2053.88	595.8
5	0.041	4495.38	1218	0.073	2053.83	650.2
6	0.017	4495.66	1328	0.025	2054.00	742.4
7	0.005	4495.77	1348	0.007	2054.02	743.1

power transmission coefficient is roughly 15…20 dB lower than at the maximum. It should be noted that both f_r and Q_{ext} increase with the number of iterations. This is not a coincidence in these two studied cases, but was noted as a general fact in all the simulations, where results were calculated for a various number of simulations. The phenomenon is neither restricted to narrow peaks. A series of 4 simulations was performed with the rectangular resonator, where the loss was varied: $\tan\delta_{\text{MUT}} = 0$, 0.0096, 0.015, and 0.02. First 5 iterations was used ($\Delta S = 0.014…0.029$) and then 7 iterations ($\Delta S = 0.004…0.008$). The values for Q_{ext} increased by 18.5%, 7.8%, 11.0%, and 10.9% respectively, when the number of iterations was increased from 5 to 7.

8.4 Behaviour of the Frequency Response Close to the Cut-Off Singularity

Several simulations were performed, where the transmission through pieces of various kinds of waveguides was simulated with the purpose of finding the cut-off frequency. The iteration frequency was in the passband and the lowest simulated frequency well below the cut-off frequency. It was then noted that resonance-like features appeared in the frequency response in the vicinity of the cut-off frequency. A typical case is shown in Fig. 8.1, illustrating the transmission through a 10 cm long cylindrical waveguide with an inner diameter of 50 mm, and with a 3 mm thick fin extending to the centre of the waveguide. The frequency response shows a strong gain peak and a subsequent attenuation peak slightly above the cut-of frequency, which are clearly unphysical. In the series of simulations performed with a varying fin thickness, the results of which are shown in Fig. 6.8, the highest encountered gain peak was 22.5 dB, and the deepest subsequent attenuation peak was –10 dB. Because of these peaks the cut-off frequency values shown in Figs. 6.8 and 6.9 were derived by fitting a model based on (4.3) to the simulations so that a good fit was obtained below the cut-off frequency, as shown in Fig. 8.1. In the other cases, where simulated results for the cut-off frequency are reported, the frequency of the gain peak was taken as the cut-off frequency. The difference is in the order of 0.7%. The errors caused by taking the frequency of the gain peak as the cut-off frequency and by the software bug that shifts the data down by one frequency step, partly compensates for each other.

It is probable that the peaks or spikes that are seen in Figs. 7.2, 7.3, 7.7, 7.11, and 7.12 in the frequency responses of the end grids were caused by the same phenomenon, and consequently also unphysical.

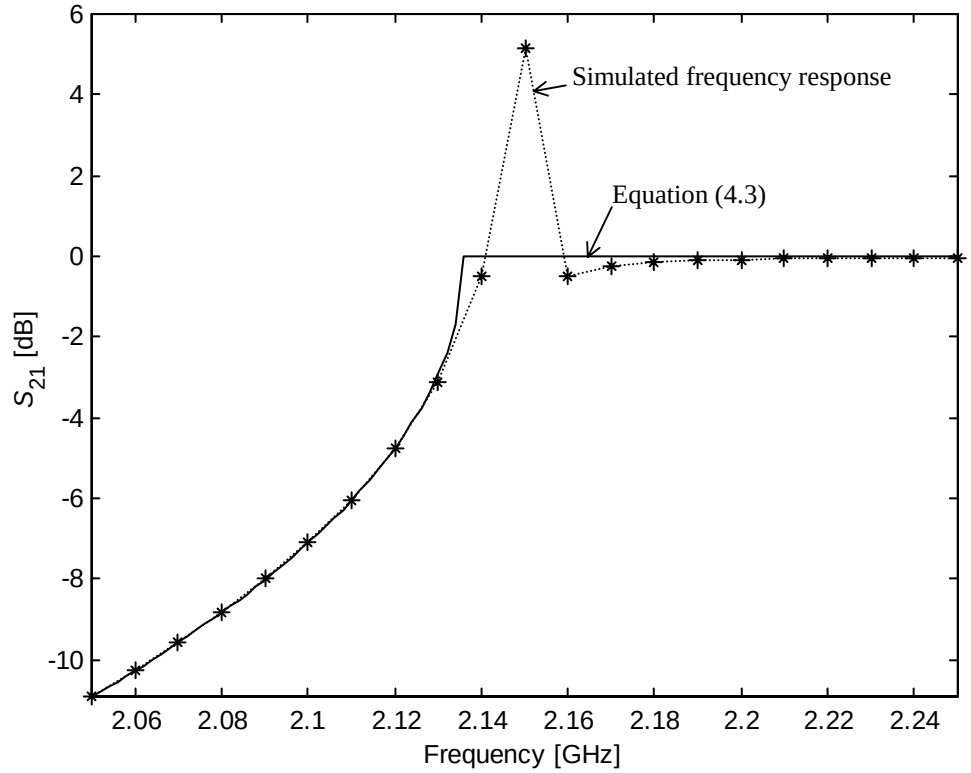

Figure 8.1 The simulated transmission through a 10 cm long cylindrical waveguide with an inner diameter of 50 mm, and with a 3 mm thick fin extending to the centre of the waveguide, displaying unphysical spikes. The fitted model is also shown.

8.5 Smoothness of Simulated Graphs

The random errors in the simulated results can be estimated from the probably unreal humps in the graphs displaying the results (see e.g. Figs. 4.6, 6.4…6.9, and 6.27). The size of the humps is somewhat difficult to estimate accurately, but generally they seem to be smaller than 0.8%. In Fig. 6.7, which has a high resolution, they are smaller than 0.5%, and in Fig. 6.8, where the simulations were performed with a high number of iterations, they are smaller than 0.1%. Again the results are worse for the quality factor. In Fig. 6.27 the humps are smaller than 10%.

8.6 Summary

The main experiences related to the accuracy of the results of the simulations with HFSS, which have been obtained in the work with the thesis, can be summerized as follows:

- The resonant frequency converges towards the final value much faster than the value of the external quality factor.
- The values of both the resonant frequency and the external quality factor increase with the degree of convergence. Because 5 iterations was used in the major part of the work to limit the size of the problem, the values of Q_{ext} reported for the CFR and the downhole sensors are probably slightly too low.

- The convergence indicator ΔS indicates slower convergence, when the iteration is performed closer to the resonant frequency, even though the results seem to show equally fast convergence.
- The default criterion for convergence ($\Delta S \leq 0.01$) can be used, when the iteration is performed at a frequency above the resonant frequency, where the power transmission coefficient is roughly 15…20 dB lower than at the maximum.
- Close to the cut-off frequency of a waveguide the simulated frequency response displays unphysical spikes.
- Judged from the smoothness of the graphs, the random errors are < 1% for the resonant frequency and < 10% for the external quality factor.
- Simulation over a broad bandwidth results in a frequency response with a good general agreement with measurements, even though the iteration is performed on a single frequency.

9 SUGGESTIONS FOR FURTHER STUDIES

The sensors that are described in the thesis all work satisfactorily and do not seem to have any major weaknesses. From a commercial point of view, apart from normal continuous product development, there is no imminent need for further studies of the sensors at the level treated in the thesis. However, from a theoretical point of view, and for being able to provide tools for designing other sensors based on the same principles as the described ones, there are a few things that need to be studied:

- The principle of providing isolation for a resonator with end grids or small enough pipes, i.e. sections, which are below cut-off at the used frequency, is largely dependent on the factor Q_{rad0}. Methods should be developed to calculate Q_{rad0} approximately. Methods developed in conjunction with the development of microwave vacuum tubes, and for calculating the reflection of plane waves from metal grids (e.g. parabolic reflectors, Fabry-Perot resonators, and microwave oven doors) can probably be applied.
- The methods for designing the probes should be studied further. An approximate model for calculating the absolute coupling should be developed, and the models describing the relative dependence on the probe dimensions should be developed further. The effect of using rounded edges on the probes should be studied.
- The dependence of the coupling on the permittivity of the MUT should be studied and an explanation to the deviation from model (6.7) in Fig. 6.15 should be found.
- More should be found out about the convergence of problems simulated with HFSS, and the accuracy of the simulation results. General directions should be compiled for how to simulate resonator sensors to reach the best results in the shortest time.

REFERENCES

Abramowitz, M., and I.A. Stegun, *Handbook of Mathematical Functions*, NewYork: Dover, 10th printing 1972, 1046 p.

The American Heritage Dictionary, Boston, MA: Houghton Mifflin Comp., 1985, 1568 p.

Arfken, G., *Mathematical Methods for Physicists*, Academic Press, 1970, 815 p.

Becher, P., *Emulsions: Theory and Practice*, New York: Reinhold, 2nd ed. 1965, 440 p.

Bramanti, E., M. Bramanti, "A wide-band dielectric characterization system for liquid materials of interest in biology", *J. Microwave Power and Electromagnetic Energy*, Vol. 30, No. 4, 1995, pp. 213-218.

Bramanti, M., E. Salerno, "Electromagnetic techniques for nondestructive testing of dielectric materials: Diffraction Tomography", *J. Microwave Power and Electromagnetic Energy*, Vol. 27, No. 4, 1992, pp. 233-240.

Brodwin, M., J. Benway, "Experimental evaluation of a microwave transmission moisture sensor", *J. Microwave Power*, Vol. 15, No. 4, 1980, pp. 261-265.

Collin, R.E., *Foundations for Microwave Engineering*, New York: McGraw-Hill, 1966, 589 p.

Collin, R.E., *Field Theory of Guided Waves*, 2nd ed., New York: IEEE Press, 1991, 852 p.

Colpitts, B., Y. Pelletier, S. Cogswell, "Complex permittivity measurement of the colorado potato beetle using coaxial probe techniques", *J. of Microwave Power and Electromagnetic Energy*, Vol. 27, No. 3, 1992, pp. 175-182.

Crain, C.M., A.P. Deam, "An airborne refractometer", *The Review of Scientific Instruments*, Vol. 23, No. 4, April 1952.

Felsen, L., N. Marcuvitz, *Radiation and Scattering of Waves*, Reissue (orig. 1973), New York: IEEE Press, 1994, 888 p.

Fischer, M., P. Vainikainen, E. Nyfors, M. Kara, "Fast moisture profile mapping of a wet paper web with a dual-mode resonator array", *Proc. 18th European Microwave Conf.*, Stockholm, September 1988, pp. 607-612.

Fischer, M., P. Vainikainen, E. Nyfors, "Dual-mode stripline resonator array for fast error compensated moisture mapping of paper web", *IEEE MTT-S Int. Microwave Symp. Digest*, Dallas, May 1990a, pp. 1133-1136.

Fischer, M., P. Vainikainen, E. Nyfors, H. Peltoniemi, ”A sensor array for fast CD- and MD-profile measurement of the water content of paper web”, *Automation Days 90*, Control Systems 90, Helsinki, September 1990b, pp. 270-277.

Fischer, M., P. Vainikainen, E. Nyfors, ”A quarter-wave stripline resonator for the measurement of the dielectric properties of substrate materials”, *Proc. 21st European Microwave Conf*., Stuttgart, September 1991, pp. 447-452.

Fischer, M., P. Vainikainen, E. Nyfors, ”Design aspects of stripline resonator sensors for industrial applications”, *J. of Microwave Power and Electromagnetic Energy*, Vol. 30, No. 4, 1995, pp. 246-257.

Fischer, M., “Microwave stripline sensors for industrial measurement applications”, Thesis for the degree of Doctor of Technology, Helsinki University of Technology, Radio Laboratory, Report S 218, 1995, 78 p.

Gaisford, S.G., J.P. Watjen, B.G. Bjørnsen, “Composition monitor and monitoring process using impedance measurements”, United States Patent, patent No. 5,103,181. April 7, 1992.

Gardiol, F.E., *Introduction to Microwaves*, Norwood, MA: Artech House, 1984, 495p.

Handbook of Multiphase Metering, Norwegian Society for Oil and Gas Measurement, NFOGM Report No. 1, 1995, 64 p.

Harrington, R.F., *Time Harmonic Electromagnetic Fields*, New York: McGraw-Hill, 1961, 480 p.

Hasted, J.B., *Aqueous Dielectrics*, London: Chapman and Hall, 1973, 302 p.

Hewlett-Packard Application Note 1217-1, *Basics of measuring the dielectric properties of materials.*

von Hippel, A.R., *Dielectric Materials and Applications*, Cambridge, MA: MIT Press, 1954, 438 p.

Inami, Y., H. Furubayashi, S. Miyoshi, T. Kinosada, Y. Otawa, M. Hijikagawa, “FET-type humidity satellite”, *Sharp Tech. J.*, No. 31, 1985, pp. 31-37.

Jachowicz, R.S., S.D. Senturia, “A thin-film capacitance humidity sensor”, *Sensors & Actuators*, No. 2, 1981, pp. 171-186.

Jakkula, P., “Method and apparatus for measuring the moisture content or dry-matter content of materials using a microwave dielectric waveguide”, US Patent No. 4,755,743, July 5, 1988.

Jakkula, P., “Microwave sensors for consistency measurements in the pulp and paper

industry", Thesis for the degree of Doctor of Technology, Helsinki University of Technology, Radio Laboratory, Report S 231, 1998, 78 p.

Kent, M., E. Kress-Rogers, "Microwave moisture and density measurement in particulate solids", *Trans. Inst. Meas. Control*, Vol. 8, No. 3, July-September 1986, pp. 161-168.

Klein, A., "Microwave determination of moisture in coal: Comparison of attenuation and phase measurement", *J. Microwave Power*, Vol. 16, No. 3-4, 1981, pp. 289-304.

Kobayashi, S., S. Miyahara, "A particulate flow meter using microwaves", *Proc. IMEKO*, Prague, 1985, pp. 112-119.

Kraszewski, A., Ed., *Microwave Aquametry, Electromagnetic Wave Interaction with Water Containing Materials*, IEEE Press, 1996, 484 p.

Marcuvitz, N., *Waveguide Handbook*, New York: McGraw-Hill, 1951, 428 p.

Meyer, W., "Helical resonators for measuring dielectric properties of materials", *IEEE Trans. Microwave Theory Tech*., Vol. MTT-29, No. 3, 1981, pp. 240-247.

Montreuil, J., M. Nachman, "Investigation of the rectilinear motion of an object inside a microwave cavity resonator", *J. Microwave Power and Electromagnetic Energy*, Vol. 27, No. 4, 1992, pp. 241-246.

Nakayama, S., "Simultaneous measurement of basis weight and moisture content of sheet materials by microwave cavity", *Japanese J. of App. Physics*, Vol. 26, No. 7, July 1987, pp. 1198-1199.

Nyfors, E., "On the dielectric properties of dry snow in the 800 MHz to 13 GHz range", Helsinki University of Technology, Radio Laboratory, Report S 135, 1982, 17 p.

Nyfors, E., P. Vainikainen, "Sensor for measuring the mass per unit area of a dielectric layer", *Proc. 14th European Microwave Conf.*, Liége, Belgium, September 1984, pp. 667-672.

Nyfors, E.G., P.-V. Vainikainen, M. Fischer, "Mittausmenetelmä ja -laite huonosti sähköä johtavien levymäisten tai kalvomaisten aineiden sähköisten ominaisuuksien tai niihin vaikuttavien fysikaalisten ominaisuuksien mittaamiseksi mitattavaan aineeseen koskematta. (Method and device for non-contact measurement of the electrical properties, or some other physical properties affecting the electrical properties, of sheet- or foil-like materials of low electrical conductivity; in Finnish)", Suomi-Finland patent No. 74816, March 10, 1988a.

Nyfors, E.G., P.-V. Vainikainen, M. Fischer, "Method and apparatus for the

measurement of properties of sheet- or foil-like materials of low electrical conductivity", United States Patent, patent No. 4,739,249. April 19, 1988b.

Nyfors E., and P. Vainikainen, *Industrial Microwave Sensors*, Norwood, MA.: Artech House, 1989a, 351 p.

Nyfors, E., P. Vainikainen, "Industrial applications of stripline resonator sensors", *Popov Radio Meeting*, Moscow, May 1989b, 6 p.

Nyfors, E.G., P.-V. Vainikainen, M. Fischer, "Radioaaltoja hyväksikäyttävä levymäisten tai kalvomaisten aineiden ominaisuuksien mittausmenetelmä. (Method for the measurement of the properties of sheet- or foil-like materials using radio waves; in Finnish)", Suomi-Finland patent No. 77936, May 10, 1989c.

Nyfors, E. M. Fisher, P. Vainikainen, "On the permittivity of wood and the measurement of moisture and mass per are in veneer sheets", *IEEE MTT-S Int. Microwave Symp., Workshop on Electromag. Wave Int. with Water and Moist Subst.*, Atlanta, June 1993, Invited.

Nyfors, E., Å. Bringsvor, "Måler, særlig for kontinuerlig måling av blandingsforholdet mellom to fluider som strømmer i et rør, f.eks. vanninnhold i olje; samt fremgangsmåte for gjennomføring av slik måling. (Meter, especially for measuring the mixture ratio of two fluids that flow in a pipe, e.g. the water content of oil, and method for performing such measurement; in Norwegian)", Norwegian patent application no. 98.2538. June 3, 1998.

Okamura, S., S. Miyagaki, Z. Ma, "Accurate resonance frequency detection in a microwave moisture measurement", *J. of Microwave Power and Electromagnetic Energy*, Vol. 33, No. 3, 1998, pp. 143-150.

Pozar, D.M., *Microwave Engineering*, Wiley, 2nd ed., 1998, 716 p.

Ramo, S., J.R. Whinnery, T. van Duzer, *Fields and Waves in Communication Electronics*, Wiley, 2nd ed. 1984, 817 p.

Saad, T.S., Ed., *Microwave Engineers' Handbook, Vol. I*, Norwood, MA: Artech House, 1971, 192 p.

Seiyama, T., N. Yamazoe, H. Arai, "Ceramic humidity sensors", *Sensors & Actuators*, No. 4, 1983, pp. 85-96.

Sihvola, A., "Note on frequency dependence of quality factor of cavity resonators", *Electron. Lett.*, Vol. 21, No. 17, 1985, pp. 736-737.

Sihvola, A., E. Nyfors, M. Tiuri, "Mixing formulae and experimental results for the dielectric constant of snow", *J. of Glaciology*, Vol. 31, No. 108, 1985, pp. 163-170.

Smith, D.M., ”Relative humidity effects in microwave resonators”, *IEEE Trans. Microwave Theory Tech.*, MTT-15, pp. 480-482.

Stuchly, M.A., and S.S. Stuchly, “Coaxial line reflection methods for measuring dielectric properties of biological substances at radio and microwave frequencies - A review”, *IEEE Trans. Instr. Meas*., Vol. IM-29, No. 3, September 1980, pp. 176-183.

Sucher, M., J. Fox, eds., *Handbook of Microwave Measurements, Vol. II*, New York: Polytechnic Press, Polytechnic Inst. of Brooklyn, 1963, 1165 p.

Tiuri, M., A. Sihvola, E. Nyfors, M. Hallikainen, ”The complex dielectric constant of snow at microwave frequencies”, *IEEE J. of Oceanic Engineering*, Vol OE-9, No. 5, 1984, pp. 377-382.

Tiuri, M.E., E.G. Nyfors, P.-V. Vainikainen, S.H. Ståhl, ”Mittausmenetelmä ja –laite kiinteän, rakeisen aineen massavirtauksen ja kosteuden tai jonkin muun ominaisuuden määräämiseksi. (Method and device for measuring the material flow and the moisture, or some other property, of a solid, granular material; in Finnish)”, Suomi-Finland patent No. 69372, January 10, 1986.

Tiuri, M.E., E.G. Nyfors, P.-V. Vainikainen, S.H. Ståhl, ”Mittausmenetelmä ja –laite huonosti sähköä johtavan ainekerroksen ominaisuuksien määräämiseksi. (Method and device for measuring the properties of a layer of a material with low electrical conductivity; in Finnish)”, Suomi-Finland patent No. 73084, August 10, 1987.

Toropainen, A., P. Vainikainen, E. Nyfors, ”Microwave humidity sensor for difficult environmental conditions”, *Proc. 17th European Microwave Conf.*, Rome, September 1987, pp. 887-891.

Toropainen, A., ”Mikroaaltoilmankosteusmittarin kehittäminen”, Thesis for the degree of Licentiate of Technology, Helsinki University of Technology, Radio Laboratory, 1989.

Vainikainen, P., E. Nyfors, ”Sensor for measuring the mass per unit area of a dielectric layer: Results of using an array of sensors in a particle board factory”, *Proc. 15th European Microwave Conf.*, Paris, September 1985, pp. 901-905.

Vainikainen, P, R. Agarwal, E. Nyfors, A. Toropainen, ”Electromagnetic humidity sensor for industrial applications”, *Electronics Letters*, Vol. 22, No. 19, 1986, pp. 985-987.

Vainikainen, P., E. Nyfors, M. Fischer, ”Sensor for measuring the moisture content

and mass per unit area of veneer", *Proc. 16th European Microwave Conf.*, Dublin, September 1986, pp. 382-387.

Vainikainen, P., E. Nyfors, M. Fischer, "Radiowave sensor for measuring the properties of dielectric sheets; Application to veneer moisture content and mass per unit area measurement", *Proc. IEEE Instrumentation and Measurement Technology Conf. (IMTC/87)*, Boston, April 1987a, pp. 193-196.

Vainikainen, P., E. Nyfors, M. Fischer, "Radiowave sensor for measuring the properties of sheetlike dielectric material; Application to veneer moisture content and mass per unit area measurement", *IEEE Trans. Instr. Meas.*, Vol. IM-36, No. 4, December 1987b, pp. 1036-1039.

Vainikainen, P., "Measurement electronics of industrial microwave resonator sensors", Thesis for the degree of Doctor of Technology, Helsinki University of Technology, Radio Laboratory, Report S 194, 1991, 108 p.

Waldron, R.A., "Perturbation theory of resonant cavities", *Proc. IEE*, Vol 107C,1960, pp. 272-274.

Wenger, N.C., J. Smetana, " Hydrogen density measurements using an open-ended microwave cavity", *IEEE Trans. Instr. Meas.*, May 1972, pp. 105-114.